Downloaded from orbit.dtu.dk on: May 05, 2023

DTU Library

Color metasurfaces in industrial perspective

Højlund-Nielsen, Emil

Publication date:
2015

Document Version
Publisher's PDF, also known as Version of record

Link back to DTU Orbit

Citation (APA):
Højlund-Nielsen, E. (2015). *Color metasurfaces in industrial perspective*. DTU Nanotech.

General rights
Copyright and moral rights for the publications made accessible in the public portal are retained by the authors and/or other copyright owners and it is a condition of accessing publications that users recognise and abide by the legal requirements associated with these rights.

- Users may download and print one copy of any publication from the public portal for the purpose of private study or research.
- You may not further distribute the material or use it for any profit-making activity or commercial gain
- You may freely distribute the URL identifying the publication in the public portal

If you believe that this document breaches copyright please contact us providing details, and we will remove access to the work immediately and investigate your claim.

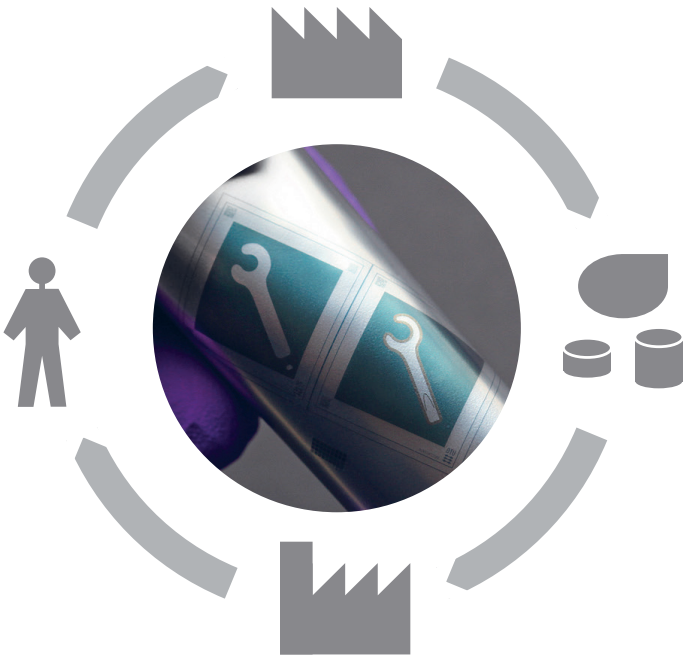

Color Metasurfaces in Industrial Perspective

Emil Højlund-Nielsen
PhD Thesis December 2015

DTU Nanotech
Department of Micro- and Nanotechnology

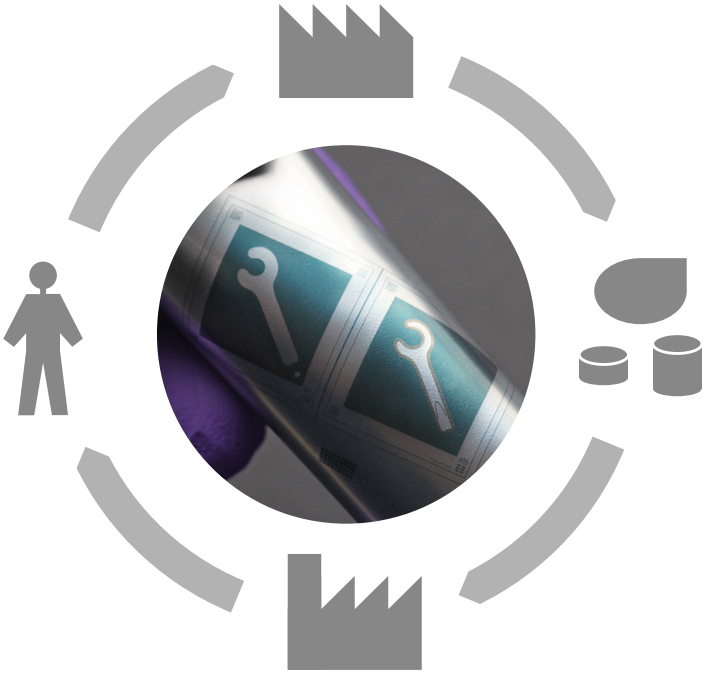

Color Metasurfaces in Industrial Perspective

PhD Thesis

Emil Højlund-Nielsen

Supervisors:

Prof. N. Asger Mortensen

Prof. Anders Kristensen

Department of Micro- and Nanotechnology,

Technical University of Denmark

December 2015

Abstract

This doctoral thesis describes the utilization of color metasurfaces in an industrial perspective, where nano-scale textures and contingent post processing replace inks, dyes and pigments in plastic production. The concept of colors by structure arguably reduces the number of raw materials and eliminates mechanical color sorting in the recycling stage.

First, the development of experimental processes, techniques and equipment is described. A single-spot electron beam lithography scheme for master pattern definition is developed, and optical characterization equipment for both laboratory and production environments is developed.

Second, the fundamental optical surface properties of dielectric materials are investigated within the framework of mass production applicability. Different colors can be realized using a single-step etching process by altering the nano-texture in high-index materials, exemplified in silicon. However, only corresponding faint colors appear in polymeric materials. The concept of all-polymer pigment-free coloration seems somewhat restricted in relation to widespread industrial employment.

Finally, a novel plasmon color technology for structural coloration in plastics is developed based on metal-coated polymer nano-textures and a protective coating system. The technology utilizes a hybrid disk-hole plasmonic mode for resonances in the visible spectrum, based on aluminum as a cheap and abundant plasmonic material. Angle-insensitive scratch-resistant colors are demonstrated, and it is shown that the dependence on polarization can be controlled. In collaboration with industry, polymer-based colored metasurfaces of square-centimeter size are demonstrated by embossing, injection molding, roll-to-roll printing, and film insert molding with full compatibility. Furthermore, post production color modification by laser ablation is briefly described. The environmental benefits are analyzed by life cycle analysis, where the high recyclability leads to reduced environmental impact compared to conventional plastic production. In summary, a promising future is anticipated for plasmonic colors as a decoration element for everyday use.

Resumé

Denne PhD-afhandling beskriver udnyttelsen af farve-metaoverflader i et industrielt perspektiv, hvor teksturer i nanoskala og passende efterprocessering erstatter blæk, farvestoffer og pigmenter i plastikproduktionen. Strukturer med farvegenskaber forventes at reducere antallet af råmaterialer og eliminere den mekaniske sortering i genbrugsfasen.

Først beskrives udviklingen af de eksperimentelle processer, teknikker og udstyr. En enkeltskudsbaseret elektronstrålelitografiproces udvikles til at definere original-mønster, og optisk karakteriseringsudstyr udvikles til både laboratorie- og produktionsmiljøer.

Dernæst undersøges de fundamentelle overfladeegenskaber af dielektriske materialer i forhold til masseproduktion. Forskellige farver kan realiseres ved brug af en etskridtsætseproces ved at ændre nanoteksturen i højindeks-materialer, hvilket eksemplificeres i silicium. Dog fremkommer kun tilsvarende svage farver i polymermaterialer. Pigmentfri farvning baseret udelukkende på polymer synes begrænset i forhold til generel industriel anvendelse.

Afslutningsvis udvikles en ny plasmon-farveteknologi til strukturel farvning i plastik baseret på metalbelagte polymerteksturer samt et beskyttende belægningssystem. Teknologien udnytter en disk-hul plasmonisk hybridtilstand til at skabe resonanser i det visuelle spektrum, hvor aluminium bruges som et billigt og tilgængeligt plasmonisk materiale. Ikke-vinkelfølsomme, ridsfaste farver demonstreres, og det vises, at polariseringsafhængigheden kan kontrolleres. I samarbejde med industrien demonstreres polymer-baserede farvede metaoverflader i kvadratcentimeterstørrelse ved termisk prægning, sprøjtestøbning, rulle-til-rulle-printning og film-indsats-støbning med fuld kompatibilitet. Ydermere beskrives kort farvemodifikation ved lasersmeltning efter produktionen. De miljømæssige fordele analyseres med en livscyklusanalyse, hvor den høje genbrugsgrad leder til en reduceret miljømæssig påvirkning sammenlignet med traditionel plastikproduktion. Sammenfattende forventes en lovende fremtid for plasmoniske farver som et dekorationselement til hverdagsbrug.

Preface

This doctoral thesis is devised at the Department of Micro and Nanotechnology at the Technical University of Denmark 2012-2015. This work concludes the PhD degree. The project has been carried out in the Optofluidics group, supervised by Prof. Niels Asger Mortensen (DTU Fotonik) and Prof. Anders Kristensen (DTU Nanotech). The underlying project has been founded by a scholarship from the Technical University of Denmark (1/3) and by the European Commission via the FP7MMP Integrated project PLAST4FUTURE (2/3). For fabrication the cleanroom facilities of the Danish National Center for Micro- and Nanofabrication, DTU Danchip, were used.

Kongens Lyngby, December 2015.

_____

Emil Højlund-Nielsen, emiho

DTU Nanotech - Department of Micro and Nanotecnology

Technical University of Denmark - DTU

Building 345 East

DK-2800 Kongens Lyngby

Denmark

Acknowledgements

Thanks to Alicia Johansson and Theodor Nielsen, NIL Technology, for a fruitful industrial collaboration with many inspiring discussions. The perspectives of these discussions are at the heart of this thesis.

Thanks to the other 13 project partners in Plast4Future, especially LEGO Concept Center and Centro Ricerche Fiat for providing access to industrial facilities.

Thanks to Tapio Mäkelä and the Technical Research Center of Finland for collaboration on roll-to-roll printing. Thanks to Prof. Uriel Levy and the Hebrew University of Jerusalem for collaboration and hospitality during my short visit February 2014.

Thanks to Tine Griebe and the rest of the Danchip staff for discussions and technical assistance in the cleanroom.

Thanks to Majken Lerche Møller for administrative assistance and excellent travel companionship across Europe and to Jesper Scheel for photography.

A thanks to the comrades in arms, Alexander B. Christiansen and Jeppe Clausen, for collaboration on a daily basis. Thanks to the Optofluidics group for a pleasant work environment.

A special thanks to my two student assistants in 2015, Lea S. Berthou and Kristoffer Mathiesen, for hard work and commitment around the clock when needed.

Thanks to supervisors Prof. N. Asger Mortensen and Prof. Anders Kristensen for providing the opportunity to take on the journey.

Thanks to my family, my friends, and my girlfriend for patience and understanding.

Finally, I would like to thank the Technical University of Denmark and the European Commission for the financial support to carry out the project.

Without the generous help of these individuals and organizations, this thesis would not have been possible.

Sincerely

Emil Højlund-Nielsen

Publication list

Articles in peer-review journals (ISI)

E. Højlund-Nielsen, J. Weirich, J. Nørregaard, J. Garnaes, N.A. Mortensen, & A. Kristensen (2014). "Angle-independent structural colors of silicon". *Journal of Nanophotonics*, 8(1), 083988. doi: 10.1117/1.JNP.8.083988. See A.3 on page 127.

E. Højlund-Nielsen, T. Greibe, N.A. Mortensen, & A. Kristensen (2014). "Single-spot e-beam lithography for defining large arrays of nano-holes", *Microelectronic Engineering*, 121, 104–107. doi: 10.1016/j.mee.2014.03.025. See A.2 on page 122.

J.S. Clausen, E. Højlund-Nielsen, A.B. Christiansen, S. Yazdi, M. Grajower, H. Taha, U. Levy, A. Kristensen, N.A. Mortensen. (2014). "Plasmonic metasurfaces for coloration of plastic consumer products" *Nano Letters*, 14(8), 4499–4504. doi: 10.1021/nl5014986. See A.4 on page 137.

E. Højlund-Nielsen, X. Zhu, M.S. Carstensen, M.K. Sørensen, C. Vannahme, N.A. Mortensen, A. Kristensen (2015). "Polarization-dependent aluminum metasurface operating at 450 nm", *Optics Express*, 23(22), 28829. doi: 10.1364/OE.23.028829. See A.5 on page 144.

X. Zhu, C. Vannahme, E. Højlund-Nielsen, N.A. Mortensen, A. Kristensen, "Plasmonic color laser printing", *Nature Nanotechnology*, advance online publication, doi: 10.1038/nnano.2015.285. See A.7 on page 157.

Work in preparation of peer-review journals (ISI)

"Plasmonic colors: Toward mass-production of metasurfaces", Højlund-Nielsen *et al.* (submitted). See A.8 on page 164.

Other publications

A.B. Christiansen, E. Højlund-Nielsen, J. Clausen, G.P. Caringal, N.A. Mortensen, A. Kristensen (2013). "Imprinted and injection-molded nano-structured optical surfaces", *Proceedings of SPIE*, 8818(881803), 1–12. doi: 10.1117/12.2025133. See A.1 on page 109.

E. Højlund-Nielsen, J. Clausen, L.H. Thamdrup, M. Zalkovskij, T. Nielsen, T. Mäkelä, J. Ahopelto, N.A. Mortensen, A. Kristensen. "Plasmonic Structural Colors For Plastic Consumer Products" ("Roll-to-roll Imprinted Plasmonic Structural Colors"), *Advanced Manufacturing, Electronics and Microsystems TechConnect Briefs 2015*, Photonic Materials & Devices Chapter 5, Nano Science and Technology Institute, CRC Press Reference, ISBN 9781498747301, pp. 143 - 146. See A.6 on page 152.

Patents

A. Kristensen, E. Højlund-Nielsen, N.A. Mortensen, J. Nørregaard. "An optical device capable of providing a structural color, and a corresponding method of manufacturing such a device", WO2014194920 (A1).

J. Clausen, N.A. Mortensen, A. Kristensen, E. Højlund-Nielsen, C. Jeppesen, A.B. Christiansen, "Nanostructures for structural colouring", WO2015028037 (A1).

X. Zhu, A. Kristensen, E. Højlund-Nielsen, C. Vannahme, N. A. Mortensen, "Photothermal modification of plasmonic structures", EP application 15171905.1.

Conference and Workshop Contributions

E. Højlund-Nielsen, J. Clausen, A.B. Christiansen, T. Greibe, N.A. Mortensen, A. Kristensen. "Fast-writing E-beam for large arrays of nano-holes", poster presented at the Micro and Nano Engineering conference (MNE) 2013, London, and at the Polymer Replication at the Nanoscale conference (PRN) 2014, Copenhagen.

E. Højlund-Nielsen, N.A. Mortensen, A. Kristensen. "Plasmonic Structural Colors for Plastic Consumer Products", poster presentation at the DTU Sustain conference 2014, Copenhagen.

E. Højlund-Nielsen, J. Clausen, X. Zhu, L. Thamdrup, M. Zalkovskij, T. Nielsen, T. Makela, J. Ahopelto, N. A. Mortensen, A. Kristensen. "Plasmonic Structural Colors For Plastic Consumer Products", talk at the TechConnect World Innovation Conference 2015, Washington.

E. Højlund-Nielsen, D. Catak, K. Mathiesen, L. Berthou, A. Kristensen. "Replication of nano-scale features by injection molding", oral presentation at the Plast4Future Workshop 2015, Billund.

Technical Reports

E. Højlund-Nielsen, T. Nielsen, N. Li Pira, L. Belforte, V. Grasso, I. Di Vora, S. Padovani, M.C. Frijia, S. Priante, A.B. Christiansen, R. Taboryski, M.R. Sonne, C. Baum, T. Gotthardt, B. Meiers, M. Diemer, E.L. Simonsen, M. Døssing, M. Ordóñez, H. Atasoy, B. Bilenberg, J. Nørregaard, K. Smistrup, L.H. Thamdrup, N.J. Mikkelsen, B. Högman, A. Kristensen. Confidential Title, Deliverable report 2.1, FP7 MMP Plast4Future (NMP2-SE-2012-314345), European Commission, 2013, 160 pages.

E. Højlund-Nielsen, J. Clausen, A. B. Christiansen, N. Li Pira, A. Kristensen. Confidential Title, Deliverable report 2.2, FP7 MMP Plast4Future (NMP2-SE-2012-314345), European Commission, 2015, 45 pages.

E. Højlund-Nielsen, A. Johansson, L. Sun, R. Taboryski, A. Kristensen. Confidential Title, Deliverable report 2.3, FP7 MMP Plast4Future (NMP2-SE-2012-314345), European Commission, 2015, 19 pages.

E. Højlund-Nielsen, E. L. Simonsen, M. Diemer, T. Nielsen, M. Døssing, N. Li Pira, A. Kristensen. Confidential Title, Deliverable report 2.4, FP7 MMP Plast4Future (NMP2-SE-2012-314345), European Commission, 2014, 18 pages.

E. Højlund-Nielsen, N. Li Pira, A. Kristensen. Confidential Title, Deliverable report 2.5, FP7 MMP Plast4Future (NMP2-SE-2012-314345), European Commission FP7, 2015, 15 pages.

E. Højlund-Nielsen, A.L. Duque, S. Olsen, A. Kristensen. Confidential title, Deliverable report 5.1, FP7 MMP Plast4Future (NMP2-SE-2012-314345), European Commission FP7, 2014, 77 pages.

Supervision

F.F. Stæger, N. Holck, R. Højlund. "Nanotekstureredе funktionelle overflader - Undervisningsmateriale til STX". Consultancy project, supervisor E. Højlund-Nielsen, Technical University of Denmark, August 2013.

D.K. Nyholm-Petersen. "Forbedring af laboratorieudstyr til nanostrukturerede overflader". Bachelor thesis (diplom afgangsprojekt), supervisors N.L. Pedersen, E. Højlund-Nielsen, Technical University of Denmark, January 2014.

A.L. Duque. "Life cycle assessment of nanostructuring for color effects in polymers". Bachelor thesis, supervisors S.I. Olsen, E. Højlund Nielsen, A. Kristensen, Technical University of Denmark, January 2014.

F. Lara, S.P. Nielsen, M. Meincke, L. Hendriksen. “Colored Paint-free Plastic by Roll-2-Roll Colored Nanoimprint film for In-Mould Labeling - Sustainable assessment”. Course project, supervisors E. Højlund-Nielsen, S.I. Olsen, K. Mølhave, Technical University of Denmark, January 2014.

N. Thomassen, L.S. Berthou. “Development of MATLAB Software for Measuring Structural Colors”. Second year university project (Fagpakkeprojekt), supervisor E. Højlund-Nielsen, Technical University of Denmark, June 2014.

B. Greenlay, E. Ha, M. Haines, M. Leung. “Passivated Anti-Reflective Inexpensive Solution (PARIS)”. Collaboration project, supervisors E. Højlund-Nielsen, A.B. Christiansen, N.A. Mortensen, A. Kristensen, University of Waterloo, 2013-2015.

M.S. Carstensen, M. Korning. “Fabrication and characterization of polarization induced surface coloring”. Course project, supervisor E. Højlund-Nielsen, Technical University of Denmark, June 2015.

Contents

Front page: Illustration of a recycle-based component life cycle and a photograph of a rolled-up embossed surface with 20 nm aluminum film, 50 μm thick polymer foil, and a protective diffuser top coating system. The color metasurface is an example of the developed plasmon color technology based on localized surface plasmon resonances. The colors are defined with a resolution of 127,000 dots-per-inch, do not fade over time and are in-sensitive to the surrounding light environment. The surface is durable, scratch-resistant and bendable. Finally, the concept of color by structure arguably reduces the number of raw materials and eliminates mechanical color sorting in the recycling stage.

Chapter 1

Introduction

The human eye can distinguish close to 10 million colors. It forms the basis of the faculty of sight, from which human beings arguably glean the most important information about their surroundings. In general, vision is considered one of the key developments in animal evolution and for human beings colors play a critical role, for example as indicators of putrid food. Besides being important for survival, the colors of nature have also been of great fascination and inspiration. This is reflected throughout history as artworks - from ancient paintings of sunsets and animals to modern art forms of geometry and contrast. In many ways, one might say, humans perceive in color. The importance of color calls for scientific study and indicates the care taken in controlling the appearance of consumer products, such as toys for children or cars for adults.

The color of an object is the result of a complex interaction of the light incident on the object, the optical characteristics of the object, and human perception [Harold, 2001]. In many products, especially plastic products, the base color is given by bulk properties. Added surface decoration provides additional cost-effective color effects, for example logos, text decoration or line art to enhance aesthetic value. This doctoral thesis describes the utilization of color metasurfaces in a plastic production perspective, where colors and materials play an important role.

Plastics materials are a key enabler of the modern mass consumption society through cost efficient and durable consumables. As an example, the European plastics industry directly employs more than 1.4 million people [PlasticsEurope, 2015]. Since 1950, the global production of plastic has seen exponential growth, see Figure 1.1a. In 2014, plastic production was 311 Mtonnes globally and 59 Mtonnes in Europe. The total registered waste generation of post-consumer plastics in Europe was 25.8 Mtonnes, where 30.8 % ended as landfill, 39.5 % was burned and only 29.7 % of the generated waste were recycled [PlasticsEurope, 2015]. Today most plastic products are burned after use or end in landfills. Less than one third of the generated waste in Europe is recycled.

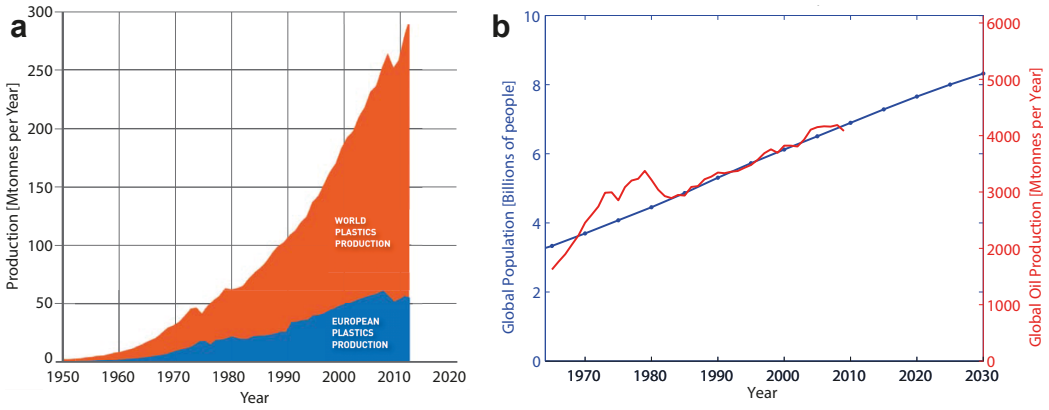

Figure 1.1: a) Global plastic production. Figure from literature [PlasticsEurope, 2013]. b) Oil production [BP, 2010] and medium variant population forecast [United-Nations, 2010].

Plastics originates from crude oil with a mass conversion-rate of about 1:2 and the conversion contributes with about 0.5 % of the global warming [Gervet, 2007]. In Figure 1.2b, the correlation between global population and oil production (crude oil, shale oil and oil sands etc.) can be seen. The time frame of the decline of oil production, as more and more resources dry out, may be discussed. The estimates of global population growth rate and increase in global living standard may also be discussed. Inevitably, the oil production will come to a halt due to a lack of resources in the earth's crust. From this point on, the world consumption must rely on synthetic oil products. Therefore, recycling and life-cycle assessment supporting a circular economy will become increasingly important, also for materials today considered of low value. In this context, the use of coloration makes recycling difficult because the powerful pigments tend to be mixed in the recycling stage. After usage, the products must be mechanically sorted by color before recycling [Al-Salem et al., 2009], limiting any large-scale efficient recycling effort.

As an alternative to chemistry-based coloring, nano-scale structural coloring has been proposed [Kumar et al., 2012] to reduce the number of materials needed and to increase pattern resolution. Here colors are created by structural based light-matter interactions in the surface. Thereby, the sorting by color can be avoided in the recycling stage as destruction of the nano-scale texture removes any color perception, leaving a (semi)-transparent bulk polymer ready for re-processing.

This doctoral thesis describes the utilization of color metasurfaces in an industrial perspective, where nano-scale textures and contingent post processing replace inks, dyes and pigments in plastic production. The concept of color by structure arguably reduces the number of raw materials and eliminates mechanical color sorting in the recycling stage providing new perspectives for the sustainability of plastic products.

1.0.1 The Replication Constraint

This project is closely related to the EC FP7 Plast4Future project platform, led by DTU Nanotech with LEGO Systems A/S as end-user for coloring. The vision of the Plast4Future platform is to develop and implement a technology that enables the use of nano-structured surfaces on injection molded plastic components. Injection molding (British english: moulding) is a manufacturing process for producing plastic parts. Different plastic materials known as granulates are fed into a barrel, where they are heated to liquid state and mixed. Then the polymer melt is injected into a mold cavity, where it cools and solidifies to the inverse shape of the cavity. Injection molding is the industry-standard for manufacturing plastic parts in large quantities, from small components in the mm-range to entire automotive body panels.

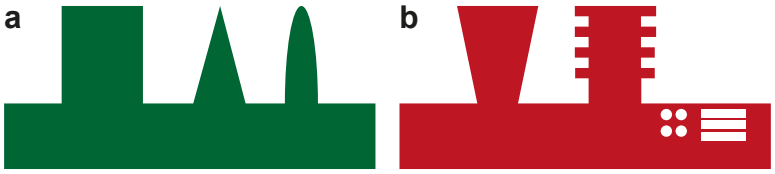

Figure 1.2: Replication constraint illustration. a) Allowed nano-topologies with vertical or positive sloped side walls. b) Disallowed nano-topologies such as negative slopes, overhang and air filled voids.

The demand for structures which allow for release after the formation of the desired surface structures is common to all molding techniques. This simple, yet fundamental, machine operation principle puts quite restrictive limitations on the allowed structural micro and nanoscale geometries. Figure 1.2 exemplifies the compatibility with injection molding technology of different types of surface topologies. Negative slopes and air-filled cavities are disallowed. This constraint on geometry will be referred to as the "replication constraint" in this thesis. It constitutes the final frontier of polymer replication techniques at the nanoscale and much commercial production does not fully exploit this constraint. The replication constraint is considered fundamental to the conducted work and the obtained results described here aim at evaluation in context of this industrial framework.

1.1 Literature Survey - State of the Art

This Literature Survey concerns structural colors found in nature and fabricated in the laboratory. In light of the replication constraint defined on page 3, the task at hand is to search the literature for topologies that may provide robust coloration and at the same time respecting the replication constraint. In the next section on page 9, a thesis statement will be given on the basis of this survey. A survey of metallic schemes is provided in Section 4.2 on page 51.

Seeking inspiration in nature is referred to as Biomimetics [Parker and Townley, 2007]. Optical biomimetics focuses on the use of conventional engineering methods to make direct analogues of the reflectors and anti-reflectors found in nature.

1.1.1 Structural Colors found in Nature

Structural colors are optical phenomena of physical origin, where micro and nanoscale structures determine the reflected spectrum of light, although an unambiguous definition has not been settled yet [Kinoshita et al., 2008, p. 2]. According to Kinoshita *et al.*, the mechanisms of structural colors can be categorized into 1) thin-film interference, 2) multilayer interference, 3) diffraction grating optical effects and 4) photonic crystal effects. Based on this thesis and the literature in general, this distinction seems reasonable. A wealth of observable natural occurring structural colors on butterflies, beetles, and other animals have been reported [Vukusic et al., 2000, Vukusic et al., 2004, Prum et al., 2006, Noyes et al., 2007, Parker and Townley, 2007, Seago et al., 2009, Saranathan et al., 2010, Teyssier et al., 2015]. Here, the focus is on selected aspects related to the replication constraint described in the previous section. That includes all-dielectric approaches and photonic crystals.

After the invention of the scanning electron microscope, a clear link between structure and color could be established. The first article known on the subject is from 1939 [Frank and Ruska, 1939], followed by the first observations of the color-producing structures on the *Morpho* butterfly [Anderson and Richards, 1942, Gentil, 1942]. The *Morpho* butterfly is among the most studied objects [Vukusic et al., 1999, Vukusic and Sambles, 2003]. In Figure 1.3, scanning micrographs can be seen. The specific structure design given in Figure 1.3b is responsible for the blue color effect. The design can be described as a periodic photonic crystal with discrete multi-layers made from cuticle and air imposed with deliberate disorder[1]. The butterfly reflects omnidirectional blue light and is visible up to a distance of 800 meters away [Vukusic and Sambles, 2003]. Although, the attractive appearance of the *Morpho* provides angle-insensitive coloring, the underlying structure is clearly not compatible with injection molding and the replication constraint.

Two different areas may also be used to create a combined color effect [Vukusic et al., 2000]. In Figure 1.4, an example of a pixel effect on the scales of the butterfly *P. palinurus* is seen. This structure produces two simultaneous colors, yellow and blue. The blue annulus is created by a double reflection from the opposite and perpendicular concavity

[1] According to [Saito et al., 2006], "*an optical interference arises for the specific wavelength within a single discrete multilayer (a shelf structure). The light is reflected in a wide angular range because of the diffraction from a small width of the shelf. The high reflectivity is attributed to the narrow gap around 300 nm or smaller between the neighboring shelves, which is less than the wavelength of the blue light. The high reflectivity is also due to the one-dimensional (line) profiles in the lateral (in-plane) structure. In fact, a two-dimensional isotropic structure such as a pixel pattern would scatter the light at all angles, and it causes a critical decrease of reflectivity at any angle of observation. Randomness in the height of the shelves and in the breaks in the line profiles has an essential role to prevent the multicolor caused by an interference effect in the usual multilayer.*"

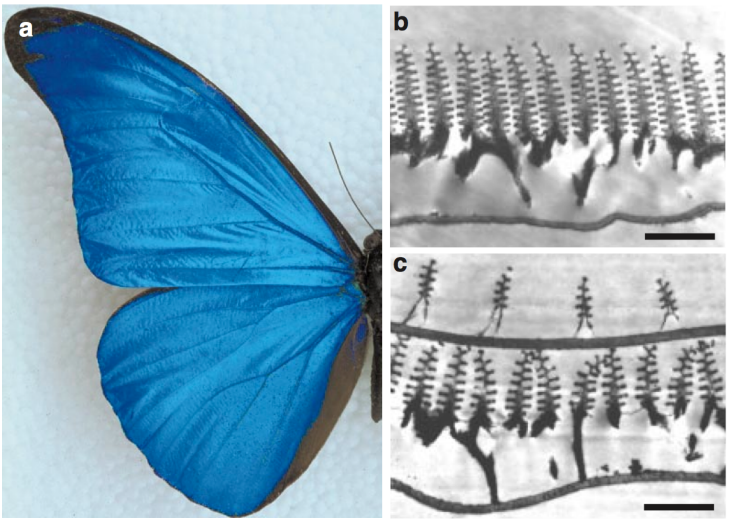

Figure 1.3: Iridescence in the butterfly *Morpho rhetenor*. a: Real color image. b: TEM image showing wing-scale cross-section. Scalebar 1.8 μm. c: TEM image of a wing-scale cross-section of the related species *Morpho didius* revealing discretely configured multilayers. Scalebar 1.3 μm. Figure from literature [Vukusic et al., 1999, Vukusic and Sambles, 2003].

sides, whereas the yellow color originates from the Bragg stack in the bottom of the cavity. The "juxtaposition" of these two colors synthesizes the green coloration perceived by the human eye. From Figure 1.4b, it is seen that the surface consists of several layers of air-material void alterations. Similar to the underlying structure of the *Morpho* butterfly, the underlying structure for the colors of the *P. palinurus* butterfly is not compatible with injection molding and the replication constraint.

Another example is active color change in chameleons by photonic crystals [Teyssier et al., 2015]. Chameleons shift color through active tuning of a lattice of guanine nanocrystals within a superficial thick layer of dermal iridophores.

Besides butterflies and chameleons, beetles also exhibit structural based optical effects. In Seago *et al.* diffraction grating structures found in nature are reviewed [Seago et al., 2009]. An example is provided in Figure 1.5. All beetle gratings investigated are found to show reflective properties. Iridescence arising from diffraction gratings always takes the form of one or more ordered spectra as discussed later in Section 3.1.2 on page 32. Based on Figure 1.5, the optical effect given by the grating on top of brown background is most likely similar to what can be expected from one-layer surface decorations in plastic on top of a bulk color.

A few words on material properties are also needed. The refractive index of the single scale microstructures of two species of *Morpho* butterfly has been measured to be $n = (1.56 \pm 0.01) + (0.06 \pm 0.01)i$ [Vukusic et al., 1999]. Measurements on a beetle *Chrysochroa raja* [Noyes et al., 2007], determined the refractive indices of two layers to

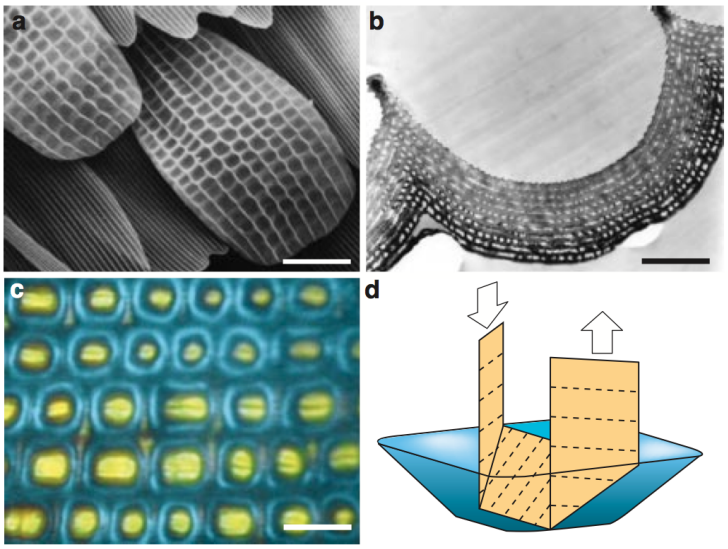

Figure 1.4: Pixel effect *P. palinurus*. (a) Scanning electron micrograph of scale with array of concavities. Scalebar 15 μm. (b) Transmission electron micrograph of concavity cross-section. (c) Unpolarized optical microscope image of dual-color scale reflection. Scalebar 6 μm. (d) Illustration of polarization providing double reflection from orthogonal concavity sides. Figure from literature [Vukusic et al., 2000].

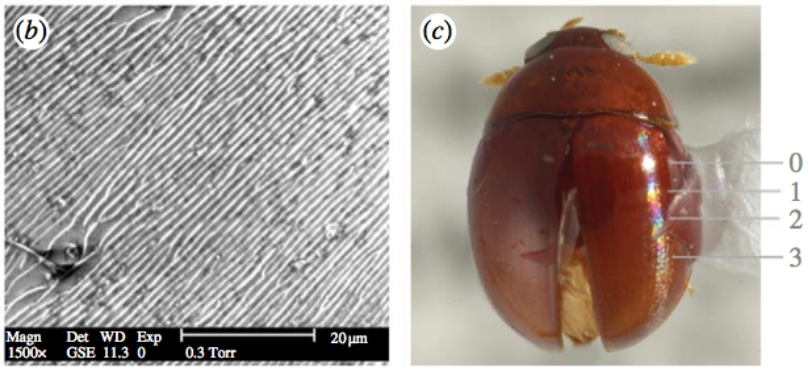

Figure 1.5: Beetle diffraction gratings. (b) Scanning electron micrograph of the species *Sphaeridiinae gen. sp. (Hydrophilidae)*. (c) *Sphaeridiinae gen. sp., habitus* view with zero, first, second and third spectral orders labelled. Figure from literature [Seago et al., 2009].

be 1.68 and 1.55. A refractive index in this range is typical for most polymeric materials, as organic material consists of long chains of carbon and hydrogen. For example acrylonitrile-butadiene-styrene (ABS) has a refractive index of 1.515 [Ariño et al., 2005]. Assuming that other beetle surface structures have a similar refractive index, the diffraction effect displayed in Figure 1.5c originates from a structure with a refractive index in the order of 1.5 to 1.6. Therefore, it seems reasonable to expect color effects similar to those seen in Figure 1.5 for diffraction patterns manufactured in plastics. This is inspiring news, because the diffraction iridescence in Figure 1.5c overrules the bulk color background where the incident light is reflected off the surface. However, it is also clear that the diffracted iridescence is only visible in the directly reflected light.

In conclusion, many different color effects can been observed in nature utilizing multilayer void structures. However, for single-layer structures compatible with the replication constraint, only diffracted iridescence seems to provide a color effect.

1.1.2 All-dielectric Artificial Structural Colors

This section provides an overview of the achievements in recent years to reproduce the structural color topologies observed in nature. The literature is rich in demonstrations [Saito et al., 2004, Saito et al., 2006, Saito et al., 2009, Chung et al., 2012, Finlayson and Baumberg, 2013]. Therefore, the focus is on selected aspects related to the replication constraint described on page 3. A survey of metallic schemes is provided in Section 4.2 on page 51.

The first efforts within the field can collectively be described as controlled serial structuring schemes, where for example an electron beam writer is used to define a pattern, that through different process steps such as dry etching, yields the final desired surface topology for a prescribed appearance. Figure 1.6a provides an example of an antireflective black structure directly defined by electron beam lithography [Kanamori et al., 1999]. These structures respect the replication constraint, although with a considerable aspect ratio.

The efforts progressed towards controlled parallel structuring schemes, where a predefined master is replicated by nano imprint lithography, injection molding, nano-casting lithography or similar. Examples include direct replication of *Morpho* multi-layer structures [Saito et al., 2004], replication of more essential features of the *Morpho* topology [Saito et al., 2006], see Figure 1.6b for scanning electron micrographs, and an one-dimensional photonic crystal pattern by injection molding [Chang and Young, 2010].

The efforts progressed onwards towards random structuring, where some process, usually a single etch step, defines randomly distributed structures across the surface, for example in the case of black silicon [Srivastava et al., 2010] or using 30 nm to 180 nm in diameter silicon rods with a length of 10 μm to create color specific irradiance [Cao et al., 2010]. Control of the structures is often limited to graded height and average density. A

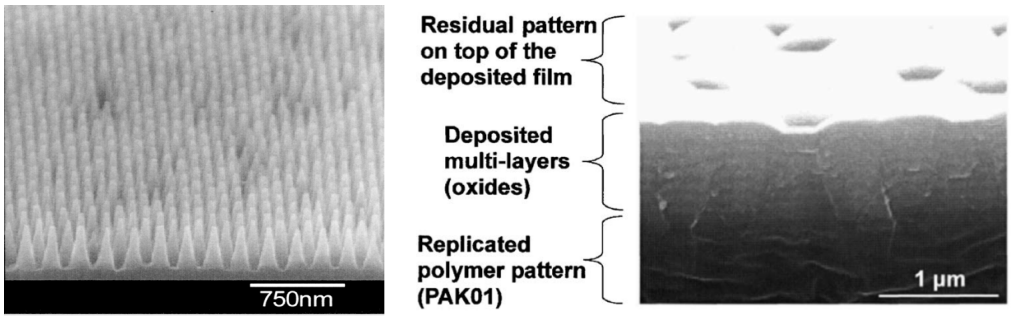

(a) Anti-reflective "black" structures.

(b) Reproduced *Morpho* structure.

Figure 1.6: Nano-structuring based on electron beam lithography. (a) Scanning-electron micrograph of sub wavelength structures in silicon. The grating period is 150 nm, and the grooves are 350 nm deep. Figure from literature [Kanamori et al., 1999]. (b) Scanning electron micrograph of the cross-sectional profile of the reproduced *Morpho* structure using replicated polymer resin by nano-casting lithography. Figure from literature [Saito et al., 2006].

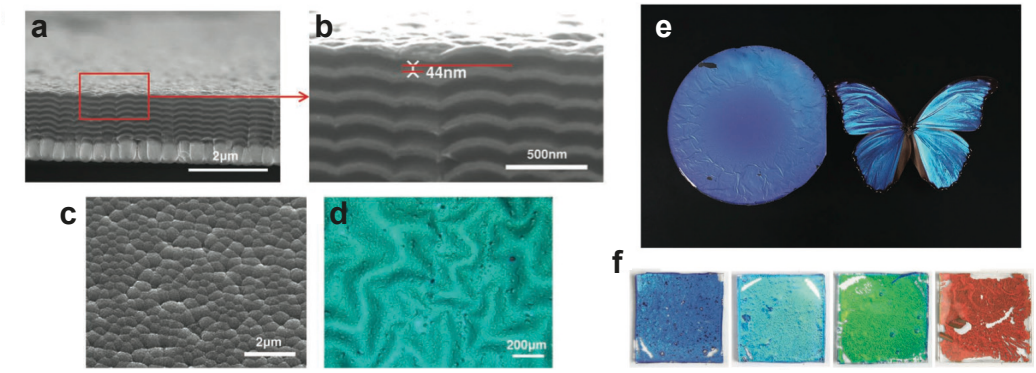

Figure 1.7: Structural comparison between butterflies and fabricated films in the literature. a) Cross-sectional SEM image of the deposited multilayer thin film. Bright layers are the SiO_2 layers and dark layers are TiO_2 layers. b) A close-up view of the multilayer, showing a vertical off-set of 44 nm between two neighboring columns. c) Top-view image of the multilayer thinfi lm. Each 'tile' corresponds to a multilayer column with a silica microsphere underneath. d) Optical microscope image of the thin film. e) Comparison of the fabricated PDMS-encased thin film with *Morpho didius*. The size of the reflector is 6 inches in diameter. f) Various colors realized by controlling the layer thicknesses. Figure assembled from literature [Chung et al., 2012].

truly periodic structure, if needed, can be hard to fabricate in this way.

In recent years, the efforts have also included chemical self-assembly schemes, where molecules or nano-spheres align themselves to create (semi)-periodic surface topologies. A new material has been reported, where the color is tunable by magnetically changing the periodicity of the nanostructure and fixable by photochemically immobilizing the structures in a polymer network [Kim et al., 2009], thereby demonstrating a flexible photonic crystal for the realization of structural color printing using a maskless lithography system.

As another example, *Morpho*-mimetic thin films have been fabricated by depositing a dielectric multilayer on top of a silica microsphere base layer with a random size distribution [Chung et al., 2012], see Figure 1.7. The combination induces a spontaneous emergence of both order and disorder across several length scales without lithography. By impregnating the structure with a polymer and lifting off, a flexible thin-film color reflector is created, see Figure 1.7.

Another example is opal polymers by 3D bulk ordering in macroscopic solid opaline films [Finlayson et al., 2011, Finlayson and Baumberg, 2013]. Common to these techniques is often a limited process window. Recently, Fano resonances on thin photonic crystal slab has been proposed [Shen et al., 2015]. The resonance-induced colors can be dynamically tuned by stretching the photonic crystal slab fabricated on an elastic substrate.

In conclusion, many different colors have been fabricated based on dielectric materials similar to plastics. All demonstrations reviewed in this survey utilize multi-layer schemes.

1.1.3 Conclusion

This survey reviewed selected aspects of the literature in relation to structural coloring found in nature and fabricated in the laboratory. Many different colors effects can been observed in nature utilizing multi-layer void structures, similar to the schemes outlined in Figure 1.2b. Many of these topologies have successfully been replicated in polymeric materials as optical biomimetics. However, all investigated single-layer surface topologies, outlined in Figure 1.2a, only lead to reports of angle-dependent diffraction or antireflection properties.

1.2 Thesis Statement - Robust Angle-insensitive Coloring

In order for structural colors to become a substitute for standard inks, dyes and pigments in plastic production, a harmonic angle dependence and robustness for everyday use are needed. In relation to the Plast4Future project, the mass production of such structures requires fabrication by injection molding. The combination of angular in-insensitive structural colors in dielectric materials and fabrication compatible with injection molding seems scientifically interesting. The statement of this thesis can be summarized in the following:

Is angle-insensitive robust structural coloration feasible by topologies and materials compatible with injection molding?

The scientific approach to answer the above question is to design and fabricate optical surface structures, and perform reflectance measurements of the fabricated structures. In conjunction, the measured reflectance should be compared to optical theory and simulations to identify the underlying trends. Using a number of design and fabrication iterations, the possibilities of angle-insensitive structural robust colors should be clarified.

1.3 Overview of the PhD Thesis

An overview of the thesis is provided here:

- In Chapter 2, the development of experimental processes, techniques and equipment is described. A single-spot electron beam lithography scheme for master pattern definition is developed. Optical characterization equipment for both laboratory and production environments is developed.
- In Chapter 3, the fundamental optical surface properties of dielectric materials are investigated within the framework of mass production applicability.
- In Chapter 4, a novel plasmon color technology for structural coloration in plastics is developed based on metal-coated polymer nano-textures. In collaboration with industry, polymer-based colored metasurfaces of square-centimeter size is demonstrated by embossing, injection molding, roll-to-roll printing, and film insert molding. Furthermore, post production color modification by laser ablation is briefly described. The environmental benefits are analyzed by life cycle analysis.

The thesis ends with a conclusion in Chapter 5 on the feasibility of structural metasurface colors based on injection molding compatible structures in an industrial perspective. Electromagnetic metasurfaces are flat, ultrathin optical components that alter the properties of electromagnetic waves, such as phase, amplitude, and/or polarization, on a length scale shorter than the free-space wavelength of the wave. In terms of electromagnetic theory, metasurfaces often modulate the behaviors of electromagnetic waves through specific boundary conditions, rather than constitutive material parameters. All dimensions of the structures and the spacing's constituting the metasurface are typically smaller than the free-space wavelength of the light.

Chapter 2

Methods & Equipment

Research requires supporting techniques and equipment. This chapter describes the developed experimental processes, techniques and characterization equipment, which have constituted the bulk part of the practical efforts. First, micro and nanofabrication are described. In an effort to reduce the fabrication cost of the master required for structural coloring, a single-spot electron beam lithography scheme for master pattern definition is developed. Secondly, optical characterization equipment for both laboratory and production environments is developed. The chapter ends with a conclusion.

2.1 Micro and Nanofabrication

Micro and nanofabrication was originally developed for the semiconductor industry. The platform offers the possibility to reproducible mass-fabrication systems with complex geometries and functionalities. Today, structures can be manufactured on scales ranging from the nanometers to centimeters providing seven orders of magnitude dimensional span, making the micro and nanofabrication platform attractive as a master pattern method. Here, macro and nanofabrication is used to produce a master pattern, which is then replicated in polymeric materials to form the final dielectric surface.

2.1.1 Electron Beam Lithography

Lithography is the technique used to transfer a computer-generated pattern onto a substrate, for example silicon. In electron beam lithography (EBL), a focused electron beam is scanned across a resist coated sample in order to either cross link (negative resist) or cut (positive resist) the polymer chains of the resist. This allows for selective removal of the resist in the subsequent development process. Positive ZEP520a resist (Zeon Chemicals

L.P.) was used for all work. The process flow for master fabrication using electron beam lithography followed by dry etching is shown in Table 2.1.

Table 2.1: Master pattern definition in silicon by semiconductor fabrication. (1) The resist is spin coated onto the substrate, (2) the resist is exposed by electron beam lithography, (3) the pattern is developed in the resist, (4) the pattern is transferred to the substrate by dry etching, and finally (5) the resist is removed and an antistiction coating is applied before the master is used for replication.

No.	Process	Sketch
1	Resist spin on	
2	Exposure	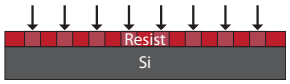
3	Development	
4	Etch	
5	Resist removal	

Since electron beam lithography is an important part of the conducted work, a sketch of the JEOL JBX-9500FS 100 keV prototype electron beam system is provided in Figure 2.1. First, the ZrO/W thermal field emitter generates the electrons (01) and the first and second anode extract them from the electron source (02 + 03). Then the electrons are accelerated to 100 kV by the acceleration electrode and pass the ground GND anode at a potential of 0 V (04 + 05) to form a high-velocity electron beam. The electron beam pass down through the first axis coil aligner and the second aligner performing the horizontal alignment and the tilt alignment (06 + 07 + 09). Then the beam continues down to the blanking on/off electrodes and the blanking aperture (08 + 10 + 11).

After the blanking aperture, the electron beam reaches the first pair of electronic lenses as seen in Figure 2.1. The second and third lenses (12 + 13) determine the beam current. The beam continues downwards to the DF corrector (14) correcting for deflection curvature. Then follows the objective aperture (15), which has six holes with varying diameters according to the writing conditions. The beam continues downwards through the DS corrector (16), correcting for deflection astigmatism, and the electromagnetic stigmator (17) for astigmatism correction at the center of the optical beam axis. Hereafter the electron

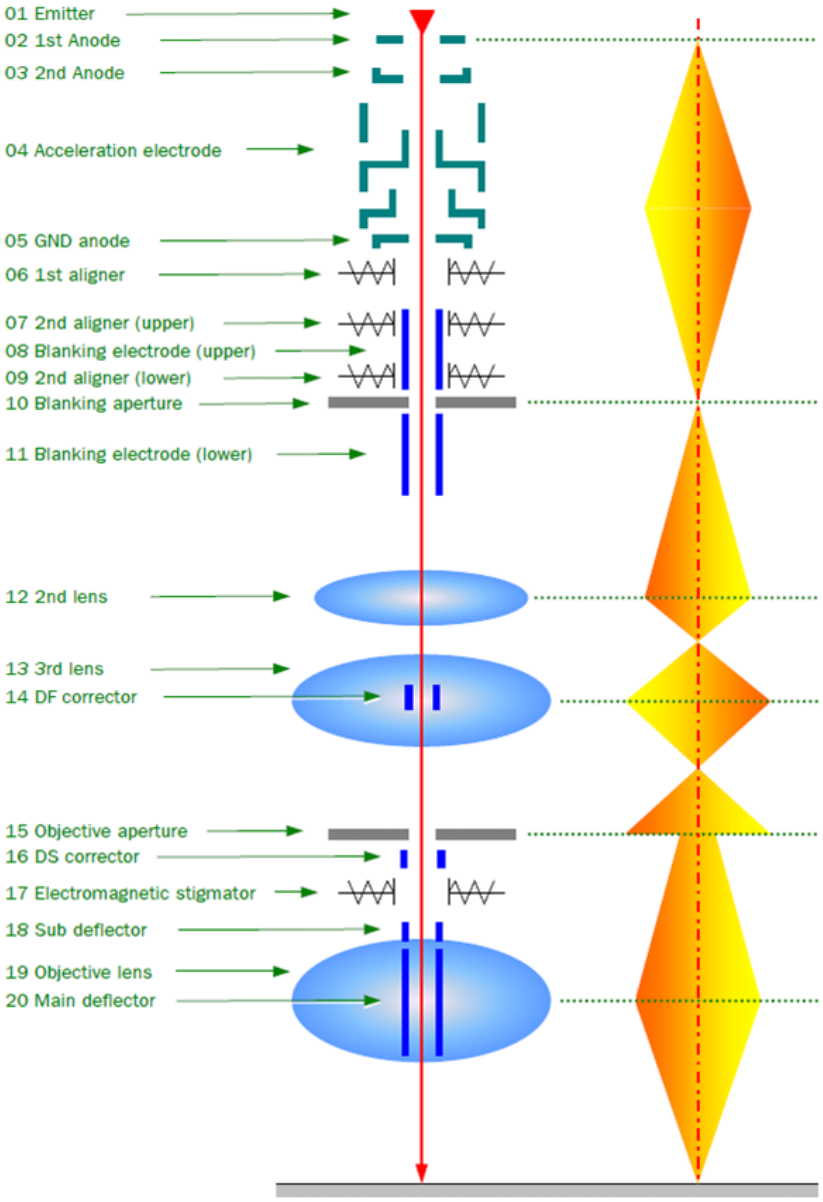

Figure 2.1: Schematic of the JEOL JBX-9500FS 100 keV prototype electron beam system. Image from the machine manual.

beam passes through the scanning sub deflector (18), the objective lens (19) forming a spot beam, and the main deflector electrode (20) for position. Finally, the electron beam hits the sample surface and exposes the resist.

2.1.2 Single-spot Lithography

The following section has been published [Højlund-Nielsen et al., 2014a]. Efficient nanoscale patterning of large areas is required for sub-wavelength optics. Here, a single-spot exposure strategy is used, where electron beam lithography (EBL) with a focused Gaussian beam is used to define shapes directly. The serial technique is optimized on the JEOL JBX-9500FS EBL system for speed and pattern fidelity to a minimum writing time of around 30 min/cm^2 for 200 nm periods in 2D lattices. The machine time and feasibility of the method are assessed in terms of the trade-off between high current and large writing field.

2.1.2.1 Introduction

Efficient nanoscale patterning of large areas is required for sub-wavelength optics. For example, photonic crystal applications may require periodic structures with a period of 200 nm or below. Such structures are conveniently fabricated by electron beam lithography. Still, the final product must be made at an economic cost. Here, a single-spot exposure strategy is used [Wendt et al., 1993, Gadegaard et al., 2003b, Golka et al., 2003, Kim et al., 2003, Jugessur et al., 2011, Greve and Holst, 2013, Cabrini and Hawata, 2012], where EBL with a focused Gaussian beam is used to define shapes directly. Conventionally, EBL uses multiple exposures of slightly overlaying spots, see Figure 2.2A. As a result, the shape time dominates the beam time, and is the major contributor to the overall writing time. Instead, the single-spot exposure strategy uses the machine as a raster scan tool to write a large rectangle, using a beam step size larger than the spot size, see Figure 2.2B.

The serial technique is optimized for speed and pattern fidelity to a minimum writing time of around 30 min/cm^2 for 200 nm periods in 2D lattices. The machine time and feasibility are assessed for different topologies and dimensions.

The single-spot electron beam technique discussed here was first described in 1993 by Wendt *et al.* [Wendt et al., 1993], which used a 6 nm beam-spot with a 5 nm resolution to define holes 50 nm in diameter by etching. This was followed by a more thorough study in 2003 by Kim *et al.* [Kim et al., 2003] showing that the single-spot exposure scheme can provide pattern quality similar to the conventional multi-spot exposure approach, but with an order-of-magnitude reduction in the required writing time. For a period of 300 nm and a dose of $30\,\mu\mathrm{C/cm^2}$ (224 nm spot), writing times were reported to be faster than one hour/cm^2 depending on the current (up to 44.4 nA). Furthermore, a modified four-spot scheme was also demonstrated for arbitrary shape definition. However, the work of Kim *et al.* is based on software estimation of the writing time, and it does not investigate small periodic structures with a high filling-ratio. In the same year Gadegaard

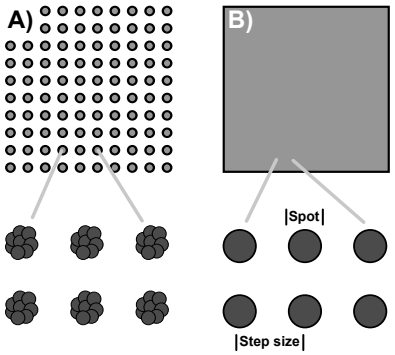

Figure 2.2: Illustration of the single spot exposure strategy. (A) The conventional method for pattern layout is to design an array of circular spots to form the final pattern. (B) Fast-writing patterns are formed directly by a single exposure with a given spot size spaced by the beam step size. Figure from publication [Højlund-Nielsen et al., 2014a].

et al. [Gadegaard et al., 2003b] examined the dot diameter as a function of dose and the shape diameter as a function of the distance to the writing field center, where a writing field side-length of 0.4 mm was found appropriate. Finally, in 2011 Jugessur *et al.* [Jugessur et al., 2011] examined hexagonal patterns with a current of 44 nA. From the literature, it seems that the components of the total writing time have not been examined in detail, which is the focus here.

2.1.2.2 Theory

As a simple model, EBL writing time per area A, t'_{writ}, has four components; beam time, shape time, stage time and calibration time:

$$t'_{\mathrm{writ}} = t'_{\mathrm{beam}} + t'_{\mathrm{stage}} + t'_{\mathrm{shape}} + t'_{\mathrm{cal}} \tag{2.1}$$

The beam time relates to exposing the resist and is given by dose D and current I as $t'_{\mathrm{beam}} = D/I$ [Parker et al., 2000]. Stage time, t'_{stage}, is related to the mechanical movement of the stage from writing field to writing field and depends on the writing field area $A_{WF} = \ell_{WF}^2$, with side length ℓ_{WF}, and on the machine parameter τ_{stage} for one average movement of the stage. The stage time can be given as $t'_{\mathrm{stage}} = \tau_{\mathrm{stage}}/A_{WF}$. The shape time can be modeled as $t'_{\mathrm{shape}} = \tau_{\mathrm{shape}} N_{\mathrm{shapes}}$, where τ_{shape} is the average time to address each of the N_{shapes} shapes. Shape time is usually negligible using the single-spot exposure strategy, which is the main argument for the method, and will not be discussed further. Calibration is critical for focus [Gadegaard et al., 2003b] and efficient calibration routines in terms of stability and drift compensation become imperative with this method. The calibration can be modeled as a continuous contribution in the form of $t'_{\mathrm{cal}} = \tau_{\mathrm{cal}} \left(t'_{\mathrm{beam}} + t'_{\mathrm{shape}} + t'_{\mathrm{stage}} \right) / \Delta t_{\mathrm{cal}}$ for a Δt_{cal} cyclic calibration interval with time

parameter τ_{cal}. Putting all together, the writing time Eq. (2.1) can be assumed to be a linear function of dose:

$$\begin{aligned} t'_{\text{writ}}(D) &= \left(\frac{D}{I} + \frac{\tau_{\text{stage}}}{A_{WF}} + \tau_{\text{shape}} N\right)\left(\frac{\tau_{\text{cal}}}{\Delta t_{\text{cal}}} + 1\right) \\ &= \alpha D + \beta, \end{aligned} \tag{2.2}$$

where α and β are fitting coefficients to be estimated from experiments. From the slope α, we may deduce the calibration time overhead, $\tau_{\text{cal}}/\Delta t_{\text{cal}} = (\alpha I - 1)$, if the current is assumed constant. Finally by plotting the β coefficients as a function of writing field area, we may deduce an expression for the stage time:

$$\beta = \left(\frac{\tau_{\text{stage}}}{A_{WF}} + \tau_{\text{shape}} N\right)\left(\frac{\tau_{\text{cal}}}{\Delta t_{\text{cal}}} + 1\right) = \gamma \frac{1}{A_{WF}} + \delta, \tag{2.3}$$

where γ and δ are fitting coefficients. Then the stage time parameter can be deduced as $\tau_{\text{stage}} = \gamma / \left(\tau_{\text{cal}}/\Delta t_{\text{cal}} + 1\right)$.

2.1.2.3 Methods

The JEOL JBX-9500FS is a prototype 100 keV Gaussian spot EBL system. The beam is generated by a ZrO/W emitter and electron-beam scanning speeds up to 100 MHz are available. By optimizing the lens focusing system and using an aperture of 200 μm, stable currents of 29 nA, 42 nA and 61 nA, can be provided with sufficiently small beam diameters, similar to previous reported 44 nA in 2011 [Jugessur et al., 2011] and two orders of magnitude higher than previous reported 0.33 nA in 2003 [Gadegaard et al., 2003b].

In terms of initial calibration, the two deflectors (position deflector and scanning deflector) are calibrated. These calibrations correct the gain and rotation deflector errors and determine the height correction coefficient, thereby influencing the homogeneity of the pattern writing over a writing field. The distortion correction values of the electron beam in the writing field are also measured. Prior to each pattern writing, the height of the substrate is measured at different positions, and the focus value of the objective lenses is corrected.

The cyclic calibration includes a current measurement, a drift measurement using a mark on the stage, and a temperature measurement on various positions in the machine. These calibrations are performed on a 5 min basis to ensure identical writing conditions.

Six experiments were carried out in order to test the influence of current and writing field on writing time and pattern quality. The dose was varied from $30\,\mu\text{C/cm}^2$ to $120\,\mu\text{C/cm}^2$ in steps of $15\,\mu\text{C/cm}^2$, yielding a total of 42 areas, each of exposure area 5 mm x 5 mm. The exposure dose interval was loosely estimated based on the clearing dose of the positive ZEP-520A resist (Nippon ZEON Company, Ltd.), which is around $30\,\mu\text{C/cm}^2$

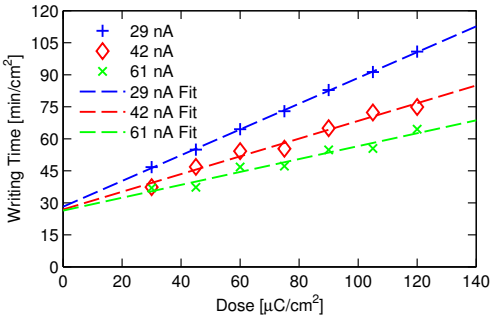

Figure 2.3: Measured writing time as function of dose and linear fits (dashed lines) for different currents with array periods of 200 nm and writing field side length of 0.2 mm. Exposure includes calibration. Initial machine calibration not included. Figure from publication [Højlund-Nielsen et al., 2014a].

according to the manufacturer data sheet. First, the current was altered; 29 nA, 42 nA, 61 nA, while keeping the writing field fixed at 0.2 mm and then the writing field was altered; 0.3 mm, 0.4 mm and 1.0 mm, while keeping the current at 29 nA. The outcome of this investigation should be a determination of the machine parameters τ_{cal} and τ_{stage}. For each exposed area the writing time was found by subtracting the end time of the exposure from the start time, both retrieved from the machine log after the exposure. The current was measured as part of the cyclic calibration and the mean current of each experiment was used for the calculations.

Devices were fabricated in silicon by exposure of the resist with thickness 158 nm, development, and reactive-ion etching.

2.1.2.4 Discussion

In Figure 2.3, the writing time per cm^2 as function of dose is given for different currents with a writing field side length of 0.2 mm. The writing time is seen to be linear dependent on the dose as expected from Eq. (2.2) with a large offset due to the 0.2 mm writing field. Still, the writing times are faster than 2 h/cm^2 for the chosen dose interval. By linear fitting, we determine α and β for the three different currents. Based on the fitting, it is given in Table 2.2 that the beam overhead is around 15 s for 301 s of calibration interval corresponding to 5.5 % overhead. Therefore, the effective current (the inverse slope in Figure 2.3) is 27.6 nA for the 29 nA exposure. From Figure 2.3, it is clear that the 61 nA current reduces the beam time. Still, the stage time constitutes the main component of the writing time and the writing time remains in the order of 45 min/cm^2.

In Figure 2.4 the writing time per cm^2 as function of dose is given for different writing field sizes with a constant current of 29 nA. The 0.2 mm data is identical to the 29 nA data in Figure 2.3. A writing time of around 30 min/cm^2 for 30 μC/cm^2 can be achieved. It is also clear that the difference between a 0.2 mm writing field and a 0.3 mm writing field

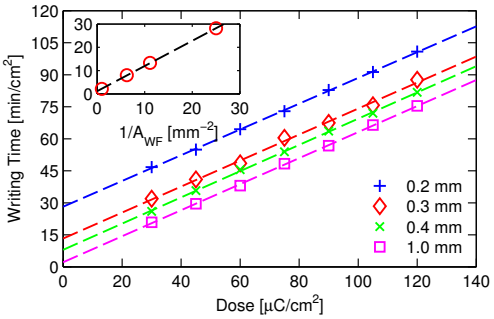

Figure 2.4: Measured writing time as function of dose and linear fits (dashed lines) for different writing field side lengths with array periods of 200 nm and current 29 nA. Exposure includes calibration. Initial machine calibration not included. Insert figure plots the y-intercept β of the linear fits in min/cm^2 as function of inverse writing field area, including linear fit (dashed line). Figure from publication [Højlund-Nielsen et al., 2014a].

Table 2.2: Overview of experiments and calculated parameters. Table from [Højlund-Nielsen et al., 2014a].

Run	I [nA]	ℓ_{WF} [mm]	$\tau_{\mathrm{cal,fit}}$ [s]	$\tau_{\mathrm{cal,meas}}$ [s]	τ_{stage} [s]	A/A_{WF}
1	28.87	0.2	13.6	14	0.62	2500
2	42.49	0.2	17.4	14	0.61	2500
3	61.02	0.2	31.7	15	0.59	2500
4	28.88	0.3	16.5	13	0.62	1111
5	28.88	0.4	19.4	13	0.61	625
6	28.88	1.0	17.1	13	0.61	100

is around 15 min/cm^2 in offset. By linear fitting, we may determine α and β for the four different writing fields. The slopes of the linear fits are seen to be almost identical for all the experiments. In the insert of Figure 2.4 the y-intercept β of the linear fits is plotted in min/cm^2 as function of the inverse writing field area. A linear correlation can be seen, which by fitting is used to determine the slope γ and the offset δ, see Eq. (2.3). From this slope, we calculate a stage movement time parameter of 0.61 s.

In Table 2.2, the details of the six experiments can be found. By examining the machine log, which has a time resolution of 1 s, it is found that calibration takes around 15 seconds with an overall trend of slightly lower overhead compared to the fitting values. In Table 2.2 the calculated stage times are also given, which depend on the calibration overheads, and the number of stage movement for each writing field size. Decreasing the written field side length from 0.3 mm to 0.2 mm more than doubles the number of stage movements, which explains the 15 min/cm^2 difference in writing time between a 0.2 mm and a 0.3 mm writing field side length observed in Figure 2.4.

In Figure 2.5 scanning electron micro-graphs of the structures transferred into silicon with a period of 200 nm are seen, exposed using a dose of 105 μC/cm^2 and different

currents. The quadratic lattice is found to be well defined. However, it is clear that the holes, in terms of roundness, degrade for higher currents. The higher current is achieved by increasing the collimating aperture size at the expense of astigmatism. This is seen in Figure 2.5C, where the high current of 61 nA causes a smaller asymmetric focal spot compared to Figure 2.5A with a current of 29 nA. A larger aperture translates to a larger numerical aperture and corresponding shorter depth of field. We did not identify charging effects [Zhang et al., 2011a, van der Drift, 1991].

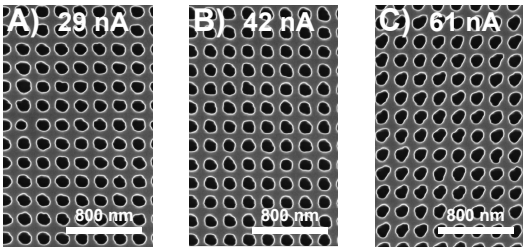

Figure 2.5: SEM micrographs of representative silicon structures with period 200 nm, written using dose 105 μC/cm^2 and different currents. (A) 29 nA. (B) 41 nA. (C) 61 nA. Figure from publication [Højlund-Nielsen et al., 2014a].

In Figure 2.6, optical microscope images are seen, taken after processing, of patterned areas exposed with different writing field sizes using a current of 29 nA and a dose of 120 μC/cm^2. Here the effect of a large writing field is directly visualized. Beam quality clearly degrades with increasing deflection due to increasing deflection aberrations. A smaller writing field prolongs the writing time as seen in Figure 2.4, but is often necessary to ensure a given quality of the pattern definition. As mentioned earlier, Gadegaard *et al.* [Gadegaard et al., 2003b] found that a writing field side-length of 0.4 mm was appropriate. We find that a field of 0.3 mm is sufficient for 29 nA, providing a writing time in the order of one hour per cm^2 for a dose of 75 μC/cm^2.

In terms of writing time, it is given from Eq. (2.2) that the sum of the dose-to-current ratio and the stage parameter-to-writing field ratio determines the writing time. This indicates the trade-off between a high current, with less well defined beam shape over the writing field, and a smaller writing field increasing stage movement with less deflection aberration. Thereby the practical upper limit for our JEOL machine and the given resist is a writing time in the order of 30 min/cm^2 for 200 nm periodic holes in 2D lattices.

2.1.2.5 Conclusion

The single-spot exposure strategy, where electron beam lithography (EBL) with a focused Gaussian beam is used to define shapes directly, was used to define 200 nm periodic arrays in silicon. The serial technique was optimized on the JEOL JBX-9500FS 100 keV prototype EBL system for speed and pattern fidelity to a typical writing time of one hour per cm^2

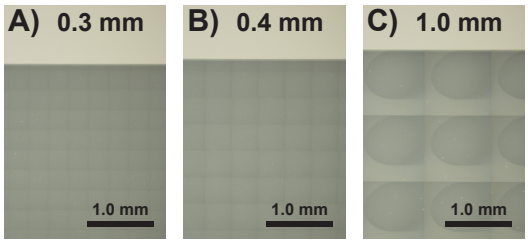

Figure 2.6: OM images after development and etch illustrating deflection aberrations of different writing field sizes for current 29 nA and dose 120 μC/cm^2. (A) 0.3 mm x 0.3 mm. (B) 0.4 mm x 0.4 mm. (C) 1.0 mm x 1.0 mm. Colors are not calibrated. Figure from publication [Højlund-Nielsen et al., 2014a].

with a minimum of around 30 min/cm^2. The machine time and feasibility of the method were assessed, discussing the trade-off between high currents and large writing fields. An EBL writing time below two hours per cm^2 provides new possibilities for sub-wavelength structures. These can be used to provide functionality, such as anti-reflective or plasmonic effects, for large area applications in a cost-effective manner, similar to traditional parallel processing techniques.

2.1.3 Reactive Ion Etching

After development, the silicon etching is the process, where the pattern is transferred from the resist to the silicon, see step 4 in Table 2.1 on page 12. In this study, dry etching in the form of reactive ion etching was used, specifically the DRIE Pegasus ASE from Surface Technology Systems (STS) plc. The etching was performed to create master originals based on electron beam lithography. For the fabrication of electron beam master originals, the process parameters were 75 sccm C_4F_8, 38 sccm SF_6, 800 W coil power, 40 mtorr pressure and a temperature of - 20 °C for all processed resist wafers. The etch rate is highly dependent on the local pattern load, however for two-dimensional 200 nm periodic lattices, a typical etch rate was around 2.1 nm / s. An etch time of 21.5 s resulted in around 46 nm deep holes measured by atomic force microscopy used for the plasmonic color structures. The pattern fidelity and reproducibility was optimized to support reproducible color production.

2.1.4 Resist Removal and Antistiction Coating

After etching, the resist must be removed and the master be prepared for polymer replication, see step 5 in Table 2.1 on page 12.

For resist removal, a plasma asher, model 300 Semi Auto Plasma Processor from TePla, was used. The process conditions are a pressure of 1.25 mbar, an oxygen gas flow of 400ml/min, a nitrogen flow of 70ml/min a and a power of 1000 watts for 10 min.

For antistiction preparation of the master original, perfluorodecyltrichlorosilane (FDTS) with the chemical formula $CF_3(CF_2)_7(CH_2)_2SiCl_3$ was used. After etching and plasma ashing, the structured silicon master wafer was antistiction coated with FDTS using molecular vapor deposition to improve release in later replication steps, for example for nano imprint lithography. Without antistiction coating, the release is difficult. With FDTS, the chlorine atoms in the end of a flourinated organosilane react with -OH groups of the surface to form a chemical bond under elimination of HCL, which allows for strong adhesion of the FDTS coating. At the same time, FDTS coating strongly modifies the surfaces energy since the terminal CF_3 groups are Teflon like and allows for easy release of the replicated polymer. The coating was done in the MVD 100 Molecular Vapor Deposition System from Applied Microstructures Inc. After cleaning of the process chamber, the multilayer deposition process was done in four deposition steps with a small amount of FDTS over about an hour.

The master original wafer is now ready to be used as stamp in a polymer replication process.

2.1.5 Polymer Replication

After fabrication of a mold or master, the next step is replication. In total, six different methods for replication were utilized in this work, including both UV casting and thermal replication techniques. The different techniques are briefly described here. Figure 2.7 provides an overview of the realized cleanroom fabrication schemes.

2.1.5.1 UV Casting of Hybrid Polymer on Glass Substrate

The UV casting method of hybrid polymer on glass substrate is a standard cleanroom technique developed by Microresist Gmbh. A liquid UV sensitive resin is used in UV-replication techniques. In this work, the organic-inorganic hybrid polymer Ormocomp (Microresist Gmbh) was used, belonging to the category of Ormocers developed by The Fraunhofer Institute. Upon UV illumination, the Ormocomp cures and becomes a transparent material with refractive index of 1.518 at a vacuum wavelength of 635 nm. The very liquid resin has a very good ability to replicate nanoscale features with high accuracy without applied pressure. The shrinkage is minimal as the process does not require a solvent.

The Ormocomp was positioned on a carrier glass substrate in order to secure flat and stiff samples. This was done by spin coating of the Ormocomp prior to imprinting or simply by pipette. The Ormocomp was cured through the glass for 5-15 min and adhered to the glass when the mold was removed.

2.1.5.2 Thermal Imprint on Glass Substrate

As an alternative to UV casting, the method of polymer embossing or thermal imprinting was developed by J. Clausen in relation to this work [Clausen et al., 2014]. First, the

polymer material was spin-coated from solution. A 75K PMMA was dissolved in Anisol (25 wt%) and spin coated onto the glass wafer (Borofloat, Boro33), which was pre-baked to drive out water and improve adhesion. For most investigations, the PMMA was spin coated at 2000 rpm for 60 s and baked for 5 minutes at 100 °C to drive out the solvent resulting in 4 μm thick PMMA films. The embossing/imprinting process itself is similar to that of bulk samples described in the next section.

2.1.5.3 Polymer Embossing

The main technique of this work is thermal embossing. A relatively flat polymer sample is placed between a structured mold and a flat mold surface, typically FDTS coated silicon wafers. A stack is formed by adding top and bottom teflon films to distribute pressure. In a parallel press or with a hydrostatic pressure, the stack is heated above the melting temperature of the polymer and pressure is applied. The polymer deforms to the shape of the mold and after a specific amount of time, the temperature is lowered below the melting temperature, while maintaining the pressure. Finally, the pressure is released when the temperature is about 20-30 °C lower than the melting temperature and the stack is separated with a razor. The specific process parameter depends on polymer and mold materials. The results of polymer embossing are described in Section 3.2.2 on page 43 and in Section 4.3.3 on page 58.

Both the thermal imprints on glass substrates and polymer embossing were performed on the EVG 520 machine and the CNI tool.

The EVG 520 Hot Embosser for nano imprint lithography is manufactured by the EVG group. The main purpose of the EVG machine is to imprint structures in polymers. In the typical case of PMMA spincoated on a borofloat wafer, a temperature of 190 °C at 15 kN for a 4 inch (100 mm diameter) wafer was applied for 30 min. The EVG includes vacuum control and provides high quality imprints, however with a typical process time of about 2.5 hours. Therefore, a significant effort was done to transfer the imprint processes from the EVG machine to the smaller CNI tool.

The CNI Tool (compact imprint tool) for thermal nanoimprint is manufactured by NIL Technology Aps. Two different machine were used, both essential CNI 1.0. The parameters were optimized for different materials and patterns. A typical example is a borofloat wafer with spin-coated PMMA and a master original silicon wafer with two-dimensional structures for structural colors. The structures were imprinted into the PMMA at 160 °C for 10 min at a pressure of 6.5 bar and demolded at 90 degrees C.

2.1.5.4 Injection Molding

Injection molding is a manufacturing process for producing parts by injecting material into a mould. The technique and results are described in Section 4.5.3 on page 74.

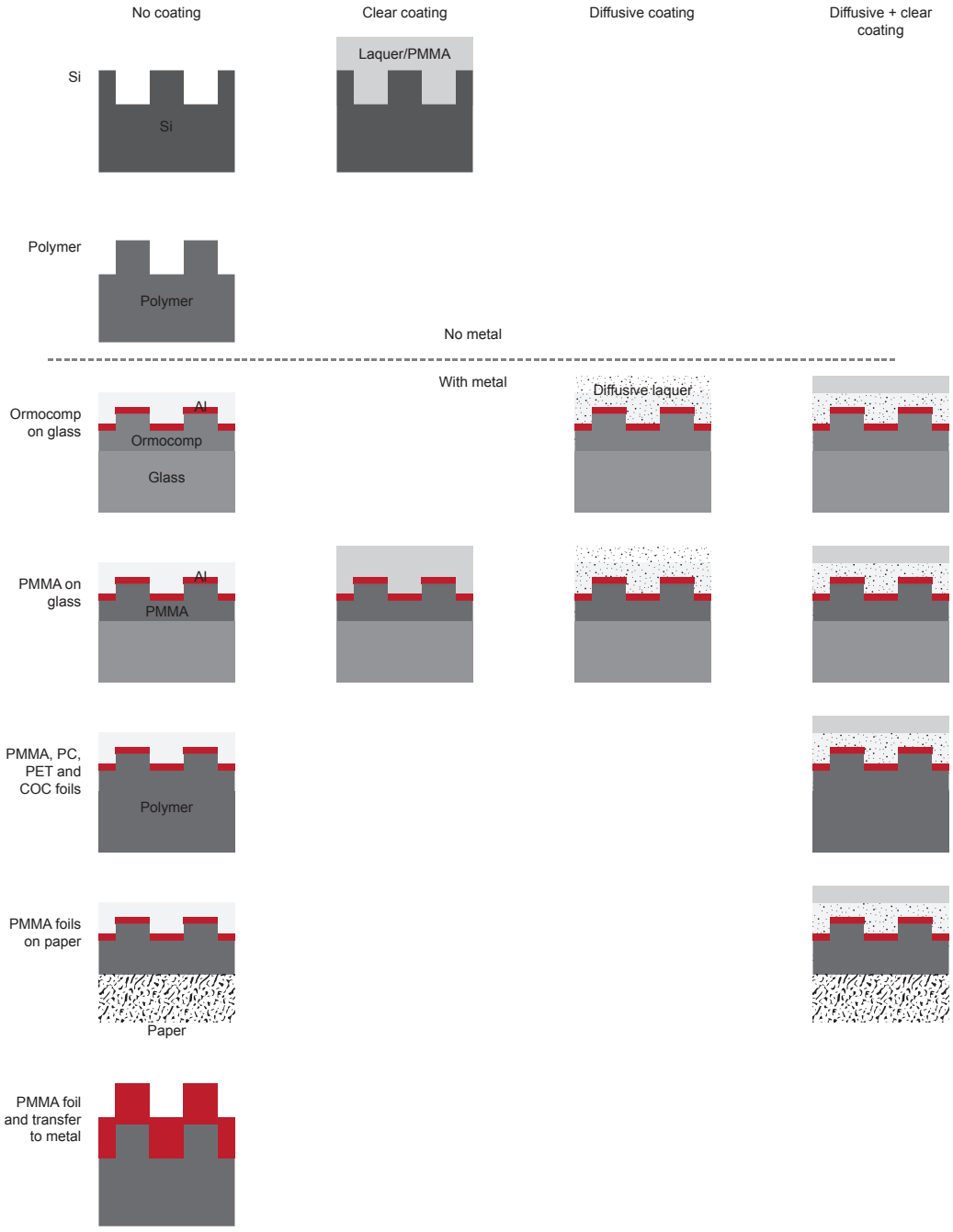

Figure 2.7: Overview of realized cleanroom-based fabrication platforms, divided by the dashed line into samples without metal described in Chapter 3 and samples with metal described in Chapter 4. The first column refers to samples without coating, the second column relates to samples with clear coating, the third column refers to samples with diffusive coating, and finally the last column refers to samples coated with a combination of a diffusive and a clear coating.

Machines at the LEGO Concept Factory in Billund were used. The injection molding of plasmonic color bricks was carried out in an Arburg 270S and an Engel machine using a commercial grade of the terpolymer acrylonitrile butadiene styrene (ABS). The polymer melt was injected at 230 °C with an injection pressure of 679 bar. After injection, a holding pressure of 800 bar for 1.5 s and then 450 bar for 2.0 s was applied. A manual variotherm process was used were the mold temperature was cooled from 131 °C to 80 °C. After demolding, the samples were metallized by electron beam deposition and coated using the same procedure as used for all other samples. The machines were operated by local staff.

For injection molding, two circular nickel shim masters were used. Nickel shims are formed by electroforming in the form of electroplating, and are inverted replica from a patterned silicon wafer. The replication fidelity from the silicon master is excellent. An optional anti-adhesion coating may be applied. One shim was provided by NILT Technology, while the other was fabricated by J. Clausen.

2.1.5.5 Roll-to-roll Printing

Roll-to-roll printing is a mass-volume production process based on rolls and a flexible plastic foil. Generally, it can refer to any process of applying coatings, printing, or performing other processes starting with a roll of a flexible material and re-reeling after the process to create an output roll. The results with the process is described in Section 4.5.1 on page 70.

The polymer replication process was carried out using a custom thermal roll-to-roll tool at the VTT Technical Research Center of Finland. The flexible pre-patterned nickel shim was wrapped around a roll with a diameter of 66 mm. Then a heated roll was pressed against a cold backing roll with a force of 600 N, resulting in a force between the rolls of approximately 1000 N. The utilized web materials included 100 m to 125 m thick polymethylmetcarylate (PMMA), polycarbonate (PC), amorphous polyethylene terephthalate (A-PET) and cellulose acetate (CA). The machine was operated by local staff, not by the PhD candidate.

2.1.5.6 Film Insert Molding

Film Insert Molding (also known as in-mold decorating/labeling, IMD/IML) is a well known industrial technique used to integrate surface coatings or decorations onto components to enhance durability and aesthetic value. The results are presented in Section 4.5.2.2 on page 74.

An injection molder for film insert molding was used at Centro Ricerche Fiat in Turin. The film insert molding tests were performed on a Sandretto 65 tons tool using 400 bars of injection pressure and a 180 °C temperature threshold. The machine back-injected PMMA, specially 8N Plexiglas from Evonik. Both PC and PMMA embossed film inserts were used. The machine was operated by an operator, not by the PhD candidate.

2.1.6 Metallization

In Chapter 4, nanostructured polymer surfaces are coated with aluminum to obtain plasmonic effects. In order for the hovering disk to be electrical separated from the background film to avoid short-circuiting, un-coated sidewalls of the polymer protrusions are required. Therefore, electron beam evaporation deposition (SCM600 Alcatel, Wordentec QCL800 Metal evaporator) is used for metallization for all samples presented in Chapter 4.

First, the metal target is heated by an electron beam inside a vacuum chamber with high vacuum 2×10^{-9} Torr. This follows the recommend order of magnitude of below 10^{-8} mTorr for plasmonic deposition [McPeak et al., 2015]. The result is a flux of evaporated atoms, which hit the sample substantially without scattering. This leads to line-of-sight depositions, where only horizontal surfaces are covered. The method has a sticking coefficient close to unity with no re-deposition on the side-walls. The thickness and the rate of the deposited metal are monitored by quartz crystal microbalance.

Another option would have been sputtering, which is more commonly used in industry. In this method, an Argon plasma is used to sputter metal atoms. In order to maintain the plasma, the process is operated at a much lower pressure than electron beam evaporation metallization, which leads to gas phase collisions and a wider angle distribution of the incident atoms. This contributes to side-wall deposition together with re-deposition due to the more energetic particles arriving at the surface. Sputtering is not suitable for metallic depositions in relation to well-defined nanoscale plasmonic topologies.

2.1.7 Coating Systems

In Chapter 4 nano-structured polymer surfaces are coated with aluminum to obtain plasmonic effects and subsequently covered with a protective coating system. An overview of the different coating systems is provided in Figure 2.7.

For successful coating design, the coatings formulator must consider the physical and chemical characteristics of the polymer substrate or plastic surface to be coated. Surface tension, modulus, coefficient of thermal expansion, response to coating, drying and curing, as well as the chemical structure and conformation of the polymer are factors that influence the type of coating required for a particular application.

After various tests at the Technical University of Denmark and at a local automotive workshop, a lacquer scheme was chosen for the protective coating based on a conventional automotive process. In the final version, samples were coated with approximately 50 μm of scratch-resistant commercial automotive lacquer in a two-step process, where the first layer of acrylic copolymer (AU175 Flattening Binder, Axalta Coating Systems) acts as a absorbing diffuser, mimicking the scattering properties of traditional paint, and the top layer (3760S Ultra Productive VOC Hi-Temp Clear, DuPont) creates a high-gloss visual appearance.

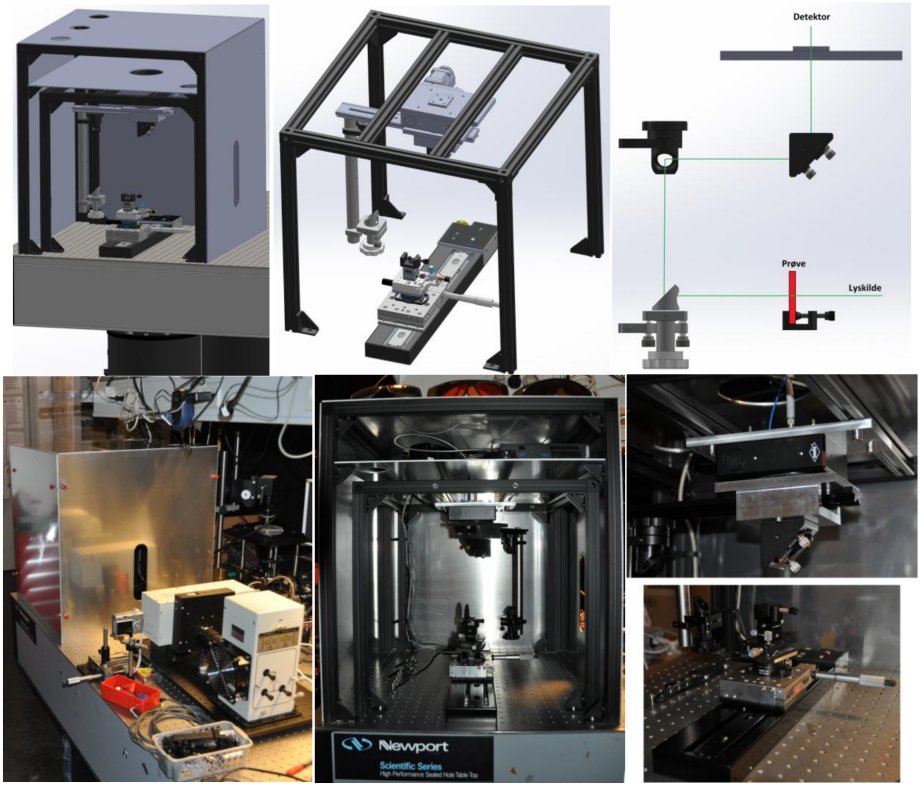

Figure 2.8: Angle-resolved setup built autumn 2013. The setup consists of two independent rotating stages for the sample and detector respectively. This allows for reflection and transmission measurements in one automated work-flow. Rendering and photographs before final black aluminum anodization and assembly. Figure from work by Petersen [Nyholm-Petersen, 2014].

2.2 Optical Characterization

Three main methods of optical characterization have been employed, each of which are described below. In all cases the spectral intensity information was recorded using a grating based spectrometer for detection (Jaz, Ocean Optics) with 2048 pixel silicon photodiode. The spectrometer covers a range from $\lambda = 250$ nm to $\lambda = 800$ nm and has an optical resolution of 1 nm.

Beside the setups described here, a number of other setups were used. The work on polarization dependence described in Section 4.4 used an another setup, described on page 63, that includes an objective due to the small sample size. Finally, the work on film insert molding was characterized in Torino by a commercial goniometer used for quality control, see Section 4.5.2.2 on page 74.

2.2.1 Automated Angle-resolved Setup

For measurement of color dependence on illumination and viewing angles, an automated setup is constructed based on an already-existing setup at DTU Nanotech by D. Pedersen in his bachelor thesis [Nyholm-Petersen, 2014] in close collaboration with E. Højlund-Nielsen. Illustrative photographs and drawings are presented in Figure 2.8.

The new constructed setup aims at automating reflection- and transmission measurements for a wide angular interval, which makes it possible to carry out more advanced measurements compared to the current installed technology. The previous setup was based on two rotating stages and homemade components. An analysis of the setup identifies a series of problems, including component quality, zeroing/mechanical calibration, errors/noise and repetitive reference measurements. Based on the analysis of the current setup, a new mechanical design is conceived, where the two rotational stages are reused. The construction is dimensioned with regards to deflection by analytical and numerical calculations. A computer model in 3D is constructed and work drawings are made for all the specially designed parts. The new construction is built using commercial components and custom-made parts.

2.2.2 Integrating Sphere

The integrating sphere used in this work is ISP-50-8-R-GT (Ocean Optics), coated with material providing a high diffuse reflectance and with a small opening in the bottom. The diameter of the sphere is 50 mm and the sample port is 8 mm. A fiber coupling allows for illumination and detection at 8 degrees with respect to the sample normal. The light hits the sample at 8 degrees and the total reflectance is detected at the other port of the instrument.

2.2.3 Diffraction Quality Control Setup

A general industrial adaptation of metasurface colors will require supporting infrastructure for nanoscale production. An effort was made to envision quality control without the need for scanning electron microscopes, atomic force microscopes and other expensive characterization equipment. In Figure 2.9, a manifestation of such a vision is presented in the form of a scalable diffraction setup for the production floor.

The setup is based on non-destructive measurements of the zero-order and first-order diffraction. In Figure 2.9a, a schematic side view of the setup can be seen. Due to the short periodicity needed to avoid diffraction in the visual spectrum, an UV-light source with a vacuum wavelength of 375 nm is used. In Figure 2.9b, the macroscopic measurement signal principle is sketched. In Figure 2.9c, the nanoscopic measurement signal principle is sketched. In Figure 2.9d, the demonstration setup can be seen in action at the LEGO factory floor.

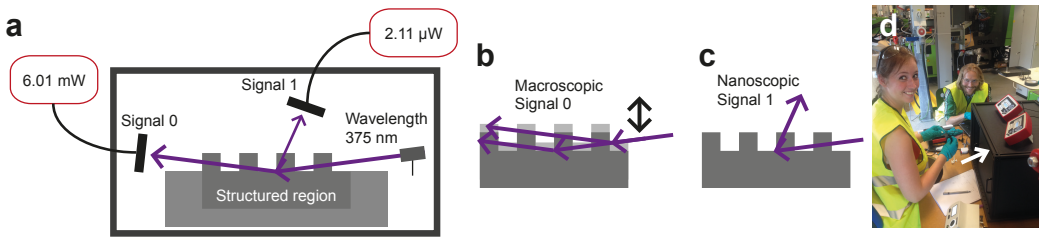

Figure 2.9: Diffraction quality control setup built spring 2015 based on a UV light source, where the zero and first diffraction orders from the structured plastic sample are measured by two detectors. a) Schematic side view with typical measurement values. b) Macroscopic measurement principle based on "Signal 0" zero-order specular reflection, where signal changes indicates height differences. c) Nanoscopic measurement principle based on "Signal 1" first order diffraction, where a larger diffracted signal indicates better replicated grating structures. d) Setup in action at the LEGO factory floor. White arrow indicates the setup in black casing.

In Figure 2.10, the diffraction measurements for the injection molding tests described in Section 4.5.3 on page 74 are plotted for signal 0 and signal 1 along with reference levels. A reference level is here defined by the lowest measured signal for a given type of ABS plastic. It is seen that the reference signal is dependent on the scattering of the material. Intuitively, white natural plastic gives a high reference (background) signal, whereas black plastic gives a much smaller signal. For each test, five bricks were measured and the measurements were averaged to provide reasonable statistics. Test 31/32 seems to perform best and can be seen in Figure 4.17.

In Figure 2.11, some data analysis is plotted. Figure 2.11a provides a comparison between the signal 0 and signal 1 for each tests. Finally, Figure 2.11b provides insight into the trends observed in signal 1, where the influence for the material has been subtracted. The tests were performed in random order, and therefore, It is expected that the measured signal strength does not correlate with the test number. In Figure 2.11b, "1" and "2" indicates the tests where the shim was coated directly with FDTS and "3" refers to the test done after the shim was coated with Al_2O_3 and then FDTS treated. Without a proper adhesive layer and FDTS coating, the subtracted signal decays with a lifetime constant in the order of 5 shots. After the Al_2O_3 and FDTS treatments, the signal does not decay. Hence, proper coating of the nickel master is important. Furthermore, based on a SEM inspection of the samples, it seems that the quality control setup performs as anticipated.

2.3 Numerical Simulations

A number of simulation methods are available for optical problems categorized as frequency-domain eigenproblems, frequency-domain responses, or as time-domain simulations [Joannopoulos et al., 2008, p. 253]. Despite the nanometric dimensions, the smallest characteristic features are still sufficiently large to allow classical electrodynamics considerations [Raza

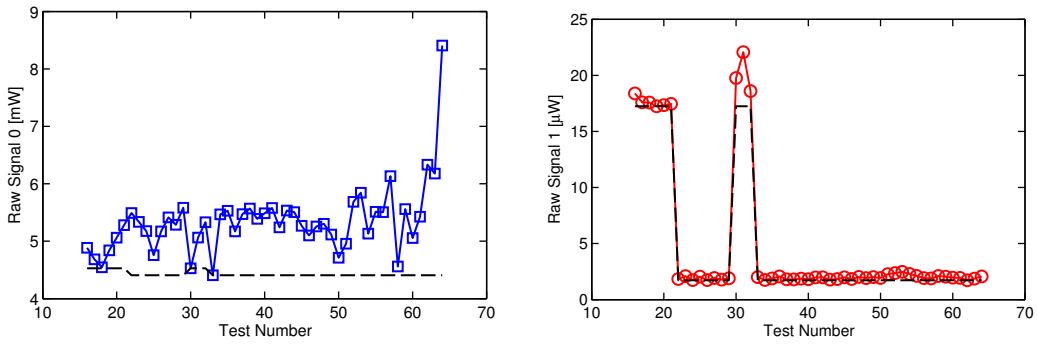

Figure 2.10: Raw diffraction measurements using the setup described in Figure 2.9 for different injection molding tests with black or natural white ABS using the same shim. The tests were done in a random test order and represent different machine process parameter sets based on injection pressure, injection speed, holding pressure, holding time, demolding pressure, demolding time, cooling time and start mold temperature. a) Signal 0 with reference level (dashed line). b) Signal 1 with reference level (dashed line), where black ABS gives a signal in the order of a few µW and white ABS gives a signal in the order of 15-20 µW.

et al., 2015].

2.3.1 Rigorous Coupled-Wave Analysis

Rigorous coupled-wave analysis (RCWA) is a simulation method, belonging to the family of frequency-domain response. A commercial available version of rigorous coupled-wave analysis was used for all dielectrics simulations (GD-CALC, KJ Innovation). According to the documentation [Johnson, 2006], this method represents the electromagnetic field and the optical dielectric constant at any particular horizontal layer in terms of their Fourier series in two lateral grating coordinates. A set of differential equations based on Maxwell equations is solved to find the propagation of the field's Fourier coefficients through the grating, and a scattering matrix is used to represent each horizontal layer. Then, the individual scattering matrices for each layer are combined by an algorithm stacking the different layers on top of each other to determine the grating's total scattering matrix. From this composite matrix, diffraction efficiencies is calculated by fast fourier factorization. Finally, reflectance and transmission can be calculated from the output diffraction efficiencies. The RCWA simulations described in this work on pages 3.2.1, 44, and 127 were performed by E. Højlund-Nielsen.

2.3.2 3D Frequency-Domain Simulations

General purpose frequency-domain solvers enable full 3D electromagnetic simulations of high frequency components. Frequency-domain solvers are very well suited for the sim-

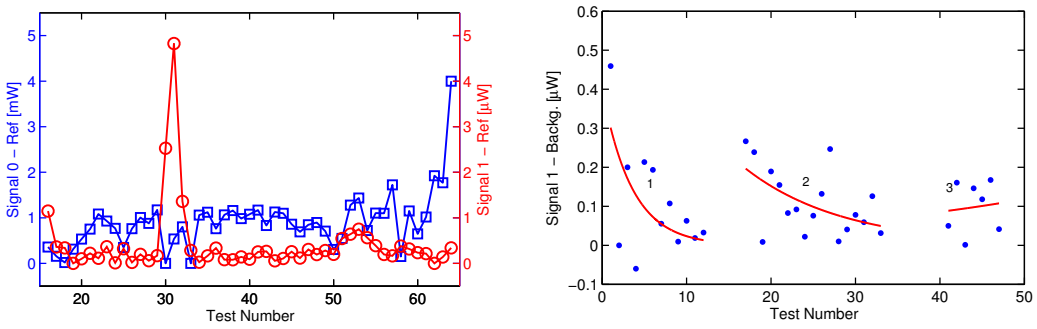

Figure 2.11: Analysis of diffraction measurements for different injection molding trials on a random background related to the individual test conditions. a) Measurement with subtracted reference, essentially the same data as in Figure 2.10. b) Signal 1 trends with exponential fits, where the relevant material dependent background is subtracted. The first tests labeled as "1" is performed based on a FDTS coating and no adhesion layer. A decreasing trend can be seen, where the signal of the first test is much higher than all other tests. The second group is performed after cleaning the shim in an acetone bath and a new FDTS coating. The group labeled as "3" indicates the data after a commercial cleaning, aluminum oxide adhesive deposition and FDTS coating. Here, it seems that the shim does not degrade any further. In terms of Test 32, SEM images can be seen in Figure 4.17.

ulation of dispersive devices, as the correct materials properties at each frequency can be used. Simulations were conducted using a general purpose frequency-domain solver with periodic boundary conditions in the surface plane (CST Microwave Studio). The frequency-domain solver can be used for frequency dependent, anisotropic media and it delivers electromagnetic near and farfields. The 3D frequency-domain simulations described in this work were performed by J. Clausen and X. Zhu.

2.4 Conclusion

In conclusion, this chapter described the developed experimental processes, techniques and characterization equipment. Micro and nanofabrication were described. In an effort to reduce the fabrication cost of the master required for structural coloring, a single-spot electron beam lithography scheme for master pattern definition was developed. Finally, optical characterization equipment for both laboratory and production environments was developed.

Chapter 3

Dielectric Colors

In Chapter 1, structural colors were reviewed. It was argued that coloring, providing sufficiently reflectance and angle-insensitivity, was exclusively based on multi-layer structures. All designs in polymeric materials, respecting the replication constraint defined in Section 1.0.1 on page 3, resulted in diffraction-based shimmer color effects.

In this chapter, the search for spectral manifestations of a colorful nature continues in context of the industrial replication constraint and the thesis statement on page 9. By the end of this chapter, the route from fundamental optics to structural colors will be clarified from a theoretical and experimental perspective, hopefully linking structural properties of a surface to a color effect under general light conditions.

First, basic theory of reflection and diffraction is provided along with a formal definition of reflectance and color. Then, color functionality based on high-index and low-index materials is described. The chapter ends with a conclusion on the applicability of all-polymer color functionality.

3.1 Theory

This section introduces the fundamental optical theory of reflection, diffraction, and colors.

3.1.1 Definition of Reflectance

In this thesis, the concepts of reflectance and transmittance are central. Consider an electric field propagating in the z-direction. The intensity (average power per unit area relative to a given surface) is given by the z-component of the Poynting vector $\mathbf{S}$ according to Poynting's theorem [Griffiths, 2008, p. 347, p. 391]:

$$I = \langle \mathbf{S} \cdot \hat{\mathbf{z}} \rangle \quad , \quad \mathbf{S} = \Re\left(\tilde{\mathbf{E}}\right) \times \Re\left(\tilde{\mathbf{H}}\right), \tag{3.1}$$

where $\Re\left(\tilde{\mathbf{E}}\right)$ and $\Re\left(\tilde{\mathbf{H}}\right)$ are the real physical parts of the electric, *E*-, and magnetic, *H*-field, respectively. From the point of energy conservation, $I_{\text{in}} = I_R + I_T$ for any interface. From this, the reflectance and transmittance can be defined as far-field intensity ratios for the given ray of light in question:

$$R \equiv \frac{I_R}{I_{\text{in}}}, \;\; T \equiv \frac{I_T}{I_{\text{in}}}, \tag{3.2}$$

implying that $R + T = 1$ for loss-less materials. In general, the reflectance of a surface is a directional property depending on the incident wavelength, the incident angle, material and topology of the surface[1]. The above definitions are central as the aim of this thesis is to control reflection by surface structuring.

3.1.2 Reflection and Diffraction

In this section, the specular and diffusive reflection of light from polymer surfaces and their implication for creating structural colors is discussed. The findings of this section have been reported [Christiansen et al., 2013].

The topology limitation described by the replication constraint generally indicates that the advanced multi-layer structures described in Section 1.1.1 on page 4 cannot be fabricated using a one-step injection molding process. These limitations have consequences for the optical performance. Importantly, it was shown by theoretical considerations in 2002 by Bao *et al.* [Bao et al., 2002] that the upper limit of surface reflectance for all one-layer periodic structures are given by the reflectance of a planar dielectric interface. The reflection of a planar dielectric interface is also known as Fresnel or specular reflection, often arising from mirror-like surfaces. This limitation applies for all values of the bulk refractive index, n_2, larger than that of the surrounding air medium, n_1.

In order to assess the magnitude of reflectance, the simplest possible case of reflectance and transmittance is given by a lossless dielectric interface between two regions, air and material. The reflectance and transmittance for normal incidence is independent on polarization and can be calculated using the Fresnel coefficients for polymer material with $n_2 = 1.5$:

$$R_{\perp} = \left(\frac{n_1 - n_2}{n_1 + n_2}\right)^2 = \left(\frac{1 - 1.5}{1 + 1.5}\right)^2 = 0.04,$$

[1]More formally, we may define the bidirectional reflectance distribution function in dimensions of sr^{-1} as [Vukusic and Stavenga, 2009, Eq. (2.1)]:

$$R_{\lambda}\left(\theta_{\text{in}}, \phi_{\text{in}}, \theta_R, \phi_R\right) = \frac{I_R\left(\theta_R, \phi_R\right) \mathrm{d}\omega_R}{I_{\text{in}}\left(\theta_{\text{in}}, \phi_{\text{in}}\right) \cos\left(\theta_{\text{in}}\right) \mathrm{d}\omega_{\text{in}}},$$

assuming light scattering from one surface point. An even more generalized description is the bidirectional scattering surface reflectance distribution function. Here, the more simple Definition (3.2) will be sufficient.

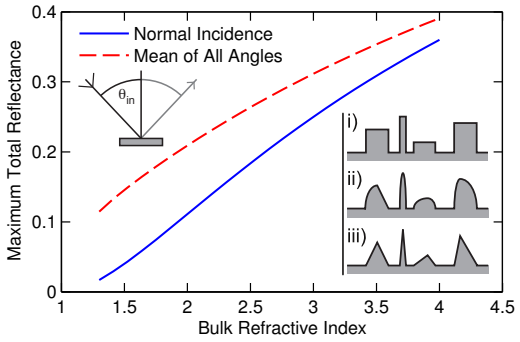

Figure 3.1: Maximum specular reflectance for replication constraint compatible topologies for unpolarized light for normal incidence (blue curve) and averaged over all incoming angles assuming a uniform intensity distribution (red curve), where examples i, ii and iii are defined with respect to an initial flat micro-scale surface. Figure from publication [Christiansen et al., 2013].

indicating that plastic materials only reflect 4 % of the incoming normal light. The remaining 96 % is transmitted into bulk. It is seen that, as the numerical difference between the two refractive indices becomes smaller, the reflection is reduced. We may define the hemispherical reflection W for un-polarized light averaged over all angles:

$$W\left(n_1, n_2\right) = \frac{1}{\pi} \int_{-\frac{\pi}{2}}^{\frac{\pi}{2}} R\left(n_1, n_2, \theta_{\text{in}}\right) \mathrm{d}\theta_{\text{in}}, \tag{3.3}$$

describing the total normalized reflection of a dielectric surface equally illuminated at all angles. In Figure 3.1, the total reflection is seen as a function of refractive index for normal incidence and averaged over all incoming angles (hemispherical reflection). For an air-plastic interface, with $n_2 = 1.5$, the accumulated reflection is 8.92 % for p-polarization and 20.2 % for s-polarization. In normal daylight, meaning uni-directional un-polarized light, only 14.6 % of the incoming light at maximum can be altered. The remaining 85.4 % of the incoming light is transmitted into bulk, where it may be absorbed or scattered. As a rule of thumb, the hemispherical reflection for common plastic materials is around 15 %. These numbers describe the fundamental limit of performance in clear plastic for any structure or design respecting the replication constraint described on page 3. In general, higher refractive index means higher reflection.

3.1.3 Periodic Structuring

In terms of structuring, a periodic nano-texturing of the surface, characterized by a period Λ, is the most simple case. If the period is longer than the wavelength of the incident light, the periodic alteration is referred to as a diffraction grating. The optical properties are described by the grating equation [Raguin and Morris, 1993, Eq. (1)] , here written in the

most general case:

$$n_1 \sin\theta_m - n_1 \sin\theta_{\text{in}} = \frac{m\lambda}{\Lambda}, \quad (\text{reflected orders}) \tag{3.4}$$

$$n_2 \sin\theta_m - n_1 \sin\theta_{\text{in}} = \frac{m\lambda}{\Lambda}, \quad (\text{transmitted orders}) \tag{3.5}$$

where n_1 and n_2 is the refractive indices of the incident medium and the transmission medium respectively, and θ_{in} is the incident angle of the light with respect to the surface normal. This is a very general formula, because Fourier series form the most fundamental solution to any linear differential equation that is subject to periodic boundary conditions. Therefore, iridescence arising from diffraction gratings always takes the form of one or more ordered spectra, although intensity may vary.

Besides the slowly varying intensity of diffracted spectral orders described by Equation (3.4), rapid variations can also be found in certain narrow frequency bands. These abnormally high or low intensities in the diffracted light are referred to as Wood's anomalies [Stewart and Gallaway, 1962]. Especially in the case of the first diffraction order appearing parallel to the surface at glancing angle, anomalies in the measured spectra can be found. According to Stewart and Gallaway [Stewart and Gallaway, 1962], the corresponding "Rayleigh" wavelengths can be found in the zero–order specular radiation yielding:

$$\lambda_R\left(\theta_{\text{in}}\right) = \frac{\Lambda}{m_\pm}\left(\pm 1 - \sin\theta_{\text{in}}\right). \tag{3.6}$$

At the Rayleigh wavelength, first order emerges at the glancing angle and the redistribution of energy results in a anomaly in the specular reflection. Anomalies have been subject to an intense study. Hessel and Oliner [Hessel and Oliner, 1965] argue that two distinct types of anomalies may exist: A Rayleigh wavelength type due to the emergence of a new spectral order at grazing angle, and a resonance type which is related to the guided complex waves supportable by the grating.

To complete the picture of optical gratings, sub-wavelength, non-diffractive gratings must also be discussed using an argument given by Raguin and Morris [Raguin and Morris, 1993]. For non-diffractive gratings, the period should be small enough that all higher diffraction orders are evanescent. From the grating equation Eq. (3.4), this requirement sets an upper limit to the period-to-wavelength ratio specified by [Raguin and Morris, 1993, Eq. (2)];

$$\frac{\Lambda}{\lambda} < \frac{1}{\max(n_2, n_1) + n_1 \sin\theta_{\max}}, \tag{3.7}$$

where $\theta_{\max}$ is the maximum angle of incidence. Since the denominator of the right-hand side of the above inequality is always larger than unity because $n_1 \geq 1$ and $n_2 \geq 1$, it is

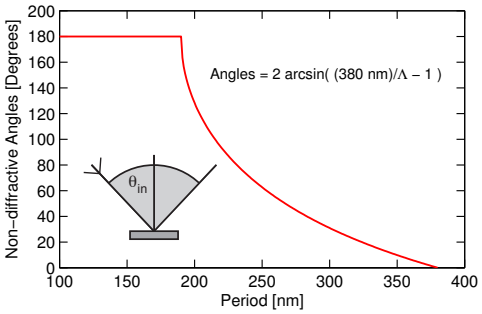

Figure 3.2: Incident angles causing no reflected diffraction in the visual spectrum as function of nanostructure period. Periods below 190 nm do not lead to diffraction at any angles in the visual spectrum. Figure from publication [Christiansen et al., 2013].

seen that the surface must always have a surface period smaller than the dimensions of the incident wavelength, hence the term sub-wavelength. It should be noted that the above argument is normally given in terms of the reflected orders, leading to an intermediate range of structures that are often anti-reflective, but still scatter light in the transmission. In the case of a period of 250 nm, the first order reflection appears at a glazing angle (horizontal along the interface) at 31° incidence, meaning that the perceived specular color is significantly changed for angles bigger than 31° incidence. Therefore, the non-diffractive angle interval is 62°, as seen in Figure 3.2. For a period of 200 nm, first order reflection does not occur until 76°. Periodic structures below 250 nm provide basis for angle-independent colors, although diffractions can be seen for angles approaching the glazing angle.

For structural color effects, the optimum is periods approximately 200 nm in order to avoid diffraction in the visual spectrum. Periods below 190 nm do not lead to diffraction at any angles in the visual spectrum, as seen in Figure 3.2, however transmission diffraction effects may still affect the specular reflection.

3.1.4 Quantitative Description of Color and Appearance

The color of an object is the result of a complex interaction of the light incident on the object, the optical characteristics of the object, and human perception [Harold, 2001]. This section is dedicated to a quantitative description of color and appearance linking optical properties of an object to a color perception under given lighting conditions. This is important, because structural colors depend not only on the structural characteristics of the surface, but also on the surroundings and especially on the light used to illuminate a given sample.

According to Robert and Ford, color is *"a visual sensation produced by a specific spectral power distribution incident on the retina of the human eye"* [Roberts and Ford, 1995].

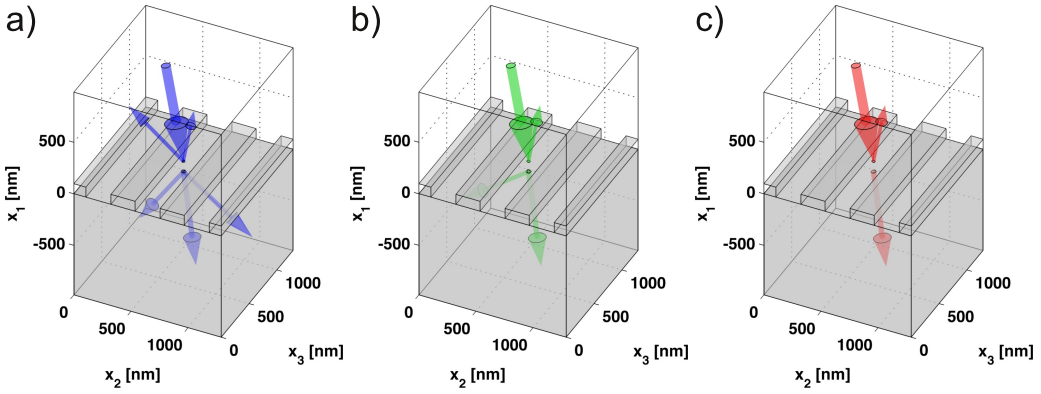

Figure 3.3: RCWA simulations illustrating the three fundamental grating regimes using 430 nm period, 100 nm height, 10° incident light and $n_2 = 1.4$. Arrows indicate magnitude on logarithmic scale. a) λ = 410 m (blue light). Several orders in both transmission and reflection. b) λ = 550 nm (green light). 0'th order in reflection, two orders in transmission. c) λ = 680 nm (red light). Only 0'th order in both reflection and transmission. Figure from publication [Christiansen et al., 2013].

Humans are in daylight trichromatic. The human eye senses color using three receptors with photo pigments of different sensitivities for the primary colors red, green, and blue. These receptors are referred to as cones and are situated on the retina on the back half sphere inside the eye, see Figure 3.4a. Furthermore the retina also contains receptor cells, known as rods, primarily for night vision and light intensity. The retina contains about 5 million cones and 92 million rods [Curcio et al., 1990]. If the receptor cells, cones or rods, are stimulated by light, signals are sent to the brain via the optical nerve trough several channels at the back of the eye [Livingstone and Hubel, 1988]. These signals are then interpreted as visual input in the visual cortex. The dual-receptor system allows the human eye to maintain sensitivity over an impressively large range of ambient light conditions. However, it should be noted, that the processes in the brain leading to color perception after the retina are not completely understood even for normal color vision [Klein, 2010, p. 113].

Perceived color is also influenced by other objects nearby, because the color perception of a given object in the brain is responsive to all inputs from all receptors cells in both eyes, known as *simultaneous contrast*. The color perception of structural colors in the brain with respect to surroundings may be very different from that of ordinary pigmentation, for example in the case of diffraction grating on top of pigmentation. However, we will in this thesis only refer to the **central color perception of the human eye** in the *fovea centralis* close to the optical nerve, where humans perceive colors most accurately. This assumes that structural colors are perceived in a similar manner as colors originating from pigmentation. The scientific understanding of how structural colors affect the brain is still limited, which may also be one of the reasons for the un-settled definition of structural colors as described in Section 1.1.1 on page 4.

In a scientific context, the color of an object can be given as the light source $S(\lambda)$, the reflection or transmission of the object $R(\lambda)$ or $T(\lambda)$ and the observer modeling the spectral sensitivity. The reflected electromagnetic spectrum that reaches the observer is given by $S(\lambda)R(\lambda)$. In 1931, the Commission internationale de l'éclairage (CIE) developed a mathematical device-independent color model [Klein, 2010, p. 125], mapping out a three dimensional color space (X, Y, Z) of observable colors, where X, Y and Z are referred to as tristimulus values. In the context of the CIE 1931, colors can be defined on integral form:

$$\begin{aligned} X &\equiv C \int_0^\infty S\left(\lambda\right) R\left(\lambda\right) \bar{x}_{\mathrm{obs}}\left(\lambda\right) \mathrm{d}\lambda, \\ Y &\equiv C \int_0^\infty S\left(\lambda\right) R\left(\lambda\right) \bar{y}_{\mathrm{obs}}\left(\lambda\right) \mathrm{d}\lambda, \\ Z &\equiv C \int_0^\infty S\left(\lambda\right) R\left(\lambda\right) \bar{z}_{\mathrm{obs}}\left(\lambda\right) \mathrm{d}\lambda, \end{aligned} \tag{3.8}$$

with the definition of the normalization in the form of the constant:

$$C \equiv \frac{1}{\int_0^\infty S\left(\lambda\right) \bar{y}_{\mathrm{obs}}\left(\lambda\right) \mathrm{d}\lambda}, \tag{3.9}$$

meaning that the Y-parameter controls the lightness normalized to green light. A few words on the model are needed.

The parameters $(\bar{x}_{\mathrm{obs}}, \bar{y}_{obs}, \bar{z}_{obs})$ describe the spectral sensitivity of the observer and roughly correspond to the sensitivity of the three cones in the eye. As already discussed, we focus on the central color perception of the human eye. More specifically, the CIE 1931 2° observer will be used with a small correction, where the observer perceives colors without any interference. This observer utilizes the region of *fovea centralis* close to the optical nerve, deviating from the optical axis of the eye by approximately 2°. The values for $(\bar{x}_{\mathrm{obs}}, \bar{y}_{\mathrm{obs}}, \bar{z}_{\mathrm{obs}})$ of the CIE 1931 2° standard observer are plotted as a function of wavelength in Figure 3.4b. Also plotted is the Judd Vos correction from 1955 and 1978 [Vos, 1978]. Here, the 1978 correction will be used due to its better replication in the ultraviolet region of the visible spectrum compared to the original 1931 standard.[2]

The illuminant (or light source) $S(\lambda)$ is also of great importance, where the radiated light of the sun or artificial light may be used. Today, the industry standard is the ISO/CIE standard illuminant D65[3] for daylight and the ISO/CIE standard illuminant A for incandescent light based on a tungsten-filament. These illuminates are plotted in Figure 3.4c together with the solar spectrum at the top of atmosphere (extraterrestrial) at mean Earth-

[2]Another reasonable choice is the Stiles & Burch 1955 2° data, which is recommend by some authors over the Judd-Vos 1978 correction, see [Stockman and Sharpe, 1999, p. 68-70].

[3]The name D65 refers to a color temperature of 6504 K. The Sun has an effective blackbody surface temperature of around 5780 K. D65 Standard ISO 11664-2:2007(E)/CIE S 014-2/E:2006.

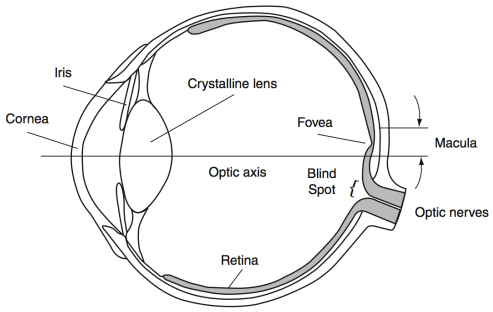

(a) Horizontal section of the human eye.

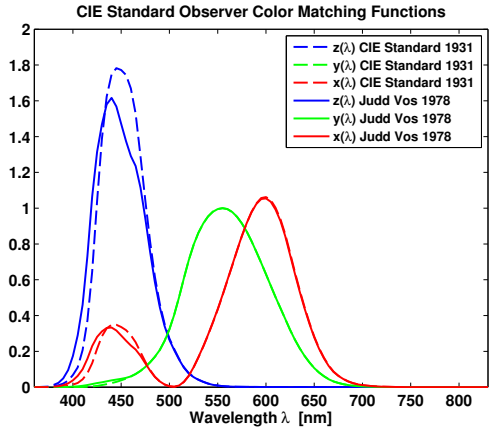

(b) Color matching functions.

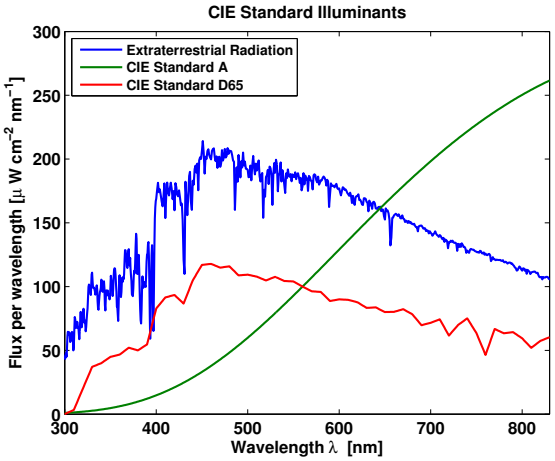

(c) Illuminants.

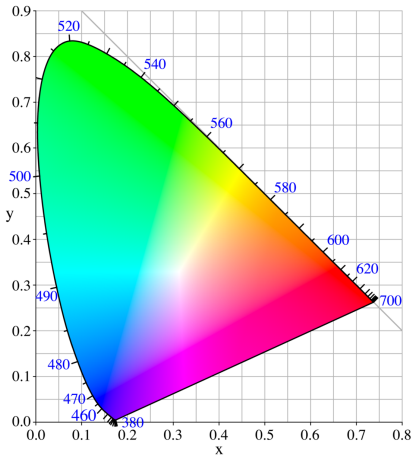

(d) Chromaticity diagram.

Figure 3.4: The CIE 1931 color space. (a) Horizontal section of the human eye. Figure from literature [Klein, 2010, p. 110] (b) CIE 2° observer color matching functions, see text. (c) CIE Illiminunats and solar spectrum at top of atmosphere at mean Earth-Sun distance [NREL, 2012]. (d) The CIE 1931 color space chromaticity diagram from [Wikipedia.org, 2012]. The outer curved boundary is the spectral locus, wavelengths in nanometers. Figure assembled in previous work [Højlund-Nielsen, 2012].

Sun distance, indicating a clear connection between D65 and the solar radiated spectrum. According to CIE, *"the standard illuminant D65 can be used in all colorimetric calculations requiring representative daylight"* [CIE, 2012]. Throughout this thesis, the D65 illuminant will be used.

The chromaticity coordinates, x and y, can be defined independent of brightness:

$$x \equiv \frac{X}{X+Y+Z}, \;\; y \equiv \frac{Y}{X+Y+Z}. \tag{3.10}$$

These are normally given when describing device-independent colorization. We will refer to the model described above as the CIE-XYZ model.

In order to accurately present color numbers, a conversion between the device-independent CIE-XYZ model and device-dependent outputs on a display (voltages expressed in RGB) or paper (CMYK) is needed. There are several conversions available, however we will adopt the sRGB conversion developed by Hewlett-Packard and Microsoft in 1995. The sRGB conversion is a colorimetric RGB specification that is based on the average performance of personal computer displays and on the CIE D65 illuminate standard [Stokes et al., 1995]. According to the documentation [Stokes et al., 1995], most computer monitors have very similar color characteristics, such as the phosphor chromaticities (primaries) and transfer function RGB spaces. Modern screen-displays can also show color gamuts covering a large number of applications. By selecting sRGB, we ensure a series of compatible steps from the measured reflectance to the calculation and display of RGB-values on a modern monitor. The drawback of this strategy is that the printed colors are not accounted for.[4] The sRGB conversion is given in two steps using the intermediate variables $V_I = \{V_R, V_G, V_B\}$:

$$\begin{bmatrix} V_R \\ V_G \\ V_B \end{bmatrix} = \begin{bmatrix} 3.2410 & -1.5374 & -0.4986 \\ -0.9692 & 1.8760 & 0.0416 \\ -0.0556 & -0.2040 & 1.0570 \end{bmatrix} \begin{bmatrix} X \\ Y \\ Z \end{bmatrix}$$

For the three color values $I_s = \{R_s, G_s, B_s\}$, the second transformation step is given by:

$$I_s = \begin{cases} 12.92 V_I & , V_I \leq 0.00304 \\ 1.055 V_I^{\frac{1}{2.4}} - 0.055 & , V_I > 0.00304 \end{cases}$$

All sRGB colors natively between 0 and 1 are referred to as the sRGB gamut. Colors outside this interval cannot be displayed properly. According to the authors of the original specification, all sRGB values are simply cut off to the interval between 0 and 1 to avoid this problem. Using the sRGB conversion, an overview of colors within the CIE-XYZ model is provided in Figure 3.4d. This is known as the color space chromaticity diagram with the axes of x and y. The image displays maximally saturated bright colors using sRGB for

[4] For printed colors, individual conversions are performed by the printer in question. For printing, the D50 illuminant is typically used together with an conversion into the CMYK color space, ideally requiring two sets of figures for on-screen-display and printing.

on-screen display.

3.2 Color Functionality

This section describes possibilities for color functionality by utilizing all-polymer nano-structured surfaces. In relation to the thesis statement described in Section 1.2 on page 9, structures respecting the replication constraint are examined.

3.2.1 High-Index Structural Colors

The section presents the findings on high index structural colors. The full work has been published [Højlund-Nielsen et al., 2014b].

High index materials typically have a refractive index above 2.0, in contrast to polymers with a typical refractive index around 1.5. As already mentioned, structural color appearances from single-material one-layer surface textures are investigated here. Silicon with a refractive index around 4 is used as a high-index model system for nano-structured dielectric surfaces suitable for polymer replication methods, such as imprinting/embossing and injection molding that uphold the replication constraint. The reflectivity of day-light colors are measured and compared to RCWA simulations, to identify different regimes and predict color appearance, see Section A.3 on page 127. The study provides an engineering method to specify a physical surface grating texture that will yield a desired novel angle-insensitive structural color, quantified by CIE XYZ color measurements.

The experimental work is based on four samples, each of size of 1 cm $\times$ 1 cm, of artificial nano-structures fabricated by NIL Technology on a single wafer using electron beam lithography and dry etching. The patterns, characterized as diffraction gratings, consist of square structures in a square lattice with periods of 500 nm, 400 nm, 300 nm, and 200 nm. Scanning electron microscope (SEM) images of the four samples can be seen in Figure 3.5a-d. The overall structures appear more rounded as the period decreases. The heights of the structures are measured by atomic force microscopy to be around 180 nm.

Figures 3.5e-h show photographs without subsequent software adjustments illustrating the angular dependence of the reflected light under daylight illumination from a window. In particular, Figure 3.5e illustrates the near normal incidence specular colors of the four samples. In Figure 3.5f, a photograph is seen, taken along the diagonal axis approximately 45° normal to the surface. Here, significant shifts in color have occurred compared to normal incidence. In general, the samples display a rich variation of reflected specular and diffraction based colors, except for the area with a 200 nm period that seems to retain a more homogenous color.

The most important experimental results are plotted in Figure 3.6. In Figure 3.6b the measured specular reflectivity of the sample with a period of 300 nm can be seen as a function of wavelength and an angle of incidence for $\phi_{\text{in}} = \{0°, 45°\}$. The near normal

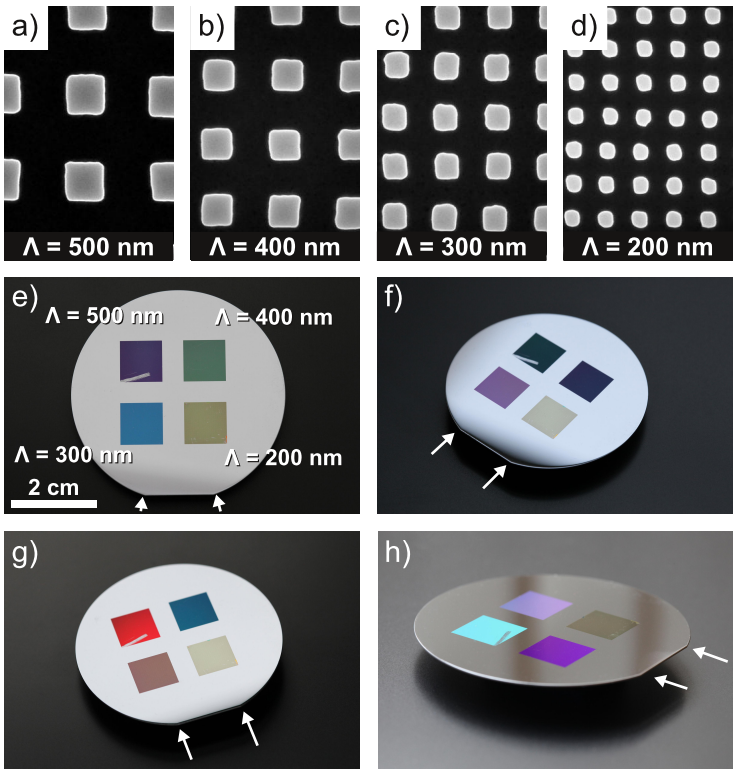

Figure 3.5: Silicon structural colors. (a-d) SEM images 1.00 μm wide of the four periodic samples. (e-h) Photographs of the four samples from different angles. In (e), the camera is slightly tilted around 10°-15° compared to normal incidence to avoid lens reflections. Figure from publication [Højlund-Nielsen et al., 2014b].

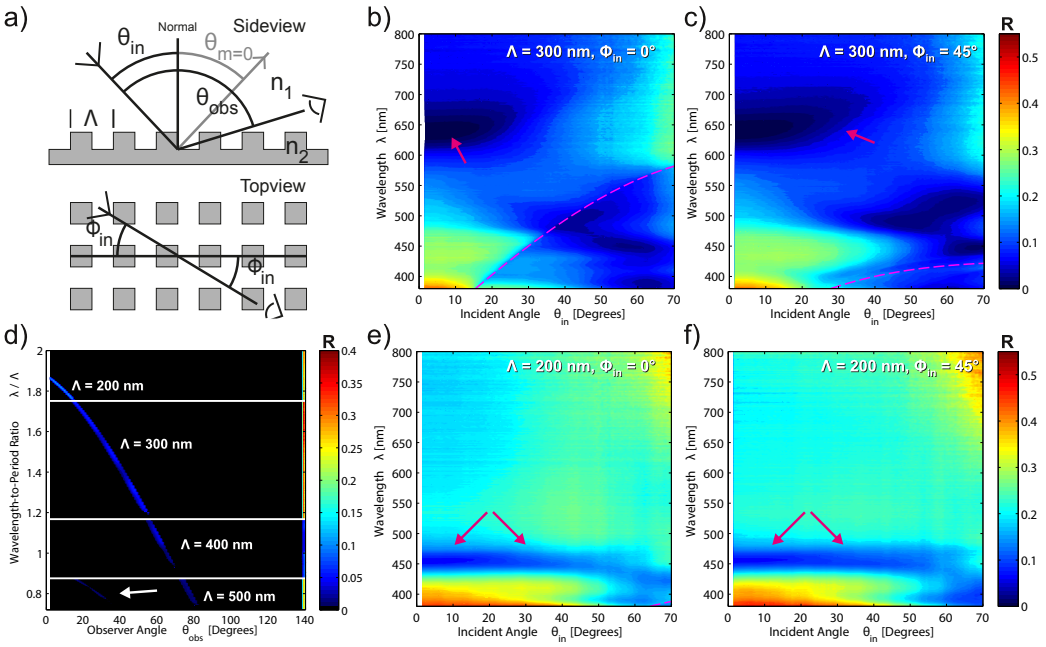

Figure 3.6: Reflection measurements. (a) Sketch of measurement setup. (b-c) Specular reflectivity for the 300 nm period sample from 0 % to 55 % as function of incidence angle and wavelength for $\phi_{\mathrm{in}} = \{0°, 45°\}$. Dashed lines mark Rayleigh line, arrows mark anomaly. (d) Measured reflectivity from 0 % to 40 % for a constant incidence angle of $70°$ as function of observer angle and normalized wavelength of the four samples. Arrow marks second order. (e-f) Specular reflectivity for the 200 nm period sample from 0 % to 55 % as function of incidence angle and wavelength for $\phi_{\mathrm{in}} = \{0°, 45°\}$. Dashed line in bottom right corner marks Rayleigh line, arrows mark anomaly. Resolution $\Delta\theta = 0.5°$. Figure from publication [Højlund-Nielsen et al., 2014b].

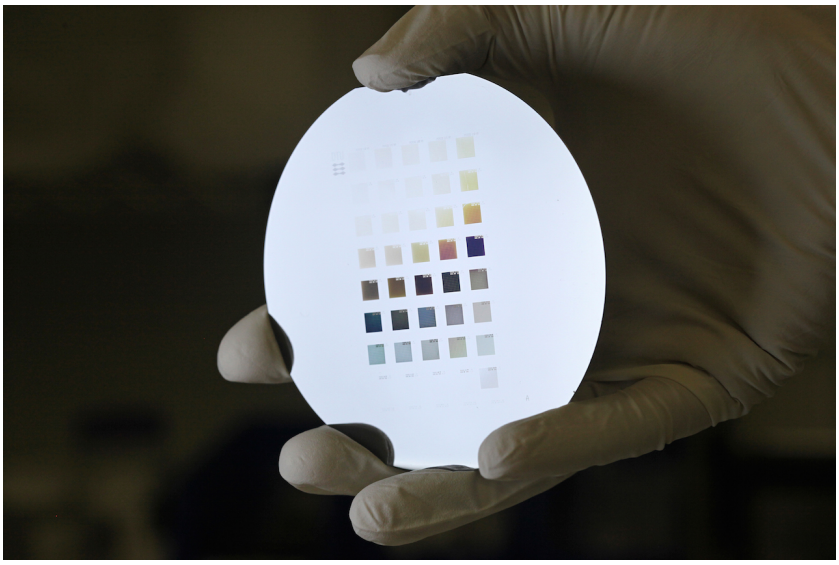

Figure 3.7: Structural colors in silicon made by electron beam lithography and dry etching.

incidence measurements show a distinctive minimum at a wavelength of 640 nm which by the simulations are found to indicate a resonance anomaly behavior with strong coupling to a leaky surface wave [Hessel and Oliner, 1965]. The relatively high reflectivity for short wavelengths can be explained as a combination of a rapidly increasing refractive index of silicon for short wavelengths and the absence of anomalies for the particular parameters [Bao et al., 2002]. Regarding angular dependence, the distinctive line of low reflectivity in Figure 3.6b can be identified as the "Rayleigh line", meaning that diffraction in the visual spectrum does not occur until $15°$ incident angle. Thereby, the measurements for a period of 300 nm capture the transition from the non-diffractive regime of exclusive specular reflectivity at normal incidence to the diffraction regime for larger incidence angles, also supported by the tendency of low reflectivity for wavelengths shorter than the Rayleigh line due to the appearance of higher reflectivity orders.

In conclusion, it is possible to create colorful appearances by structure alone for high index materials in daylight environments.

3.2.2 Low-Index Structural Colors

This section presents the findings on low index structural colors in relation to the thesis statement described in Section 1.2 on page 9. Low index materials typically have a refractive index below 2.0, which include polymers with a typical refractive index around 1.5. Given the fabrication platform developed in all-polymer, what possible colors may be produced?

An answer to that question is provided by the specular color map in Figure 3.8 for normal incidence and $45°$ incidence. The map was constructed by simulating the reflection of squared two-dimensional silicon gratings converted into a color using the CIE 1931 XYZ-model color space with the 1978 Judd Vos correction [Vos, 1978] of the CIE 1931 $2°$ observer [Smith and Guild, 1931] and the ISO/CIE standard illuminant D65 [Judd et al., 1964]. For plotting, the XYZ-values were converted into sRGB values, as described in Section 3.1.4 on page 35. The colors may appear darker due to the overlaying reflection spectra data. The filling factor is defined in terms of the diameter of the protrusion:

$$F \equiv \frac{\text{Prutrusion area}}{\text{Unit cell area}} = \frac{\pi r^2}{\Lambda^2} = \frac{\pi D^2}{4\Lambda^2}.$$

Based on these numbers, RCWA simulations were conducted. The results are provided in Figures 3.8 and 3.9. It is found, that the filling factor is more important than the exact shape of the nano-structures. Two structures with the same filling factor, such as a square structure and a circular structure, provide a similar optical response. It is noted that a rather high filling factor of around 40 % - 50 % is needed to create colors. Furthermore, it is also clear that the height plays a crucial role for the interference creating color and a "one-height-fits-all-colors-solution" is not possible. These simulations have also been published, see [Christiansen et al., 2013].

To experimentally verify this conclusion, lab-scale samples were fabricated. One example is seen in Figure 3.10. Comparing these blue colors with the imprint master original shown in Figure 3.7, it is clear that low-index materials can only provide a limited response. It seems that under the replication constraint, the produced effects are either weak or with a high degree of iridescence. The latter may be seen as an advantage under some circumstances, as it offers possibilities for decorative effects, which are not available using standard pigmentation.

A related problem, which has not been discussed until this point, is the mechanical durability of the proposed surfaces. Since the structures are defined in the surface of the plastic parts, any wear of the surface will cause the effects to disappear. A solution would be to protect the structures with a protective coating. However, typical coatings are based on polymers, and since the diffraction effects are based on index contrast, the color effect will disappear.

In conclusion, it is possible to create colorful appearances by structure alone for low index materials only under very special circumstances in bright light environments, not in everyday light environments. Furthermore, any color effect is lost by index-matching if a protective coating is applied to protect the nano-structures.

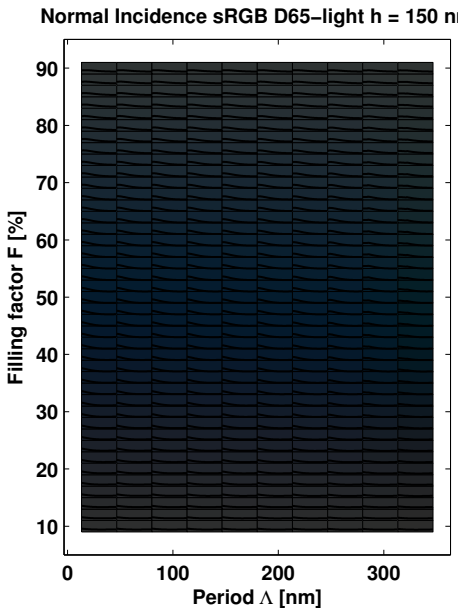

(a) $h = 150$ nm, $\theta = 0°$.

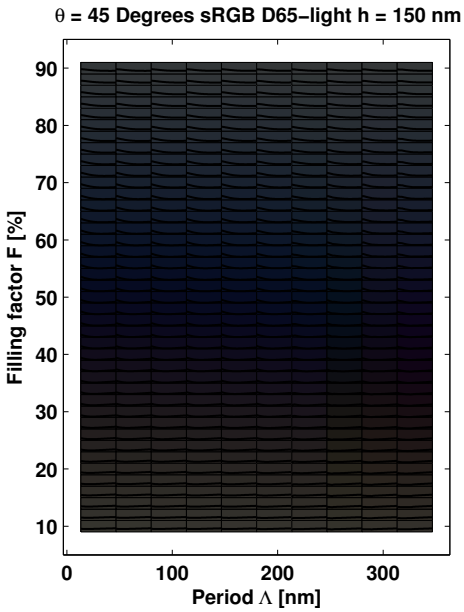

(b) $h = 150$ nm, $\theta = 45°$.

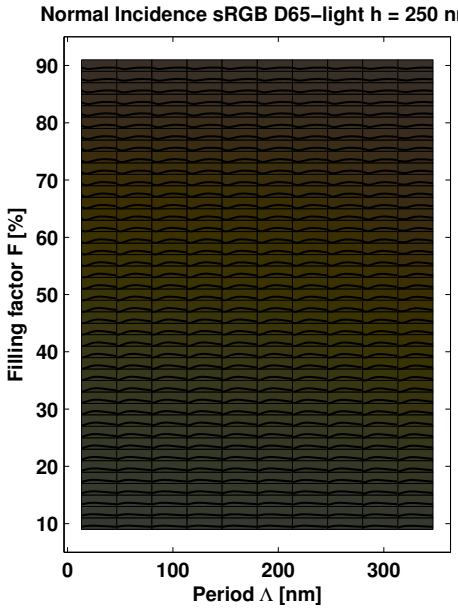

(c) $h = 250$ nm, $\theta = 0°$.

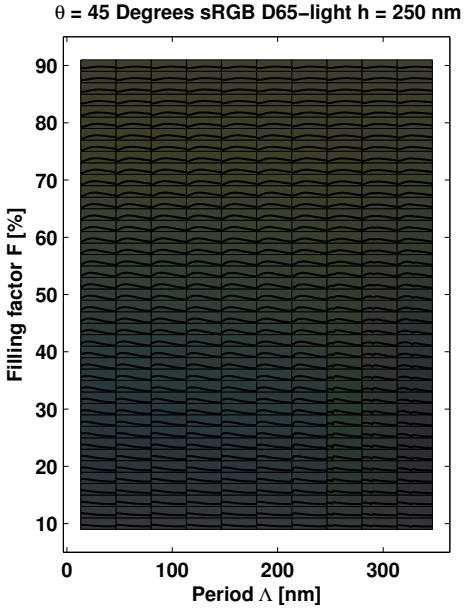

(d) $h = 250$ nm, $\theta = 45°$.

Figure 3.8: Calculated daylight colors spectra for binary structures with $n = 1.5$. Each square shows RCWA simulated specular colors and spectra for given parameters.

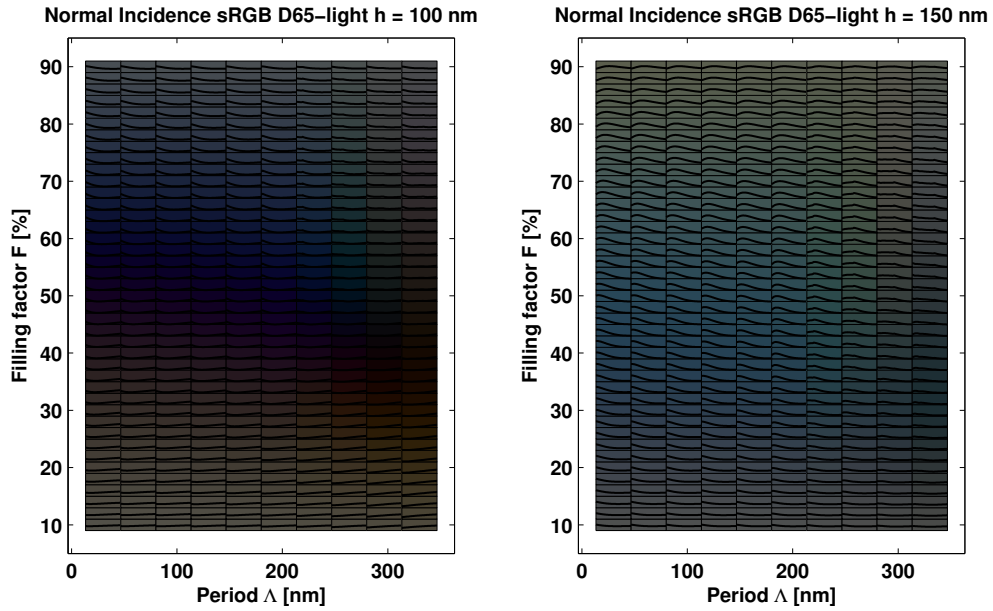

(a) $h = 100$ nm. (b) $h = 150$ nm.

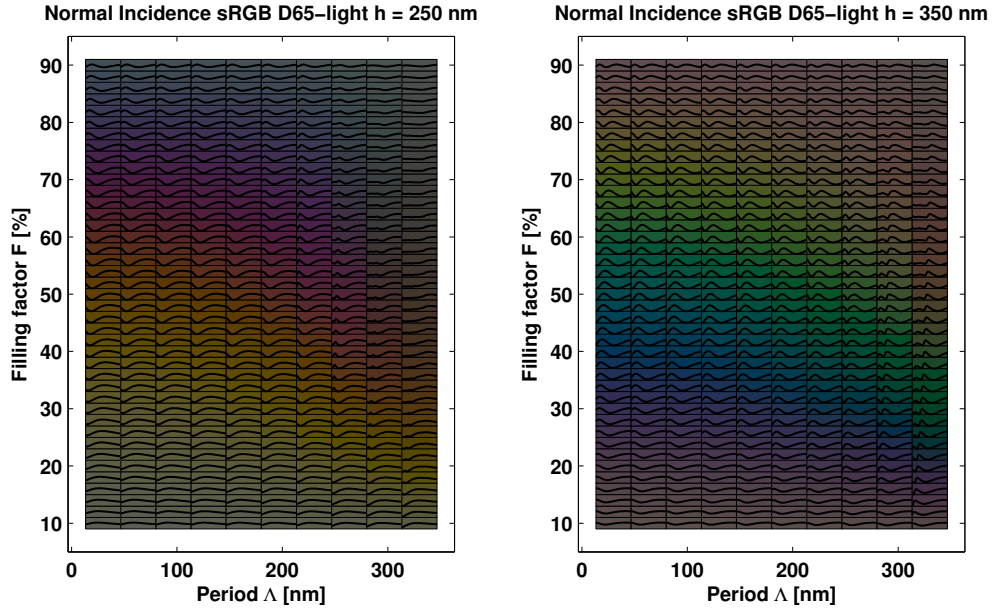

(c) $h = 250$ nm. (d) $h = 350$ nm.

Figure 3.9: Calculated colors spectra for binary structures with $n = 2.0$, see text.

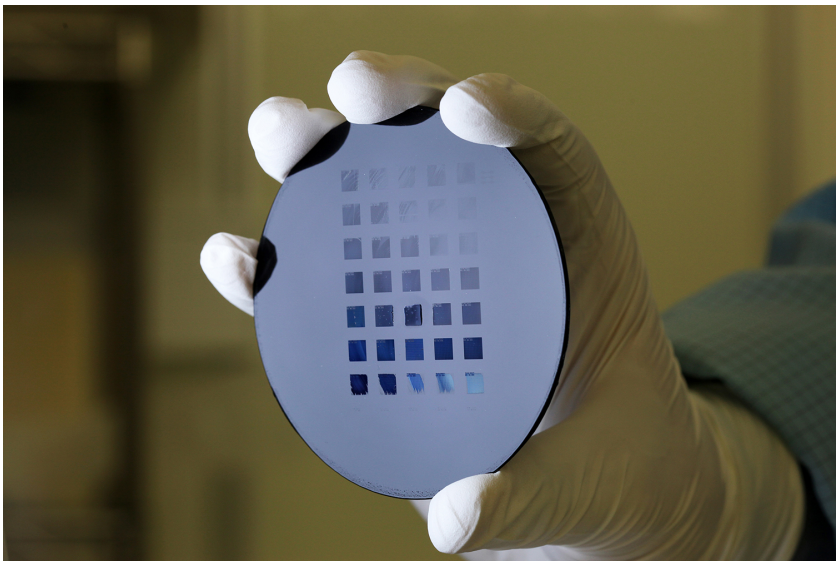

Figure 3.10: Structural colors in polymers. Imprint using master original shown in Figure 3.7.

3.3 Conclusion

The fundamental optical surface properties of dielectric materials were investigated within the framework of mass production applicability. Different colors could be realized using a single-step etching process by altering the nano-texture in high-index materials, exemplified in silicon. However, only corresponding faint colors appeared in polymeric materials.

In relation to the thesis statement described in Section 1.2 on page 9, the concept of all-polymer pigment-free coloration seems somewhat restricted in relation to widespread industrial employment. The surfaces may be used for other applications, where the iridescence and low mechanical strength are advantageous.

Chapter 4

Plasmon Color Technology

In Chapter 1 and 3, all-polymer structural colors were discussed. Now, a metallic deposition is added to the polymer structures, which leads to bright and vivid colors. A novel plasmon color platform is developed based on polymer, aluminum and coating.

The title of this chapter is “plasmon color technology”. Bain defines technology as:

> "*Technology includes all tools, machines, utensils, weapons, instruments, housing, clothing, communicating and transporting devices and the skills by which we produce and use them.*" [Bain, 1937].

In the context of coloration, the structural color effects must possess at least three important properties [Clausen et al., 2014]. First, the color effect should be insensitive to varying viewing angles. Furthermore, it should be robust for everyday use. Finally, it should be up-scalable and economically affordable.

Here, Technology Readiness Levels (TRLs) can be used as a systematic metric to assess the maturity of a particular technology in comparison with other types of technologies [Mankins, 1995]. The levels are based on a scale from 1 to 9, with 9 being the most mature technology.

In this chapter, we present laboratory samples and pilot production trials described in Section 4.5 on page 68. We show, that the concept of plasmonic colors has been levitated from the laboratories at the Technical University of Denmark (TRL 3) to industrial facilities in Denmark, Finland and Italy, supporting the three dominating plastic mass production techniques (TRL 5). The plasmonic colors are defined with a resolution up to 127,000 dots-per-inch, do not fade over time and are insensitive to the light environment. The surface is durable, scratch-resistant and bendable. However, to our knowledge, the concept of surface plasmonic colors has not yet been introduced to the market, although key developments have been accomplished [Zalkovskij et al., 2015], and the economical affordability remains a subject for discussion. Still, we argue, that the results are sufficient to sustain the claim of a “plasmon color technology” in the classical understanding by Bain.

This chapter begins with an introduction to plasmonics and a survey of recent developments. Then, the core technology is described. Angle-insensitive scratch-resistant colors are demonstrated, and it is shown that the dependence on polarization can be controlled. After describing the core principles, the industrial developments are discussed, where polymer-based colored metasurfaces of square-centimeter size are demonstrated by embossing, injection molding, roll-to-roll printing and film insert molding with full compatibility. Furthermore, post production color modification by laser ablation is briefly described. Finally, the environmental benefits are analyzed by life cycle analysis, where the high recyclability leads to reduced environmental impact compared to conventional plastic production. The chapter ends with a conclusion on the applicability of the technology in light of the thesis statement in Section 1.2 on page 9.

4.1 Introduction

This section provides an introduction to metals and to relevant aspects of the field of Plasmonics. Starting from a simple observation, polished metal surfaces appear shiny and reflect a large amount of the incident light. This indicates that a large amount of light may be manipulated to create color effects. It also indicates, that index matching due to coating will not occur, as in the case of all-polymer structures discussed on page 44.

The optical properties of metals and metallic nano-structures also support more advanced concepts. Specifically, the concept of localized surface plasmon resonances (LSPR) is explored in order to produce bright angle-insensitive colors.

4.1.1 Optical Properties of Metals

This section provides an introduction to the optical properties of metals. Metals, unlike polymers, possess the ability to conduct current due to the existence of free electrons in the conduction band, which are not bound to the atomic core [Ritchie, 1957]. The interaction of metals with electromagnetic fields can be understood in the framework of Maxwell's equations. Even metallic nanostructures can be described without a need to resort to quantum mechanics, since the high density of free carriers results in minute spacings of the electron energy levels compared to thermal excitations of energy, $k_B T$, at room temperature [Maier, 2007]. Despite the nanometric dimensions, the smallest characteristic features are still sufficiently large to allow classical electrodynamics considerations [Raza et al., 2015].

Over a wide frequency range, the optical properties of metals can be explained by the Drude plasma model, where a gas of free electrons of number density, n, moves against a fixed background of positive ion cores. In this simple model, the relative permittivity can be derived [Maier, 2007, Eq. (1.22)]:

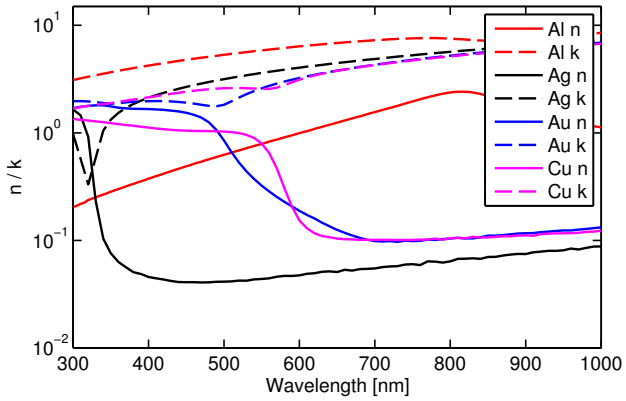

Figure 4.1: Optical properties of selected metals by thermal evaporation. Data [McPeak et al., 2015].

$$\epsilon_r = 1 - \frac{\omega_p^2}{\omega^2 + i\gamma\omega}, \tag{4.1}$$

where γ is the damping coefficient (collision frequency), due to collisions of the electron on the stationary positive atomic cores, and ω_p is the plasma frequency given by:

$$\omega_p = \sqrt{\frac{Ne^2}{\epsilon_0 m}}, \tag{4.2}$$

where ϵ_0 is the vacuum permittivity, e is the electron charge, m is the free electron mass, and N is the density of free electrons calculated from the number of valence electrons and the density of atoms of the metal in question.

In Figure 4.1, the optical properties of metals common within plasmonics are plotted. The properties of gold are dominated by an interband transition threshold in the middle of the visible spectrum, leading to large absorption for shorter wavelengths, which gives the metal its golden color. A similar transition is present in copper and silver, although the threshold for silver is in the ultraviolet part of the spectrum. For aluminum, interband transitions does not occur in the visible spectrum and the transition probability is very low in the visible spectrum. Therefore, silver and aluminum have excellent properties for plasmonic colors, in order to provide a “white” background.

4.1.2 Localized Surface Plasmons

In this section, localized surface plasmons are introduced. These are non-propagating excitations of the conduction electrons of metallic nanostructures coupled to the electromagnetic field [Maier, 2007]. These modes arise naturally from scattering of small, sub-wavelength conductive nanoparticles in an oscillating electromagnetic field. Localized

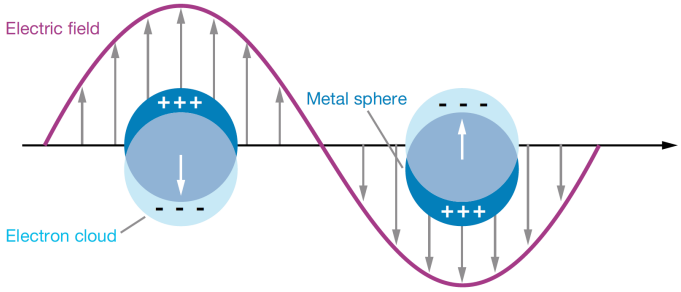

Figure 4.2: Localized surface plasmon. Illustration of the dipole polarizability of a spherical metal nanoparticle under the influence of a plane wave. Figure from literature [Willets and Van Duyne, 2007].

surface plasmons have been around for quite some time. Brilliant shades of red, yellow and green have graced the stained glass windows of cathedrals and medieval pottery for hundreds of years. These colors arise when light excites plasmons on the surface of noble metal nanoparticles present in the glass or clay matrix [Odom, 2012].

In conductive nanoparticles, the motion of the free electrons is limited by the geometrical shape of the metal, such as a sphere or disk, see Figure 4.2. The electron cloud starts to move due to the applied electric field and charge builds up at the surface of the particle. Positive charge is accumulated at the surface in the direction of the electric field and negative charge on the opposite surface. This leads to a restoring force and the system starts to oscillate similar to a mass-spring system with a characteristic resonance frequency, which leads to field amplification both inside and in the near-field zone outside the particle. At resonance, the electric field drives the electron cloud at its natural frequency, which causes large separation of charges, see Figure 4.2. Localized surface plasmon resonances (LSPR) can be excited directly by light illumination.

4.2 Color Plasmonics - State of the Art

Section 1.1 described the state-of-the-art of all-dielectric artificial structural colors. Here follows a survey on metallic structures. Over the last decade, the field of color plasmonics has emerged as a hot topic in photonics [Graydon, 2015]. This survey reviews the latest developments within the field.

Aluminum has attractive properties, as discussed in Section 4.1.1. In 2000, it was shown that an amorphous oxide film atop its aluminum substrate is stable [Jeurgens et al., 2000]. In 2005, the aluminum oxide was found to be about 2.5 nm in thickness with a part amorphous and part crystalline nature [Ramaswamy and Kaste, 2005]. The rapid formation of a thin layer of the oxide prevents further attacks by oxygen and retards chemical reactions. In 2008, scanning electron microscope and atomic force microscope studies confirmed the presence of a thin native Al_2O_3 layer [Chan et al., 2008]. In 2008, strong

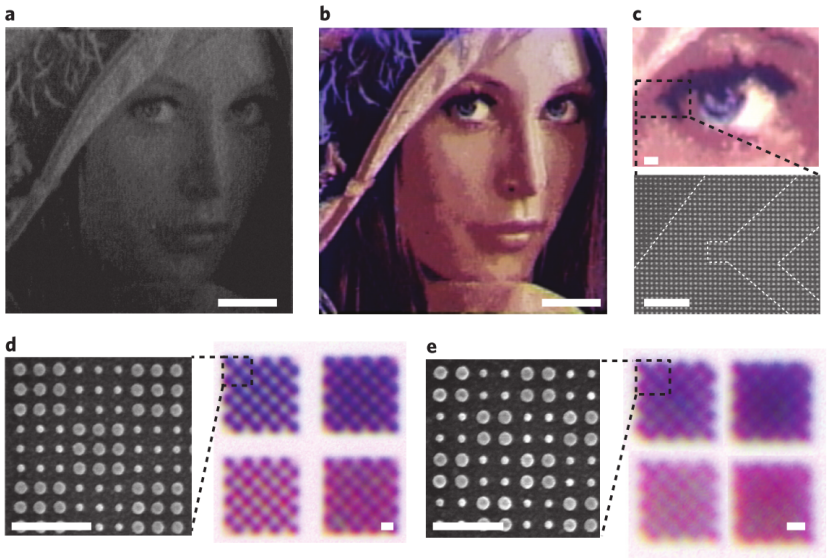

Figure 4.3: Full-color printing and resolution test patterns. a,b) Optical micrographs of the Lena image before (a) and after (b) metal deposition. c) Optical micrograph of an enlarged region of the image, showing the remarkable detail and color rendition on a micrometre-scale level. The SEM image shows that the nanostructures that make up the image have a similar periodicity of 125 nm, but exhibit different colors in the optical image due to a small (30 nm) variation in nanodisk sizes. Each pixel consists of a 2×2 array of disks with a pitch of 250 nm. d,e, Chequerboards approaching (d) and at (e) the optical diffraction limit. In d, a set of chequerboards consists of a combination of two colors, one darker than the other. Each square of the chequerboard is 375 nm in size and consists of an array of 3×3 structures, as shown in the corresponding SEM image. e) A similar chequerboard with color squares of 250 nm consists of an array of 2×2 structures, as shown in the SEM image. The chequerboard pattern is only barely observable at the optical diffraction limit. Scale bars: 10 mm(a, b), 1 mm(c), 500 nm (d, e). Figure from literature [Kumar et al., 2012].

and well-defined localized surface plasmon resonances in the visual spectrum were described in aluminum [Langhammer et al., 2008]. In 2010, the high plasma frequency and the quality factor were described [West et al., 2010]. Furthermore, the energy of the plasmon resonance was found to be determined by the percentage of oxide present within the aluminum [Knight et al., 2014]. Therefore, aluminum has attractive properties compared to typical plasmonic materials [Gérard and Gray, 2015], such as silver [Si et al., 2013] and gold [Roberts et al., 2014], due to its natural abundance, low cost, protective oxide layer for high durability and plasmonic properties in the visible range [Zhang et al., 2011b, Zorić et al., 2011].

In 2012, Kumar *et al.* levitated the field of plasmonic colors by printing color at the optical diffraction limit [Kumar et al., 2012], see Figure 4.3. The highest possible resolution for printed color images is determined by the diffraction limit of visible light. Individual color elements with a pitch of 250 nm were realized. The color-mapping strategy produced images with both sharp color changes and fine tonal variations.

In 2013, Lochbihler *et al.* [Lochbihler, 2013] showed that subwavelength gratings coated with metal-dielectric-metal layers and embedded in a dielectric display color properties. The reflected color of incident unpolarized white light was tuned by the modulation depth of the grating. Reflective colored images could be reproduced by using different grating depths.

The year of 2014 marks a number of significant contributions based on the work of Kumar *et al.* in 2012. In the next section, the core plasmonic technology of this thesis is presented based on the publication by Clausen *et al.*, where aluminum is used as a cheap and abundant plasmonic material [Clausen et al., 2014]. Two weeks before Clausen *et al.* published in Nano Letters, Tan *et al.* published a remarkably similar paper in Nano Letters on plasmonic color palettes for photorealistic printing with aluminum nanostructures [Tan et al., 2014]. Like Clausen *et al.,* described on page 56, the work of Tan *et al.* expanded the visible color space through spatially mixing and adjusting the nanoscale spacing of discrete nanostructures, see Figure 4.4.

Also in 2014, Roberts *et al.* demonstrated plasmonic color printing with subwavelength resolution using circular gap-plasmon resonators arranged in 340 nm period arrays of square unit cells and fabricated with single-step electron-beam lithography [Roberts et al., 2014]. Like Clausen *et al.*, the fabricated color print could be protected with a transparent dielectric overlay for ambient use. Olson *et al.* showed that vivid, highly polarized, and broadly tunable color pixels can be produced from periodic patterns of oriented nanorods [Olson et al., 2014]. Whereas the nanorod longitudinal plasmon resonance is largely responsible for pixel color, far-field diffractive coupling was used to narrow the plasmon linewidth, enabling monochromatic coloration and significantly enhancing the far-field scattering intensity of the individual nanorod elements. Finally, Goh *et al.* demonstrated independently tunable biaxial color pixels composed of isolated nanoellipses [Goh et al., 2014]. The pixels exhibited a full range of colors with linear polarization dependence, as also described in Section 4.4 on page 61.

Color plasmontics has also been proposed in the context of display pixels. In 2013, Wu *et al.* proposed a new scheme through localized resonance in metallic nanoslits by light funneling [Wu et al., 2013]. Angle insensitive color filters were achieved, capable of wide color tunability across the entire visible band with a pixel size beyond the diffraction limit. In 2015, Yun *et al.* proposed a structure comprising of a metal cavity and a nanoaperture to simultaneously control the color and intensity of transmitted light in a single pixel [Yun et al., 2015]. The metal cavity constructed plasmonic standing waves to organize the spatial distribution of amplitudes. The nanoaperture permitted light with a specific wavelength and amplitude to pass through it, depending on the nanoaperature's relative position in the cavity and the polarization state of the incident light.

Silver nanoparticles can also be employed. In 2014, Tsuboi *et al.* demonstrated a localized surface plasmon resonance multicolor inorganic electro-chromic device [Tsuboi et al., 2014]. The device enabled reversible color changes, including the three primary

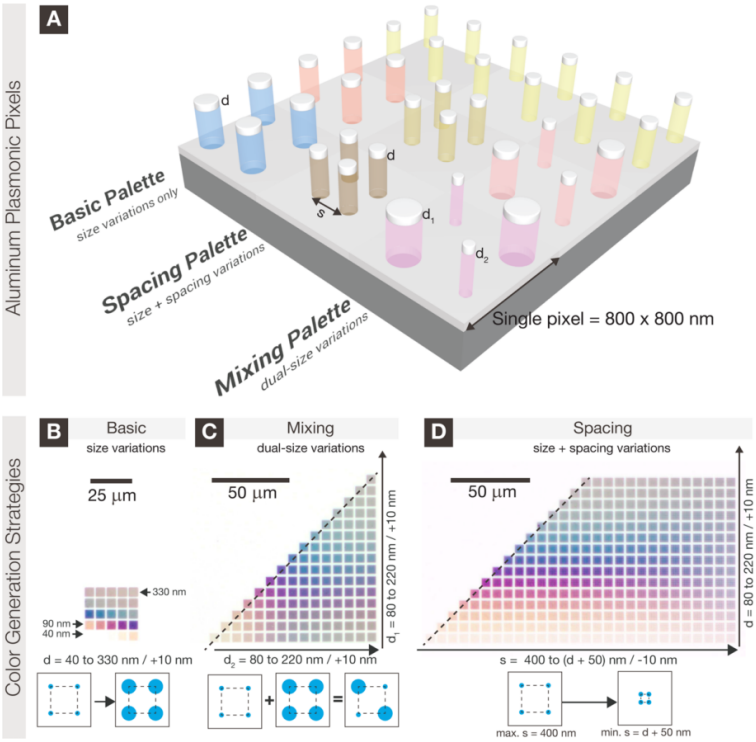

Figure 4.4: Plasmonic pixels. (A) Isolated aluminum nanodisks on HSQ nanopillars with an aluminum backreflector substrate. (B) basic color palette with only size variation and a fixed pitch of 400 nm, (C) mixing colors with two size variations among four nanodisks within an 800 × 800 nm pixel, with a fixed spacing of 400 nm between nanodisks, and (D) spacing color palette with both size variations and spacing variations among four nanodisks within an 800 × 800 nm pixel. Optical images were normalized to a white background. Figure from literature [Tan et al., 2014].

colors cyan, magenta and yellow in a single cell.

In the context of filtering, surface plasmon-based nanostructures are attractive due to their small dimensions and the ability to efficiently manipulate light. In 2010, Xu *et al.* demonstrated conversion between free-space waves and spatially confined modes in plasmonic nanoresonators formed by subwavelength metal-insulator-metal stack arrays and showed that the transmission spectra can be well controlled [Xu et al., 2010]. In 2012, Yokogawa *et al.* reported on plasmonic hole arrays as color filters designed for state-of-the-art silicon CMOS image sensors [Yokogawa et al., 2012]. The hole arrays were composed of hexagonally packed subwavelength sized holes on a 150 nm Al film designed to operate at the primary colors of red, green, and blue. In 2013, Zeng *et al.* reported on a plasmonic subtractive color filtering scheme that exploited extraordinary low transmission through an ultrathin nanostructured metal film [Zeng et al., 2013]. This approach achieved high transmission efficiencies for simple architectures.

Colored photovoltaics was demonstrated in 2014. Lee *et al.* introduced a dual-function solar cell, based on ultrathin dopant-free amorphous silicon embedded in an optical cavity, that displayed distinctive colors with the angle-insensitive appearances [Lee et al., 2014]. Light-energy-harvesting colored signage was demonstrated.

Imprinted color structures have also been shown in 2015. Franklin *et al.* demonstrated a tunable polarization-independent reflective surface by a nanostructured plasmonic surface in conjunction with a high birefringence liquid crystal [Franklin et al., 2015]. The color of the surface was changed as a function of applied voltage. A full range of colours spanning the entire visible spectrum was achieved. Cheng *et al.* demonstrated a structural color printing method based on plasmonic metasurfaces for perfect light absorption [Cheng et al., 2015]. Near perfect light absorption were obtained to realize high-resolution, angle-insensitive plasmonic color printing with high color saturation and brightness.

Stainless-steel decoration was also demonstrated in 2015. Luo *et al.* fabricated nanostructures on the stainless steel surfaces by a nanosecond laser operated in air, oxygen, nitrogen and argon [Luo et al., 2015]. The structures were affected by laser scanning speed as well as gaseous environment. The multicolor effect was found to be attributed to both feature dimension and chemical composition of the structures.

Finally, all-metal colors were also discussed in 2015 by Ng *et al.* using nanoprotrusions on a bulk silver layer with narrow near-perfect absorption peaks [Ng et al., 2015]. A constant structure height of 50 nm and pitch of 250 nm were used. The described implementation is limited to one absorption peak, instead of two peaks for the design chosen in the work described in the next section. Still, the results indicate significant industrial potential, as the structures are reasonable to fabricate, can be made with sputtering described in Section 2.1.6 on page 25, and lead to tunable reflected colors.

In conclusion, the field of color plasmonics has seen a rapid rise in recent years. For color plasmonics, there are still hurdles to overcome, especially in terms of fabrication

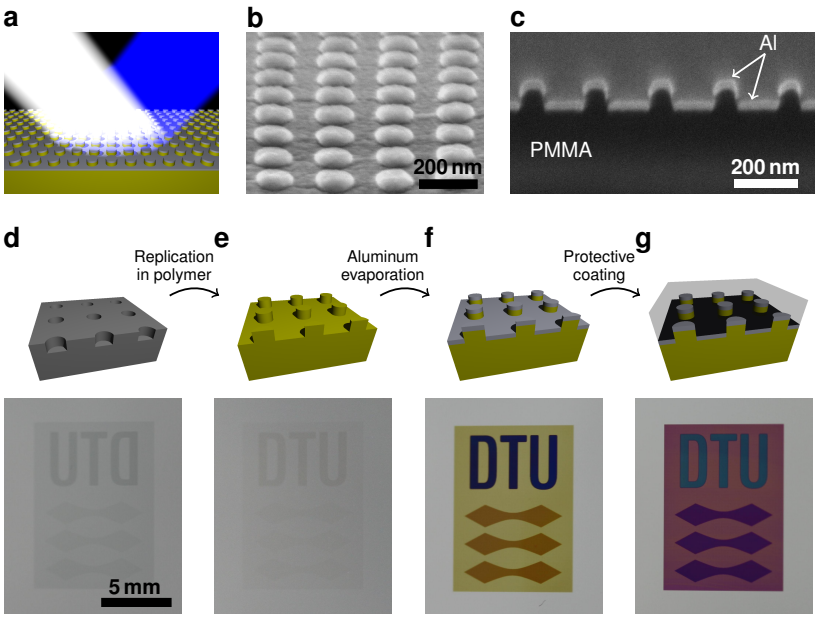

Figure 4.5: Basic concept. (a) Absorption resonances in the plasmonic nanostructure lead to colored reflections upon white-light illumination. (b) A SEM image of fabricated disks elevated above the holey plane seen from 15° above the horizon. (c) Cross-sectional SEM image by focused ion-beam for sample preparation. (d) A master mold comprising nanohole arrays is used fabrication by hot embossing or injection molding. The photography shows a macroscopic sample with three different hole sizes leading to three different colors in the final sample. (e) A polymer pillar array replication of the master mold. (f) Aluminum is evaporated on top, creating the disk-hole structure. (g) The structure is coated with a transparent material to protect. The resonance redshift leads to altered colors. Figure from publication [Clausen et al., 2014].

costs for industrial manufacturing [Dean, 2015]. However, the flexibility of plasmonic nanostructures, and their intrinsic ability to manipulate light at the nanoscale, positions them as candidates for a number of applications, such as security, stenography, optical filters and high-density encoded optical data storage.

4.3 Core Concept

Color effects based on pure dielectrics were described in the previous chapter. The concept of all-polymer pigment-free coloration respecting the replication constraint seems somewhat restricted in relation to widespread industrial adaptation.

This section describes the development of a novel plasmon color technology for structural coloration in plastics based on metal-coated polymer nano-textures and a protective coating system, see Figure 4.5a. The technology utilizes a hybrid disk-hole plasmonic mode for resonances in the visible spectrum, based on aluminum as a cheap and abun-

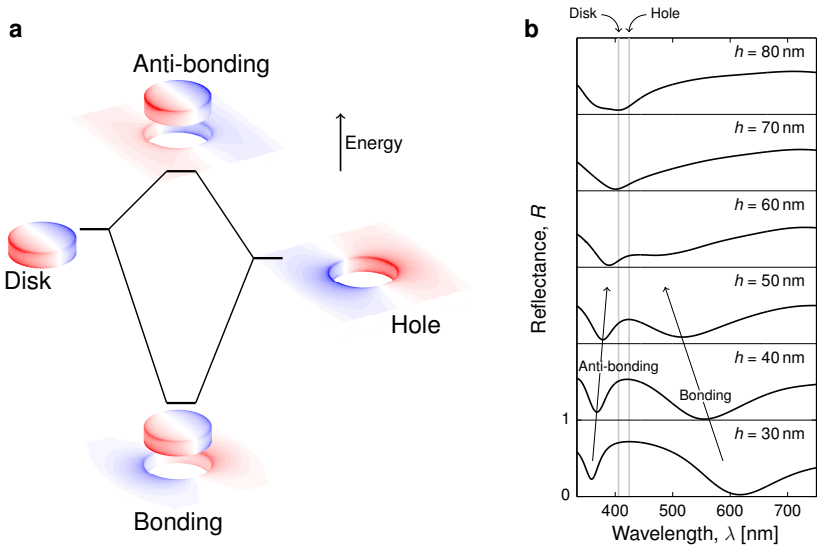

Figure 4.6: Plasmon hybridization due to disk-hole coupling. (a) Energy diagram illustrating the hybridization of the coupled plasmonic modes of the disks and holes of the structure into a low energy mode (bonding) and a high energy mode (antibonding). The simulated charge distributions of the pure disk and hole arrays show the dipolar nature of their resonances. For the full structure, the symmetric and antisymmetric coupling leads to an energy splitting. The shown structure is for D = 80 nm, Λ = 200 nm, h = 50 nm, and t = 20 nm embedded in material of refractive index of 1.5. It shows the symmetric and antisymmetric coupling between the disks and holes. (b) Reflectance spectra for same parameters as panel a but for varying pillar height, h. The two modes are seen as dips in the spectra. Figure from publication [Clausen et al., 2014].

dant plasmonic material. Examples of the active surface can be seen in Figure 4.5b-c. The findings of this section have been published [Clausen et al., 2014].

4.3.1 PMMA-on-glass Samples

The fabrication scheme is presented in Figure 4.5d−g. A master mold was fabricated in silicon using electron-beam lithography (EBL) and dry etching. The finalized master consisted of periodic hole arrays with period Λ, hole diameter D, and hole depth h. The master was a negative of the desired polymer surface, a periodic pillar array, which was fabricated in a hot-embossing step. After replication, the desired pattern was practically invisible as the polymer−air index contrast is too low to significantly alter the surface reflectance of the nano-structured polymer surface. However, bright and angle-independent colors emerged when a thin aluminum film of thickness t was deposited on top of the textured polymer surface, see Figure 4.5f. The metal deposition must be directional in order to facilitate the creation of isolated metal disks.

Finally, a protective coating was deposited on top with a thickness significantly larger than the coherence length of broadband white light in order to avoid Fabry−Peŕot inter-

ference affecting the color experience. The coating caused an increase in the effective refractive index surrounding the disk-hole nanostructure, which lead to a redshift of the resonances in the system and a corresponding color change, see the last step in Figure 4.5. The top coating is necessary to protect the structure.

4.3.2 Physical Principle

Figure 4.6 illustrates the physical principle behind the color creation. The colors of the structure are due to resonant absorption in the aluminum nano-structures. Both the disks and holes possess dipolar resonances, which leads to increased absorption at specific wavelengths. The two modes hybridize into two new modes for small dimensions, known as a "bonding" mode characterized by a lower resonance frequency and an "antibonding" mode with higher resonance frequency. Simulated surface charge distributions of the relevant modes are shown in Figure 4.6a. The low-energy mode is characterized by the charge oscillations in the disk and the hole being out-of-phase, whereas the high energy mode exhibit charge oscillations in phase. The effect on the reflectance spectrum is illustrated in Figure 4.6b, where each of the two hybrid modes appear as significant dips in the reflectance spectra. The energy splitting decreases, when the pillar height increases, thereby decreasing the coupling between the resonators. It is also seen, that the strength of the "bonding" mode is highly dependent on low pillars (large coupling). Above $h = 70$ nm, the hybridization is not observed. For even higher pillars, the behavior of the system moves toward a Fabry−Peŕot-like regime, where the disk array and the hole array act as separate mirrors with distinct resonant reflection coefficients. A strong resonance of the hybrid "bonding" mode is key to the creation of tunable colors.

The range of colors that may be produced is illustrated in Figure 4.7. In Figure 4.7d, the experimentally measured spectra have been converted to CIE1931 chromaticity coordinates, thereby illustrating the color gamut of the method. Some colors are difficult to produce when the effect is based on a spectral dip originating from resonant absorption. Red and green with high chromaticity are examples of such colors. In Figure 4.8, a photograph of PMMA-on-glass color samples are provided, illustrating the large degree of color tuning ability.

4.3.3 Polymer Foil Samples

In Figure 4.9, embossed samples can be seen. After a significant process optimization over about a year, the samples were made in polymer by a pattern for blue color without coating. A SEM image of the master original can be seen in Figure 4.9a. The sample was fabricated by transferring a specific nanopattern from an electron beam written silicon master to a 50 μm PMMA plastic film by hot-embossing. Then approximately 20 nm Al was applied by electron beam evaporation to create plasmonic colors. A SEM of the foil

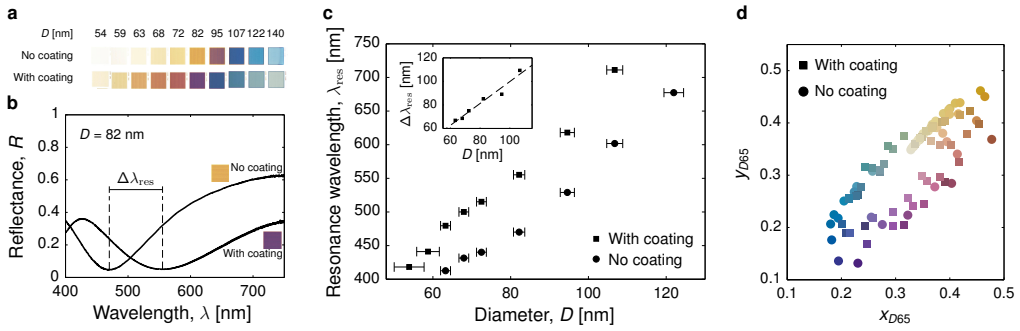

Figure 4.7: Diameter-dependent resonance and colors. (a) Images in bright-field microscopes of 0.8 $\times$ 0.8 mm^2 squares with period Λ = 200 nm and varying diameter. The coating-induced redshift is evident. (b) Reflectance spectra of structure with D = 82 $\pm$ 2 nm with and without coating indicating the change in resonance wavelength $\Delta\lambda_{\mathrm{res}}$ due to the coating. (c) Resonance position as a function of disk diameter for Λ = 200 nm. The shift in resonance due to the coating is seen to be approximately linear with diameter. (d) CIE 1931 chromaticity coordinates of the fabricated samples for both the coated and the uncoated case. The color of each spot indicates the color of the corresponding sample. Figure from publication [Clausen et al., 2014].

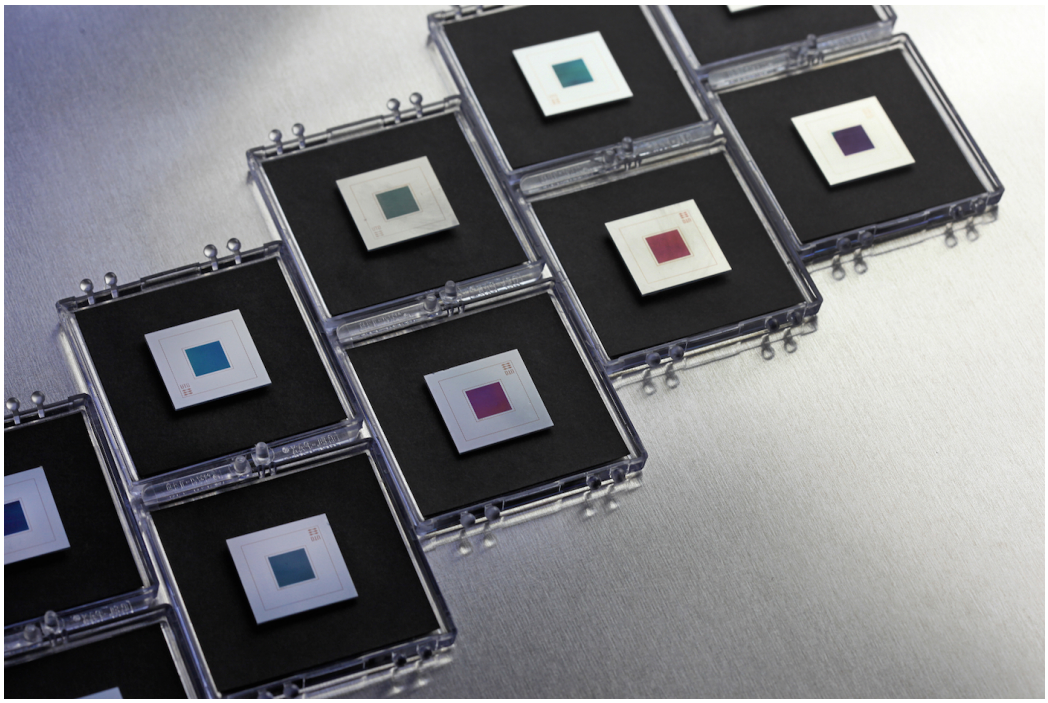

Figure 4.8: Plasmonic color samples. PMMA on glass with diffusive and clear top coating, as described in Figures 4.7 and 2.7.

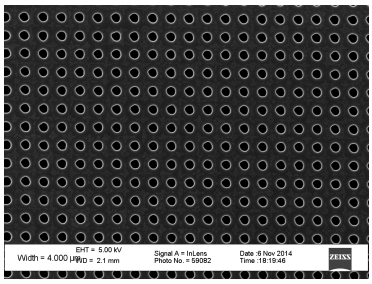

(a) Silicon Master Original.

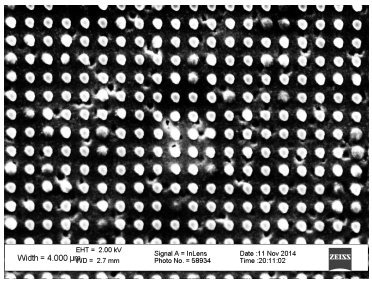

(b) PMMA foil replica.

(c) Foil before coating.

Figure 4.9: Bended plasmonic colored plastic surface by embossing (see Figure 2.7) from a 200 nm periodic pattern for blue color without coating. (a) SEM image of silicon master original. (b) SEM image of PMMA foil replica with Al. (c) Photograph after imprint of foil. SEM Image widths 4000 nm.

with Al can be seen in Figure 4.9b. The front page shows a sample with green color after coating. The coating includes light-scattering particles similar to color pigments, which makes the surface appear painted, see 25. The redshift from blue to green color is clearly seen when comparing Figure 4.9c and Figure 4.14a (front-page).

4.3.4 Conclusion

In conclusion, angle-insensitive scratch-resistant structural colors were demonstrated, where aluminum was used as a cheap and abundant plasmonic material. We utilized a hybrid disk-hole plasmonic mode, which provides angle-independent resonances tunable across the entire visible spectrum. Expensive nano-lithography should only be carried out once due to the subsequent replication-based fabrication. The functional structures were covered by a protective dielectric coating, causing a redshift of the plasmon resonance.

4.4 Polarization Dependence

This section describes the work on polarization dependence. The section has been published [Højlund-Nielsen et al., 2015].

The polarization of light is a fundamental attribute of electromagnetic waves, providing information about its spacial travel direction and clues to its past. Polarization properties have interesting applications within display technologies, high-density optical storage, anti-counterfeiting and bio-sensing [Goh et al., 2014, Petryayeva and Krull, 2011]. Here, a polarization dependent plasmonic aluminum-based high-density metasurface operating at blue wavelengths is presented. The sensory element performs in reflection mode and provides the possibility to detect polarization information by visual means.

The polarization dependent metasurface described here is based on sub-wavelength plasmonic rectangular structures. Similar freely suspended elongated ellipsoidal nanoparticles were first described as polarization dependent in 1912 by Gans [Gans, 1912], who predicted the splitting of surface plasmons into two distinct oscillation modes, namely the high-energy transverse and the low-energy longitudinal oscillation of conduction band electrons [Papavassiliou, 1979, Link and El-Sayed, 2000]. Unfortunately, freely suspended particles lack precise orientation control, which limits filter resolution.

In contrast, microfabricated plasmonic metasurfaces allow individual control of the shape, position and orientation of the active entities. In particular, two-dimensional metasurfaces of well-controlled spatial arrangements have attracted considerable attention over the last two decades for their simple design and fabrication, and for their ability to enhance electromagnetic fields. Metasurfaces have been demonstrated to manipulate visible and infrared absorption [Haug et al., 2008, Le et al., 2008, Adato et al., 2009] at high polarization conversion efficiencies for sensor applications [Zhu et al., 2012, Chen et al., 2015, Stewart et al., 2008, Lu et al., 2012].

Polarization dependent aluminum metasurfaces have also been demonstrated for full-color stereoscopic printing by Goh *et al.* [Goh et al., 2014]. However the metasurface was based on electron beam lithography in hydrogen silsesquioxane directly on a silicon substrate, impeding fabrication scalability. Furthermore, the ellipse dimensions were varied from 100 nm to 190 nm within a lattice of period 400-500 nm, which indicates poor color contrast and angular dependence, see Section 3.1.3 on page 33.

Here, a similar ultra-thin high-density platform is presented, but with a sub-wavelength period of 250 nm for better angular insensitivity and fabricated by a scalable nano-replication process in hybrid polymer. Compared to Goh *et al.* [Goh et al., 2014], the presented platform is about four times smaller per unit-cell, is mass-producible, and constitutes an important step towards application of polarization-dependent metasurfaces.

To enhance the performance of the metasurface, the structure is rotated with respect to the square lattice in order to elongate the plasmonic structure and increase the resonance strength. The concept of elongation and rotation of the base structure to utilize the hybrid

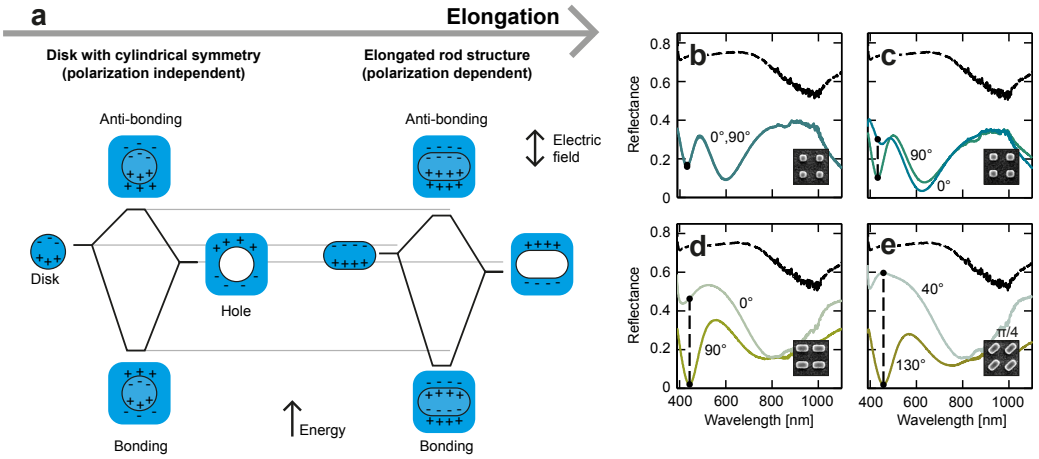

Figure 4.10: Hybrid transverse mode concept by elongation of base plasmonic structure. a) Energy hybridization diagrams of circular and elongated structures at transverse polarization. b-e Representative reflectance spectra for different polarizations of various structures with CIE/sRGB calculated color coding. Top dashed lines show spectrum for non-structured surface. Figure from publication [Højlund-Nielsen et al., 2015].

transverse mode is illustrated in Figure 4.10. In Figure 4.10(a), energy hybridization diagrams for the transverse mode and the structure itself are sketched. In Figure 4.10(b)-(e), typical reflectance spectra for different polarizations of various structures (insets) are plotted using CIE/sRGB calculated color coding. The resonance enhancement by rotation of the polarization-dependent resonance behavior around 450 nm is clearly seen.

4.4.1 Fabrication

The plasmonic color filter was fabricated by UV nanoreplication, as sketched in Figure 4.11(a)-(e). A silicon master containing areas with two-dimensional periodic structures was fabricated by electron beam lithography and dry etching, see Figure 4.11(a). The master was anti-stiction coated with a few monolayers of perfluorodecyltrichlorosilane (FDTS) using molecular vapor deposition.

The sample replica was prepared by dispensing an UV curable hybrid polymer (Ormo-Comp, Micro Resist Technology GmbH, Germany) onto a borosilicate glass wafer acting as carrier substrate, see Figure 4.11(b). The master was brought into contact with the soft hybrid polymer between the opaque silicon master and the transparent glass substrate. The polymer was cured by ultra-violet (UV) light through the glass substrate for 18 min, as shown in Figure 4.11(c). After curing, the master and the hybrid polymer were manually separated, leaving the solidified hybrid material on the glass substrate with a nano-structured surface created as a negative of the master pattern, see Figure 4.11(d). Finally, a 18 nm thin film of aluminum was deposited on top of the structure by electron

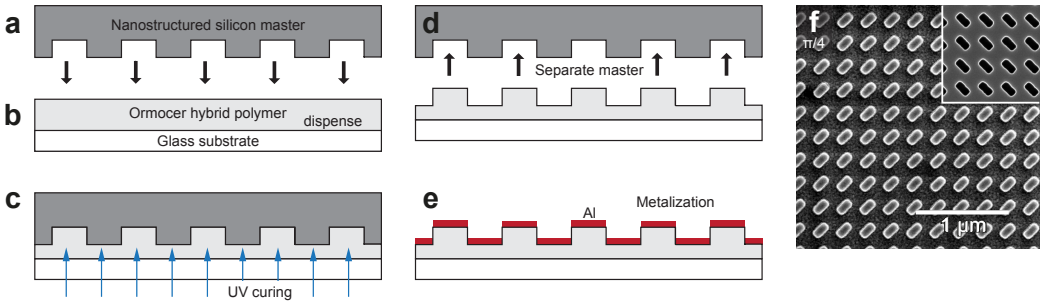

Figure 4.11: Fabrication process for 250 nm periodic structures from pattern definition to metalized polymer replica. a-e) Sketch of fabrication process, see text. f) SEM image of metalized polymer replica for 45° rotation inside unit-cell. Corresponding SEM image of Si master can be seen as inset. Figure from publication [Højlund-Nielsen et al., 2015].

beam evaporation in vacuum at a rate of about 1.0 nm/s. The vertical side walls and the height differences of about 50 nm of the polymer topology lead to the formation of isolated metal islands on top of the polymer pillars, as seen in Figure 4.11(d).

Representative SEM images of patterns on the polymer replica and the corresponding master area can be seen in Figure 4.11(f). The mirror symmetry between master and replica due to the replication process can be seen. The rectangular structures are rounded at the corners. In general, the fabrication process was optimized for a high yield and SEM inspections of the master and final samples did not reveal defects or pattern deviations.

4.4.2 Experiments

Figure 4.12 presents the experimental results. In Figure 4.12(a), the polarization angle and the rotation angle of the structure are defined with respect to the basis lattice vector of the square lattice (x-axis). Normal incidence reflectance spectra were obtained for the metalized polymer samples using a modification of an experimental setup previously used for photonic crystal characterization [Vannahme et al., 2015, Hermannsson et al., 2015].

The setup is schematically illustrated in Figure 4.12(b). Light from a broadband laser-driven light source (Energetiq EQ-99XFC) was fed to the setup via an optical fiber and collimated with a fiber collimator. A linear polarizer on a rotational stage was used to control the polarization of the light. The light was then focused with a lens and reflected into a 10x microscope objective by a beam splitter. The light then emerged collimated from the other side of the objective and illuminated the device at normal incidence. The reflected light traveled backwards through the objective and beam splitter and was then simultaneously focused by a microscope tube lens onto the slit of an imaging spectrometer (Acton SP-2756 Imaging Spectrograph with PIXIS100B Digital built-in camera and grating 150 g/mm) and a CCD camera via another beam splitter. Thus, positioning was controlled and recorded with the CCD camera while the reflected spectrum was analyzed with the

spectrometer. Intensity counts were acquired from the spectrometer and signal counts were calculated by subtracting corresponding dark background spectra. In order to calculate the absolute reflectance, polished silicon was used as reference using well-established tabulated optical properties of silicon [Green and Keevers, 1995]. The reflectance was calculated as function of wavelength depending on polarization angle for a given sample area.

In Figure 4.12(c), reflectance spectra for different polarization angles are shown for the structures seen in Figure 4.11(f), respectively. The spectra are represented by calculated colors, as described in Section 3.1.4 on page 35, where the reflectance is converted to a CIE XYZ color using a standard D65 light source and 2° CIE observer, and finally converted to sRGB color space for screen viewing. The resulting reflectance depends strongly on polarization. In Figure 4.12(d), the reflectance is plotted as function of polarization angle at resonance wavelength for the series of elongated structures seen as insets in Figure 4.12(l)-(n). In Figure 4.12(e), the corresponding resonance wavelengths are plotted. Finally, in order to provide an overview, Figure 4.12(f)-(n) visualize the reflectance spectra using contour-plots for different polarization angles for all nine investigated topologies with corresponding SEM images as insets.

4.4.3 Numerical simulations

In order to support the experimental findings, simulations were conducted using a frequency-domain solver with periodic boundary conditions in the surface plane (CST Microwave Studio). Despite the nanometric dimensions, the smallest characteristic features are still sufficiently large to allow classical electrodynamics considerations [Raza et al., 2015]. Normal to the structures, the simulation domain was extending 300 nm away from the metal and at the boundaries Floquet ports were used. The frequency-dependent permittivity used for aluminum were from the handbook of Palik [Palik, 1986]. Substrate and coating were assumed to have a refractive index of 1.5.

Figure 4.13 presents the simulation results. In Figure 4.13(a), the corresponding reflectance spectra of the structures in Figure 4.11(n) at 40° and 130° polarization angle are seen, showing good agreement with the experimental results. In Figure 4.13(b), the detailed 2D simulated reflectance spectra of the structures in Figure 4.11(f) are seen, showing the resonance evolution with similar trends as seen in Figure 4.12(n). In order to further illustrate this, an absolute field profile is presented in Figure 4.13(c) based on the scaling seen in Figure 4.13(d).

Based on the scaling seen in Figure 4.13(e), the z-component of the electric field cross-section profiles in the center of the patches can be seen in Figure 4.13(f)-(n). The unit cell supports complex field distributions extending both into the metal-air interface and the surroundings. This mode corresponds to a hybrid transverse mode resonating along the short axis of the plasmonic structure with a strong coupling at its resonant frequency. Even-

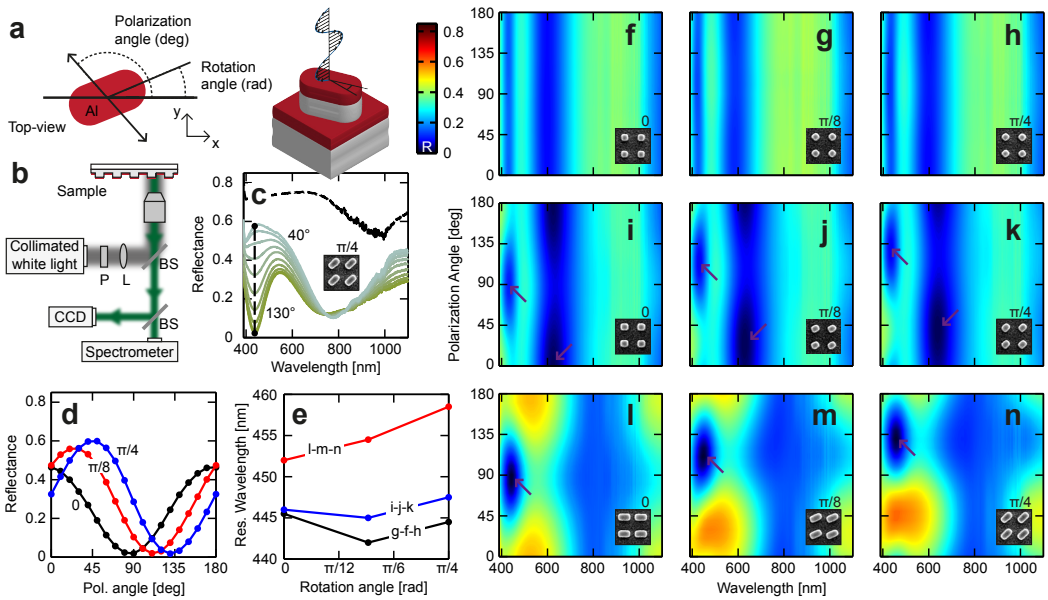

Figure 4.12: Measured normal incidence reflectance spectra for metalized polymer samples. a) Definition of coordinate system and angles. b) Schematic illustration of optical setup. c) Reflectance as function of wavelength for different polarizations in the case of structure "n" with CIE/sRGB calculated color coding. Top dashed line shows spectrum for non-structured surface. d) Reflectance as function of polarization angle at resonance wavelength for elongated structures "l", "m", and "n". e) Resonance wavelengths as function of rotation angle. f-n) Reflectance as function of wavelength and polarization angle for all nine investigated topologies. Arrows indicate transverse (450 nm) and longitudinal (630 nm) resonances. Figure from publication [Højlund-Nielsen et al., 2015].

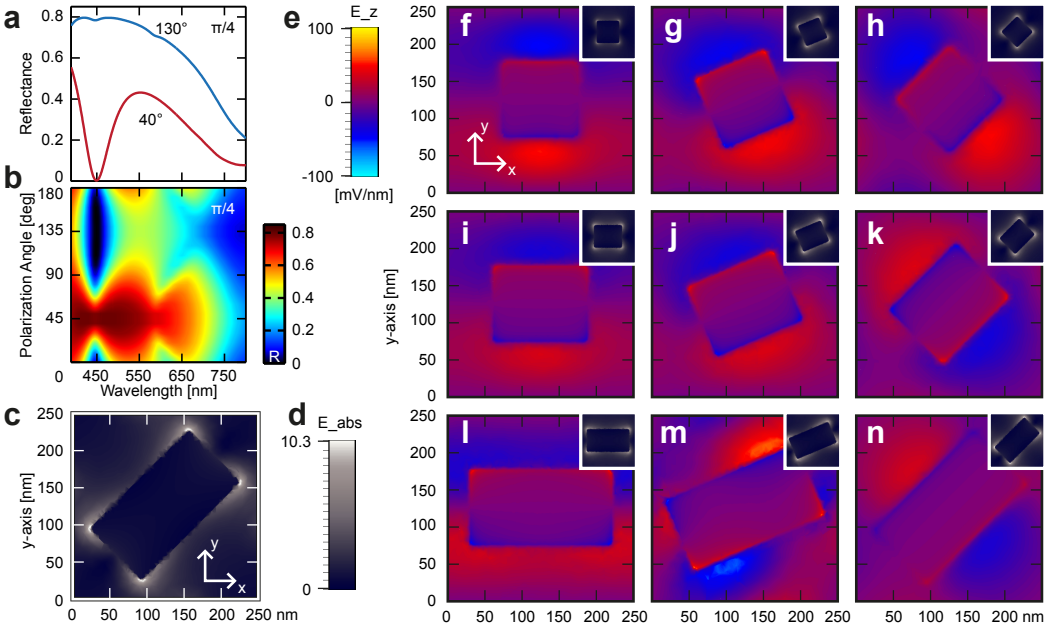

Figure 4.13: Simulations. a) Reflectance spectra for structure "n" at 40° and 130° polarization angle. b) Reflectance contour-plot for structure "n". c) Absolute electric field intensity for structure "n". d) Scale for absolute field intensity with maximum of 800 mV/nm. e) Scale for z-component of electric field for input field of 76.6 mV/nm. f-n) Plots of the electric field z-component inside the unit-cell, with inserts of the corresponding absolute field intensity for structures "f"-"n" at the high-energy resonance for optimal polarization angle (90°, 113°, 135°) and phase. The hybrid transverse mode can be seen. Figure from publication [Højlund-Nielsen et al., 2015].

tually these plasmonic resonances presented here lead to the enhanced absorption and thereby reduced reflection. As a result, at the frequencies of these modes, the electric field concentrates at the sharp corners (as shown in the corresponding insets in Figure 4.13(f)-(n) and in Figure 4.13(c)), which support a strong enhancement of the localized fields.

4.4.4 Discussion

From the experimental and numerical simulation results, a number of trends can be observed. First, two resonances can be observed for rounded-square structures, see Figure 4.12(f). These resonances correspond to the well-known hybridization between LSPR modes [Prodan et al., 2003] in aluminum nanodisks and nanoholes. The high energy resonance in the blue part of the spectra is seen to be more spectrally narrow than the low energy resonance in the red part of the visual spectrum. It is also clear that rotating the 100 nm rounded-square structure does not disturb the hybridization between the polarization-independent LSPR modes and hence no significant dependence of the re-

flectance on polarization angle can be observed, see Figure 4.12(g)-(h).

Secondly, elongating the base structures about 25 nm in one direction causes the reflectance to become somewhat polarization dependent, see Figure 4.12(b). The high energy resonance is present when the polarized light is perpendicular to the base structure, e.g. at 90° for structure "i", see Figure 4.12(i). The reflectance minimum follows accordingly for rotation of the rectangular structure with respect to the lattice, such that the minimum reflectance around a wavelength of 450 nm shifts to 135° for structure "k" with rotation 45°, see. Figure 4.12(k). This clearly indicates that the polarization dependence is connected to a transverse plasmonic mode of the metal disks.

Finally, elongating the length to about 190 nm (width ca. 110 nm) causes the reflectance at blue wavelengths to become strongly polarization dependent, see Figure 4.12(l). It is also clear that the resonance strength is clearly enhanced, while the reflectance off-resonance is also higher. By elongating the plasmonic base structure, the hybridization modes become polarization dependent, such that the high energy mode has the character of a hybrid transverse mode. This is also seen in the simulations, see Fig 4.13(l). By rotation of the base structure, the resonance strength is further improved and the resonance wavelength increases slightly. In the case of 45° rotation angle for structure "n", the normal-incidence reflectance drops around the blue resonance wavelength (457 nm) from about 60% to below 1.6%. This "on/off" ratio of 33.4 creates a visible color discrepancy, see Fig 4.12(b), which agrees well with the simulations, see Fig 4.13(n).

4.4.5 Conclusion

In conclusion, a polarization dependent plasmonic aluminum-based metasurface operating at blue wavelengths was described. The fabricated subwavelength structures displayed strong, localized, plasmonic resonances able to control linear polarization. Best performance was achieved by rotating an elongated rectangular structure of length 180 nm and width 110 nm inside a square lattice of period 250 nm. In the case of 45° rotation of the structure with respect to the lattice, the normal-incidence reflectance decreased around the resonance wavelength of 457 nm from about 60 percent to below 2 percent with a ratio of 33, thereby providing on/off controllability of reflectance.

4.5 Industrial Developments

In this section, the industrial developments are described in relation to the thesis statement described in Section 1.2 on page 9. This section has been submitted by Højlund-Nielsen *et al.* for publication.

Plasmonic metasurface coloration has attracted considerable attention in recent years due to its industrial potential. So far, demonstrations have been limited to small patterned areas fabricated using expensive techniques with limited scalability. Here we levitate the technology beyond the common size and volume-limitations of nanofabrication and demonstrate aluminum-coated polymer-based colored metasurfaces of square-centimeter size by embossing, injection molding, roll-to-roll printing, and film insert molding. We compare the different techniques and discuss the requirements and bottlenecks in terms of master fabrication, replication, metallization, and protection coating for large scale production of sub-wavelength metasurfaces. Most notably, we demonstrate that plasmonic metasurface colors are compatible with film insert molding. The results indicate a promising future for plasmonic colors as a viable alternative for decorating mass-produced polymer parts.

Today, colorants, such as pigments or dyes, are used to color plastic consumer products, either as base for bulk-colored products or in inks for surface decoration. Given the high societal attention to environment and recycling of waste materials, used plastic products must be mechanically sorted by color before recycling [Al-Salem et al., 2009]. This poses limitations on the efficiency of large scale recycling efforts. As an alternative to chemistry-based coloring, nano-scale structural coloring has been proposed [Kumar et al., 2012] to minimize usage of additives and post-production steps and to increase pattern resolution. Here, colors are achieved by means of resonant light-matter interactions on a nano-patterned surface. Specifically, we propose a inter-compatible polymer-metal-coating system, as seen in Figure 4.14. Thereby, the sorting by color can arguably be avoided in the recycling stage, see Figure 4.14a, as destruction of the nano-scale surface topology removes the color properties thus leaving the bulk polymer ready for re-processing, with only a ppm-level residue of aluminum for recycling. As such, nano-scale metasurface coloring provides new perspectives for the sustainability of plastic products.

Recently, aluminum-coated plasmonic structures have been firmly established as a route towards creating colorful polymeric materials [Clausen et al., 2014, Tan et al., 2014]. Aluminum has been argued to be superior to typical plasmonic materials, such as silver [Si et al., 2013] and gold [Roberts et al., 2014], due to its natural abundance, low cost, protective oxide layer for high durability [Ramaswamy and Kaste, 2005, Jeurgens et al., 2000, Chan et al., 2008] and attractive plasmonic properties in the visible range [West et al., 2010, Knight et al., 2012, Zhang et al., 2011b, Kulkarni et al., 2013, Langhammer et al., 2008, Chen and Cumming, 2010, Knight et al., 2014, Zorić et al., 2011]. Based on aluminum, reflective plasmonic colors utilizing the concept of localized surface plasmon

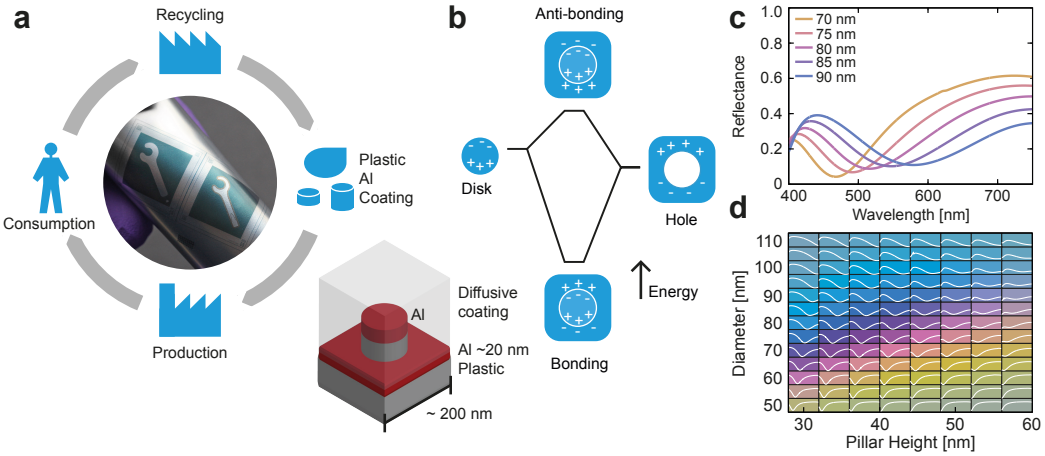

Figure 4.14: Metasurface color concept based on localized surface plasmon resonances. a) Recycle-based component life cycle and photograph of a rolled-up embossed 50 μm thick polymer with 20 nm aluminum and a protective diffusive top coating system. Macroscopic bending does not affect the color properties. b) Energy hybridization band diagram and sketch of typical geometries. c) Simulated normal-incidence reflectance spectra based on a refractive index of 1.5 for both plastic and clear coating. d) Similar simulated reflectance spectra for typical dimensions converted into colors.

resonances (LSPR) have been presented [Clausen et al., 2014, Tan et al., 2014, Lochbihler, 2013, Olson et al., 2014], see Figure 4.14b. Here, the hybridization between LSPR modes [Prodan et al., 2003] in aluminum nano-disks and nano-holes has been used to design and fabricate bright colors that are tunable in the visible spectrum. Finally, the structural color effects can be made robust for everyday use by applying a protective coating on top, which leads to a red-shift of the plasmonic resonances [Clausen et al., 2014]. Simulated reflectance spectra are provided in Figure 4.14c. Previously reported demonstrations have been limited to patterned areas only visible under an optical microscope and to expensive techniques of limited scalability.

Here, we consider polymer replication techniques that are suited for mass production. Polymers have been known for a long time as a replication material with nanometer resolution [Reimer and Schulte, 1966], although the underlying solidification mechanisms are still being debated [Schift et al., 2000]. Today, commercial injection molding is routinely used to replicate dense features down to 150 nm in the case of Blu-Ray discs and 5 nm lateral replication resolution has been achieved [Macintyre and Thoms, 1998, Gadegaard et al., 2003a, Matschuk and Larsen, 2013, Matschuk et al., 2010]. This suggests, that the lower limit of replication is primarily determined by the topology of the master and independent of polymer-chain dimensions. Here, we combine polymer replication with plasmonic metasurfaces based on LSPR modes to produce color metasurfaces with industrial applicability.

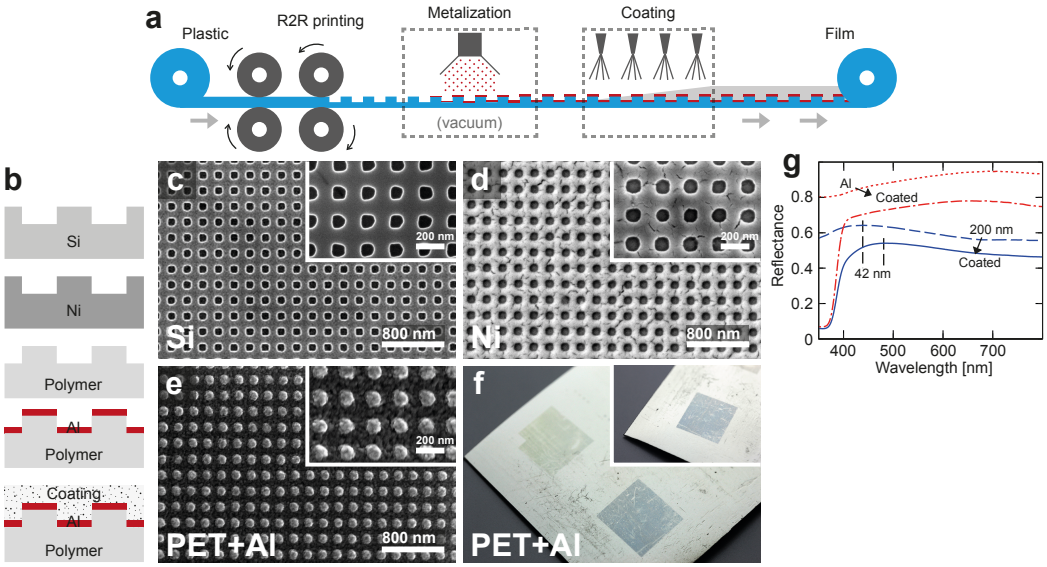

Figure 4.15: Roll-to-roll nano-printing. a) Schematic of roll-to-roll process. b) Sketch of fabrication process from pattern definition to metalized polymer replica. c) SEM images of Si master. d) SEM images of nickel master. e) SEM images of roll-to-roll polymer replication with aluminum on top. f) Photographs of the finished A-PET polymer surface without coating for 200 nm period (blue) and 300 nm period (green) areas of size 0.5 mm x 0.5 mm. (g) Measured reflectance spectra by integrating sphere at 8 degrees incidence of 200 nm period area (blue curves) compared to non-structured aluminum surface (red curves) with (solid lines) and without coating (dashed lines). A red-shift is seen after coating.

4.5.1 Roll-to-roll Printing

Roll-to-roll printing is an emerging technology in the field of manufacturing micro- and nano-scale patterns and it has been attracting interest because of its inherent advantages of low cost, high throughput and large area patterning [Schleunitz et al., 2011, Mäkelä et al., 2011, Kooy et al., 2014, Peng et al., 2014, Chang et al., 2006, Yeo et al., 2009]. In recent years, a number of commercial applications have emerged, particularly optical displays, functional coatings and multifunctional films based on micron-sized structures [Dumond and Yee Low, 2012]. Roll-to-roll thermal nanoimprint lithography with 100 nm linear grooves has been demonstrated [Kooy et al., 2014], however general adaptation from the micro-scale to the nano-scale has proven difficult due to viscoelastic recovery experienced in the relatively fast printing process. Therefore, strict control of the temperature and utilized pressure on the imprinted foil is crucial. Roll-to-roll extrusion coating has also been demonstrated [Murthy et al., 2015]. Based on previous work [Unno et al., 2014, Mäkelä et al., 2011], we demonstrate two-dimensional 115 nm surface plasmon resonance structures with a high edge quality suitable for plasmonic coloring on a relatively large area, see Figure 4.15.

4.5.1.1 Roll-to-roll Fabrication

The fabrication process for making the colored samples is outlined in Figure 4.15b. First a silicon master was patterned by electron beam lithography and anisotropic dry etching. Subsequently, the silicon master was used in a double pattern inversion scheme to make a nickel shim with a thickness of 100 μm and a structure depth of 44 nm. The nickel shim thickness was tuned to allow for a high degree of bendability.

The polymer replication process was carried out using a custom thermal roll-to-roll tool described in detail in the literature [Schleunitz et al., 2011]. The flexible pre-patterned nickel shim was wrapped around a roll with a diameter of 66 mm. Then a heated roll was pressed against a cold backing roll with a force of 600 N, resulting in a force between the rolls (NIP) of approximately 1000 N. The utilized web materials included 100 μm to 125 μm thick polymethylmetcarylate (PMMA), polycarbonate (PC), amorphous polyethylene terephthalate (A-PET) and cellulose acetate (CA).

The temperature of the imprinting roll was adjusted to be above the film softening temperature, which is typically slightly below the glass transition temperature T_g of the different materials. Roll-to-roll process printing temperatures are usually kept slightly below the glass transition or the melting temperature to avoid bending, wrinkling or other changes to the surface occurring at the glass transition temperature. The glass transition temperature for CA and PMMA films is 105 °C. For the A-Pet film, the glass transition temperature is 72 °C and the melting temperature is 250 °C. A speed of 0.3 m/min was used, leading to an imprint time of roughly 0.3 s with a 3 mm contact length between the rolls. The contact length was varied by tuning the hardness of the backing roll. The best replication was obtained when considering pillars with a diameter of 115 nm (SEM) and a height of 40 nm (AFM) on A-PET at a printing temperature of 110 °C (± 2 °C).

After production of the polymer samples, an aluminum layer was deposited by electron beam evaporation in 2×10^{-9} bar vacuum, see Figure 4.15e. The deposition rate was 0.5 nm/s for a thickness of 16 nm measured by quartz crystal microbalance during deposition. Finally, samples were coated by approximately 50 μm of scratch-resistant commercial automotive lacquer in a two step process, where the first layer acts as a diffuser, mimicking the scattering properties of traditional paint, and the top layer creates a high-gloss visual appearance.

4.5.1.2 Roll-to-roll Results

Photographs, taken under fixed light conditions, of the sample after coating are shown in Figure 4.15f. The sample scratches are due to the industrial grade film itself and wear-and-tear mold degradation. The pattern with 200 nm period yields a distinct blue color-response, in agreement with the simulation results shown in Figure 4.14d. Combined with the protective properties of the coating, our approach provides scalable mass production of durable structural colors. In contrast to the blue 200 nm period pattern, the color-response

of the 300 nm period pattern varies strongly with the orientation of the sample with respect to the light source and camera. This dependence is well-described in literature [Højlund-Nielsen et al., 2014b, Clausen et al., 2014] and illustrates the requirement, due to the frequency-range of the human visible spectrum, for nano-scale patterns with periodicities on the order of 200 nm or smaller.

In Figure 4.15g, measured reflection spectra by integrating sphere using a silicon specular reference can be seen for the 200 nm period pattern compared to the non-structured aluminum sample surface. A maximum in reflectance around a vacuum wavelength of 439 nm in the blue part of the spectrum is observed, as longer wavelengths are absorbed to a higher degree by the LSPR located in the red part of the spectrum. After coating, a red-shift of the maximum reflectance of approximately 42 nm can been be measured (the low ultra-violet reflectance is a property of the coating). The red-shift of the maximum reflectance corresponds to a LSPR red-shift [Clausen et al., 2014] and implies that the optical properties of the coating must be included in any design considerations.

Even though the printing speed used here is modest (0.3 m/min), the nature of the continuous roll process inherently makes it possible to process e.g. 500 m of film without stopping. By optimizing printing parameters, higher manufacturing speeds may be achieved if the pressure can be increased correspondingly. The web width (currently 60 mm) is completely scalable and thereby the system offers mass production capabilities. The use of roll-to-roll printing enables large volume fabrication of consumer products with nano-scale polymer surface coloration for a wide range of applications.

4.5.2 Film Insert Molding

Film Insert Molding (also known as in-mold decorating/labeling, IMD/IML) is a well-known industrial technique [Kim et al., 2008, Lee et al., 2013] used to apply surface coatings or decorations onto components to enhance durability and aesthetic value [Leong et al., 2004]. The one-step decoration technique is often favored due to its simplicity over multi step processes, such as silk-screen printing and painting [Leong et al., 2007]. Figure 4.16 summarizes the results. The main advantage of the technique, in terms of nanoreplication, is the use of conventional equipment and processes without modifications.

Figure 4.16a outlines an industrial implementation scheme for achieving metasurfares. In the configuration used here, the outer surface is nano-patterned which calls for a protective coating to be implemented. The manufactured metasurface is produced by embossing in this work, however other techniques such as roll-to-roll printing or injection molding can be used to increase flexibility and speed.

4.5.2.1 Film Insert Molding Fabrication

The fabrication process for making the plasmon colored samples is outlined in Figure 4.16b. First, the metasurface insert was prepared. The pattern was defined by electron

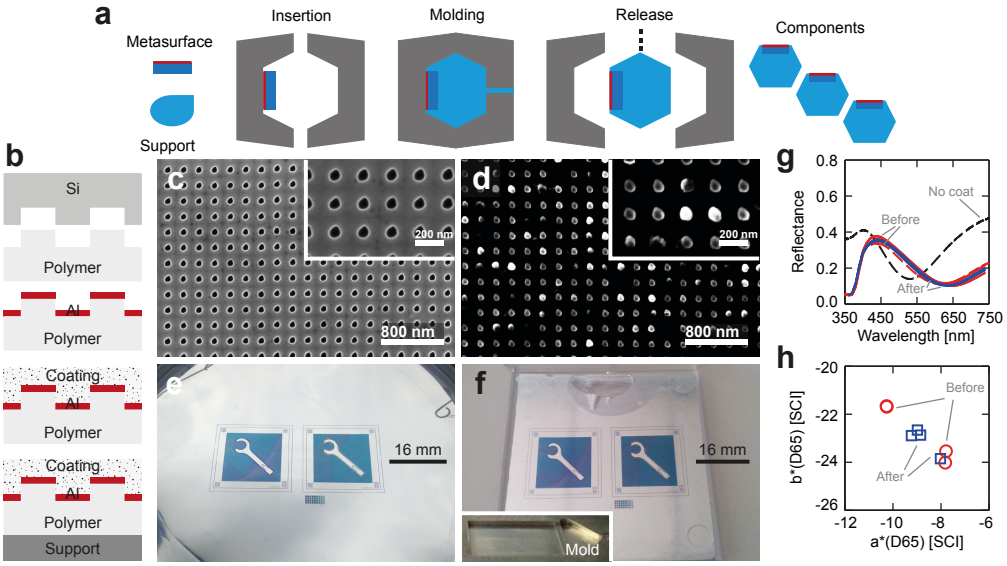

Figure 4.16: Film Insert Molding. a) Schematic of general film insert process. b) Sketch of fabrication process for 200 nm periodic structures from pattern definition to metalized polymer component. c) SEM images of Si master. d) SEM images of polymer metasurface by embossing with 20 nm aluminum on top. e) Photograph of aluminum coated PMMA foil based on 200 nm periodic pattern. f) Photograph of film insert molding component after 400 bars of injection pressure and 180 °C threshold for back-injecting PMMA material. g) Reflectance spectra of sample before and after film insert molding. h) Plots of the shift in colormetric values.

beam lithography and anisotropic dry etching in silicon and subsequently transferred by embossing (CNI tool, NIL Technology) PC and PMMA foils using a pressure of 6.5 bar at a temperature of 150 °C for 8 min. Then Al was deposited using the same process as for the roll-to-roll printed samples.

The film insert molding tests were performed on a Sandretto 65 tons tool using 400 bars of injection pressure and a 180 °C temperature threshold. The machine back-injected PMMA (PLEXIGLAS® 8N, Evonik) exhibiting good flow, high mechanical strength, surface hardness and abrasion resistance. Both PC and PMMA embossed film inserts were used.

4.5.2.2 Film Insert Molding Results

The results can be seen in Figure 4.16e-h. The foil shown in Figure 4.16e comprises a thin film of aluminum embedded between a patterned PMMA carrier foil and a protective surface coating. A 200 nm periodic 2D array of nanoscale cylinders was replicated on the surface of the PMMA foil to obtain the blue plasmonic metasurface. Variations in the pillar replication fidelity introduce purple shades to the otherwise blue pattern. In Figure 4.16d, the same sample foil forms the surface of a molded component by back-injection. The artifacts on the top of the component are due to the double sided tape on an otherwise flat mold surface holding the metasurface in place before molding. This indicates that the thickness of the metasurface film should be increased for more demanding mold geometries in order to withstand shear forces during molding.

In terms of color, no changes can be seen by the eye when comparing Figure 4.16e and Figure 4.16f. To quantify this, Figure 4.16g plots the reflectance spectra of two samples before and after the film insert molding and Figure 4.16h plots the corresponding colorimetric values with a non-observable CIELAB 1976 color difference metric of $\Delta E^* \cong 1.30$. Intuitively, the durable top coating system prevents the nano-pillars from collapsing. Instead the pressure is distributed throughout the macroscale component thereby eliminating shear forces at the aluminum interface. Thereby, we demonstrate that implementing plasmonic colors by film insert molding on large freeform plastic components is possible without degradation of the color properties as a result of the high process pressure.

4.5.3 Injection Molding

Injection molding is the preferred industrial process for polymer replication due to low cycle times and the multitude of technologies established for full process automation [Giboz et al., 2007, Yang et al., 2013]. The results of the injection molding trials are provided in Figure 4.17.

In conventional injection molding, the polymer solidification is coupled to the cavity filling process [Kim and Suh, 1986]. As the molten polymer is injected into the cold mold cavity, it starts to cool and solidify from the mold surface where the melt comes in contact. Consequently, the polymer molecules near the surface are elongated due to shear flow

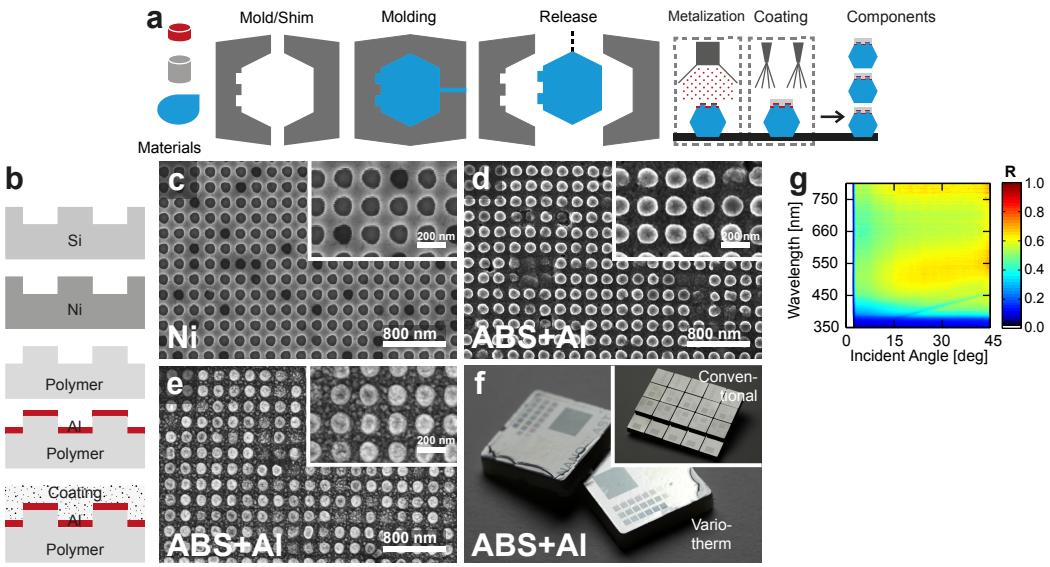

Figure 4.17: Injection molding. a) Schematic of process. b) Sketch of fabrication process for 200 nm periodic structures from pattern definition to metalized polymer component. c) SEM images of master. d) SEM images of variotherm metalized replica. e) SEM images of metalized conventional replica. e) Photographs of samples produced using a variotherm process and a conventional monotherm process (inset). g) Specular reflectance angular-resolved spectra.

and elongation flow and freeze when they come in contact with the cold mold surface, creating a frozen-in molecular orientation in the ”skin layer” [Viana, 2004]. To avoid this, the bulk mold temperature or at least the contact surface often needs to be above the glass-transition temperature of the polymer. Therefore, the most important factor for achieving good replication of micro and nano-structures is generally agreed to be a strict control of the mold temperature [Matschuk and Larsen, 2013, Liou and Chen, 2006].

Commonly, a variotherm process is utilized during injection molding. Here, active heating and cooling of the mold is employed during each cycle. Whereas conventional injection molding uses cycle times from 1–30 s, variotherm processes may require 100–300 s for each replication when accurate thermal control is required [Gornik, 2004]. To avoid variotherm processes, other solutions based on insulation layers have been proposed [Kim and Suh, 1986, Liou and Suh, 1989, Yao and Kim, 2002]. Advanced mold designs and manipulators have been developed to reduce the cycle time below 30 s at the price of more complex and expensive mold fabrication schemes and less thermal control of the mold surface. These involve heating of the mold material itself by Joule [Kim et al., 2005, Xiao and Huang, 2014, Wang et al., 2012] or induction heating [Park and Lee, 2010, Bekesi et al., 2010]. Other methods employ external heating of the mold surface, such as infrared heating [Chang and Hwang, 2006] or steam heating [Liu et al., 2011]. Laser-heating of the mold has also been used to achieve extremely rapid mold heating on the order of

300 °C per second [Michaeli and Klaiber, 2009], although with a spatially inhomogeneous temperature profile over a small area. Several of these methods have demonstrated cycle times comparable to conventional injection molding. However, with considerable added hardware complexity.

In the context of nanoreplication, a schematic for large scale implementation can be seen in Figure 4.17a. First, the mold or an insert is prepared with the inverse nano-structured topology. Then the plastic is injected and the component is released. Finally the necessary post-processing in the form of metallization and coating completes the production cycle. The direct injection molding requires nano-structures embedded in the mold surface, which was solved in this work by utilizing a nickel shim insert fabricated by electroplating from a silicon master.

4.5.3.1 Injection Molding Fabrication

In Figure 4.17b, the fabrication process is outlined. The nickel-shim for injection molding was made in the same manner as the roll-to-roll nickel shim.

The injection molding was carried out in an Arburg 270S machine using a commercial grade of the terpolymer acrylonitrile butadiene styrene (ABS). The polymer melt was injected at 230 °C with an injection pressure of 679 bar. After injection, a holding pressure of 800 bar for 1.5 s and then 450 bar for 2.0 s was applied. A manual variotherm process was used were the mold temperature was cooled from 131 °C to 80 °C. After demolding, the samples were metallized by electron beam deposition and coated using the same procedure as used for all other samples.

4.5.3.2 Injection Molding Results

The results can be seen in Figure 4.17c-h for 200 nm periodic structures from pattern definition to metalized polymer component. In Figure 4.17c, SEM images of the nickel shim can be seen, while Figure 4.17d shows the replicated structures based on a variotherm process. The pattern defect is found to be related to degradation of the polymer material as a result of long cycle times, as it does not appear during conventional molding as seen in Figure 4.17e. In Figure 4.17f, photographs of the final samples after metallization can be seen.

4.5.4 Discussion

The replication of micro and nano-structures is governed by the rheological properties of the polymer (e.g. non-newtonian fluid-dynamics) and thermodynamics at the interface between polymer and the surface of the replicating tool. The initial contact temperature at the interface between two semi-infinite solid bodies with different initial temperatures T_1 and T_2 is determined by [Liou and Suh, 1989]:

$$\frac{T_1 - T_0}{T_0 - T_2} = \left(\frac{(\kappa \rho c_p)_2}{(\kappa \rho c_p)_1} \right)^{\frac{1}{2}}, \tag{4.3}$$

where κ is the thermal conductivity, ρ is the density, c_p is the specific heat capacity, and subscripts 1 and 2 refer to the polymer and tool respectively. Equation (4.3) is strictly speaking only valid for semi-infinite bodies, however, in many cases, it provides reasonable quantitative estimates. For conventional molding with a nickel master, the impact surface temperature of the polymer melt is below the glass transition temperature for a broad range of parameters and materials, which explains the low quality of the roll-to-roll and injection molding trials. Chrome-based coatings or hydrogen silsesquioxane can be used to increase the impact surface temperature at isothermal mold conditions [Hobæk et al., 2015, Stormonth-Darling and Gadegaard, 2012].

4.5.5 Conclusion

In conclusion, we reported on different techniques for mass-producing plasmonic colors based on aluminum thin film coating by LSPR using roll-to-roll printing, film insert molding and direct injection molding of polymeric materials. The use of mass production techniques demonstrates a route for scalable production, which may lead to low-cost pattering and commercial uptake of plasmonic colors. Most notably, we demonstrated that plasmonic metasurface colors by film insert molding is possible without degradation of the color under high pressure. Nano-scale structural coloring provides new perspectives for recycling and sustainability of plastic products, as the colors are based on removable physical structures in the surface rather than traditional chemistry-based that in some cases are distributed throughout the bulk volume of polymer parts.

Finally, we note that the present approach to plasmonic metasurface fabrication may be combined with the recent demonstration of a sub-sequent laser-post-processing for high-resolution printing of vivid colors [Zhu et al., 2015], as described in the next section.

4.6 Laser Ablation Color Modification

The described technology for plasmonic metasurface fabrication may be combined with sub-sequent laser-post-processing for high-resolution printing of vivid colors. This section briefly describes selected aspects of this comprehensive novel enhancement of the basic plasmon color technology. The results of this section have been published [Zhu et al., 2015].

Color generation by plasmonic nanostructures and metasurfaces has several advantages over dye technology, such as reduced pixel area, sub-wavelength resolution and the production of bright and non-fading colors. However, plasmonic color patterns need to be

pre-designed and printed either by e-beam lithography, both expensive and not scalable processes that are not suitable for post-processing customization. Here, a method of color printing on nanoimprinted plasmonic metasurfaces using laser post-writing is presented. Laser pulses induce transient local heat generation that leads to melting and reshaping of the imprinted nanostructures. Depending on the laser pulse energy density, different surface morphologies that support different plasmonic resonances leading to different color appearances can be created. Using this technique, primary colors can be printed with a speed of 1 ns per pixel, resolution up to 127,000 dots-per-inch and power consumption down to 0.3 nJ per pixel.

For a laser pulse of nanosecond duration, the instant energy is sufficiently high to heat the selected surface region above the melting temperature. The disks may thus transform their shapes into thicker disks or spheres in a crystallographic phase-transition process and finally they may be ablated away. By the excitation of a surface plasmon resonance with electric field confinement, light energy is redistributed and concentrated in specific regions of the disk–hole unit cell, enabling a fine-tuning of the morphology by adjusting the input pulse energy density. In return, the change of morphology shifts the resonant frequency of the surface plasmon resonance, leading to a variation in reflected colors. This allows printing of colors on a specific plasmonic surface by controlling the laser parameters, as well as the position of the laser spot.

To realize a desired color from laser irradiation, the surface plasmon resonance is modified through single-pulse laser exposure (1 ns, $\lambda = 532$ nm). As the input laser energy dosage is increased from 0–535 nJ in the focal plane of a 4× objective (spot size $\sim$50 μm in diameter), the main surface plasmon resonance blueshifts from 600 to 500 nm and the printed color varies from cyan to yellow, see Figure 4.18a. With sufficient laser intensity, the nanodisks can be annealed at their rims and evolved into spherical objects, see Figure 4.18b.

A simplified model of the complex thermodynamic phase transistion is presented to describe the morphology transformation of the Al disks. Neglecting gravity, the thickness of the round-cornered disks is varied, while preserving the overall metal volume of the initial disks. In Figure 4.18c, simulations with this model can be seen, which predict the blueshift of SPRs and demonstrate a qualitative agreement with the corresponding measurements for different thermo-transition states. The field is strongly localized at the sharp corners of the unchanged disks, see Figure 4.18d. In Figure 4.18e, the simulated temperature evolutions during the initial nanoseconds for different structural morphologies can be seen. In Figure 4.18e, the temperature distribution resulting from thermo–plasmonic heating is seen.

Based on the trait of local plasmon heating, the plasmonic metasurfaces can be embedded in transparent polymers for laser printing, see Figure 4.19a. With the excitation of the surface plasmon resonance, the plasmon-enhanced photo-thermal melting ensures that the writing process only takes place at the plasmonic metasurface within the focal plane.

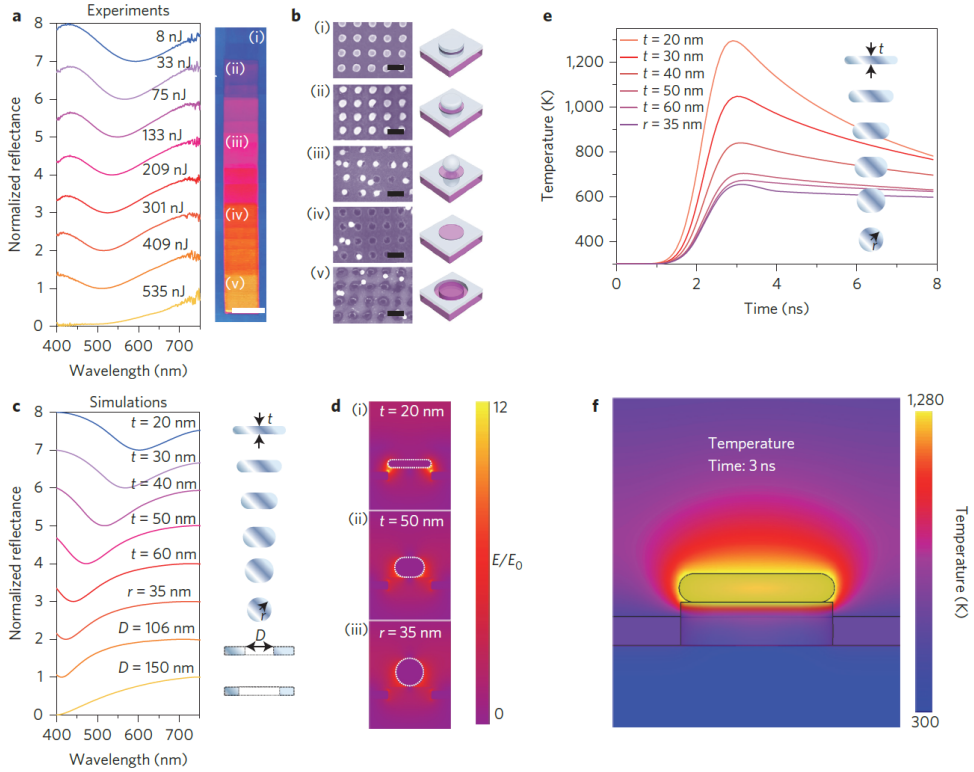

Figure 4.18: Spectral and geometry analyses and numerical simulations. a, Left, measured spectra of the metasurface for D = 106 nm. Single-pulse laser exposure (1 ns, λ = 532nm, spot size: 50μm). Right, corresponding 500 μm × 500 μm color squares printed with a 10 μm step size. Scale bar: 500μm. b, Left, SEM images of the color areas in a (i)–(v). Scale bars: 200 nm. The related pulse energies are 0 (unexposed), 33, 133, 301 and 535 nJ. Right, 3D diagrams demonstrating the corresponding morphology evolutions. c, Simulated spectra of models by imitating the morphology transformation in measurements. d, Simulated electric field enhancements (at λ = 532 nm) for selected morphologies of (i) t=20 nm, (ii) t = 50 nm and (iii) r = 35 nm (sphere). e, Simulated temperature evolutions during the initial nanoseconds, change from a disk shape into a spherical particle. The cross-sectional views indicate the morphological change. f, The corresponding temperature distribution in the initial structure after 3.0 ns when the initial thickness of the disk is t = 20 nm. Figure from publication [Zhu et al., 2015].

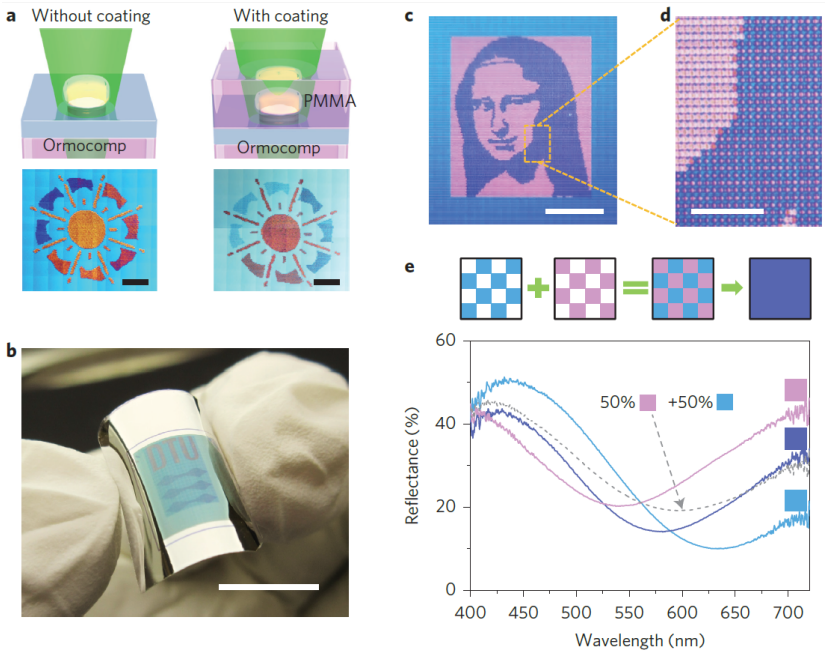

Figure 4.19: Flexible and robust samples for color printing and color mixing. a, Illustrations and examples of laser printing on samples without (left) and with (right) polymer coating. Scale bars: 500 μm. b, A large-scale sample with plasmonic colors printed by a laser transmitted through the protecting polymer. Scale bar: 1 cm. c, A printed portrait of Mona Lisa photographed by a camera with a macro lens. Scale bar: 2 mm. d, A magnified image taken by a microscope exhibits color dots with different dimensions. Scale bar: 500 μm. e, Corresponding reflection spectra of selected pixels with different colors: the background cyan color, the printed magenta color and the mixed blue-violet color. Mixed color dots make a new color and a new spectrum. Figure from publication [Zhu et al., 2015].

The coating leads to a redshift of the resonances in the system and a corresponding color change before and after laser printing because of the increased refractive index of the surroundings. The technology can be combined with a top coat, see Figure 4.19b. In Figure 4.19c-d, it is illustrated that the spot size is well below the resolution of the human eye, meaning that the spatially distributed dots can be seen as a single mixed blue–violet color. A simple averaging of two different color spectra yields a similar result to the reflection spectrum of the mixed color, see Figure 4.19e.

In summary, full-color laser printing on plasmonic metasurfaces with sub-diffraction-limit resolution was demonstrated. The nanoimprinted metasurfaces were composed of a 20 nm Al film buried in a thin-film polymer that is flexible, economic and recyclable. Reconfigured by plasmon resonances, colors were printed when only a single unit cell was modified by laser heating with individual pixels of 200 nm $\times$ 200 nm squares, thus enabling laser printing of colors at a resolution of $\sim$127,000 dots-per-inch. This technology promises exciting avenues from large-scale color printing and decoration to nanoscale color patterning, encryption and data storage, where high information densities are pursued.

4.7 Life Cycle Analysis

This section briefly describes the Life Cycle Analysis done by A. L. Duque in her bachelor thesis “Life cycle assessment of nanostructuring for color effects in polymers” in autumn 2013 in close collaboration with E. Højlund-Nielsen. The work can described as a comparative Life Cycle Assessment (LCA) from cradle to grave of two different production systems based on injection molding to produce colorful plastic parts. The basis of the study was the colored parts produced by the LEGO Group and used by children to play. The life cycle of a specific mini figure torso was analyzed in detail. The results may not be generally applicable for other kinds of plastic parts.

The comparative LCA study had as main objective to determine which one of the analyzed systems was more environmentally friendly. The aim of the study was an LCA study, in accordance with the ISO 14040 and 14044 standards, which includes the goal and scope definition, an inventory analysis (LCI) and an impact assessment (LCIA). The results have been analyzed, interpreted and evaluated with completeness, uncertainty and sensitivity checks.

Two systems were analyzed for comparison. The first was the Reference LEGO system based on the traditional injection molding scheme applied by LEGO that uses pigment in the raw material to create a base color and subsequently painting steps for decoration. The second was the plasmon color system described in this chapter, which is based on structural coloring, where different nano-scale surface topographies define colors without the use of pigments, see Figure 4.20.

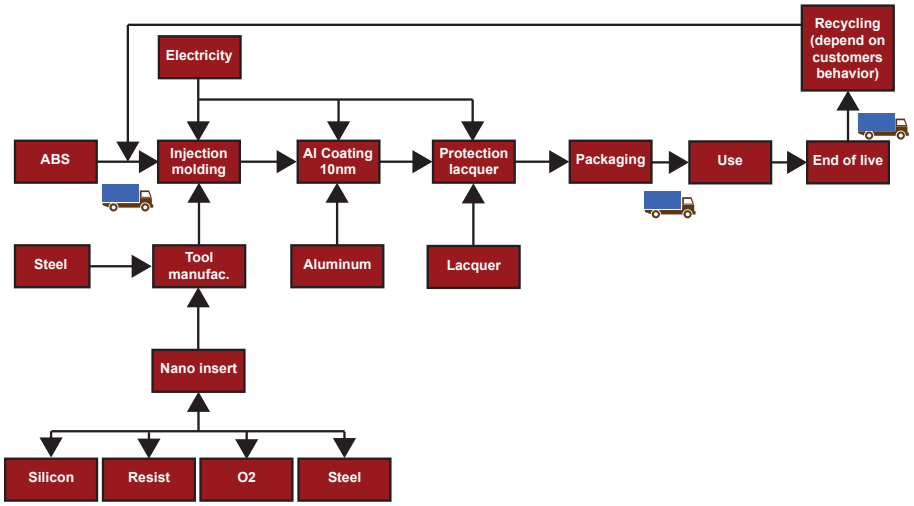

Figure 4.20: Process steps of the plasmon color system from Cradle to Grave.

The life cycle of both systems was examined based on a functional unit of 1220 ABS colored units of the mini figure torso. In the current LEGO process, a white base color and five decoration colors are used, whereas the plasmon color process defines all colors by a nano-structured mold and two common post processing steps, which eliminates the color contamination from pigments in the recycling stage. This study has compared the two systems in order to determine which one is more environmental friendly.

Partners in the FP7 Plast4Future project provided data for the analysis. Otherwise data was collected from reliable sources, or estimated. In the Life Cycle Inventory phase (LCI) the data was grouped into the different processes within the system boundaries of the study, avoiding identical processes in order to provide a clear focus on the difference between the systems. A number of important assumptions were made, especially regarding energy consumption, mold life time and recycling potential of 80 % for the plasmon color system, which limits the study to the described scenario.

For the Life cycle Impact Assessment phase, the two systems were modeled using the GaBi software and the IMPACT 2002+ methodology. Based on the findings in the LCIA, and within the limitations of this study, the most environmentally friendly system is found to be the plasmon color system, which had the lowest scores in the overall assessment, see Figure 4.21. However, this system is not fully developed, and the level of uncertainty is higher than the Reference LEGO system.

The main process in the LCIA was found to be disposal; this was the most different stage between both systems. For the Reference LEGO system, the disposal is 82% landfill and 12% incineration, which contributes by giving energy from the process, but this process also gives some dangerous emissions to air and water. On the other hand, for the plasmon

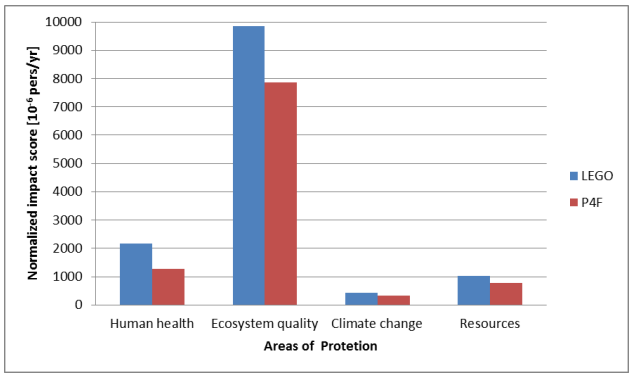

Figure 4.21: Life cycle analysis. Normalized impact score across the different areas of protection.

color system, the LCIA revealed that the total impact scores for this system across most of the categories are lower.

Based on the LCIA, a sensitivity analysis was conducted to further investigate the influence of recycling with respect to the environmental impact of the plasmon color technology. The best case recycling potential, estimated to be 80 %, is highly dependent on a number of factors, including consumer behavior, and the uncertainty is rather high. Within the limitations of this study, the results of the sensitivity analysis seem non-conclusive under 40 % recycling. However, in the case of around 40 % or higher recycling rate, the sensitivity analysis shows that the most environmentally friendly system is the plasmon color system based on the impact categories in the IMPACT 2002+ methodology. The results suggest that the most important advantage of the plasmon color system, with respect to the Reference LEGO system, is the possibility of large scale recycling of plastic waste.

Finally, this LCA study suffers from technical limitations regarding data collection and a high number of assumptions, which causes a high uncertainty in the results. The study is based on a scenario limited by data and the results may not be representative for variations in the systems.

4.8 Conclusion

In conclusion, angle-insensitive scratch-resistant structural colors were demonstrated, where aluminum was used as a cheap and abundant plasmonic material. The technology utilized a hybrid disk-hole plasmonic mode, which provided angle-independent resonances tunable across the entire visible spectrum. The technology holds potential for large scale implementation of structural colors in plastic products for daily use.

In collaboration with industry, polymer-based colored metasurfaces of square-centimeter size were demonstrated by embossing, injection molding, roll-to-roll printing, and film insert molding with full compatibility. Furthermore, post production color modification by

laser ablation was briefly described. The environmental benefits were analyzed by life cycle analysis, where the high recyclability led to a reduced environmental impact compared to conventional plastic production.

Chapter 5

Conclusion

This doctoral thesis described the utilization of color metasurfaces in an industrial perspective, where nano-scale textures and contingent post processing replace inks, dyes and pigments in plastic production. The concept of colors by structure arguably reduces the number of raw materials and eliminates mechanical color sorting in the recycling stage.

First, the development of experimental processes, techniques and equipment was described. A single-spot electron beam lithography scheme for master pattern definition was developed. Optical characterization equipment for both laboratory and production environments was developed.

Second, the fundamental optical surface properties of dielectric materials were investigated within the framework of the replication constraint. Different colors could be realized using a single-step etching process by altering the nano-texture in high-index materials, exemplified in silicon. However, only corresponding faint colors appeared in polymeric materials. The concept of all-polymer pigment-free coloration seemed somewhat restricted in relation to widespread industrial employment.

Finally, a novel plasmon color technology for structural coloration in plastics was developed based on metal-coated polymer nano-textures. Angle-insensitive scratch-resistant colors were demonstrated where aluminum was used as a cheap and abundant plasmonic material. The technology utilized a hybrid disk-hole plasmonic mode for resonances in the visible spectrum and a protective coating system. In collaboration with industry, polymer-based colored metasurfaces of square-centimeter size were demonstrated by embossing, injection molding, roll-to-roll printing, and film insert molding with full compatibility. Furthermore, post production color modification by laser ablation was briefly described. The environmental benefits were analyzed by life cycle analysis, where the high recyclability lead to a reduced environmental impact compared to conventional plastic production.

Bibliography

[Adato et al., 2009] Adato, R., Yanik, A. A., Amsden, J. J., Kaplan, D. L., Omenetto, F. G., Hong, M. K., Erramilli, S., and Altug, H. (2009). Ultra-sensitive vibrational spectroscopy of protein monolayers with plasmonic nanoantenna arrays. *Proc. Natl. Acad. Sci.*, 106(46):19227–19232. 61

[Al-Salem et al., 2009] Al-Salem, S. M., Lettieri, P., and Baeyens, J. (2009). Recycling and recovery routes of plastic solid waste (PSW): a review. *Waste Manag.*, 29(10):2625–43. 2, 68

[Anderson and Richards, 1942] Anderson, T. F. and Richards, A. G. (1942). An electron microscope study of some structural colors of insects. *J. Appl. Phys.*, 13(12):748–758. 4

[Ariño et al., 2005] Ariño, I., Kleist, U., Mattsson, L., and Rigdahl, M. (2005). On the Relation Between Surface Texture and Gloss of Injection-Molded Pigmented Plastics. *Polym. Eng. Sci.*, 45(10):1343–1356. 7

[Bain, 1937] Bain, R. (1937). Technology and State Government. *Am. Sociol. Rev.*, 2(6):860–874. 48

[Bao et al., 2002] Bao, G., Dobson, D. C., and Ramdani, K. (2002). A Constraint on the Maximum Reflectance of Rapidly Oscillating Dielectric Gratings. *SIAM J. Control Optim.*, 40(6):1858–1866. 32, 43

[Bekesi et al., 2010] Bekesi, J., Kaakkunen, J. J. J., Michaeli, W., Klaiber, F., Schoengart, M., Ihlemann, J., and Simon, P. (2010). Fast fabrication of super-hydrophobic surfaces on polypropylene by replication of short-pulse laser structured molds. *Appl. Phys. A*, 99(4):691–695. 75

[BP, 2010] BP (2010). Statistical Review of World Energy. Technical report, BP p.l.c. 2

[Cabrini and Hawata, 2012] Cabrini, S. and Hawata, S. (2012). *Nanofabrication Handbook*. CRC Press. 14

[Cao et al., 2010] Cao, L., Fan, P., Barnard, E. S., Brown, A. M., and Brongersma, M. L. (2010). Tuning the Color of Silicon Nanostructures. *Nano Lett.*, 10(7):2649–2654. 7

[Chan et al., 2008] Chan, G. H., Zhao, J., Schatz, G. C., and Duyne, R. P. V. (2008). Localized Surface Plasmon Resonance Spectroscopy of Triangular Aluminum Nanoparticles. *J. Phys. Chem. C*, 112(36):13958–13963. 51, 68

[Chang and Young, 2010] Chang, C.-H. and Young, W.-B. (2010). Fabrication of the plastic component for photonic crystal using micro injection molding. *Microsyst. Technol.*, 16(6):941–946. 7

[Chang et al., 2006] Chang, C. Y., Yang, S. Y., and Sheh, J. L. (2006). A roller embossing process for rapid fabrication of microlens arrays on glass substrates. *Microsyst. Technol.*, 12(8):754–759. 70

[Chang and Hwang, 2006] Chang, P.-C. and Hwang, S.-J. (2006). Experimental investigation of infrared rapid surface heating for injection molding. *J. Appl. Polym. Sci.*, 102(4):3704–3713. 75

[Chen and Cumming, 2010] Chen, Q. and Cumming, D. R. S. (2010). High transmission and low color cross-talk plasmonic color filters using triangular-lattice hole arrays in aluminum films. *Opt. Express*, 18(13):14056–14062. 68

[Chen et al., 2015] Chen, W., Tymchenko, M., Gopalan, P., Ye, X., Wu, Y., Zhang, M., Murray, C. B., Alu, A., and Kagan, C. R. (2015). Large-Area Nanoimprinted Colloidal Au Nanocrystal-Based Nanoantennas for Ultrathin Polarizing Plasmonic Metasurfaces. *Nano Lett.*, 15(8):5254–5260. 61

[Cheng et al., 2015] Cheng, F., Gao, J., Luk, T. S., and Yang, X. (2015). Structural color printing based on plasmonic metasurfaces of perfect light absorption. *Sci. Rep.*, 5:11045. 55

[Christiansen et al., 2013] Christiansen, A. B., Højlund-Nielsen, E., Clausen, J., Caringal, G. P., Mortensen, N. A., and Kristensen, A. (2013). Imprinted and injection-molded nano-structured optical surfaces. *Proc. SPIE*, 8818(881803):1–12. 32, 33, 35, 36, 44

[Chung et al., 2012] Chung, K., Yu, S., Heo, C.-J., Shim, J. W., Yang, S.-M., Han, M. G., Lee, H.-S., Jin, Y., Lee, S. Y., Park, N., and Shin, J. H. (2012). Flexible, Angle-Independent, Structural Color Reflectors Inspired by Morpho Butterfly Wings. *Adv. Mater.*, 24(18):2375–2379. 7, 8, 9

[CIE, 2012] CIE (2012). CIE Colorimetry - Part 2: Standard Illuminants for Colorimetry, http://cie.co.at, ISO 11664-2:2007(E)/CIE S 014-2/E:2006. 39

[Clausen et al., 2014] Clausen, J. S., Højlund-Nielsen, E., Christiansen, A. B., Yazdi, S., Grajower, M., Taha, H., Levy, U., Kristensen, A., and Mortensen, N. A. (2014). Plasmonic Metasurfaces for Coloration of Plastic Consumer Products. *Nano Lett.*, 14(8):4499–4504. 21, 48, 53, 56, 57, 59, 68, 69, 72

[Curcio et al., 1990] Curcio, C. A., Sloan, K. R., Kalina, R. E., and Hendrickson, A. E. (1990). Human photoreceptor topography. *J. Comp. Neurol.*, 292(4):497–523. 36

[Dean, 2015] Dean, N. (2015). Colouring at the nanoscale. *Nat. Nanotechnol.*, 10(1):15–16. 56

[Dumond and Yee Low, 2012] Dumond, J. J. and Yee Low, H. (2012). Recent developments and design challenges in continuous roller micro- and nanoimprinting. *J. Vac. Sci. Technol. B Microelectron. Nanom. Struct.*, 30(1):010801. 70

[Finlayson and Baumberg, 2013] Finlayson, C. E. and Baumberg, J. J. (2013). Polymer opals as novel photonic materials. *Polym. Int.*, 62(10):1403–1407. 7, 9

[Finlayson et al., 2011] Finlayson, C. E., Spahn, P., Snoswell, D. R. E., Yates, G., Kontogeorgos, A., Haines, A. I., Hellmann, G. P., and Baumberg, J. J. (2011). 3D Bulk Ordering in Macroscopic Solid Opaline Films by Edge-Induced Rotational Shearing. *Adv. Mater.*, 23(13):1540–1544. 9

[Frank and Ruska, 1939] Frank, F. and Ruska, H. (1939). Übermikroskopische Untersuchung der Blaustruktur der Vogelfeder. *Naturwissenschaften*, 27(14):229–230. 4

[Franklin et al., 2015] Franklin, D., Chen, Y., Vazquez-Guardado, A., Modak, S., Boroumand, J., Xu, D., Wu, S.-T., and Chanda, D. (2015). Polarization-independent actively tunable colour generation on imprinted plasmonic surfaces. *Nat. Commun.*, 6:7337. 55

[Gadegaard et al., 2003a] Gadegaard, N., Mosler, S., and Larsen, N. B. (2003a). Biomimetic Polymer Nanostructures by Injection Molding. *Macromol. Mater. Eng.*, 288(1):76–83. 69

[Gadegaard et al., 2003b] Gadegaard, N., Thoms, S., Macintyre, D. S., Mcghee, K., Gallagher, J., Casey, B., and Wilkinson, C. D. W. (2003b). Arrays of nano-dots for cellular engineering. *Microelectron. Eng.*, 68:162–168. 14, 15, 16, 19

[Gans, 1912] Gans, R. (1912). Über die Form ultramikroskopischer Goldteilchen. *Ann. Phys.*, 342(5):881–900. 61

[Gentil, 1942] Gentil, K. (1942). Elektronmikroskopische Untersuchung des Feinbaues schillernder Leisten von Morpho-Schuppen. *Zeitschrift fiir Morphol. und Okol. der Tiere*, 38(2):344–355. 4

[Gérard and Gray, 2015] Gérard, D. and Gray, S. K. (2015). Aluminium plasmonics. *J. Phys. D. Appl. Phys.*, 48(18):184001. 52

[Gervet, 2007] Gervet, B. (2007). The use of crude oil in plastic making contributes to global warming. Technical report, Renewable Energy Research Group, Division of Architecture and Infrastructure, Lule{å} University of Technology, SE-97187 Lule{å}, Sweden. 2

[Giboz et al., 2007] Giboz, J., Copponnex, T., and Mélé, P. (2007). Microinjection molding of thermoplastic polymers: a review. *J. Micromechanics Microengineering*, 17(6):R96–R109. 74

[Goh et al., 2014] Goh, X. M., Zheng, Y., Tan, S. J., Zhang, L., Kumar, K., Qiu, C.-W., and Yang, J. K. W. (2014). Three-dimensional plasmonic stereoscopic prints in full colour. *Nat. Commun.*, 5:5361. 53, 61

[Golka et al., 2003] Golka, S., Heidrich, H., and Steingruber, R. (2003). Useful and cost efficient fabrication of dot arrays for photonic crystals by direct write electron-beam lithography. *Microelectron. Eng.*, 68:157–161. 14

[Gornik, 2004] Gornik, C. (2004). Injection Moulding of Parts with Microstructured Surfaces for Medical Applications. *Macromol. Symp.*, 217(1):365–374. 75

[Graydon, 2015] Graydon, O. (2015). View from... SPP7: A colourful future? *Nat. Photonics*, 9(8):487–488. 51

[Green and Keevers, 1995] Green, M. A. and Keevers, M. J. (1995). Optical properties of intrinsic silicon at 300 K. *Prog. Photovoltaics Res. Appl.*, 3(3):189–192. 64

[Greve and Holst, 2013] Greve, M. M. and Holst, B. (2013). Optimization of an electron beam lithography instrument for fast, large area writing at 10 kV acceleration voltage. *J. Vac. Sci. Technol. B Microelectron. Nanom. Struct.*, 31(4):043202. 14

[Griffiths, 2008] Griffiths, D. J. (2008). *Introduction to Electrodynamics*. Pearson Education Inc, third edition. 31

[Harold, 2001] Harold, R. W. (2001). An Introduction to Appearance Analysis. *Graph. Arts Tech. Found.*, (No. 84):1–7. 1, 35

[Haug et al., 2008] Haug, F.-J., SoÌĹderstroÌĹm, T., Cubero, O., Terrazzoni-Daudrix, V., and Ballif, C. (2008). Plasmonic absorption in textured silver back reflectors of thin film solar cells. *J. Appl. Phys.*, 104(6):064509. 61

[Hermannsson et al., 2015] Hermannsson, P. G., Sørensen, K. T., Vannahme, C., Smith, C. L., Klein, J. J., Russew, M.-M., Grützner, G., and Kristensen, A. (2015). All-polymer photonic crystal slab sensor. *Opt. Express*, 23(13):16529. 63

[Hessel and Oliner, 1965] Hessel, A. and Oliner, A. A. (1965). A New Theory of WoodâĂŹs Anomalies on Optical Gratings. *Appl. Opt.*, 4(10):1275. 34, 43

[Hobæk et al., 2015] Hobæk, T. C., Matschuk, M., Kafka, J., Pranov, H. J., and Larsen, N. B. (2015). Hydrogen silsesquioxane mold coatings for improved replication of nanopatterns by injection molding. *J. Micromechanics Microengineering*, 25(3):035018. 77

[Højlund-Nielsen, 2012] Højlund-Nielsen, E. (2012). Angle-independant Structural Colors. Master's thesis, Department of Micro- Nanotechnology, Technical University of Denmark. 38

[Højlund-Nielsen et al., 2014a] Højlund-Nielsen, E., Greibe, T., Mortensen, N. A., and Kristensen, A. (2014a). Single-spot e-beam lithography for defining large arrays of nano-holes. *Microelectron. Eng.*, 121:104–107. 14, 15, 17, 18, 19, 20

[Højlund-Nielsen et al., 2014b] Højlund-Nielsen, E., Weirich, J., Nørregaard, J., Garnaes, J., Mortensen, N. A., and Kristensen, A. (2014b). Angle-independent structural colors of silicon. *J. Nanophotonics*, 8(1):083988. 40, 41, 42, 72

[Højlund-Nielsen et al., 2015] Højlund-Nielsen, E., Zhu, X., Carstensen, M. S., Sørensen, M. K., Vannahme, C., Asger Mortensen, N., and Kristensen, A. (2015). Polarization-dependent aluminum metasurface operating at 450 nm. *Opt. Express*, 23(22):28829. 61, 62, 63, 65, 66

[Jeurgens et al., 2000] Jeurgens, L., Sloof, W., Tichelaar, F., and Mittemeijer, E. (2000). Thermodynamic stability of amorphous oxide films on metals: Application to aluminum oxide films on aluminum substrates. *Phys. Rev. B*, 62(7):4707–4719. 51, 68

[Joannopoulos et al., 2008] Joannopoulos, J. D., Johnson, S. G., Winn, J. N., and Meade, R. D. (2008). *Photonic Crystals - Molding the flow of light*. Princeton University Press, second edition. 28

[Johnson, 2006] Johnson, K. C. (2006). Grating Diffraction Calculator (GD-Calc) – Coupled-Wave Theory for Biperiodic Diffraction Gratings (manual). 29

[Judd et al., 1964] Judd, D. B., Macadam, D. L., Wyszecki, G. G., Budde, H. W., Condit, H. R., Henderson, S. T., and Simonds, J. L. (1964). Spectral Distribution of Typical Daylight as a Function of Correlated Color Temperature. *J. Opt. Soc. Am.*, 54(8):1031. 44

[Jugessur et al., 2011] Jugessur, a. S., Yagnyukova, M., and Aitchison, J. S. (2011). Nanofabrication of photonic crystal-based devices using electron beam spot lithography. *J. Vac. Sci. Technol. B Microelectron. Nanom. Struct.*, 29(6):06FF06. 14, 15, 16

[Kanamori et al., 1999] Kanamori, Y., Sasaki, M., and Hane, K. (1999). Broadband antireflection gratings fabricated upon silicon substrates. *Opt. Lett.*, 24(20):1422. 7, 8

[Kim and Suh, 1986] Kim, B. H. and Suh, N. P. (1986). Low Thermal Inertia Molding (LTIM). *Polym. Plast. Technol. Eng.*, 25(1):73–93. 74, 75

[Kim et al., 2009] Kim, H., Ge, J., Kim, J., Choi, S.-e., Lee, H., Lee, H., Park, W., Yin, Y., and Kwon, S. (2009). Structural colour printing using a magnetically tunable and lithographically fixable photonic crystal. *Nat. Photonics*, 3(9):534–540. 9

[Kim et al., 2003] Kim, S., Chong, H., Rue, R. M. D. L., Marsh, J. H., and Bryce, a. C. (2003). Electron-beam writing of photonic crystal patterns using a large beam-spot diameter. *Nanotechnology*, 14(9):1004–1008. 14

[Kim et al., 2008] Kim, S. Y., Lee, S. H., Baek, S. J., and Youn, J. R. (2008). Thermoviscoelastic Behavior of Film-Insert-Molded Parts Prepared under Various Processing Conditions. *Macromol. Mater. Eng.*, 293(12):969–978. 72

[Kim et al., 2005] Kim, Y., Choi, Y., and Kang, S. (2005). Replication of high density optical disc using injection mold with MEMS heater. *Microsyst. Technol.*, 11(7):464–469. 75

[Kinoshita et al., 2008] Kinoshita, S., Yoshioka, S., and Miyazaki, J. (2008). Physics of structural colors. *Rep. Prog. Phys.*, 71(7):076401. 4

[Klein, 2010] Klein, G. A. (2010). *Industrial Color Physics*, volume ISSN 0342-. Springer Science+Business Media, first edition. 36, 37, 38

[Knight et al., 2014] Knight, M. W., King, N. S., Liu, L., Everitt, H. O., Nordlander, P., and Halas, N. J. (2014). Aluminum for Plasmonics. *ACS Nano*, 8(1):834–840. 52, 68

[Knight et al., 2012] Knight, M. W., Liu, L., Wang, Y., Brown, L., Mukherjee, S., King, N. S., Everitt, H. O., Nordlander, P., and Halas, N. J. (2012). Aluminum plasmonic nanoantennas. *Nano Lett.*, 12(11):6000–6004. 68

[Kooy et al., 2014] Kooy, N., Mohamed, K., Pin, L., and Guan, O. (2014). A review of roll-to-roll nanoimprint lithography. *Nanoscale Res. Lett.*, 9(1):320. 70

[Kulkarni et al., 2013] Kulkarni, V., Prodan, E., and Nordlander, P. (2013). Quantum Plasmonics: Optical Properties of a Nanomatryushka. *Nano Lett.*, 13(12):5873–5879. 68

[Kumar et al., 2012] Kumar, K., Duan, H., Hegde, R. S., Koh, S. C. W., Wei, J. N., and Yang, J. K. W. (2012). Printing colour at the optical diffraction limit. *Nat. Nanotechnol.*, 7(August):557–561. 2, 52, 68

[Langhammer et al., 2008] Langhammer, C., Schwind, M., Kasemo, B., and Zorić, I. (2008). Localized surface plasmon resonances in aluminum nanodisks. *Nano Lett.*, 8(5):1461–1471. 52, 68

[Le et al., 2008] Le, F., Brandl, D. W., Urzhumov, Y. A., Wang, H., Kundu, J., Halas, N. J., Aizpurua, J., and Nordlander, P. (2008). Metallic Nanoparticle Arrays: A Common Substrate for Both Surface-Enhanced Raman Scattering and Surface-Enhanced Infrared Absorption. *ACS Nano*, 2(4):707–718. 61

[Lee et al., 2013] Lee, D., Chen, W.-A., Huang, T.-W., and Liu, S.-J. (2013). Factors Influencing the Warpage in In-Mold Decoration Injection Molded Composites. *Int. Polym. Process.*, 28(2):221–227. 72

[Lee et al., 2014] Lee, K.-T., Lee, J. Y., Seo, S., and Guo, L. J. (2014). Colored ultrathin hybrid photovoltaics with high quantum efficiency. *Light Sci. Appl.*, 3(10):e215. 55

[Leong et al., 2007] Leong, Y. W., Kotaki, M., and Hamada, H. (2007). Effects of the molecular orientation and crystallization on film-substrate interfacial adhesion in poly(ethylene terephthalate) film-insert moldings. *J. Appl. Polym. Sci.*, 104(4):2100–2107. 72

[Leong et al., 2004] Leong, Y. W., Yamaguchi, S., Mizoguchi, M., Hamada, H., Ishiaku, U. S., and Tsujii, T. (2004). The effect of molding conditions on mechanical and morphological properties at the interface of film insert injection molded polypropylene-film/polypropylene matrix. *Polym. Eng. Sci.*, 44(12):2327–2334. 72

[Link and El-Sayed, 2000] Link, S. and El-Sayed, M. A. (2000). Shape and size dependence of radiative, non-radiative and photothermal properties of gold nanocrystals. *Int. Rev. Phys. Chem.*, 19(3):409–453. 61

[Liou and Chen, 2006] Liou, A.-C. and Chen, R.-H. (2006). Injection molding of polymer micro- and sub-micron structures with high-aspect ratios. *Int. J. Adv. Manuf. Technol.*, 28(11-12):1097–1103. 75

[Liou and Suh, 1989] Liou, M. J. and Suh, N. P. (1989). Reducing residual stresses in molded parts. *Polym. Eng. Sci.*, 29(7):441–447. 75, 76

[Liu et al., 2011] Liu, J., Zhao, G., Wang, G., and Guan, Y. (2011). Fully Coupled Transient Heat Transfer and Melt Filling Simulations in Rapid Heat Cycle Molding with Steam Heating. *Polym. Plast. Technol. Eng.*, 50(4):423–437. 75

[Livingstone and Hubel, 1988] Livingstone, M. and Hubel, D. (1988). Segregation of Form, Color, Movement, and Depth- Anatomy, Physiology, and Perception. *Science*, 240(4853):740–749. 36

[Lochbihler, 2013] Lochbihler, H. (2013). Reflective colored image based on metal-dielectric-metal-coated gratings. *Opt. Lett.*, 38(9):1398. 53, 69

[Lu et al., 2012] Lu, H., Liu, X., Mao, D., and Wang, G. (2012). Plasmonic nanosensor based on Fano resonance in waveguide-coupled resonators. *Opt. Lett.*, 37(18):3780. 61

[Luo et al., 2015] Luo, F., Ong, W., Guan, Y., Li, F., Sun, S., Lim, G., and Hong, M. (2015). Study of micro/nanostructures formed by a nanosecond laser in gaseous environments for stainless steel surface coloring. *Appl. Surf. Sci.*, 328(0):405–409. 55

[Macintyre and Thoms, 1998] Macintyre, D. and Thoms, S. (1998). The fabrication of high resolution features by mould injection. *Microelectron. Eng.*, 41-42:211–214. 69

[Maier, 2007] Maier, S. A. (2007). *Plasmonics: Fundamentals and Applications*. Springer. 49, 50

[Mäkelä et al., 2011] Mäkelä, T., Haatainen, T., and Ahopelto, J. (2011). Roll-to-roll printed gratings in cellulose acetate web using novel nanoimprinting device. *Microelectron. Eng.*, 88(8):2045–2047. 70

[Mankins, 1995] Mankins, J. C. (1995). Technology Readiness Levels - A White Paper. Technical report, Advanced Concepts Office, Office of Space Access and Technology, NASA. 48

[Matschuk et al., 2010] Matschuk, M., Bruus, H., and Larsen, N. B. (2010). Nanostructures for all-polymer microfluidic systems. *Microelectron. Eng.*, 87(5-8):1379–1382. 69

[Matschuk and Larsen, 2013] Matschuk, M. and Larsen, N. B. (2013). Injection molding of high aspect ratio sub-100 nm nanostructures. *J. Micromechanics Microengineering*, 23(2):025003. 69, 75

[McPeak et al., 2015] McPeak, K. M., Jayanti, S. V., Kress, S. J. P., Meyer, S., Iotti, S., Rossinelli, A., and Norris, D. J. (2015). Plasmonic Films Can Easily Be Better: Rules and Recipes. *ACS Photonics*, 2(3):326–333. 25, 50

[Michaeli and Klaiber, 2009] Michaeli, W. and Klaiber, F. (2009). Development of a system for laser-assisted molding of micro- and nanostructures. *J. Vac. Sci. Technol. B Microelectron. Nanom. Struct.*, 27(3):1323. 76

[Murthy et al., 2015] Murthy, S., Matschuk, M., Huang, Q., Mandsberg, N. K., Feidenhans'l, N. A., Johansen, P., Christensen, L., Pranov, H., Kofod, G., Pedersen, H. C., Hassager, O., and Taboryski, R. (2015). Fabrication of Nanostructures by Roll-to-Roll Extrusion Coating. *Adv. Eng. Mater.*, pages n/a–n/a. 70

[Ng et al., 2015] Ng, R. J. H., Goh, X. M., and Yang, J. K. W. (2015). All-metal nanostructured substrates as subtractive color reflectors with near-perfect absorptance. *Opt. Express*, 23(25):32597. 55

[Noyes et al., 2007] Noyes, J. A., Vukusic, P., and Hooper, I. R. (2007). Experimental method for reliably establishing the refractive index of buprestid beetle exocuticle. *Opt. Express*, 15:4351–4358. 4, 5

[NREL, 2012] NREL (2012). Electric Systems Center at the National Renewable Energy Laboratory, Astm g173- 03 reference spectra derived from smarts(simple model of the radiative transfer of sunshine) v. 2.9.2, http://rredc.nrel.gov/solar/spectra/am1.5/ASTMG173/ASTMG173.html . 38

[Nyholm-Petersen, 2014] Nyholm-Petersen, D. K. (2014). *Forbedring af laboratorieudstyr til nanostrukturerede overflader*. Diplom afgangsprojekt, Technical University of Denmark. 26, 27

[Odom, 2012] Odom, T. W. (2012). Colours at the nanoscale: Printable stained glass. *Nat. Nanotechnol.*, 7(9):550–551. 51

[Olson et al., 2014] Olson, J., Manjavacas, A., Liu, L., Chang, W.-S., Foerster, B., King, N. S., Knight, M. W., Nordlander, P., Halas, N. J., and Link, S. (2014). Vivid, full-color aluminum plasmonic pixels. *Proc. Natl. Acad. Sci.*, 111(40):14348–14353. 53, 69

[Palik, 1986] Palik, E. D. (1986). *Handbook of optical constants of solids*. Academic Press, San Diego. 64

[Papavassiliou, 1979] Papavassiliou, G. (1979). Optical properties of small inorganic and organic metal particles. *Prog. Solid State Chem.*, 12(3-4):185–271. 61

[Park and Lee, 2010] Park, K. and Lee, S.-I. (2010). Localized mold heating with the aid of selective induction for injection molding of high aspect ratio micro-features. *J. Micromechanics Microengineering*, 20(3):035002. 75

[Parker and Townley, 2007] Parker, A. R. and Townley, H. E. (2007). Biomimetics of photonic nanostructures. *Nat. Nanotechnol.*, 2(6):347–353. 4

[Parker et al., 2000] Parker, N. W., Brodie, A. D., and McCoy, J. H. (2000). High-throughput NGL electron-beam direct-write lithography system. In Dobisz, E. A., editor, *Proc. Soc. photo-optical Instrum. Eng. (SPIE), Emerg. Lithogr. Technol. iv*, volume 3997, pages 713–720. 15

[Peng et al., 2014] Peng, L., Deng, Y., Yi, P., and Lai, X. (2014). Micro hot embossing of thermoplastic polymers: a review. *J. Micromechanics Microengineering*, 24(1):013001. 70

[Petryayeva and Krull, 2011] Petryayeva, E. and Krull, U. J. (2011). Localized surface plasmon resonance: Nanostructures, bioassays and biosensingâĂŤA review. *Anal. Chim. Acta*, 706(1):8–24. 61

[PlasticsEurope, 2013] PlasticsEurope (2013). Plastics - the Facts 2013: An analysis of European latest plastics production, demand and waste data. Technical report, Association of plastics manufacturers, Avenue E. van Nieuwenhuyse 4/3 1160 Brussels - Belgium. 2

[PlasticsEurope, 2015] PlasticsEurope (2015). Plastics - the facts 2015: An analysis of European plastics production, demand and waste data. Technical report, Association of plastics manufacturers, Avenue E. van Nieuwenhuyse 4/3 1160 Brussels - Belgium. 1

[Prodan et al., 2003] Prodan, E., Radloff, C., Halas, N. J., and Nordlander, P. (2003). A hybridization model for the plasmon response of complex nanostructures. *Science*, 302(5644):419–422. 66, 69

[Prum et al., 2006] Prum, R. O., Quinn, T., and Torres, R. H. (2006). Anatomically diverse butterfly scales all produce structural colours by coherent scattering. *J. Exp. Biol.*, 209(Pt 4):748–65. 4

[Raguin and Morris, 1993] Raguin, D. H. and Morris, G. M. (1993). Analysis of antireflection-structured surfaces with continuous one-dimensional surface profiles. *Appl. Opt.*, 32(14):2582. 33, 34

[Ramaswamy and Kaste, 2005] Ramaswamy, A. L. and Kaste, P. (2005). A Nanovision of the Physiochemical Phenomena Occurring in Nanoparticles of Aluminum. *J. Energ. Mater.*, 23(1):1–25. 51, 68

[Raza et al., 2015] Raza, S., Bozhevolnyi, S. I., Wubs, M., and Asger Mortensen, N. (2015). Nonlocal optical response in metallic nanostructures. *J. Phys. Condens. Matter*, 27(18):183204. 28, 49, 64

[Reimer and Schulte, 1966] Reimer, L. and Schulte, C. (1966). Elektronenmikroskopische Oberflächenabdriicke und ihr Auflösungsvermögen. *Naturwissenschaften*, 9(19):489–97. 69

[Ritchie, 1957] Ritchie, R. H. (1957). Plasma Losses by Fast Electrons in Thin Films. *Phys. Rev.*, 106(5):874–881. 49

[Roberts and Ford, 1995] Roberts, A. and Ford, A. (1995). Colour Space Conversions, http://www.martinreddy.net/gfx/faqs/colorconv.faq (checked 2012-04-23). 35

[Roberts et al., 2014] Roberts, A. S., Pors, A., Albrektsen, O., and Bozhevolnyi, S. I. (2014). Subwavelength Plasmonic Color Printing Protected for Ambient Use. *Nano Lett.*, 14(2):783–787. 52, 53, 68

[Saito et al., 2009] Saito, A., Miyamura, Y., Ishikawa, Y., Murase, J., Akai-Kasaya, M., and Kuwahara, Y. (2009). Reproduction, mass production, and control of the Morpho butterfly's blue. volume 7205, pages 720506–720506–9. 7

[Saito et al., 2006] Saito, A., Miyamura, Y., Nakajima, M., Ishikawa, Y., Sogo, K., Kuwahara, Y., and Hirai, Y. (2006). Reproduction of the Morpho blue by nanocasting lithography. *J. Vac. Sci. Technol. B*, 24(6):3248–3251. 4, 7, 8

[Saito et al., 2004] Saito, A., Yoshioka, S., and Kinoshita, S. (2004). Reproduction of the Morpho butterfly's blue: arbitration of contradicting factors. *Opt. Syst. Degrad. Contam. Stray Light Eff. Meas. Control. Ed. by Philip T. C. Chen, John C. Fleming, Michael G. Dittman, Proc. SPIE Vol. 5526 (SPIE, Bellingham, WA, 2004)*. 7

[Saranathan et al., 2010] Saranathan, V., Osuji, C. O., Mochrie, S. G. J., Noh, H., Narayanan, S., Sandy, A., Dufresne, E. R., and Prum, R. O. (2010). Structure, function, and self-assembly of single network gyroid (I4132) photonic crystals in butterfly wing scales. *Proc. Natl. Acad. Sci.*, 107(26):11676–11681. 4

[Schift et al., 2000] Schift, H., David, C., Gabriel, M., Gobrecht, J., Heyderman, L., Kaiser, W., Köppel, S., and Scandella, L. (2000). Nanoreplication in polymers using hot embossing and injection molding. *Microelectron. Eng.*, 53(1-4):171–174. 69

[Schleunitz et al., 2011] Schleunitz, A., Spreu, C., Mäkelä, T., Haatainen, T., Klukowska, A., and Schift, H. (2011). Hybrid working stamps for high speed roll-to-roll nanoreplication with molded sol-gel relief on a metal backbone. *Microelectron. Eng.*, 88(8):2113–2116. 70, 71

[Seago et al., 2009] Seago, A. E., Brady, P., Vigneron, J.-P., and Schultz, T. D. (2009). Gold bugs and beyond: a review of iridescence and structural colour mechanisms in beetles (Coleoptera). *J. R. Soc. Interface*, 6(Suppl_2):S165–S184. 4, 5, 6

[Shen et al., 2015] Shen, Y., Rinnerbauer, V., Wang, I., Stelmakh, V., Joannopoulos, J. D., and Soljačić, M. (2015). Structural Colors from Fano Resonances. *ACS Photonics*, 2(1):27–32. 9

[Si et al., 2013] Si, G., Zhao, Y., Lv, J., Lu, M., Wang, F., Liu, H., Xiang, N., Huang, T. J., Danner, A. J., Teng, J., and Liu, Y. J. (2013). Reflective plasmonic color filters based on lithographically patterned silver nanorod arrays. *Nanoscale*, 5(14):6243–6248. 52, 68

[Smith and Guild, 1931] Smith, T. and Guild, J. (1931). The C.I.E. colorimetric standards and their use. *Trans. Opt. Soc.*, 33(3):73–134. 44

[Srivastava et al., 2010] Srivastava, S. K., Kumar, D., Singh, P. K., Kar, M., Kumar, V., and Husain, M. (2010). Excellent antireflection properties of vertical silicon nanowire arrays. *Sol. Energy Mater. Sol. Cells*, 94(9):1505–1511. 7

[Stewart and Gallaway, 1962] Stewart, J. E. and Gallaway, W. S. (1962). Diffraction Anomalies in Grating Spectrophotometers. *Appl. Opt.*, 1(4):421. 34

[Stewart et al., 2008] Stewart, M. E., Anderton, C. R., Thompson, L. B., Maria, J., Gray, S. K., Rogers, J. a., and Nuzzo, R. G. (2008). Nanostructured Plasmonic Sensors. *Chem. Rev.*, 108(2):494–521. 61

[Stockman and Sharpe, 1999] Stockman, A. and Sharpe, L. T. (1999). *Color Tision: from genes to perception - Cone spectral sensitivities and color matching*. Cambridge University Press, first edition. 37

[Stokes et al., 1995] Stokes, M., Anderson, M., Chandrasekar, S., and Motta, R. (1995). A Standard Default Color Space for the Internet - sRGB http://www.w3.org/Graphics/Color/sRGB.html (checked 2013-04-20). 39

[Stormonth-Darling and Gadegaard, 2012] Stormonth-Darling, J. M. and Gadegaard, N. (2012). Injection Moulding Difficult Nanopatterns with Hybrid Polymer Inlays. *Macromol. Mater. Eng.*, 297(11):1075–1080. 77

[Tan et al., 2014] Tan, S. J., Zhang, L., Zhu, D., Goh, X. M., Wang, Y. M., Kumar, K., Qiu, C.-W., and Yang, J. K. W. (2014). Plasmonic Color Palettes for Photorealistic Printing with Aluminum Nanostructures. *Nano Lett.*, 14(7):4023–4029. 53, 54, 68, 69

[Teyssier et al., 2015] Teyssier, J., Saenko, S. V., van der Marel, D., and Milinkovitch, M. C. (2015). Photonic crystals cause active colour change in chameleons. *Nat. Commun.*, 6:6368. 4, 5

[Tsuboi et al., 2014] Tsuboi, A., Nakamura, K., and Kobayashi, N. (2014). Multicolor Electrochromism Showing Three Primary Color States Based on Size- and Shape-Controlled Silver Nanoparticles. *Chem. Mater.*, 26(22):6477–6485. 53

[United-Nations, 2010] United-Nations (2010). World Population Prospects: The 2010 Revision. Technical report, Population Division of the Department of Economic and Social Affairs of the United Nations Secretariat. 2

[Unno et al., 2014] Unno, N., Mäkelä, T., and Taniguchi, J. (2014). Thermal roll-to-roll imprinted nanogratings on plastic film. *J. Vac. Sci. Technol. B, Nanotechnol. Microelectron. Mater. Process. Meas. Phenom.*, 32(6):06FG03. 70

[van der Drift, 1991] van der Drift, E. (1991). Thermal effects in high voltage e-beam lithography. *J. Vac. Sci. Technol. B Microelectron. Nanom. Struct.*, 9(6):3470. 19

[Vannahme et al., 2015] Vannahme, C., Dufva, M., and Kristensen, A. (2015). High frame rate multi-resonance imaging refractometry with distributed feedback dye laser sensor. *Light Sci. Appl.*, 4(4):e269. 63

[Viana, 2004] Viana, J. (2004). Development of the skin layer in injection moulding: phenomenological model. *Polymer (Guildf).*, 45(3):993–1005. 75

[Vos, 1978] Vos, J. J. (1978). Colorimetric and photometric properties of a 2Âř fundamental observer. *Color Res. Appl.*, 3(3):125–128. 37, 44

[Vukusic and Sambles, 2003] Vukusic, P. and Sambles, J. R. (2003). Photonic structures in biology. *Nature*, 424(6950):852–855. 4, 5

[Vukusic et al., 2000] Vukusic, P., Sambles, J. R., and Lawrence, C. R. (2000). Colour mixing in wing scales of a butterfly. *Nature*, 404(6777):457. 4, 6

[Vukusic et al., 2004] Vukusic, P., Sambles, J. R., and Lawrence, C. R. (2004). Structurally assisted blackness in butterfly scales. *Proc. R. Soc. B Biol. Sci.*, 271:S237—-S239. 4

[Vukusic et al., 1999] Vukusic, P., Sambles, J. R., Lawrence, C. R., and Wootton, R. J. (1999). Quantified interference and diffraction in single Morpho butterfly scales. *Proc. R. Soc. B Biol. Sci.*, 266(April):1403–1411. 4, 5

[Vukusic and Stavenga, 2009] Vukusic, P. and Stavenga, D. G. (2009). Physical methods for investigating structural colours in biological systems. *J. R. Soc. Interface*, 6(January):133–148. 32

[Wang et al., 2012] Wang, G., Zhao, G., and Guan, Y. (2012). Thermal response of an electric heating rapid heat cycle molding mold and its effect on surface appearance and tensile strength of the molded part. *J. Appl. Polym. Sci.*, 128:n/a–n/a. 75

[Wendt et al., 1993] Wendt, J. R., Vawter, G. A., Gourley, P. L., Brennan, T. M., and Hammons, B. E. (1993). Nanofabrication of photonic lattice structures in GaAs/AlGaAs. *J. Vac. Sci. Technol. B Microelectron. Nanom. Struct.*, 11(6):2637. 14

[West et al., 2010] West, P., Ishii, S., Naik, G., Emani, N., Shalaev, V., and Boltasseva, A. (2010). Searching for better plasmonic materials. *Laser Photon. Rev.*, 4(6):795–808. 52, 68

[Wikipedia.org, 2012] Wikipedia.org (2012). Source is choosen because sRGB is used: http://en.wikipedia.org/wiki/File:CIExy1931.png (checked 2012-04-03). 38

[Willets and Van Duyne, 2007] Willets, K. A. and Van Duyne, R. P. (2007). Localized Surface Plasmon Resonance Spectroscopy and Sensing. *Annu. Rev. Phys. Chem.*, 58(1):267–297. 51

[Wu et al., 2013] Wu, Y.-K. R., Hollowell, A. E., Zhang, C., and Guo, L. J. (2013). Angle-Insensitive Structural Colours based on Metallic Nanocavities and Coloured Pixels beyond the Diffraction Limit. *Sci. Rep.*, 3:1194. 53

[Xiao and Huang, 2014] Xiao, C.-L. and Huang, H.-X. (2014). Multiobjective optimization design of heating system in electric heating rapid thermal cycling mold for yielding high gloss parts. *J. Appl. Polym. Sci.*, 131(6):n/a–n/a. 75

[Xu et al., 2010] Xu, T., Wu, Y.-K., Luo, X., and Guo, L. J. (2010). Plasmonic nanoresonators for high-resolution colour filtering and spectral imaging. *Nat. Commun.*, 1(5):1–5. 55

[Yang et al., 2013] Yang, C., Yin, X.-H., and Cheng, G.-M. (2013). Microinjection molding of microsystem components: new aspects in improving performance. *J. Micromechanics Microengineering*, 23(9):093001. 74

[Yao and Kim, 2002] Yao, D. and Kim, B. (2002). Development of rapid heating and cooling systems for injection molding applications. *Polym. Eng. Sci.*, 42(12):2471–2481. 75

[Yeo et al., 2009] Yeo, L. P., Ng, S. H., Wang, Z., Wang, Z., and de Rooij, N. F. (2009). Micro-fabrication of polymeric devices using hot roller embossing. *Microelectron. Eng.*, 86(4-6):933–936. 70

[Yokogawa et al., 2012] Yokogawa, S., Burgos, S. P., and Atwater, H. a. (2012). Plasmonic Color Filters for CMOS Image Sensor Applications. *Nano Lett.*, 12(8):4349–4354. 55

[Yun et al., 2015] Yun, H., Lee, S.-Y., Hong, K., Yeom, J., and Lee, B. (2015). Plasmonic cavity-apertures as dynamic pixels for the simultaneous control of colour and intensity. *Nat. Commun.*, 6(May):7133. 53

[Zalkovskij et al., 2015] Zalkovskij, M., Thamdrup, L. H., Smistrup, K., Andén, T., Johansson, A. C., Mikkelsen, N. J., Madsen, M. H., Garnæs, J., Kristiansen, T. T., Diemer, M., Døssing, M., Minzari, D., Tang, P. T., Kristensen, A., Taboryski, R., Essendrop, S., Nielsen, T., and Bilenberg, B. (2015). Smart plastic functionalization by nanoimprint and injection molding. 9423:94230T. 48

[Zeng et al., 2013] Zeng, B., Gao, Y., and Bartoli, F. J. (2013). Ultrathin Nanostructured Metals for Highly Transmissive Plasmonic Subtractive Color Filters. *Sci. Rep.*, 3:2840. 55

[Zhang et al., 2011a] Zhang, J., Fouad, M., Yavuz, M., and Cui, B. (2011a). Charging effect reduction in electron beam lithography with nA beam current. *Microelectron. Eng.*, 88(8):2196–2199. 19

[Zhang et al., 2011b] Zhang, J., Ou, J.-Y., Papasimakis, N., Chen, Y., MacDonald, K. F., and Zheludev, N. I. (2011b). Continuous metal plasmonic frequency selective surfaces. *Opt. Express*, 19(23):23279–23285. 52, 68

[Zhu et al., 2015] Zhu, X., Vannahme, C., Højlund-Nielsen, E., Mortensen, N. A., and Kristensen, A. (2015). Plasmonic colour laser printing. *Nat. Nanotechnol.*, (December):1–6. 77, 79, 80

[Zhu et al., 2012] Zhu, X., Xiao, S., Shi, L., Liu, X., Zi, J., Hansen, O., and Mortensen, N. A. (2012). A stretch-tunable plasmonic structure with a polarization-dependent response. *Opt. Express*, 20(5):5237. 61

[Zorić et al., 2011] Zorić, I., Zäch, M., Kasemo, B., and Langhammer, C. (2011). Gold, platinum, and aluminum nanodisk plasmons: Material independence, subradiance, and damping mechanisms. *ACS Nano*, 5(4):2535–2546. 52, 68

List of Abbreviations and Standard Terms

Abbreviation	Name	Category	Description
AFM	Atomic force microscopy	Characterization	Atomic-force microscopy is a scanning probe microscopy technique with subnanometer resolution.
OM	Optical Microscopy	Characterization	Optical microscopy is a type of microscopy which uses visible light and lenses to magnify images of small samples.
SEM	Scanning electron microscopy	Characterization	Scanning electron microscopy is a type of electron microscopy that produces images of a sample by scanning it with a focused beam of electrons.
-	Casting	Fabrication	Casting is a manufacturing process in which a liquid material is poured into a mold with a hollow cavity and then allowed to solidify creating the inverse shape.
CCD	Charge-coupled device	Fabrication	A charge-coupled device is used to move electrical charge, for example in digital imaging where pixels are represented by phosphorus-doped metal-oxide-semiconductor capacitors.
CMOS	Complementary metal–oxide–semiconductor	Fabrication	Complementary metal–oxide–semiconductor is a technology platform for constructing integrated circuit used in microprocessors and other electronic components.
-	Electron beam evaporation deposition	Fabrication	Electron beam evaporation deposition is a form of physical vapor deposition in which a target anode is bombarded with an electron beam under high vacuum causing target atoms to coat everything within line of sight with a thin layer of the anode material under high voltage.

Abbreviation	Name	Category	Description
EBL	Electron beam lithography	Fabrication	Electron beam lithography is the practice of scanning a focused beam of electrons to define custom shapes on a surface.
-	Embossing	Fabrication	Embossing is a stamping process for producing raised or sunken designs or reliefs with micro and nano fabrication.
-	Gaussian beam	Fabrication	A Gaussian beam is a beam of monochromatic electromagnetic radiation field amplitude profiles are given by the Gaussian function, implying a Gaussian irradiance profile.
-	Metallization	Fabrication	Metallization is the general name for the technique of coating metal on the surface of objects. Electron beam lithography can be categorized as a metallization process.
FDTS	Perfluoro-decyltrichlorosilane	Fabrication	FDTS is a colorless liquid chemical forming self-assembled monolayers. With FDTS, the chlorine atoms in the end of a flourinated organosilane react with -OH groups of the surface to form a chemical bond under elimination of HCL, which allows for strong adhesion of the FDTS coating. At the same time, FDTS coating strongly modifies the surfaces energy since the terminal CF_3 groups are Teflon like and allows for easy release of the replicated polymer.
-	Photoresist	Fabrication	In semiconductor fabrication, a photoresist is a thin layer used to transfer a pattern to the semiconductor substrate..
-	Plasma ashing	Fabrication	Plasma ashing is the process of removing photoresist from an etched wafer, where the reactive species (oxygen or fluorine) combines with the photoresist to form ash which is removed with a vacuum pump.
-	Shim	Fabrication	Nickel shims are formed by electroforming in the form of electroplating, and are inverted replica from a patterned silicon wafer.
-	Single-spot electron beam lithography	Fabrication	Single-spot electron beam lithography is a technique where electron beam lithography with a focused Gaussian beam is used to define shapes directly.

Abbreviation	Name	Category	Description
-	Wafer	Fabrication	A wafer is a thin slice of semiconductor material, such as a crystalline silicon, used in electronics for semiconductor fabrication of integrated circuits and solar cells.
TRL	Technology Readiness Levels	General	Technology Readiness Levels are a method of estimating technology maturity..
IMPACT 2002+	IMPACT 2002+ impact assessment	Life cycle	The IMPACT 2002+ life cycle impact assessment methodology links all types of life cycle inventory results via 14 midpoint categories to four damage categories; Human Health, Ecosystem Quality, Climate Change and Resources.
LCIA	Impact assessment	Life cycle	Life cycle impact assessment connects each life cycle inventory result to the corresponding environmental impacts.
LCI	Inventory analysis	Life cycle	Life cycle inventory results describe elementary flows or other intervention.
-	Normalized impact score.	Life cycle	Normalized impact score within life cycle assessment describes the generated score normalized by a reference factor.
-	Sensitivity analysis	Life cycle	Sensitivity analysis studies the uncertainty in the output of a model that can be apportioned to different sources of uncertainty in its inputs.
-	Sustainability	Life cycle	Sustainability is difficult to define, however, it is the endurance of systems and processes, including ecology, economics, politics and culture.
CA	Cellulose acetate	Material	Cellulose acetate is the acetate ester of cellulose.
-	High index materials	Material	Material with a refractive index around or above 2.
-	Hybrid Polymer	Material	Hybrid materials are composites consisting of two constituents at the nanometer or molecular level. Commonly one of these compounds is inorganic and the other one organic in nature.
HSQ	Hydrogen silsesquioxane	Material	Hydrogen silsesquioxane is a class of inorganic compounds consisting of silicon, hydrogen and oxygen.
-	Low index materials	Material	Material with a refractive index significantly below 2.
-	Ormocer	Material	A material class of inorganic-organic hybrid polymers.
-	Plexiglas	Material	Plexiglas is a commercial PMMA material.

Abbreviation	Name	Category	Description
PMMA	Poly(methyl 2-methylpropenoate)	Material	PMMA, also known as acrylic, is a transparent thermoplastic.
PC	Polycarbonate	Material	Polycarbonates are a group of thermoplastic polymers containing carbonate groups in their chemical structures.
PET	Polyethylene terephthalate	Material	Polyethylene terephthalate is the most common thermoplastic polymer of the polyester family.
ABS	Terpolymer acrylonitrile butadiene styrene	Material	Acrylonitrile butadiene styrene is a common thermoplastic polymer.
-	Angle-insensitive colors	Optics	Angle-insensitive colors exhibit only small changes in color over a large incoming light angular range. It is closely related to angle robust and angle-independent coloring.
-	Central color perception	Optics	Central color perception is perception within the fovea on the retina of the eye, in contrast to peripheral color perception.
-	Chromaticity coordinates	Optics	The chromatic variables are derived from the tristimulus values by normalizing each to their sum..
CIELAB	CIE L*a*b*	Optics	CIE L*a*b* is a modern color space, describing all the colors visible to the human eye.
ΔE*	Color difference metric	Optics	The color difference metric is defined by CIE as the euclidean distance in the corresponding device independent color space.
-	Illuminant	Optics	An illuminant is a source of visible light, whereas a standard illuminant is a theoretical source of visible light with a known spectral power distribution.
-	Index-matching	Optics	Index-matching occurs between two materials with the same refractive index in contact, thereby neglecting reflection and refraction at the interface.
CIE	International Commission on Illumination	Optics	Commission Internationale de l'Eclairage is the international authority on light, illumination, color, and color spaces.
-	Reflectance	Optics	Reflectance is the fraction of incident electromagnetic power that is reflected at an interface.

Abbreviation	Name	Category	Description
-	Simultaneous contrast	Optics	Simultaneous contrast is the change in perception of two colors when displayed side by side, in contrast to individual display.
-	Specular reflectance	Optics	Specular reflection is the mirror-like reflection of light from a surface described by the law of refraction, in which light from a single incoming direction is reflected into a single outgoing direction.
sRGB	sRGB color space	Optics	sRGB is a standard RGB color space created cooperatively by HP and Microsoft in 1996 for use on consumer monitors.
-	Transmittance	Optics	Transmittance is the fraction of incident electromagnetic power that is transmitted through a sample, in contrast to the transmission coefficient, which is the ratio of the transmitted to incident electric field.
-	Tristimulus values	Optics	The tristimulus values uniquely represent a perceivable hue within color theory.
-	Diffraction grating	Photonics	A diffraction grating is an optical component with a periodic structure, splitting and diffracting light into several beams in different directions.
-	Hybridization	Photonics	Hybridization is the concept of mixing states into new hybrid states with different energies, shapes, etc., than the component states.
-	Interband transition	Photonics	An interband transition is a transition between two states in the same electronic band trough a momentum transfer.
-	Irradiance	Photonics	Irradiance is the radiant flux received by a surface per unit area in the unit of watt per square metre.
LSPR	Localized surface plasmon resonances	Photonics	Localized surface plasmon resonance is an optical phenomena generated by light when it interacts with conductive nanoparticles that are smaller than the incident wavelength.
LSP	Localized surface plasmons	Photonics	Localized Surface Plasmon is the result of the confinement of a surface plasmon in a nanoparticle of size smaller than the wavelength of light.

Abbreviation	Name	Category	Description
-	Metasurface	Photonics	An metasurface is one- and two-dimensional arrays of subwavelength periodicity with negligible thickness compared to the wavelength of operation and capable of modulation of light.
-	Optical biomimetics	Photonics	Optical biomimetics is the extraction or inspiration of optical design or problem solving from nature.
-	Photonic crystals	Photonics	A photonic crystal is a periodic optical nanostructure that affects the motion of photons similar to how ionic lattices affect electrons in solids.
-	Photonics	Photonics	Photonics is the science of photon generation, detection, and manipulation through a number of processes.
-	Plasmonics	Photonics	Plasmonics is the study of the interaction between electromagnetic field and free electrons in a metal.
-	Rayleigh line	Photonics	The Rayleigh line and the Rayleigh wavelength marks the transition from a nondiffractive to a diffractive reflection grating, where first-order emerges at glancing angle.
-	Stereoscopy	Photonics	Stereoscopyis a technique for creating the illusion of depth in an image by presenting two offset images separately to the left and right eye of the viewer.
-	Thin-film interference	Photonics	Thin-film interference occurs when incident light waves reflected by the upper and lower boundaries of a thin film interfere to form a new wave.
FIM	Film insert molding	Production	Film Insert Molding is a labeling method which uses a printed plastic film, inserted into a designated mold, and molten material under pressure to be cooled and solidify.
IM	Injection molding	Production	Injection molding is a manufacturing process for producing parts by injecting material, typically thermoplastic, into a mould.
R2R	Roll-to-roll printing	Production	Roll-to-roll printing is the process of creating components on a roll of flexible plastic.
-	Web (roll-to-roll)	Production	Web is the material for processing in a roll-to-roll process.
-	Eigenproblems	Simulation	Eigenproblems is related to linerar algebra and describe a special type of matrix equations.

Abbreviation	Name	Category	Description
-	Frequency domain simulations	Simulation	Frequency domain simulations is performed with respect to frequency and typically a Fourier transform is used to relate the time domain to the frequency domain.
RCWA	Rigorous coupled-wave analysis	Simulation	Rigorous coupled-wave analysis is a semi-analytical method in computational electromagnetics that is applied to solve scattering problems from periodic dielectric structures.
-	Time-domain simulations	Simulation	Time domain simulations is performed with respect to time.
-	Binary structures	Structures	Binary structures are generally structures in only two planes.

Appendix A

Publications

A.1 Christiansen et al. 2013

A.B. Christiansen, E. Højlund-Nielsen, J. Clausen, G.P. Caringal, N.A. Mortensen, A. Kristensen (2013). "Imprinted and injection-molded nano-structured optical surfaces", *Proceedings of SPIE*, 8818(881803), 1–12. doi: 10.1117/12.2025133.

Invited Paper

Imprinted and injection-molded nano-structured optical surfaces

Alexander B. Christiansen[a], Emil Højlund-Nielsen[a], Jeppe Clausen[b], Gideon P. Caringal[a], N. Asger Mortensen[b], and Anders Kristensen[a]

[a]Department of Micro and Nanotechnology, Technical University of Denmark, Oersteds Plads, Building 345B, DK-2800 Kgs. Lyngby, Denmark;
[b]Department of Photonics Engineering, Technical University of Denmark, Oersteds Plads, Building 343, DK-2800 Kgs. Lyngby, Denmark

ABSTRACT

Inspired by nature, nano-textured surfaces have attracted much attention as a method to realize optical surface functionality. The moth-eye antireflective structure and the structural colors of Morpho butterflies are well-known examples used for inspiration for such biomimetic research. In this paper, nanostructured polymer surfaces suitable for up-scalable polymer replication methods, such as imprinting/embossing and injection-molding, are discussed. The limiting case of injection-moulding compatible designs is investigated. Anti-reflective polymer surfaces are realized by replication of Black Silicon (BSi) random nanostructure surfaces. The optical transmission at normal incidence is measured for wavelengths from 400 nm to 900 nm. For samples with optimized nanostructures, the reflectance is reduced by 50 % compared to samples with planar surfaces. The specular and diffusive reflection of light from polymer surfaces and their implication for creating structural colors is discussed. In the case of injection-moulding compatible designs, the maximum reflection of nano-scale textured surfaces cannot exceed the Fresnel reflection of a corresponding flat polymer surface, which is approx. 4 % for normal incidence. Diffraction gratings provide strong color reflection defined by the diffraction orders. However, the apperance varies strongly with viewing angles. Three different methods to address the strong angular-dependence of diffraction grating based structural color are discussed.

Keywords: Structural Color, diffraction gratings, anti-reflective coatings, polymer replication

1. INTRODUCTION

Within the past decades, nano-textured surfaces have attracted much attention as a method to realize optical surface functionality. The moth-eye antireflective structure[1] and the structural colors of Morpho butterflyes[2,3] are well-known examples. In this paper, nanostructured polymer surfaces suitable for up-scalable polymer replication methods, such as imprinting/embossing and injection-molding, are discussed. The limiting case of injection-moulding compatible designs is investigated.

This study is motiviated by the need for efficient and large scale recycling, due to an increasing world population and declining natural resources. Much of the waste generated stems from plastic products. Here the base color is given by bulk properties based on pigmentation. Added surface decoration provides additional color effects, for example logos, text decoration or line art, thereby providing cost effective color effects. However, the addition of decoration also makes recycling difficult, because the powerful pigments used for the thin decoration layers tend to pollute the base color of the bulk material in the recycling state. Here we propose functional surfaces for structural colors and other optical effects to produce decoration art, thereby enabling a direct decomposition into raw materials of the consumed product. The vision is multi-functional surfaces, where surface topography added to a material creates new functionalities, such as color, anti-reflective and self-cleaning properties for plastic parts.

The nano-texture anti-reflective surface of moth-eyes was first reported in 1967 by Bernhard,[1] who observed the tapered nano-structure by scanning electron microscopy of slices of the moth-eye lens. The broadband anti-reflective functionality was confirmed by micro-wave experiments. In 1973, Clapham realized the first artificial

Corresponding author: A.K. (anders.kristensen@nanotech.dtu.dk).

Nanostructured Thin Films VI, edited by Tom G. Mackay, Akhlesh Lakhtakia, Yi-Jun Jen, Motofumi Suzuki,
Proc. of SPIE Vol. 8818, 881803 · © 2013 SPIE · CCC code: 0277-786X/13/$18 · doi: 10.1117/12.2025133

Downloaded From: http://proceedings.spiedigitallibrary.org/ on 07/11/2014 Terms of Use: http://spiedl.org/terms

anti-reflective moth-eye structure in the visible range by interference lithography in a thin photo resist film on a glass substrate, yielding 200 nm protuberances.[4] Already these first papers clarified the underlying physics; that the structures function as an effective gradient in refractive index of the material reducing reflections from the surface. Furthermore, it was shown by modeling that minimum reflectance can be acheived with $d/\lambda = 0.4$, where d is the height of the tapered protuberances and λ is the vacuum wavelength for glass materials. More general numerical modeling was reported by Stephens and Cody in 1977.[5] The advancement of nano-scale lithography has enabled further research; a few examples are electron beam lithography defined silicon nanocone arrays,[6] silicon and polymer surfaces by plasma etching and replication[7] and anti-reflection anti-fogging silica surfaces.[8]

Structural colors are optical phenomena, where the topography of a surface determines the reflected spectrum of light, although an unambiguous definition has not been settled yet.[9] In recent years, structural coloration has attracted considerable attention within the field of optics.[10–13] The mechanisms of structural colors are categorized into thin-film interference, multi-layer interference, diffraction grating optical effects, and photonic crystal effects.[9] In nature, structural colors are found among butterflies and beetles, such as the Morpho butterfly,[14] reflecting omnidirectional blue light due to a multilayer topography.

The structures found in nature often consist of several layers. Here the focus is on one-layer structures that comply with injection-molding, the industry standard for high volume plastic production. This only allows for simple single-material surface textures, and may not, for example, comprise closed air-filled regions inside the material.

Anti-reflective polymer surfaces are realized by replication of Black Silicon (BSi) random nanostructure surfaces. The specular and diffusive reflection of light from polymer surfaces and their implication for creating structural colors is discussed. In the case of injection-moulding compatible designs, the maximum reflection of nano-scale textured surfaces is discussed. Diffraction gratings provide strong color reflection defined by the diffraction orders. However, the apperance varies strongly with viewing angles. Three different methods to address the strong angular-dependence of diffraction grating based structural color are discussed.

2. REFLECTION FROM A POLYMER SURFACE

In this section, the specular and diffusive reflection of light from polymer surfaces and their implication for creating structural colors is discussed. The limitations imposed by the injection moulding production platform itself is considered. Injection-moulding requires that the parts are able to be separated from the molding tool without damage. Therefore, any topography must consist of one layer only of alteration without closed air-filled regions inside the material. Any structure may only consist of one layer of alteration on top of bulk. All individual structures or combinations may be periodic or semi-periodic. We will refer to these single-material structures of one layer, that have zero or positively sloped sidewalls, as injection-moulding compatible surface textures, because they in general allow for the separation in an injection-molding machine. Examples are given in Fig. 1.

The topography limitations described above generally indicate that the advanced multi-layer structures often found in nature, on butterfly scales and similar,[15] cannot be fabricated using a one-step injection molding process. These limitations have consequences for the optical performance. It has been shown by Bao[16] that the upper limit of surface reflection for all injection-molding compatible periodic structures are given by the reflectance of a plane dielectric interface, where the largest difference in refractive index occurs and thus the largest reflection of energy. The reflection of a planar dielectric interface is also known as Fresnel or specular reflection, often arising from mirror like surfaces. This limitation applies for all values of the bulk refractive index, n_2, larger than that of the surrounding air medium, n_1. The simplest possible case of reflection and transmission is given by of a lossless dielectric interface between two regions, air and material. The reflection and transmission for normal incidence is independent on polarization and can be calculated using the Fresnel coefficients:

$$R_\perp = r^2 = \left(\frac{n_1 - n_2}{n_1 + n_2}\right)^2 = \left(\frac{1 - 1.5}{1 + 1.5}\right)^2 = 0.04,$$

indicating that plastic materials only reflect 4 % of the incoming normal light. The remaining 96 % is transmitted into bulk. It is seen that, as the numerical difference between the two refractive indices becomes smaller, the

Downloaded From: http://proceedings.spiedigitallibrary.org/ on 07/11/2014 Terms of Use: http://spiedl.org/terms

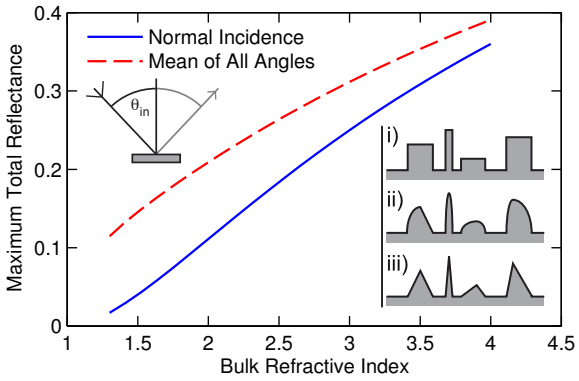

Figure 1: Maximum specular reflectance for Injection-molding compatible topograhies for unpolarized light for normal incidence (blue curve) and averaged over all incoming angles assuming a uniform intensity distribution (red curve), where examples i, ii and iii are defined with respect to an initial flat micro-scale surface.

reflection is reduced. We define the hemispherical reflection W for un-polarized light averaged over all angles: $W(n_1, n_2) = \frac{1}{\pi} \int_{\theta_{\text{in}}=-\frac{\pi}{2}}^{\frac{\pi}{2}} R(n_1, n_2, \theta_{\text{in}})\, \mathrm{d}\theta_{\text{in}}$, describing the total normalized reflection of a dielectric surface equally illuminated at all angles. In Fig. 1, the total reflection is seen as function of refractive index for normal incidence and averaged over all incoming angles (hemispherical reflection). For an air-plastic interface, with $n_2 = 1.5$, we find an accumulated reflection of 8.92 % for p-polarization and 20.2 % for s-polarization. This means, that in normal daylight, meaning uni-directional un-polarized light, we may only alter 14.6 % of the incoming light at maximum. The remaining 85.4 % of the incoming light is transmitted into bulk, where it may be absorbed or scattered. As an rule of thumb, the hemispherical reflection for common plastic materials is around 15 %. These numbers describe the fundamental limit of performance in clear plastic for any structure or design respecting the injection-molding compatibility condition. In general, higher refractive index means higher reflection.

We now consider a periodic nano-texturing of the surface, characterized by a period Λ. If the period of the texture is longer than the wavelength of the incident light, we refer to this periodic alteration as a diffraction grating. We find the grating equation [17, Eq. (1)], here written in the most general case:

$$\begin{aligned} n_1 \sin\theta_m - n_1 \sin\theta_{\text{in}} &= \frac{m\lambda}{\Lambda}, \quad (\text{reflected orders}) \\ n_2 \sin\theta_m - n_1 \sin\theta_{\text{in}} &= \frac{m\lambda}{\Lambda}, \quad (\text{transmitted orders}) \end{aligned} \tag{1}$$

where n_1 and n_2 is the refractive indices of the incident medium and the transmission medium respectively, and θ_{in} is the incident angle of the light with respect to the surface normal. This is a very general formula because Fourier series form the most fundamental solution to any linear differential equation that is subject to periodic boundary conditions. Therefore iridescence arising from diffraction gratings always takes the form of one or more ordered spectra although intensity may vary. Besides the slowly varying intensity of diffracted spectral orders described by the grating equation (1), rapid variations can also be found in certain narrow frequency bands. These abnormally high or low intensities in the diffracted light are referred to as Wood's anomalies.[18] Especially in the case of the first diffraction order appearing parallel to the surface at glancing angle, anomalies in the measured spectra can be found. According to Stewart and Gallaway,[18] the corresponding "Rayleigh" wavelengths can be found in the zero–order specular radiation yielding:

$$\lambda_R(\theta_{\text{in}}) = \frac{\Lambda}{m_\pm}\left(\pm 1 - \sin\theta_{\text{in}}\right). \tag{2}$$

At the Rayleigh wavelengths first order emerges at glancing angle and the redistribution of energy results in a anomaly in the specular reflection. Anomalies have been subject to an intense study. Hessel and Oliner[19] argue that two distinct types of anomalies may exist: A Rayleigh wavelength type due to the emergence of a new

Downloaded From: http://proceedings.spiedigitallibrary.org/ on 07/11/2014 Terms of Use: http://spiedl.org/terms

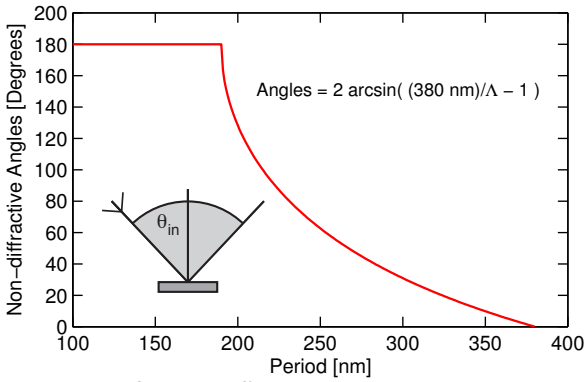

Figure 2: Incident angles causing no reflected diffraction in the visual spectrum as function of nanostructure period. Periods below 190 nm does not lead to diffraction at any angles in the visual spectrum.

spectral order at grazing angle, and a resonance type which is related to the guided complex waves supportable by the grating.

To complete the picture of optical gratings, we also discuss, sub-wavelength, non-diffractive gratings using an argument given by Raguin and Morris.[17] For non-diffractive gratings the period should be small enough that all higher diffraction orders are evanescent. From the grating equation, this requirement sets an upper limit to the period-to-wavelength ratio specified by [17, Eq. (2)]; $\frac{\Lambda}{\lambda} < \frac{1}{\max(n_2,n_1)+n_1 \sin\theta_{\max}}$, where $\theta_{\max}$ is the maximum angle of incidence. Since the denominator of the right-hand side of the above inequality is always larger than unity because $n_1 \geq 1$ and $n_2 \geq 1$, it is seen that the surface must always have a surface period smaller than the dimensions of the incident wavelength, hence the term sub-wavelength. It should be noted that the above argument is normally only given in terms of the reflected orders, leading to an intermediate range of structures that are often anti-reflective, but still scatters light in the transmission. In the case of a period of 250 nm, the first order reflection appears at glazing angle (horizontal along the interface) at 31 degrees incidence, meaning that the perceived specular color is significantly changed for angles bigger than 31 degrees incidence. Therefore, the non-diffractive angle interval is 62 degrees, as seen in Fig. 2. For a period of 200 nm, first order reflection does not occur until 76 degrees. Periodic structures below 250 nm provides basis for angle-independent colors, although diffractions can be seen for angles approaching glazing angle. For structural color effects, the optimum is periods approximately 200 nm in order to avoid diffraction in the visual spectrum. Periods below 190 nm do not lead to diffraction at any angles in the visual spectrum, as seen in Fig. 2, however transmission diffraction effects may still affect the specular reflection.

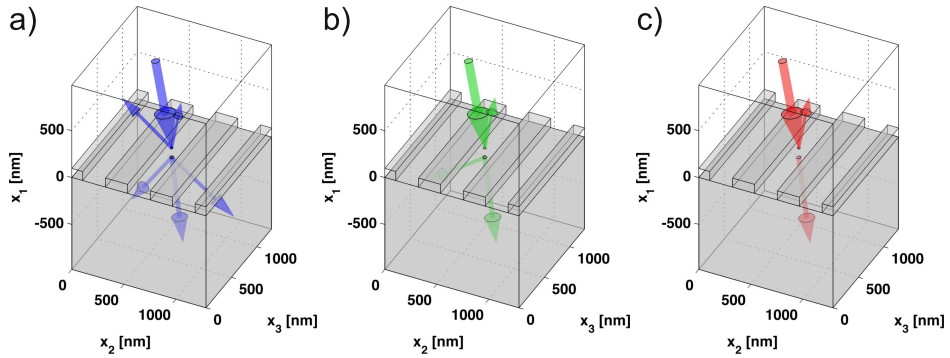

Figure 3: RCWA simulations illustrating the three fundamental grating regimes using 430 nm period, 100 nm height, 10° incident light and $n_2 = 1.4$. Arrows indicate magnitude on logarithmic scale. a) $\lambda = 410$ m (blue light). Several orders in both transmission and reflection. b) $\lambda = 550$ nm (green light). 0'th order in reflection, two orders in transmission. c) $\lambda = 680$ nm (red light). Only 0'th order in both reflection and transmission.

Downloaded From: http://proceedings.spiedigitallibrary.org/ on 07/11/2014 Terms of Use: http://spiedl.org/terms

As illustrated in Fig. 3 three optical regimes can be distinguished: 1) For short wavelengths, several orders in both the transmission and reflection exist, 2) for wavelengths longer than the period, only the zero–order in reflection but still several orders in transmission exist, and finally, 3) for long wavelengths only zero–order in both reflection and transmission exist. These three optical regimes are fundamental to the reflection and transmission of optical gratings.

3. ANTIREFLECTIVE STRUCTURES

Anti-reflective coatings, as widely applied in many optical components, is conventionally realized by adding one or more layers of dielectric or metallic thin films on the surface. It is widely known that a single layer can reduce the reflectance of a glass surface to a mean value of approximately 2.5% in the visible spectrum. Multi-layer coatings, typically with 3-6 layers can reduce the reflectance to below 0.5% in the visible spectrum. At 45° incident angle the reflectance of such a coating is approximately 1%.

Antireflective properties can also be obtained by structuring the surface on the nanoscale. In the sub-wavelength regime, light cannot resolve the individual features of the surface. The structures function as a gradient in the effective refractive index of the material, reducing Fresnel reflections from the surface.[1,4] Antireflective structures can be realized in different ways. It can be random structures or periodic structures in one or more dimensions. For fabrication of such such nano-texture by casting or molding, the master structures can be fabricated in a range of different ways. Random textures have been fabricated by anodized aluminium oxide[20] and by so-called black silicon,[7,21] whereas periodic textures have been realized by interference lithography[4] and electron-beam lithography.[6]

In 2008 Ting *et al.* reported antireflective structures in PMMA, fabricated by hot embossing with a Ni-Co stamp.[22] The high aspect ratio structures were fabricated in Si using electron cyclon resonance (ECR) etching, and the Ni-Co shim was subsequently electroplated from the Si master. They report reflectances below 0.5% in the visible spectrum for structures with aspect ratio higher than 2.6. In 2010 Hong *et al.* reported the fabrication of antireflective nanostructures in COC by hot embossing from a black silicon master. After hot embossing, the master was dissolved as it was not possible to release it from the imprinted COC. the transmittance of COC was increased from 90% to 95% by nanostructuring both sides of the COC film. The aspect ratio of the structures was up to 12, and the tip of the structures was below 20 nm. Jang *et al.* reported laser interference patterns in Si hot embossed in polycarbonate. Transmittance increased from 90% to 93.5% (single side)[23] and drops in transmittance are observed when diffraction occurs for small wavelengths. For example, a grating with a period of 227 nm has a cutoff wavelength around 375 nm, whereas a 300 nm period yields a cutoff wavelength of approximately 475 nm.

The black silicon method[24] has been chosen for this study. This is a cheap and fast method to cover large areas with random conical-shape nanostructures. For comparison, the price-per-area for e-beam exposed masters can be four orders of magnitude higher. Black silicon etching is a mask less reactive ion etching (RIE) process, which can form large areas of random tapered nanostructures. Black silicon etches can be performed in many different ways. The simplest one uses just SF_6 and O_2.[25] SF_6 supplies the fluorine atoms that react with silicon to make a volatile SiF_4 gas. The oxygen reacts with fluorine and silicon to make a passivating layer of $Si_xF_yO_z$. Any protrusion that will exist or is formed on the surface will be slightly more protected by the passivation layer compared to the planar regions of the surface. As the etching continues, any roughness will be enhanced

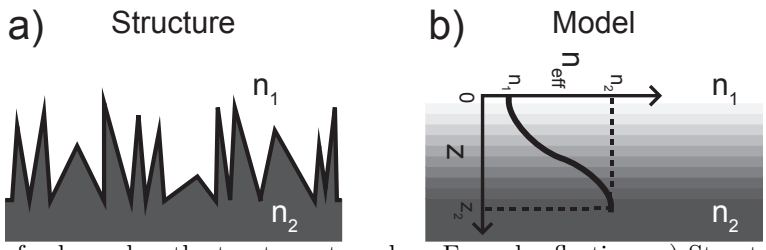

Figure 4: Illustration of subwavelength structures to reduce Fresnel reflection. a) Structure. b) Modeling by a gradient in the effective refractive index of the material.

Downloaded From: http://proceedings.spiedigitallibrary.org/ on 07/11/2014 Terms of Use: http://spiedl.org/terms

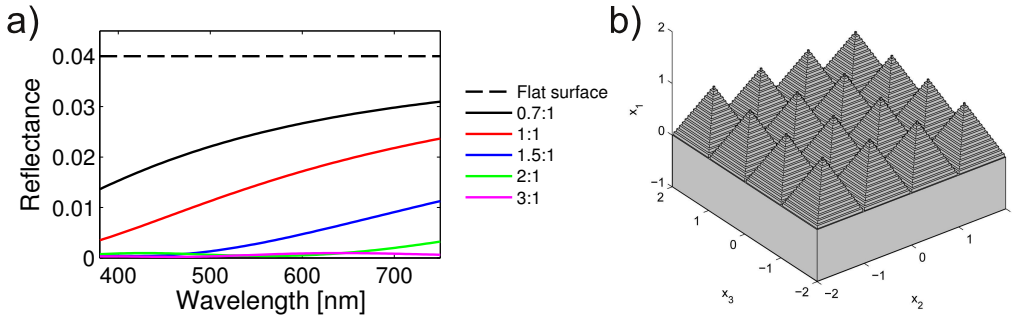

Figure 5: Reflectance of pyramid texture as function of wavelength for various aspect ratios. a) Calculation by 100 layers with transfer matrix approach and effective medium theory. b) Schematic of modelled structure.

and eventually form cone or needle-like structures. The surfaces formed by this method are statistical in nature due to the random formation process. Thus it is not a lithography method. However, by controlling the critical etching parameters[7] such as pressure, platen power, gas flows and temperature, the average lateral sizes and aspect ratios of the structures can be tuned. The black silicon can then be used as a master, for replication in polymer by hot embossing or by UV nano-imprint lithography (UV-NIL).

The antireflective effect can be described by dividing the structured region of the surface in thin layers of increasing refractive index. Instead of a single interface, the surface now consist of a multiple of interfaces, each with a small increment in the refractive index, see Fig. 4. Due to the non-linear dependence on the refractive index of the Fresnel coeffients, the total reflectance from such a system will be smaller than that of a single interface. From this model, the reflectance of a polymer surface can be calculated, using the transfer matrix method.[26] The refractive index of each of the layers can be described from the geometry of the structures, and an effective medium theory. The result of such a model is given in Fig. 5, for a surface with pyramid shaped structures. It is seen that by increasing the height of the structures, the reflectance can effectively be reduced to zero. However, large-aspect-ratio structures can be challenging to fabricate. Thus, significant anti-reflective effect is seen for structures with an aspect ratio of only 1.5:1.

The random nanostructures will inherently scatter light. This is a drawback for our applications. If the structures are too large, they will scatter light in the visible spectrum, rendering the surface of an otherwise clear polymer milky white. As shown by the authors,[27] the scattering properties of black silicon can be tailored to function as color filters in directly transmitted light. Furthermore, the scattering from the randomly textured black silicon can be minimized, as reported by the authors.[21] By controlling the black silicon etching process, the characteristic lateral spatial frequency of the nanostructures can be maximized to minimize scattering. An example of such a surface is shown in Fig. 6. The sample is fabricated using black silicon as a master for a UV-NIL process, using the UV curable resin, Ormocomp (a transparent organic-inorganic hybrid polymer from

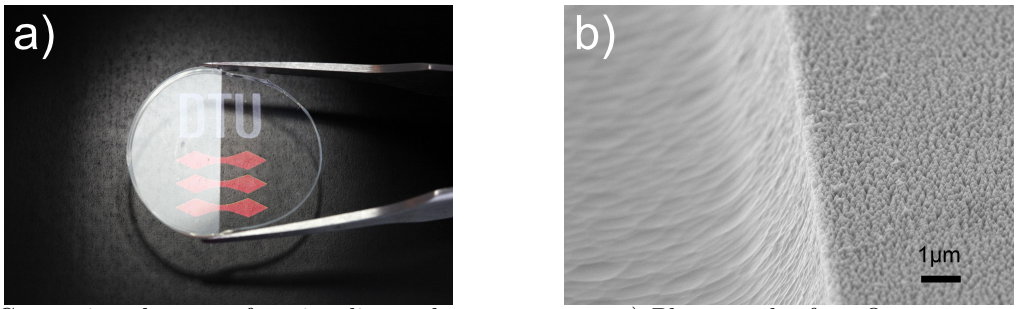

Figure 6: Comparison between functionality and nano-texture. a) Photograph of an Ormocomp sample with antireflective functionality of the nanostructures fabricated by UV-NIL, using black silicon as a master (right part of sample), compared to a non-textured surface (left part of sample). b) SEM image of the interface between the nano-textured and non-textured surface.

Downloaded From: http://proceedings.spiedigitallibrary.org/ on 07/11/2014 Terms of Use: http://spiedl.org/terms

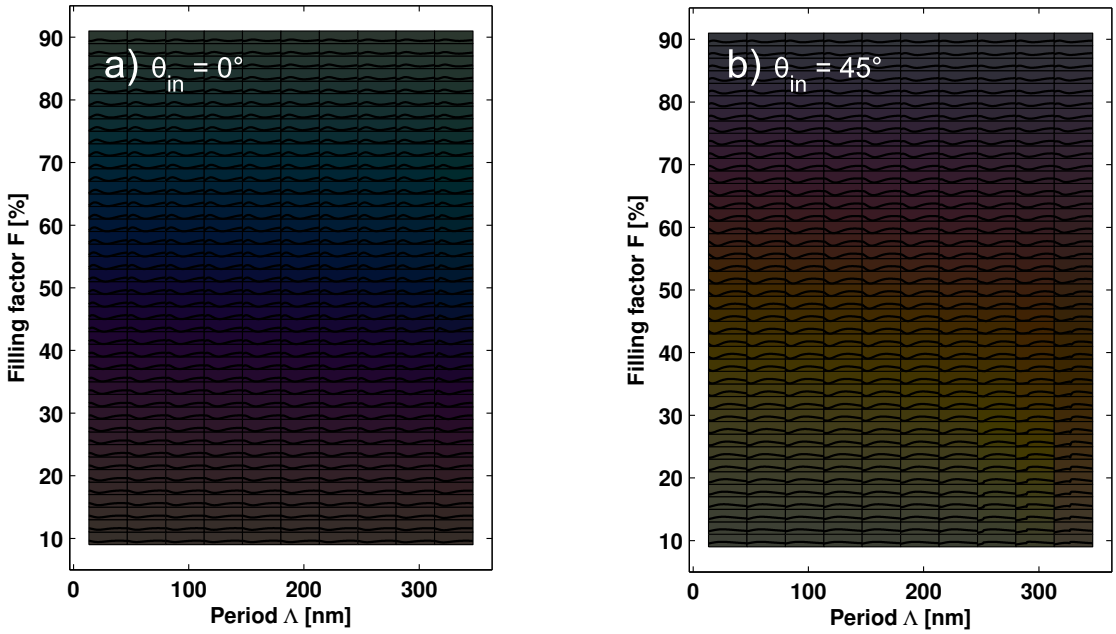

Figure 7: Example of plastic (n=1.5) surface daylight color effects based on a square lattice. a) Normal incidence. b) 45° incidence. Each square shows RCWA simulated specular colors for given parameters.

Micro resist technology Gmbh, Berlin). The left side of the sample is a planar Ormocomp surface on both front and backside, whereas the right side is nanostructured on both front and back. The sample is placed on a paper with a DTU logo printed on a black background and illuminated by a white light source for specular reflection into the camera. It is clearly seen that the nanostructured surface suppress a large part of the specularly reflected light. The nanostructures reduce Fresnel reflection by 50%, even though they only have an aspect ratio of 1.3. The structures are 200 nm tall, and have a characteristic distance between each nanostructure of 160 nm correpsonding to a lateral spatialt frequency of 6 μm^{-1}.

4. ANGLE-INDEPENDENT STRUCTURAL COLORS

Structural colors can originate from nano-textured surfaces. As a first approach to address the strong angular-dependence of diffraction grating based structural color, we discuss the possibilties of strucutral color in the case of polymer surfaces from sub-wavelength diffraction gratings. The grating scattering properties are studied by RCWA,[28] using a commercial solver (GD-Calc, KJ Innovation) for simulating the absolute values of reflection and transmission. Due to the dependence on the exact structural dimensions, each point in the $(\theta_{\mathrm{in}}, \phi_{\mathrm{in}}, \lambda)$ parameter space must be individually assessed for given structural dimensions.

For background, the color of an object is the result of a complex interaction between the light source $S(\lambda)$ incident on the object, the reflection or transmission of the object $R(\lambda)$ or $T(\lambda)$, and the observer modeling the spectral sensitivity of human perception. In the CIE 1931 XYZ-model,[29] colors can be defined on integral form:

$$\begin{bmatrix} X \\ Y \\ Z \end{bmatrix} \equiv C^{-1} \int_0^{\infty} S(\lambda)\, R(\lambda) \begin{bmatrix} \bar{x}_{\mathrm{obs}}(\lambda) \\ \bar{y}_{\mathrm{obs}}(\lambda) \\ \bar{z}_{\mathrm{obs}}(\lambda) \end{bmatrix} \mathrm{d}\lambda, \tag{3}$$

with normalization $C \equiv \int_0^{\infty} S(\lambda)\, \bar{y}_{\mathrm{obs}}(\lambda)\, \mathrm{d}\lambda$. The parameters $(\bar{x}_{\mathrm{obs}}, \bar{y}_{obs}, \bar{z}_{obs})$ describe the spectral sensitivity of the observer and roughly correspond to the sensitivity of the three cones (fovea centralis) of the human eye. Here, we use the 1978 Judd Vos correction[30] of the CIE 1931 2° observer[29] and the ISO/CIE standard illuminant D65.[31] In order to accurately present color values, a conversion between the device-independent CIE-XYZ model

Downloaded From: http://proceedings.spiedigitallibrary.org/ on 07/11/2014 Terms of Use: http://spiedl.org/terms

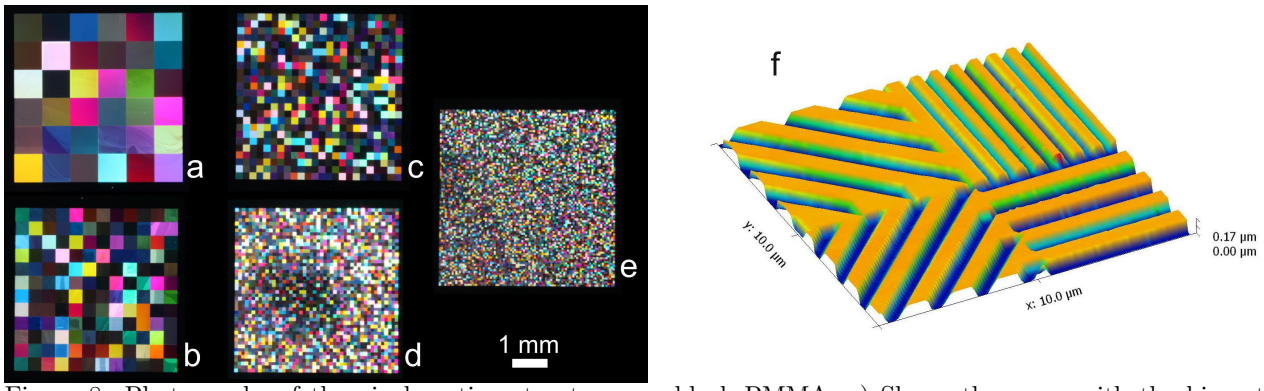

Figure 8: Photographs of the pixel grating structures on black PMMA. a) Shows the array with the biggest pixels, 800 micron. b) 400 micron. c) 200 micron. d) 100 micron. e) Down to 50 micron, barely resolvable with the human eye. f) AFM image of the Si master, showing an intersection between four different pixels. The different orientations and periods of the diffraction gratings give rise to the pseudo angle-independent color effect.

and device-dependent outputs on a display (voltages expressed in RGB) or paper (CMYK) is needed. Here we adopt the sRGB conversion for display.[32]

Given the fabrication platform developed, what possible colors may be produced? An answer to that question is given by the color map in Fig. 7 for normal incidence and 45° incidence. The map is constructed by simulating the reflection of squared two-dimensional silicon gratings converted into a color via Eq. (3). The colors may appear darker due to the overlaying reflection spectra data.

From the figures, it is seems that bright angle in-dependent color effects in polymer material by sub-wavelength diffraction gratings are challeging. The results confirm the basic observation that the total reflectance cannot exceed the Fresnel reflection of the corresponding planar surface.

5. ANGLE-DEPENDENT COLOR EFFECTS BY DIFFRACTION GRATING PIXELS

Even though the reflectance of polymers is low, diffraction gratings can provide bright reflected angular dependent color effects on a black polymer substrate by diffracting light into several beams traveling in different directions. Despite the angular-dependent nature of diffraction, it is possible to obtain what we will refer to as an pseudo-angular independent color effect. This can be achieved by combining multiple gratings of different types in a pixel-array. Each pixel, consisting of a single grating, will be highly angle-dependent, however the overall glitter effect of the entire array will appear homogeneous and independent of viewing angle as a second approach to adress angle-dependence.

The individual gratings are chosen to be one-dimensional line gratings. A 2D-grating would provide more diffraction orders, thereby increasing the chance of an order being seen by the observer, but the individual orders would also be significantly weaker. By choosing 1D gratings there will be fewer orders, but the ones existing will be much stronger. The period of a grating determines the direction of the diffraction orders for light with a given incident angle. Here we use 8 different periods ranging from 700 nm to 1400 nm with 100 nm spacing in a uni-form distribution. This interval is chosen to provide orders for large intervals of solid angles, while still maintaining bright individual orders. To even out the azimuthal angle dependence, the gratings are oriented in four different directions. The height and filling factor are chosen to maximize the diffraction efficiency for a wide range of wavelengths and incident angles. Based on RCWA simulations, it is found that a height of 135 nm and a filling factor of 50 % leads to a optimum of diffraction efficiency, with respect to incident angle and wavelength.

The diffraction gratings were defined using electron beam lithography on a silicon wafer. The structures were transfered to a black PMMA substrate, using hot embossing. An AFM image of the fabricated master is shown in Fig. 8f, where four different pixels can be seen. The fabricated PMMA sample was photographed using a digital single-lens reflex camera with a Canon MP-E 65mm f/2.8 1-5x Macro lens, and a white light source. The

Downloaded From: http://proceedings.spiedigitallibrary.org/ on 07/11/2014 Terms of Use: http://spiedl.org/terms

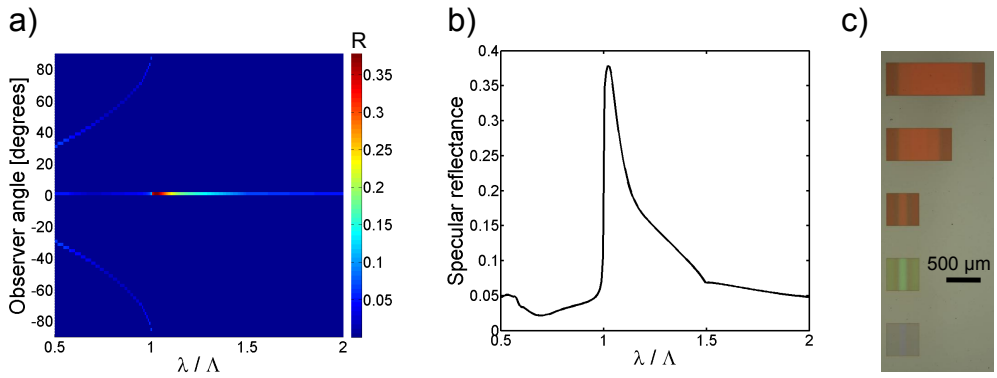

Figure 9: Calculated reflectance values for a thick foil with a grating on the front illuminated at normal incidence. a) Reflectance for a given wavelength and observer angle. For the given wavelength interval 0'th order as well as $\pm$ 1'st order are present b) The 0'th order reflectance showing a large peak just above $\lambda/\Lambda = 1$. c) Microscope image of gratings with three different periods leading to three different colors.

photographs, seen in Fig. 8, were taken directly above the sample, with the light source directed at the sample from the side. The lens can resolve features not visible to the human eye. The 50 micron pixels, for example, are easily seen in the photo with the help of the lens. Each array is 4.8×4.8 mm^2, (a) is the 800 micron pixels, (b) 400 micron; halved each time, down to (e) with 50 microns.

6. DIFFRACTION GRATINGS ON THICK TRANSPARENT FOILS

Until this point the nano-textured polymer surface has been considered as an isolated system with the reflectance of the surface being the only contribution to the observed color. This is for example the case for a black pigmented polymer, where practically all light entering the polymer is absorbed. As a third apporach to overcome angular dependence, we now discuss the inclusion of backside reflections.

Angle-independent color effects can be achieved with a reflectance exceeding the corresponding planar Fresnel surface reflectance, for example in the case of a thick transparent foil. A thick foil can be defined as a slab of material with parallel front and back sides and with a thickness larger than the coherence length of the light under consideration. This implies no interference between reflections on the front and back. Therefore all surface effect calculations can be treated separately using RCWA and Fresnel coefficients for diffraction gratings and flat surfaces respectively.

The system under consideration is a transparent foil, of refractive index n_2, with a diffraction grating of period Λ on the top side. The foil is illuminated by white light at normal incidence. The back side is flat. With the given constraints, it is straight forward to set up a calculation of the efficiency of the reflected and transmitted orders of the full system using ray tracing. First, the incoming light interacts with the grating in the top surface producing both transmitted and reflected orders, of which the efficiencies may be calculated using RCWA. The transmitted orders propagate to the back side where they partly escape into the air and partly reflect back into the substrate. The reflected light from the back will again approach the front surface, now from the inside and it is again reflected and transmitted based to the grating geometry. By tracing all orders the total reflectance and transmittance can be found by summation of the escaped light.

Such a calculation has been made for a binary line grating of which both the protrusion height and width equals half the period. The reflectance as function of wavelength and observer angle is seen in Fig. 9a. The zero'th order reflection is located at 0 degrees, whereas the ± 1 orders are present for wavelengths smaller than the period at varying angles according to the diffraction equation.

In Fig. 9b the 0 order reflectance is seen. Most noticeable is a large peak for wavelengths just higher than the period, reaching a level almost 10 times the Fresnel reflection of a flat surface. At the same time the peak is relatively sharp enabling bright colors to be produced. Three examples of such colors are seen in Fig. 9c, where

Downloaded From: http://proceedings.spiedigitallibrary.org/ on 07/11/2014 Terms of Use: http://spiedl.org/terms

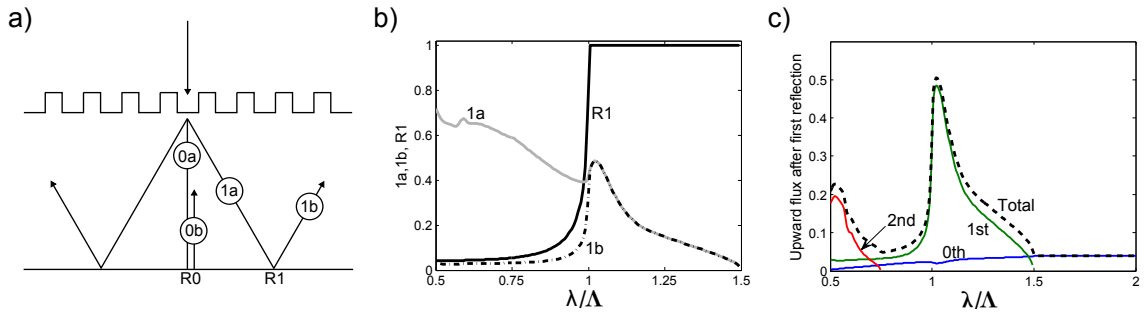

Figure 10: a) Illustration of different orders relevant for the creation of the sharp reflectance peak. b) The 1st order fluxes before (1a) and after (1b) reflection on the back side as well as back side reflectance, R1. c) Contributions to the upwards flux after one reflection on the back.

a 0.1 mm thick topas foil with imprinted gratings of periods 425 nm (blue), 505 nm (green), and 615 nm (red) is seen trough a bright field microscope. The gratings, which are here 350 nm deep, were originally fabricated in a silicon master using e-beam lithography and dry etching and then replicated in the foil using thermal imprint.

The strong peak in the zero'th order reflection is based on total internal reflection on the backside of the transmitted orders of the first interaction with the grating. For wavelengths satisfying $\Lambda < \lambda < n_2\Lambda$ the foil will support three orders (-1,0, and 1) while the air will only support one. This leads to total internal reflection of the ± 1 orders on the backside of the foil. For wavelength satisfying $\lambda < \Lambda$ there exists more orders in the air which the ± 1 can couple to, thereby lowering the Fresnel reflection on the backside. The process producing the strong peak is illustrated in Fig. 11, where the strengths of the first order fluxes are shown after the initial interaction with the grating (1a) and after reflection at the back side (1b). The Fresnel reflectance of the first orders on the back is also shown.

It is clear that two conditions must be fulfilled in order to get high strength of upwards going fluxes. The ± 1 order efficiency must be high and it should be totally reflected on the back. These conditions are only fulfilled for wavelengths just above the period leading to the significant peak. In Fig. 11c are the contributions to the total upwards flux after one reflection on the back shown. Here it is clear that the ± 1 orders are responsible for the existence of the peak.

With the knowledge that the color information is lying in the total internally reflected first order fluxes (1b) it is possible to create a structure which facilitates a diffuse colored reflection upon normal incident light, rather than having the color information only in the specular direction. The principle is illustrated in Fig. 11a. The

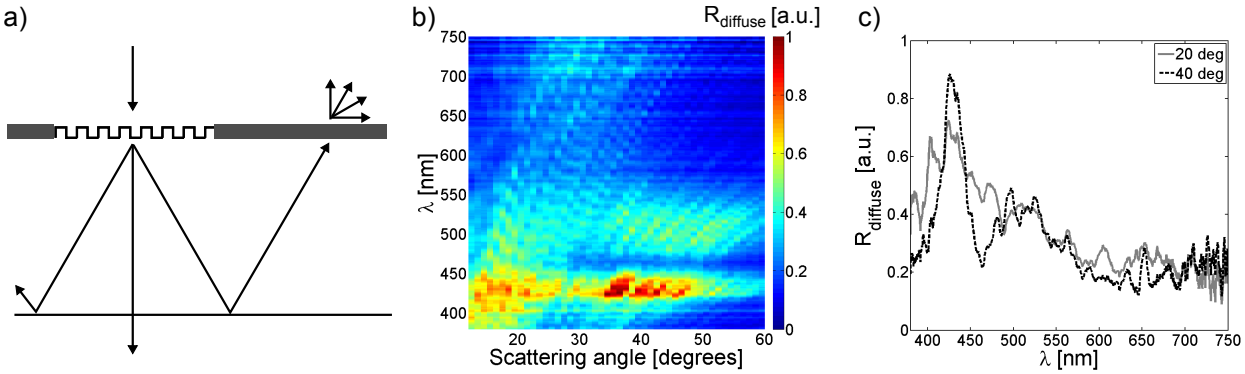

Figure 11: a) Conceptual sketch of alternating grating and diffuser sections. b) Angle resolved measurement of diffuse reflectance from gratings with period 405 nm for normal incident light is used c) Spectra at 20 and 40 degrees observer positions.

Downloaded From: http://proceedings.spiedigitallibrary.org/ on 07/11/2014 Terms of Use: http://spiedl.org/terms

surface of the foil is covered by alternating sections of grating and diffuser elements. The diffuser elements, which enables the out coupling of the first order modes in various directions, could be fabricated in several ways. Refractive elements, such as micro lens arrays are effective diffusers,[33] but the structure size of the lenses is not compatible with the design used her. Instead random binary diffusers[34] are used. In this ways the periodic gratings and diffusers may be fabricated in the same fabrication step. The widths of the sections are designed such that all total internal reflected first orders of the peak wavelength hits a diffuser.

Angle resolved measurement of the diffuse reflection for such a surface with a grating period of 405 nm is seen in Fig. 11b. A clear enhancement of the blue light in a wide angle interval is observed as also illustrated by the spectra at 20 and 40 degrees in Fig. 11c. The spectra somewhat noisy character of the spectra originates from the diffractive nature of the diffusers.

ACKNOWLEDGMENTS

We acknowledge J. Scheel, DTU Nanotech, for photography. J. Weirch, Danish Fundamental Metrology, and J. Nørregaard, NIL Technology Aps, are acknowledghed for fruitfull discusions. This work was supported by the Danish National Advanced Technology Foundation (Contract No.: 007-2010-2) and by the European Commision via the FP7 MMP Integrated project PLAST4FUTURE (NMP2-SE-2012-314345).

REFERENCES

[1] Bernhard, C. G., "Structural and functional adaptation in a visual system," *Endeavour* , 79–84 (1967).

[2] Parker, A. R. and Townley, H. E., "Biomimetics of photonic nanostructures," *Nature Nanotechnology* **2**, 347–353 (June 2007).

[3] Vukusic, P., Sambles, J. R., and Lawrence, C. R., "Colour mixing in wing scales of a butterfly," *Nature* **404**, 457 (Mar. 2000).

[4] Clapham, P. B. and Hutley, M. C., "Reduction of Lens Reflexion," *Nature* **244**(281) (1973).

[5] Stephens, R. B. and Cody, G. D., "Optical Reflectance and transmission of a textured surface," *Thin Solid Films* **45**, 19–29 (1977).

[6] Kanamori, Y., Sasaki, M., and Hane, K., "Broadband antireflection gratings fabricated upon silicon substrates," *Optics Letters* **24** (Oct. 1999).

[7] Sainiemi, L., Jokinen, V., Shah, A., Shpak, M., Aura, S., Suvanto, P., and Franssila, S., "Non-reflecting silicon and polymer surfaces by plasma etching and replication.," *Advanced materials* **23**, 122–6 (Jan. 2011).

[8] Park, K.-C., Choi, H. J., Chang, C.-H., Cohen, R. E., McKinley, G. H., and Barbastathis, G., "Nanotextured Silica Surfaces with Robust Superhydrophobicity and Omnidirectional Broadband," *ACS Nano* **6**(5), 3789–3799 (2012).

[9] Kinoshita, S., Yoshioka, S., and Miyazaki, J., "Physics of structural colors," *Rep. Prog. Phys.* **71**, 1 (Jan. 2008).

[10] Chung, K., Yu, S., Heo, C.-J., Shim, J. W., Yang, S.-M., Han, M. G., Lee, H.-S., Jin, Y., Lee, S. Y., Park, N., and Shin, J. H., "Flexible, Angle-Independent, Structural Color Reflectors Inspired by Morpho Butterfly Wings," *Advanced Materials* **24**, 2375–2379 (2012).

[11] Ribot, C., Lee, M.-S. L., Collin, S., Bansropun, S., Plouhinec, P., Thenot, D., Cassette, S., Loiseaux, B., and Lalanne, P., "Broadband and Efficient Diffraction," *Advanced Optical Materials* , n/a–n/a (July 2013).

[12] Cao, L., Fan, P., Barnard, E. S., Brown, A. M., and Brongersma, M. L., "Tuning the color of silicon nanostructures.," *Nano letters* **10**, 2649–54 (July 2010).

[13] Walia, J., Dhindsa, N., Khorasaninejad, M., and Saini, S. S., "Color Generation and Refractive Index Sensing Using Diffraction from 2D Silicon Nanowire Arrays.," *Small (Weinheim an der Bergstrasse, Germany)* , 1–8 (June 2013).

[14] Vukusic, P. and Sambles, J. R., "Photonic structures in biology," *Nature* **424**, 852 (Aug. 2003).

[15] Prum, R. O., Quinn, T., and Torres, R. H., "Anatomically diverse butterfly scales all produce structural colours by coherent scattering.," *The Journal of experimental biology* **209**, 748–65 (Mar. 2006).

[16] Bao, G., Dobson, D. C., and Ramdani, K., "A constraint on the maximum reflectance of rapidly oscillating dielectric gratings," *SIAM J. Control Optim.* **40**, 1858–1866 (Mar. 2002).

Downloaded From: http://proceedings.spiedigitallibrary.org/ on 07/11/2014 Terms of Use: http://spiedl.org/terms

[17] Raguin, D. H. and Morris, G. M., "Analysis of antireflection-structured surfaces with continuous one-dimensional surface profiles," *Appl. Optics* **32**, 2582 (May 1993).
[18] Stewart, J. E. and Gallaway, W. S., "Diffraction Anomalies in Grating Spectrophotometers," *Appl. Optics* **1**, 421 (July 1962).
[19] Hessel, A. and Oliner, A. A., "A New Theory of Wood's Anomalies on Optical Gratings," *Appl. Optics* **4**(10), 1275 (1965).
[20] Deniz, H., Khudiyev, T., Buyukserin, F., and Bayindir, M., "Room temperature large-area nanoimprinting for broadband biomimetic antireflection surfaces," *Applied Physics Letters* **99**(18), 183107 (2011).
[21] Christiansen, A. B., Clausen, J., Mortensen, N. A., and Kristensen, A., "Minimizing scattering from antireflective surfaces replicated from low-aspect-ratio black silicon," *Applied Physics Letters* **101**(13), 131902 (2012).
[22] Ting, C.-J., Huang, M.-C., Tsai, H.-Y., Chou, C.-P., and Fu, C.-C., "Low cost fabrication of the large-area anti-reflection films from polymer by nanoimprint/hot-embossing technology.," *Nanotechnology* **19**, 205301 (May 2008).
[23] Jang, H. S., Kim, J. H., Kim, K. S., Jung, G. Y., Lee, J. J., and Kim, G. H., "Improvement of Transmittance by Fabricating Broadband Subwavelength Anti-Reflection Structures for Polycarbonate," *Journal of Nanoscience and Nanotechnology* **11**, 291–295 (Jan. 2011).
[24] Jansen, H., Boer, M. D., Legtenberg, R., and Elwenspoek, M., "The black silicon method: a universal method for determining the parameter setting of a fluorine-based reactive ion etcher in deep silicon trench etching with profile control," *Journal of Micromechanics and Microengineering* **5**, 115–120 (June 1995).
[25] Kumaravelu, G., Alkaisi, M. M., and Bittar, A., "Surface texturing for silicon solar cells using reactive ion etching technique," *Conference Record of the Twenty-Ninth IEEE Photovoltaic Specialists Conference* , 258–261 (2002).
[26] Pedrotti, F. L., Pedrotti, L. S., and Pedrotti, L. M., [*Introduction to Optics*], Pearson Prentice Hall, third ed. (2007).
[27] Clausen, J., Christiansen, A. B., Garnaes, J., Mortensen, N. A., and Kristensen, A., "Color effects from scattering on random surface structures in dielectrics.," *Optics express* **20**, 4376–81 (Feb. 2012).
[28] Nevière, M. N. and Popov, M. N. E., [*Light Propagation in Periodic Media: Differential Theory and Design*], Optical Engineering Series, Marcel Dekker, Inc. New York (2003).
[29] Smith, T. and Guild, J., "The C.I.E. colorimetric standards and their use," *Trans. Opt. Soc.* **33**(3), 73.
[30] Vos, J. J., "Colorimetric and photometric properties of a 2-deg fundamental observer," *Color Res. Appl.* **3**, 125–128 (1978).
[31] Judd, D. B., Macadam, D. L., Wyszecki, G., Budde, H. W., Condit, H. R., Henderson, S. T., and Simonds, J. L., "Spectral Distribution of Typical Daylight as a Function of Correlated Color Temperature," *J. Opt. Soc. Am.* **54**(8), 1031 (1964).
[32] Stokes, M., Anderson, M., Chandrasekar, S., and Motta, R., "A Standard Default Color Space for the Internet - sRGB http://www.w3.org/Graphics/Color/sRGB.html (checked 2012-04-20)," (1995).
[33] Chang, S.-I., Yoon, J.-B., Kim, H., Kim, J.-J., Lee, B.-K., and Shin, D. H., "Microlens array diffuser for a light-emitting diode backlight system," *Optics letters* **31**, 3016–8 (Oct. 2006).
[34] Kurtz, C. N., "Transmittance Characteristics of Surface Diffusers and the Design of Nearly Band-Limited Binary Diffusers*," *JOSA* **62**(8), 982–989 (1972).

Downloaded From: http://proceedings.spiedigitallibrary.org/ on 07/11/2014 Terms of Use: http://spiedl.org/terms

A.2 Højlund-Nielsen et al. 2014a

E. Højlund-Nielsen, T. Greibe, N.A. Mortensen, & A. Kristensen (2014). "Single-spot e-beam lithography for defining large arrays of nano-holes", *Microelectronic Engineering*, 121, 104–107. doi: 10.1016/j.mee.2014.03.025.

Microelectronic Engineering 121 (2014) 104–107

Contents lists available at ScienceDirect

Microelectronic Engineering

journal homepage: www.elsevier.com/locate/mee

Single-spot e-beam lithography for defining large arrays of nano-holes

Emil Højlund-Nielsen [a], Tine Greibe [b], N. Asger Mortensen [c], Anders Kristensen [a,*]

[a] Department of Micro- and Nanotechnology, Technical University of Denmark, Oersteds Plads, Building 345B, DK-2800 Kgs. Lyngby, Denmark
[b] National Center for Micro- and Nanofabrication, Oersteds Plads, Bygning 347, 2800 Kongens Lyngby, Denmark
[c] Department of Photonics Engineering, Oersteds Plads, Bygning 343, 2800 Kongens Lyngby, Denmark

ARTICLE INFO

Article history:
Received 27 October 2013
Received in revised form 14 March 2014
Accepted 22 March 2014
Available online 3 April 2014

Keywords:
Electron beam lithography
Direct-writing
Single-shot writing
Nanofabrication

ABSTRACT

Efficient nanoscale patterning of large areas is required for sub-wavelength optics. Here we use the single-spot exposure strategy, where electron beam lithography (EBL) with a focused Gaussian beam is used to define shapes directly. The serial technique is optimized on the JEOL JBX-9500FS 100 keV prototype EBL system for speed and pattern fidelity to a minimum writing time of around 30 min/cm^2 for 200 nm periods in 2D lattices. The machine time and feasibility of the method are assessed in terms of the trade-off between high current and large writing field.

© 2014 Elsevier B.V. All rights reserved.

1. Introduction

Efficient nanoscale patterning of large areas is required for sub-wavelength optics. For example, photonic crystal applications may require periodic structures with a period of 200 nm or below. Such structures are conveniently fabricated by electron beam lithography. Still, the final product must be made at an economic cost. Here we use a single-spot exposure strategy [1–7], where EBL with a focused Gaussian beam is used to define shapes directly. Conventionally, EBL uses multiple exposures of slightly overlaying spots, see Fig. 1A. As a result, the shape time dominates the beam time, and is the major contributor to the overall writing time. Instead, the single-spot exposure strategy uses the machine as a raster scan tool to write a large rectangle, using a beam step size larger than the spot size, see Fig. 1B. The serial technique is optimized for speed and pattern fidelity to a minimum writing time of around 30 min/cm^2 for 200 nm periods in 2D lattices. The machine time and feasibility are assessed for different topographies and dimensions.

The single-spot electron beam technique discussed in this paper was first described in 1993 by Wendt et al. [1], which used a 6 nm beam-spot with a 5 nm resolution to define holes 50 nm in diameter by etching. This was followed by a more thorough study in 2003 by Kim et al. [4] showing that the single-spot exposure scheme can provide pattern quality similar to the conventional multi-spot exposure approach, but with an order-of-magnitude reduction in the required writing time. For a period of 300 nm and a dose of 30 μC/cm^2 (224 nm spot), writing times were reported to be faster than 1 h/cm^2 depending on the current (up to 44.4 nA). Furthermore, a modified four-spot scheme was also demonstrated for arbitrary shape definition. However, the work of Kim et al. is based on software estimation of the writing time, and it does not investigate small periodic structures with a high filling-ratio. Same year Gadegaard et al. [2] examined the dot diameter as function of dose and the shape diameter as function of the distance to the writing field center, where a writing field side-length of 0.4 mm was found appropriate. Finally, in 2011 Jugessur et al. [5] examined hexagonal patterns with a current of 44 nA. From the literature, it seems that the components of the total writing time has not been examined in detail, which is the focus here.

2. Theory

As a simple model, EBL writing time per area A, t'_{writ}, has four components; beam time, shape time, stage time and calibration time:

$$t'_{\text{writ}} = t'_{\text{beam}} + t'_{\text{stage}} + t'_{\text{shape}} + t'_{\text{cal}} \tag{1}$$

The beam time relates to exposing the resist and is given by dose D and current I as $t'_{\text{beam}} = D/I$ [8]. Stage time, t'_{stage}, is related to the mechanical movement of the stage from writing field to writing field and depends on the writing field area $A_{WF} = \ell^2_{WF}$, with side length ℓ_{WF}, and on the machine parameter τ_{stage} for one average movement of the stage. The stage time can be given as $t'_{\text{stage}} = \tau_{\text{stage}}/A_{WF}$. The shape

* Corresponding author. Tel.: +45 45256331; fax: +45 45887762.
E-mail address: anders.kristensen@nanotech.dtu.dk (A. Kristensen).

http://dx.doi.org/10.1016/j.mee.2014.03.025
0167-9317/© 2014 Elsevier B.V. All rights reserved.

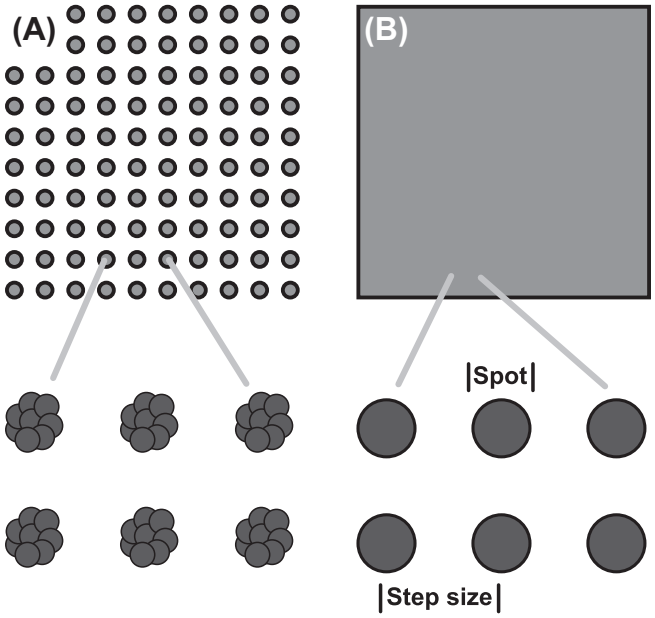

Fig. 1. Illustration of the single-spot exposure strategy. (A) The conventional method for pattern layout is to design an array of circular spots to form the final pattern. (B) Fast-writing patterns are formed directly by a single exposure with a given spot size spaced by the beam step size.

time can be modeled as $t'_{\text{shape}} = \tau_{\text{shape}} N_{\text{shapes}}$, where τ_{shape} is the average time to address each of the N_{shapes} shapes. Shape time is usually negligible using the single-spot exposure strategy, which is the main argument for the method, and will not be discussed further. Calibration is critical for focus [2] and efficient calibration routines in terms of stability and drift compensation become imperative with this method. The calibration can be modeled as a continuous contribution in the form of $t'_{\text{cal}} = \tau_{\text{cal}}\left(t'_{\text{beam}} + t'_{\text{shape}} + t'_{\text{stage}}\right)/\Delta t_{\text{cal}}$ for a Δt_{cal} cyclic calibration interval with time parameter τ_{cal}. Putting all together, the writing time Eq. (1) can be assumed to be a linear function of dose:

$$\begin{aligned} t'_{\text{writ}}(D) &= \left(\tfrac{D}{I} + \tfrac{\tau_{\text{stage}}}{A_{WF}} + \tau_{\text{shape}} N\right)\left(\tfrac{\tau_{\text{cal}}}{\Delta t_{\text{cal}}} + 1\right) \\ &= \alpha D + \beta, \end{aligned} \tag{2}$$

where α and β are fitting coefficients to be estimated from experiments. From the slope α, we may deduce the calibration time overhead, $\tau_{\text{cal}}/\Delta t_{\text{cal}} = (\alpha I - 1)$, if the current is assumed constant. Finally by plotting the β coefficients as function of writing field area, we may deduce an expression for stage time:

$$\beta = \left(\frac{\tau_{\text{stage}}}{A_{WF}} + \tau_{\text{shape}} N\right)\left(\frac{\tau_{\text{cal}}}{\Delta t_{\text{cal}}} + 1\right) = \gamma \frac{1}{A_{WF}} + \delta, \tag{3}$$

where γ and δ are fitting coefficients. Then the stage time parameter can be deduced as $\tau_{\text{stage}} = \gamma/(\tau_{\text{cal}}/\Delta t_{\text{cal}} + 1)$.

3. Methods

The JEOL JBX-9500FS is a prototype 100 keV spot EBL system. The beam is generated by a ZrO/W emitter and electron-beam scanning speeds up to 100 MHz are available. By optimizing the lens focusing system and using an aperture of 200 μm, stable currents of 29 nA, 42 nA and 61 nA, can be provided with sufficiently small beam diameters, similar to previous reported 44 nA in 2011 [5] and two orders of magnitude higher than previous reported 0.33 nA in 2003 [2].

In terms of initial calibration, the two deflectors (position deflector and scanning deflector) are calibrated. These calibrations correct the gain and rotation deflector errors and determine the height correction coefficient, thereby influencing the homogeneity of the pattern writing over a writing field. The distortion correction values of the electron beam in the writing field are also measured. Prior to each pattern writing, the height of the substrate is measured at different positions, and the focus value of the objective lenses is corrected.

The cyclic calibration includes a current measurement, a drift measurement using a mark on the stage, and a temperature measurement on various positions in the machine. These calibrations are performed on a 5 min basis to ensure identical writing conditions.

Six experiments were carried out in order to test the influence of current and writing field on writing time and pattern quality. The dose was varied from 30 μC/cm^2 to 120 μC/cm^2 in steps of 15 μC/cm^2, yielding a total of 42 areas, each of exposure area 5 mm × 5 mm. The exposure dose interval was loosely estimated based on the clearing dose of the positive ZEP-520A resist (Nippon ZEON Company, Ltd.), which is around 30 μC/cm^2 according to the manufacturer data sheet. First, the current was altered; 29 nA, 42 nA, 61 nA, while keeping the writing field fixed at 0.2 mm and then the writing field was altered; 0.3 mm, 0.4 mm and 1.0 mm, while keeping the current at 29 nA. The outcome of this investigation should be a determination of the machine parameters τ_{cal} and τ_{stage}. For each exposed area the writing time was found by subtracting the end time of the exposure from the start time, both retrieved from the machine log after the exposure. The current was measured as part of the cyclic calibration and the mean current of each experiment was used for the calculations.

Devices were fabricated in silicon by exposure of the resist with thickness 158 nm, development, and reactive-ion etching.

4. Discussion

In Fig. 2, the writing time per cm^2 as function of dose is given for different currents with a writing field side length of 0.2 mm. The writing time is seen to be linear dependent on the dose as expected from Eq. (2) with a large offset due to the 0.2 mm writing field. Still, the writing times are faster than 2 h/cm^2 for the chosen dose interval. By linear fitting, we determine α and β for the three different currents. Based on the fitting, it is given in Table 1 that the beam overhead is around 15 s for 301 s of calibration interval corresponding to 5.5% overhead. Therefore, the effective current, that is the inverse slope in Fig. 2, is 27.6 nA for the 29 nA exposure. From Fig. 2, it is clear that the 61 nA current reduces the beam time. Still the stage time constitutes the main component of the writing time and the writing time remains in the order of 45 min/cm^2.

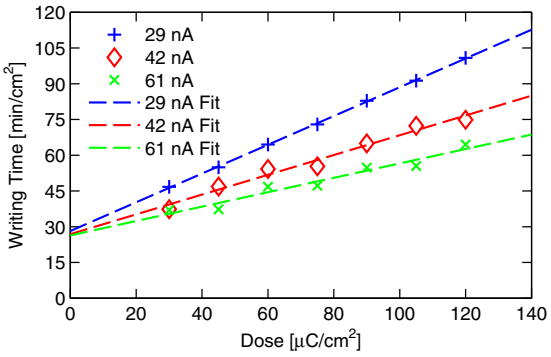

Fig. 2. Measured writing time as function of dose and linear fits (dashed lines) for different currents with array periods of 200 nm and writing field side length of 0.2 mm. Exposure includes calibration. Initial machine calibration not included.

Table 1
Overview of experiments and calculated parameters.

Run	I (nA)	ℓ_{WF} (mm)	$\tau_{cal,fit}$ (s)	$\tau_{cal,meas}$ (s)	τ_{stage} (s)	A/A_{WF}
1	28.87	0.2	13.6	14	0.62	2500
2	42.49	0.2	17.4	14	0.61	2500
3	61.02	0.2	31.7	15	0.59	2500
4	28.88	0.3	16.5	13	0.62	1111
5	28.88	0.4	19.4	13	0.61	625
6	28.88	1.0	17.1	13	0.61	100

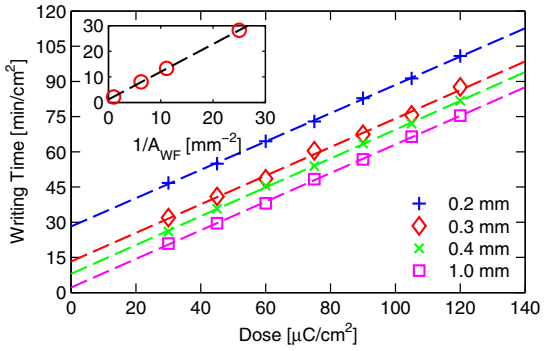

Fig. 3. Measured writing time as function of dose and linear fits (dashed lines) for different writing field side lengths with array periods of 200 nm and current 29 nA. Exposure includes calibration. Initial machine calibration not included. Insert figure plots the y-intercept β of the linear fits in min/cm^2 as function of inverse writing field area, including linear fit (dashed line).

In Fig. 3 the writing time per cm^2 as function of dose is given for different writing field sizes with a constant current of 29 nA. The 0.2 mm data is identical to the 29 nA data in Fig. 2. A writing time of around 30 min/cm^2 for 30 μC/cm^2 can be achieved. It is also clear that the difference between a 0.2 mm writing field and a 0.3 mm writing field is around 15 min/cm^2 in offset. By linear fitting, we may determine α and β for the four different writing fields. The slopes of the linear fits are seen to be almost identical for all the experiments. In the insert of Fig. 3 the y-intercept β of the linear fits is plotted in min/cm^2 as function of the inverse writing field area. A linear correlation can be seen, which by fitting is used to determine the slope γ and the offset δ, see Eq. (3). From this slope, we calculate a stage movement time parameter of 0.61 s.

In Table 1 the details of the six experiments can be found. By examining the machine log, which has a time resolution of 1 s, it is found that calibration takes around 15 s with an overall trend of slightly lower overhead compared to the fitting values. In Table 1 the calculated stage times are also given, which depend on the calibration overheads, and the number of stage movement for each writing field size. Decreasing the written field side length from 0.3 mm to 0.2 mm more than doubles the number of stage movements, which explains the 15 min/cm^2 difference in writing time between a 0.2 mm and a 0.3 mm writing field side length observed in Fig. 3.

In Fig. 4 scanning electron micro-graphs of the structures transferred into silicon with a period of 200 nm are seen, exposed using a dose of 105 μC/cm^2 and different currents. The quadratic lattice

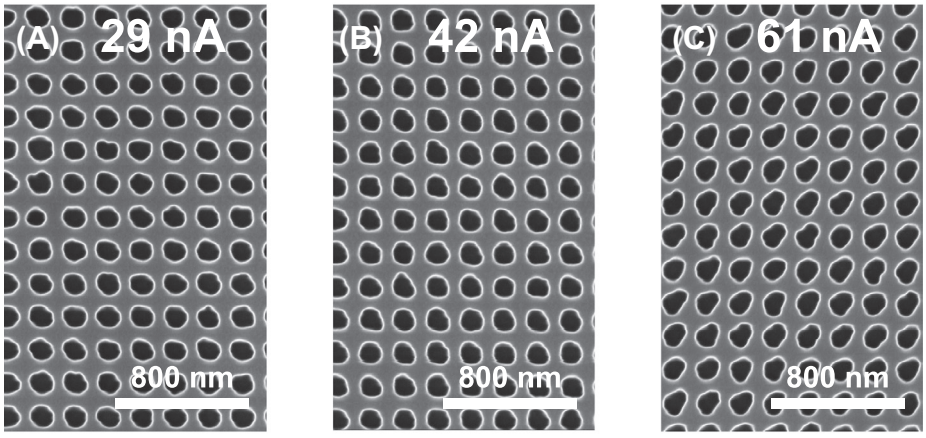

Fig. 4. SEM micrographs of representative silicon structures with period 200 nm, written using dose 105 μC/cm^2 and different currents. (A) 29 nA. (B) 41 nA. (C) 61 nA.

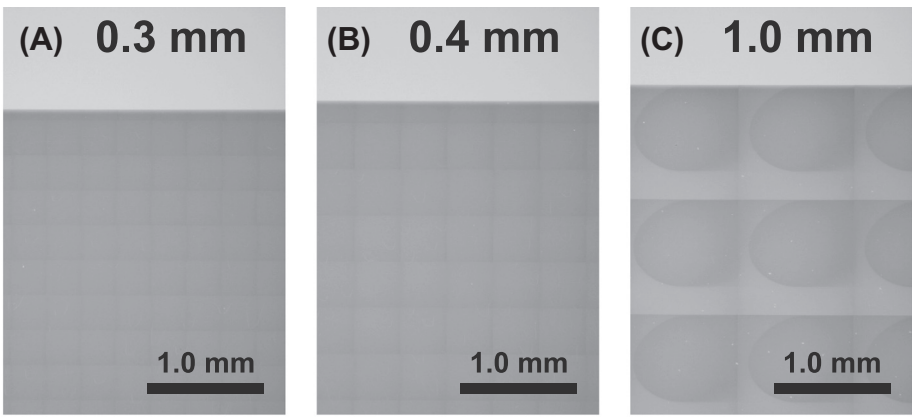

Fig. 5. OM images after development and etch illustrating deflection aberrations of different writing field sizes for current 29 nA and dose 120 μC/cm^2. (A) 0.3 mm × 0.3 mm. (B) 0.4 mm × 0.4 mm. (C) 1.0 mm × 1.0 mm.

is found to be well defined. However, it is clear that the holes, in terms of roundness, degrade for higher currents. The higher current is achieved by increasing the collimating aperture size at the expense of astigmatism. This is seen in Fig. 4C, where the high current of 61 nA causes a smaller asymmetric focal spot compared to Fig. 4A with a current of 29 nA. A larger aperture translates to a larger numerical aperture and corresponding shorter depth of field. We did not identify charging effects [9,10].

In Fig. 5 optical microscope images are seen, taken after processing, of patterned areas exposed with different writing field sizes using a current of 29 nA and a dose of 120 $\mu C/cm^2$. Here the effect of a large writing field is directly visualized. Beam quality clearly degrades with increasing deflection due to increasing deflection aberrations. A smaller writing field prolongs the writing time as seen in Fig. 3, but is often necessary to ensure a given quality of the pattern definition. As mentioned earlier Gadegaard et al. [2] found that a writing field side-length of 0.4 mm was appropriate. We find that a field of 0.3 mm is sufficient for 29 nA, providing a writing time in the order of 1 h/cm^2 for a dose of 75 $\mu C/cm^2$.

In terms of writing time, it is given from Eq. (2) that the sum of the dose-to-current ratio and the stage parameter-to-writing field ratio determines the writing time. This indicates the trade-off between a high current, with less well defined beam shape over the writing field, and a smaller writing field increasing stage movement with less deflection aberration. Thereby the practical upper limit for our JEOL machine and the given resist is a writing time in the order of 30 min/cm^2 for 200 nm periodic holes in 2D lattices.

5. Conclusion

The single-spot exposure strategy, where electron beam lithography (EBL) with a focused Gaussian beam is used to define shapes directly, was used to define 200 nm periodic arrays in silicon. The serial technique was optimized on the JEOL JBX-9500FS 100 keV prototype EBL system for speed and pattern fidelity to a typical writing time of 1 h/cm^2 with a minimum of around 30 min/cm^2. The machine time and feasibility of the method were assessed, discussing the trade-off between high currents and large writing fields. An EBL writing time below 2 h/cm^2 provides new possibilities for sub-wavelength structures. These can be used to provide functionality, such as anti-reflective or plasmonic effects, for large area applications in a cost-effective manner, similar to traditional parallel processing techniques.

This work was supported by the European Commission via the FP7 MMP Integrated project PLAST4FUTURE (NMP2-SE-2012-314345).

References

[1] J.R. Wendt, G.A. Vawter, P.L. Gourley, T.M. Brennan, B.E. Hammons, J. Vac. Sci. Technol., B: Microelectron. Nanom. Struct. 11 (6) (1993) 2637.
[2] N. Gadegaard, S. Thoms, D.S. Macintyre, K. Mcghee, J. Gallagher, B. Casey, C.D.W. Wilkinson, Microelectron. Eng. 68 (2003) 162–168.
[3] S. Golka, H. Heidrich, R. Steingruber, Microelectron. Eng. 68 (2003) 157–161.
[4] S. Kim, H. Chong, R.M.D.L. Rue, J.H. Marsh, a.C. Bryce, Nanotechnology 14 (9) (2003) 1004–1008.
[5] A.S. Jugessur, M. Yagnyukova, J.S. Aitchison, J. Vac. Sci. Technol., B: Microelectron. Nanom. Struct. 29 (6) (2011) 06FF06.
[6] M.M. Greve, B. Holst, J. Vac. Sci. Technol., B: Microelectron. Nanom. Struct. 31 (4) (2013) 043202.
[7] S. Cabrini, S. Hawata, Nanofabrication Handbook, CRC Press, 2012.
[8] N.W. Parker, A.D. Brodie, J.H. McCoy, High-throughput NGL electron-beam direct-write lithography system, Proc. Soc. Photo-optical Instrum. Eng. (SPIE), Emerg. Lithogr. Technol. iv 3997 (2000) 713–720.
[9] J. Zhang, M. Fouad, M. Yavuz, B. Cui, Microelectron. Eng. 88 (8) (2011) 2196–2199.
[10] E. van der Drift, Thermal effects in high voltage e-beam lithography, J. Vac. Sci. Technol., B: Microelectron. Nanom. Struct. 9 (6) (1991) 3470.

A.3 Højlund-Nielsen et al. 2014b

E. Højlund-Nielsen, J. Weirich, J. Nørregaard, J. Garnaes, N.A. Mortensen, & A. Kristensen (2014). "Angle-independent structural colors of silicon". *Journal of Nanophotonics*, 8(1), 083988. doi: 10.1117/1.JNP.8.083988.

Angle-independent structural colors of silicon

Emil Højlund-Nielsen,[a] Johannes Weirich,[b] Jesper Nørregaard,[c] Joergen Garnaes,[b] N. Asger Mortensen,[d] and Anders Kristensen[a,*]

[a]Technical University of Denmark, DTU Nanotech, Ørsteds Plads, Building 345E, DK-2800 Kgs. Lyngby, Denmark

[b]DFM A/S, Matematiktorvet 307, DK-2800 Kgs. Lyngby, Denmark

[c]NIL Technology ApS, Diplomvej 381, DK-2800 Kgs. Lyngby, Denmark

[d]Technical University of Denmark, DTU Fotonik, Ørsteds Plads, Building 343, DK-2800 Kgs. Lyngby, Denmark

Abstract. Structural colors are optical phenomena of physical origin, where microscale and nanoscale structures determine the reflected spectrum of light. Artificial structural colors have been realized within recent years. However, multilayer structures require substantial fabrication. Instead we considered one-layer surface textures of silicon. We explored four patterns of square structures in a square lattice with periods of 500, 400, 300, and 200 nm. The reflectivity and daylight-colors were measured and compared with simulations based on rigorously coupled-wave analysis with excellent agreement. Based on the 200-nm periodic pattern, it was found that angle-independent specular colors up to 60 deg of incidence may be provided. The underlying mechanisms include (1) the suppression of diffraction and (2) a strong coupling of light to localized surface states. The strong coupling yields absorption anomalies in the visual spectrum, causing robust colors to be defined for a large angular interval. The result is a manifestation of a uniformly defined color, similar to pigment-based colors. These mechanisms hold potential for color engineering and can be used to explain and predict the structural-color appearance of silicon-based textures for a wide range of structural parameters. © *2014 Society of Photo-Optical Instrumentation Engineers (SPIE)* [DOI: 10.1117/1.JNP.8.083988]

Keywords: structural color; diffraction gratings; silicon; rigorously coupled-wave analysis; viewing angles.

Paper 13135SS received Dec. 1, 2013; revised manuscript received Apr. 2, 2014; accepted for publication Apr. 2, 2014; published online May 13, 2014.

1 Introduction

Structural colors are optical phenomena of physical origin, where microscale and nanoscale structures determine the reflected spectrum of light, although an unambiguous definition has not been settled yet.[1] The mechanisms of structural colors are categorized into thin-film interference, multilayer interference, diffraction-grating optical effects, and photonic crystal effects.[1] Two examples of structural color are silicon nanowires on oxide thin-film creating color specific resonant scattering[2] and the Morpho butterfly reflecting omnidirectional blue light due to a multilayer topography.[3] Artificial multilayer topographies require substantional fabrication. In this article, we investigate the structural color appearances from single-material one-layer surface textures, which in our view is better up-scalable compared to typical approaches for structural coloration. We consider silicon as a high-index model system for nanostructured dielectric surfaces suitable for polymer replication methods, such as imprinting/embossing and injection-molding. The reflectivity mode devices discussed allow for a number of applications, where surface decoration provides color effects, for example logos, text decoration, or line art. The reflectivity of daylight colors is measured and compared to rigorously coupled-wave analysis (RCWA) simulations, to identify different regimes and predict color appearance. Our study

*Address all correspondence to: Anders Kristensen, E-mail: anders.kristensen@nanotech.dtu.dk

0091-3286/2014/$25.00 © 2014 SPIE

provides an engineering method to specify a physical surface grating texture that will yield a desired novel angle-independent structural color, quantified by color measurements.

The experimental work presented here is based on four samples, each of size of 1×1 cm^2, of artificial nanostructures fabricated on a single wafer using electron beam lithography and dry etching. The patterns, characterized as diffraction gratings, consist of square structures in a square lattice with periods of 500, 400, 300, and 200 nm. Scanning electron microscope images of the four samples can be seen in Figs. 1(a)–1(d). The overall structures appear more rounded as the period decreases. The heights of the structures are measured by atomic force microscopy (not shown) to be around 180 nm. Figures 1(e)–1(h) show photographs without subsequent software adjustments of the wafer illustrating the angular dependence of the reflected light under daylight illumination from a window. In particular, Fig. 1(e) illustrates the near-normal incidence specular colors of the four samples. In Fig. 1(f), a photograph is seen, taken along the diagonal axis and ~45 deg normal to the surface. Here, significant shifts in color have occurred compared to normal incidence. In general, the samples display a rich variation of reflected specular and diffraction-based colors, except for the area with a 200-nm period that seems to retain a more homogeneous color.

2 Theory

For background, the reflectivity and transmission angular distribution of periodic structures are given by the well-known grating equation,[4] which qualitatively describes the studied two-dimensional (2-D) system:

$$n_1 \sin \theta_m - n_1 \sin \theta_{\text{in}} = \frac{m\lambda}{\Lambda}, \quad (\text{reflec.orders}), \tag{1}$$

$$n_2 \sin \theta_m - n_1 \sin \theta_{\text{in}} = \frac{m\lambda}{\Lambda}, \quad (\text{trans.orders}), \tag{2}$$

where n_1 and n_2 are the refractive indices of the incident medium (air) and transmission medium (silicon), respectively, θ_{in} is the incident angle of the light, and θ_m is the angle of the m'th order

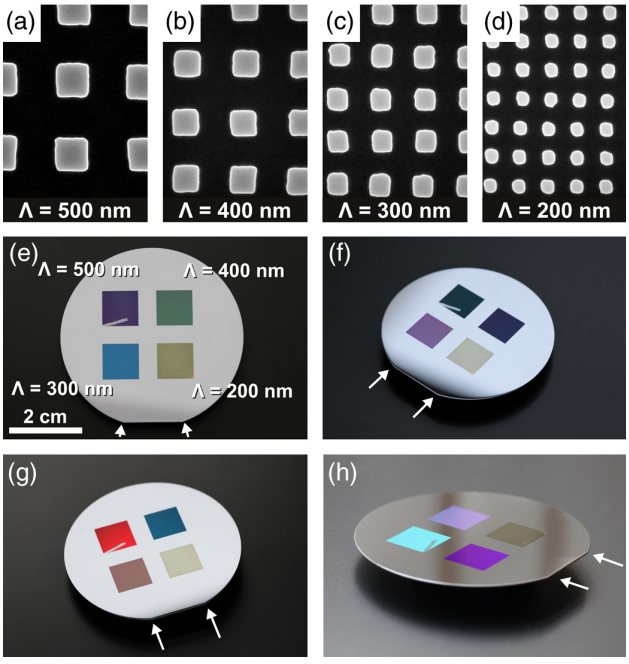

Fig. 1 Silicon structural colors. (a–d) Scanning electron microscope images 1.00 μm wide of the four periodic samples. (e–h) Photographs of the four samples from different angles. In (e), the camera is slightly tilted around 10 to 15 deg compared with normal incidence to avoid lens reflections.

reflectivity, both with respect to the surface normal, see Fig. 4(a). The transition from a nondiffractive to a diffractive reflective grating occurs at the corresponding Rayleigh wavelength;[5] $\lambda_R(\theta_{\text{in}}) = \Lambda(\sin\,\theta_{\text{in}} + 1)$, where first-order ($m = 1$) emerges at glancing angle and the redistribution of energy results in an anomaly (rapid variation) in the specular reflectivity. In addition, a resonance type linked to leaky surface modes exists.[6]

In order to study these surface modes, finite element method frequency simulations are performed for the corresponding one-dimensional (1-D) grating in order to investigate near-field properties in side-view. A TM electromagnetic wave is normal incident on the 1-D grating, and a periodic phase-matched Floquet (Bloch) boundary condition is used. Results from a commercial available solver (Comsol 4.2, COMSOL Inc., Burlington, Massachusetts) can be seen in Fig. 2. It seems that a confinement of light, in the form of a high-electric field magnitude, occurs between the corners for wavelengths around 650 to 700 nm. The field is "short-circuited" between the vertical walls of the grating as described by Hessel and Oliner,[6] to the extent that the corners almost appear to function as classical electromagnetic antennas. The field is concentrated in the air ($n = 1$). The boundary conditions force a discontinuity of the perpendicular electric field at the vertical grating walls due to the index contrast between the dielectric material and air, also utilized in the operation of slot-waveguides, as described by Almeida et al.[7]

In Fig. 3, the specular reflectivity calculated by RCWA for a 2-D grating is plotted as function of height and frequency. A period of 300 nm, a filling factor of 25%, a height of 180 nm, and a refractive index of 4.0 are used. The axes are normalized with respect to period exploiting the scale-invariance of Maxwell's equations in the nondiffractive grating regime. In general, Fig. 3 holds great complexity. The features of reflectivity can be categorized into nonasymptotically features limited to certain heights and asymptotically features present at even large values of height. Regarding the nonasymptotically features, we find that they have similarities with the TM polarization features of the corresponding 1-D grating, similar to the results in Fig. 2. Regarding the asymptotically features, there exists no direct 1-D analogy. Instead, the authors find by band-structure calculations that these features to some extent can be understood as coupling the in-plane H-field to the corresponding 2-D photonic crystal modes at the Γ-point.

2.1 *Color*

The color of an object is the result of a complex interaction between the light source $S(\lambda)$ incident on the object, the reflectivity of the object $R(\lambda)$, and the observer. In the CIE (Commission Internationale de l´Eclairage) 1931 XYZ-model,[8] colors can be defined on integral form:

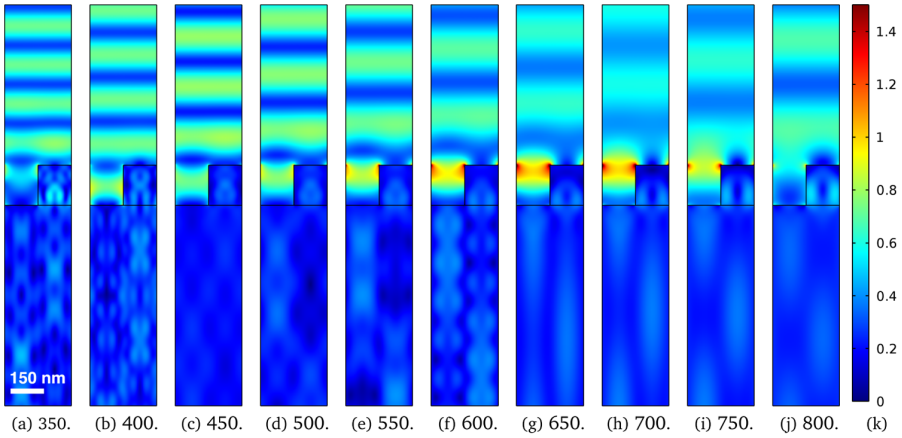

Fig. 2 Finite element method simulations of one-dimensional periodic grating and normal incidence TM electromagnetic wave. Contour plots of the electric field magnitudes with the air region to the left and the grating region to the right. Period 300 nm, width 150 nm, height 180 nm, and refractive index 4. (a–j) Total field magnitudes in millivolts per nanometers for an input power of 1 W. Numbers are wavelengths in nanometers. (k) Scale bar with a maximum of 1.5 (mV/nm).

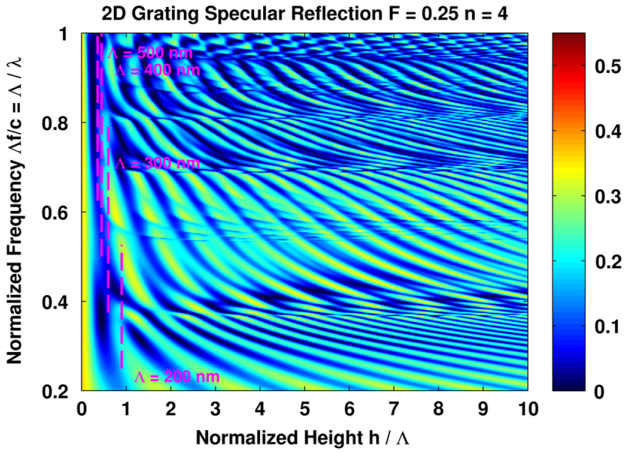

Fig. 3 Specular normal incidence reflectivity of a two-dimensional (2-D) square grating as function of normalized height and frequency simulated by rigorously coupled-wave analysis (RCWA) (350×400 points). Blue color indicates low reflectivity and red color indicates high reflectivity. A contour level of 0.3 corresponds to 30% of reflectivity. Refractive index 4. Dashed lines: 180-nm height.

$$\begin{bmatrix} X \\ Y \\ Z \end{bmatrix} \equiv C^{-1} \int_0^\infty S(\lambda) R(\lambda) \begin{bmatrix} \bar{x}_{\mathrm{obs}}(\lambda) \\ \bar{y}_{\mathrm{obs}}(\lambda) \\ \bar{z}_{\mathrm{obs}}(\lambda) \end{bmatrix} \mathrm{d}\lambda, \tag{3}$$

with normalization $C \equiv \int_0^\infty S(\lambda)\bar{y}_{\mathrm{obs}}(\lambda)\mathrm{d}\lambda$. Furthermore, we may define the chromaticity coordinates, independent of brightness $x \equiv X/(X+Y+Z)$, $y \equiv Y/(X+Y+Z)$. The parameters $(\bar{x}_{\mathrm{obs}}, \bar{y}_{\mathrm{obs}}, \bar{z}_{\mathrm{obs}})$ describe the spectral sensitivity of the observer. Here, we use the 1978 Judd Vos correction[9] of the CIE 1931 2° observer[8] and the ISO/CIE standard illuminant D65.[10] In order to accurately present color values, a conversion between the device-independent CIE-XYZ model and device-dependent outputs on a display (RGB) or paper (CMYK) is needed. Here, we adopt the sRGB conversion for display.[11] The grating scattering properties based on tabulated optical properties of silicon[12] are studied by RCWA,[13] using a commercial solver (GD-Calc, KJ Innovation, Santa Clara, California).

The influence of specular and diffusive reflections on color perception under different light conditions has been discussed for a long time.[14–18] In this letter, we focus on specular color effects. Conventionally, in color analysis, the specular part is often subtracted to give a more accurate description of color. However, in the case where the specular reflection provides a constant distinct output spectrum for a wide range of angles, the manifestation can be a more homogeneous color perception, if the illumination instead contains a diffusive component. The concept is justified by the photographs of Area 4 in Fig. 1.

3 Experimental Results

Reflection measurements are performed for TE/TM (not shown), and unpolarized light, using a xenon lamp (HPX-2000), two rotational stages, and a spectrometer (Jaz, Ocean Optics, Dunedin, Florida). The broad-spectrum white light from the xenon lamp is coupled via a multimode fiber to illuminate the sample at an angle of incidence θ_{in}. The reflected light is collected at an observer angle θ_{obs}, by the end of a multimode fiber and led into the spectrometer. With the definitions in Fig. 4(a), specular reflectivity is given by $\theta_{\mathrm{obs}} = 2\theta_{\mathrm{in}}$. The measurements are performed for $\phi_{\mathrm{in}} = \{0 \text{ deg}, 45 \text{ deg}\}$, which is the maximum disparity for a symmetrical quadratic pattern. The absolute reflectivity is calculated using a reference measurement before and after each measurement.

The most important experimental results are plotted in Fig. 4. In Fig. 4(b), the measured specular reflectivity of the sample with a period of 300 nm can be seen as function of wavelength and angle of incidence for $\phi_{\mathrm{in}} = \{0 \text{ deg}, 45 \text{ deg}\}$. The near-normal incidence measurements

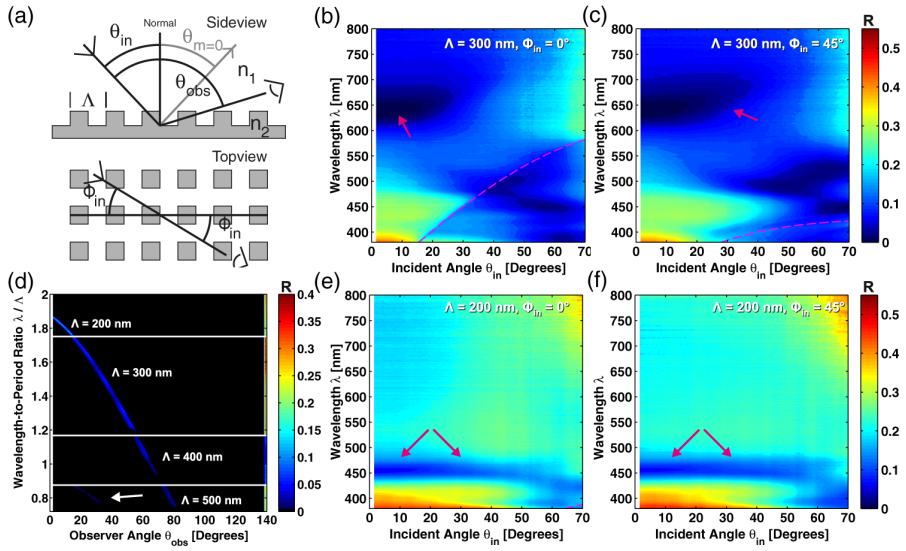

Fig. 4 Reflection measurements. (a) Sketch of measurement setup. (b) and (c) Specular reflectivity for the 300-nm period sample from 0% to 55% as function of incidence angle and wavelength for $\phi_{in} = \{0 \text{ deg}, 45 \text{ deg}\}$. Dashed lines mark Rayleigh line, arrows mark anomaly. (d) Measured reflectivity from 0% to 40% for a constant incidence angle of 70 deg as function of observer angle and normalized wavelength of the four samples. Arrow marks second order. (e) and (f) Specular reflectivity for the 200-nm period sample from 0% to 55% as function of incidence angle and wavelength for $\phi_{in} = \{0 \text{ deg}, 45 \text{ deg}\}$. Dashed line in bottom right corner marks Rayleigh line, arrows mark anomaly. Resolution $\Delta\theta = 0.5$ deg.

show a distinctive minimum at a wavelength of 640 nm, corresponding to a normalized frequency of $\Lambda/\lambda = 0.47$ and a normalized height of $h/\Lambda = 0.58$, which by the simulations displayed in Figs. 2 and 3 are found to indicate a resonance anomaly behavior with strong coupling to a leaky surface wave.[6] The relatively high reflectivity for short wavelengths can be explained as a combination of a rapidly increasing refractive index of silicon for short wavelengths and the absence of anomalies for the particular parameters.[19] Regarding angular dependence, the distinctive line of low reflectivity in Fig. 4(b) can be identified as the "Rayleigh line," meaning that diffraction in the visual spectrum does not occur until 15-deg incident angle. Thereby, the measurements for a period of 300 nm capture the transition from the nondiffractive regime of exclusive specular reflectivity at normal incidence to the diffraction regime for larger incidence angles, also supported by the tendency of low reflectivity for wavelengths shorter than the Rayleigh line due to the appearance of higher reflectivity orders.

In Figs. 4(e)–4(f), the measured specular reflectivity of the sample with a period of 200 nm can be seen as function of wavelength and angle of incidence, performed for $\phi_{in} = \{0 \text{ deg}, 45 \text{ deg}\}$ in Fig. 4(a). A high near-normal incidence reflectivity for short wavelengths below 400 nm is seen together with a sharp feature of low reflectivity around 455 nm. The minimum corresponds to a normalized frequency of 0.44. Assuming that a filling factor of 25% and a refractive index of 4 is reasonable here, we read of Fig. 3 a minimum at 0.44 for a normalized height of 171 nm/200 nm = 0.86. Compared to the other three samples, the high-reflection wavelengths above 455 nm can be understood by the movement to the right in Fig. 3 away from the first air resonance and by the "scaling" of the normalized frequency, where the interval given by the visual spectrum is less broad compared with the 300-nm period. The scaling of the normalized frequency indicates the trade-off for small periods between avoiding diffraction for large incident angles and the normal incidence anomaly density, as the number of anomalies decreases for lower frequencies. Furthermore, it is clear that the anomalies do not shift wavelength for a large angle interval, indicating the coupling to a intrinsic localized surface state, and not a thin-film reflection from a effective medium, where a shift in minimum wavelength for larger incidence angles would have been observed. Regarding diffraction described by Eqs. (1) and (2), this does not occur in reflection mode until 64 deg for 200-nm periodic

structures in the visual spectrum ($\lambda_R = 380$ nm). Therefore, the structural colors originating from 200-nm periodic structures only exhibit minor angular dependence up to 60 deg incidence in all azimuthal directions, as seen in Fig. 4, due to the suppression of diffraction and the substituted strong coupling of light to localized surface states.

Besides measuring the specular reflectivity, one measurement for each sample is conducted as a sanity check, where the incidence angle is held constant at an angle of $\theta_{in} = 70$ deg along the horizontal direction, while the observer angle is varied. The measured TM reflectivity can be seen in Fig. 4(d), confirming that the angle distribution of the reflectivity is due to diffraction described by Eq. (1), supporting that diffraction must be suppressed before coupling to surface states can be utilized for wide angular illumination.

4 Discussion

The calculated sRGB color values of the measurements and corresponding simulations are plotted and displayed as function of incident angle in Figs. 5(a) and 5(b) for the horizontal ($\phi_{in} = 0$ deg) and diagonal directions ($\phi_{in} = 45$ deg). In terms of color, the sample with a period of 300 nm appears blue due to a low reflectivity of red light around the earlier mentioned minimum at 640 nm and high reflectivity around 400 nm. The shift to a brown/orange color at 30 deg incidence seen in Fig. 1(g) is due to the appearance of first-order diffraction cutting off the normal incidence features and the increase in Fresnel reflectivity for larger incidence angles.

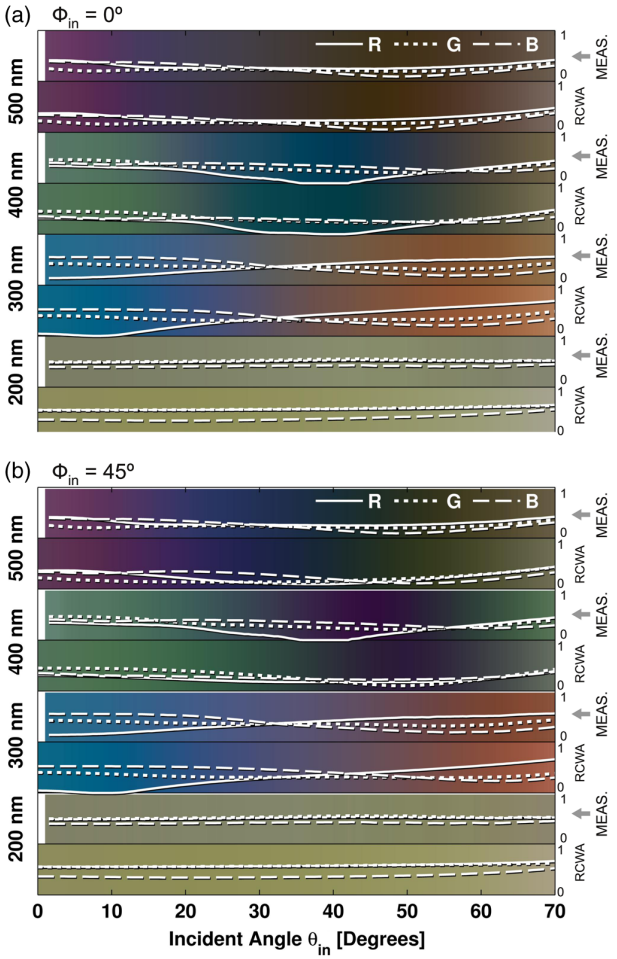

Fig. 5 Measured and RCWA-simulated silicon specular structural sRGB colors, scaled from 0 to 1, of the four samples as function of incident angle. (a) $\phi_{in} = 0$ deg and (b) $\phi_{in} = 45$ deg.

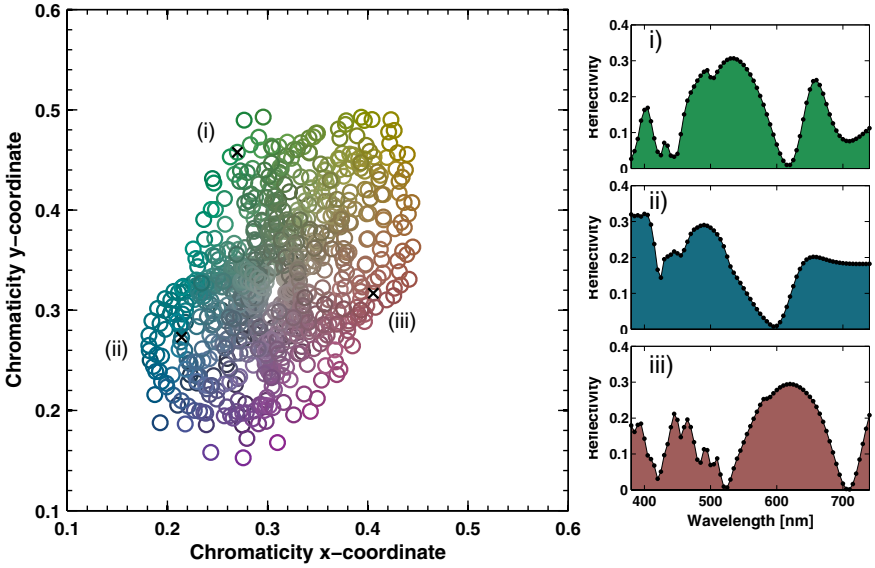

Fig. 6 Simulated silicon normal incidence specular colors by 2-D square gratings. (x, y) CIE chromaticity coordinates of the resulting spectra colored by the corresponding sRGB colors. Inset (i) Example of green color by parameters height 250 nm, period 240 nm, and filling factor 30%. Inset (ii) Example of blue color by parameters height 180 nm, period 210 nm, and filling factor 50%. Inset (iii) Example of red color by parameters height 300 nm, period 240 nm, and filling factor 48%.

The main differences between the horizontal and diagonal reflectivities, leading to shifts in color, can be understood by the shorter projected effective period Λ' seen by the diffracted light for the diagonal direction, ideally $\Lambda/\sqrt{2}$ for an incident angle of 90 deg. In general, the calculated colors in Fig. 5 are found by visual inspection to resemble daylight color accurately.

We may combine the colors portrayed here with the earlier measured diffraction results, by viewing a given grating sample under two incoherent light sources, such that the main specular reflectivity is observed using one source and a diffraction order is observed using the other source, similar to the red color seen in Fig. 1(g). As the diffraction order redirects light in the direction of the observer, the combination yields additive color mixing, in contrast to the specular absorptive colors. The implication, illustrated in Figs. 1(g) and 1(h), is the marvel of color effects taking place when the specular color appearances are accompanied by diffraction effects pointing to the difficulty of unambiguously defining structural colors.

Given the binary geometry used in this letter, what possible colors may be produced? In Fig. 6, an answer is given in the form of plotting the normalized chromaticity coordinates of normal incidence specular reflectivity simulations converted into a color via Eq. (3). Squared 2-D silicon gratings are modeled with parameters of 30- to 300-nm periods, structure heights of 120 to 300 nm, and filling factors between 10% and 90%. The color gamut seen in Fig. 6 indicates the possibilities of the technology. In general, it is found that colors become stronger for shorter periods below 240 nm.

One application for angular independent textures with periods in the 200 nm range is color reference cards used in the graphics industry. Today paper charts with pigments are used, which tend to fade after few years in service. The colors displayed in Fig. 6 can be fabricated in silicon with a high durability. With an appropriate coating applied to protect the nanostructures, the robustness and lifetime of the device may be significantly extended compared to current technology.

5 Conclusion

In conclusion, the structural color appearance of silicon diffraction gratings was examined based on four samples with periods of 500, 400, 300, and 200 nm. The reflectivity and

daylight-colors were measured and compared to simulations based on RCWA and CIE color theory. The method was used to predict the structural color appearance for a wide range of design parameters. Finally, nondiffractive angle-independent colors up to 60 deg of incidence may be provided by suppressing diffraction and instead couple to normal incidence absorption anomalies.

Acknowledgments

We acknowledge DTU colleagues T. Buss for experimental assistance and J. Scheel for photography. This work was supported by the Danish National Advanced Technology Foundation (Contract No.: 007-2010-2) and by the European Commission via the FP7 MMP Integrated project Plast4Future (NMP2-SE-2012-314345). Emil Højlund-Nielsen did the experimental work, the simulations, and prepared the manuscript. Johannes Weirch assisted the RCWA simulations and performed the data fitting, Jesper Nørregaard provided the sample and supervised, Joergen Garnaes did the AFM measurements. Finally, N. Asger Mortensen and Anders Kristensen supervised.

References

1. S. Kinoshita, S. Yoshioka, and J. Miyazaki, "Physics of structural colors," *Rep. Prog. Phys.* **71**(7), 076401 (2008), http://dx.doi.org/10.1088/0034-4885/71/7/076401.
2. L. Cao et al., "Tuning the color of silicon nanostructures," *Nano Lett.* **10**(7), 2649–2654 (2010), http://dx.doi.org/10.1021/nl1013794.
3. P. Vukusic and J. R. Sambles, "Photonic structures in biology," *Nature* **424**, 852–855 (2003), http://dx.doi.org/10.1038/nature01941.
4. D. H. Raguin and G. M. Morris, "Analysis of antireflection-structured surfaces with continuous one-dimensional surface profiles," *Appl. Opt.* **32**(14), 2582–2598 (1993), http://dx.doi.org/10.1364/AO.32.002582.
5. J. E. Stewart and W. S. Gallaway, "Diffraction anomalies in grating spectrophotometers," *Appl. Opt.* **1**(4), 421–430 (1962), http://dx.doi.org/10.1364/AO.1.000421.
6. A. Hessel and A. A. Oliner, "A new theory of woods anomalies on optical gratings," *Appl. Opt.* **4**(10), 1275–1297 (1965), http://dx.doi.org/10.1364/AO.4.001275.
7. V. R. Almeida et al., "Guiding and confining light in void nanostructure," *Opt. Lett.* **29**(11), 1209–1211 (2004), http://dx.doi.org/10.1364/OL.29.001209.
8. T. Smith and J. Guild, "The C.I.E., colorimetric standards and their use," *Trans. Opt. Soc.* **33**(3), 73–134 (1931), http://dx.doi.org/10.1088/1475-4878/33/3/301.
9. J. J. Vos, "Colorimetric and photometric properties of a 2 fundamental observer," *Color Res. Appl.* **3**(3), 125–128 (1978), http://dx.doi.org/10.1002/(ISSN)1520-6378.
10. D. B. Judd et al., "Spectral distribution of typical daylight as a function of correlated color temperature," *J. Opt. Soc. Am.* **54**(8), 1031–1040 (1964), http://dx.doi.org/10.1364/JOSA.54.001031.
11. M. Stokes et al., "A standard default color space for the Internet—sRGB http://www.w3.org/Graphics/Color/sRGB.html (checked 2013-04-20)" (1995).
12. M. A. Green and M. J. Keevers, "Optical properties of intrinsic silicon at 300 K," *Prog. Photovoltaics Res. Appl.* **3**(3), 189–192 (1995), http://dx.doi.org/10.1002/(ISSN)1099-159X.
13. M. N. Nevière and M. N. E. Popov, *Light Propagation in Periodic Media: Differential Theory and Design*, Optical Engineering Series, Marcel Dekker, Inc., New York (2003).
14. H.-C. Lee, "Method for computing the scene-illuminant chromaticity from specular highlights," *J. Opt. Soc. Am. A* **3**(10), 1694–1699 (1986), http://dx.doi.org/10.1364/JOSAA.3.001694.
15. R. Shapley, "Neural mechanisms for color perception in the primary visual cortex," *Curr. Opin. Neurobiol.* **12**(4), 426–432 (2002), http://dx.doi.org/10.1016/S0959-4388(02)00349-5.
16. J. N. Yang and L. T. Maloney, "Illuminant cues in surface color perception: tests of three candidate cues," *Vision Res.* **41**(20), 2581–2600 (2001), http://dx.doi.org/10.1016/S0042-6989(01)00143-2.

17. S. K. Nayar, X.-S. Fang, and T. Boult, "Separation of reflection components using color and polarization," *Int. J. Comput. Vision* **21**(3), 163–186 (1997), http://dx.doi.org/10.1023/A:1007937815113.
18. S. Tominaga, "Surface identification using the dichromatic reflection model," *IEEE Trans. Pattern Anal. Mach. Intell.* **13**(7), 658–670 (1991), http://dx.doi.org/10.1109/34.85656.
19. G. Bao, D. C. Dobson, and K. Ramdani, "A constraint on the maximum reflectance of rapidly oscillating dielectric gratings," *SIAM J. Control Optim.* **40**(6), 1858–1866 (2002), http://dx.doi.org/10.1137/S036301290037435X.

Emil Højlund-Nielsen is a PhD student within structural colors at the Technical University of Denmark, where he also received his MSc degree within physics and nanotechnology in 2012. He develops nanoscale designs for structural coloration. He is experienced within teaching, cleanroom fabrication, numerical modeling, and optical characterization of micro- and nanosystems.

Johannes Weirich is a staff scientist at DFM A/S. He received his PhD degree within optics in liquid crystal photonic bandgap fiber devices from Technical University of Denmark in 2010. He does development and application of numerical and experimental optical methods. More specifically, he has experience in optics (fiber optics, lasers, optical micro- and nanostructures), modeling and numerical methods (finite element, finite difference), and design and implementation of simulation tools (based on Python, C/C++, and Fortran).

Jesper Nørregaard is R&D manager at NIL Technology ApS. He has many years of experience with high-tech startups and large experience with the development of business models and maturation of products. He received his PhD in physics from University of Copenhagen in 1989 and has been working mainly in private companies as a manager of R&D or manufacturing of semiconductors or photonic devices. He also serves as a board member in smaller companies and holds several patents.

Joergen Garnaes is staff scientist at DFM A/S. He received his PhD in 1991 from Laboratory of Applied Physics, Technical University of Denmark. He does research within surface metrology and scanning probe microscopy investigations of industrial and applied surfaces. He is coauthor of more than 50 publications in international refereed scientific journals, two of which have been in *Nature* and one in *Science*.

N. Asger Mortensen is professor at the Technical University of Denmark (DTU) from which he also received the MSc, PhD, and Dr. Techn. degrees in 1998, 2001, and 2006, respectively. His research interest and experience are centered on theoretical and computational physics, including condensed matter theory, photonics, optofluidics, plasmonics, and metamaterials. He is the author of more than 160 journal papers and has written three book chapters.

Anders Kristensen is professor in miniaturized sensor and actuator technology at the Technical University of Denmark. He received his MSc and PhD degrees in physics from the University of Copenhagen in 1991 and 1984, respectively. He is the author of more than 120 peer-reviewed journal papers and has written three book chapters. His current research interests include optofluidics, nanofluidics, nanoimprint lithography, and structural colors. He is the coordinator of several international research projects.

A.4 Clausen et al. 2014

J.S. Clausen, E. Højlund-Nielsen, A.B. Christiansen, S. Yazdi, M. Grajower, H. Taha, U. Levy, A. Kristensen, N.A. Mortensen. (2014). "Plasmonic metasurfaces for coloration of plastic consumer products" *Nano Letters*, 14(8), 4499–4504. doi: 10.1021/nl5014986.

NANO LETTERS

Letter

pubs.acs.org/NanoLett

Plasmonic Metasurfaces for Coloration of Plastic Consumer Products

Jeppe S. Clausen,[†] Emil Højlund-Nielsen,[‡] Alexander B. Christiansen,[‡] Sadegh Yazdi,[§] Meir Grajower,[∥] Hesham Taha,[⊥] Uriel Levy,[∥] Anders Kristensen,*[,‡] and N. Asger Mortensen*[,†]

[†]Department of Photonics Engineering, [‡]Department of Micro and Nanotechnology, and [§]Center for Electron Nanoscopy, Technical University of Denmark, DK-2800 Kongens Lyngby, Denmark

[∥]Department of Applied Physics, The Benin School of Engineering and Computer Science, The Center for Nanoscience and Nanotechnology, The Hebrew University of Jerusalem, Jerusalem 91904, Israel

[⊥]Nanonics Imaging Ltd., Hartum 19, Har Hotzvim, Jerusalem 97775, Israel

Supporting Information

ABSTRACT: We present reflective plasmonic colors based on the concept of localized surface plasmon resonances (LSPR) for plastic consumer products. In particular, we bridge the widely existing technological gap between clean-room fabricated plasmonic metasurfaces and the practical call for large-area structurally colored plastic surfaces robust to daily life handling. We utilize the hybridization between LSPR modes in aluminum nanodisks and nanoholes to design and fabricate bright angle-insensitive colors that may be tuned across the entire visible spectrum.

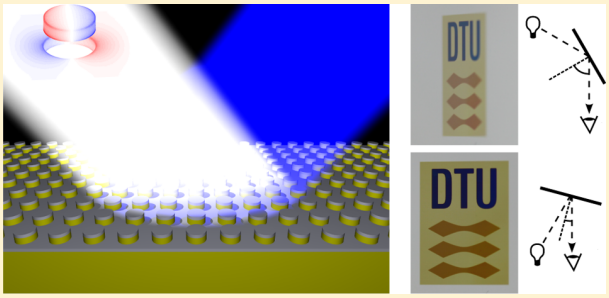

KEYWORDS: *Plasmonics, structural color, hybridization, nanofabrication*

Pigment-based coloring of polymers is used in the fabrication of almost any type of plastic-based consumer product, either as base color in the bulk polymer or in surface-decoration inks. The mixing of many colorants in a single product is both costly and limits the possibilities for recycling as separation of the different colorants is impossible. Structural colors offer an attractive approach to reduce the number of needed materials in a given product and it provides new perspectives for recycling and sustainability.

Various strategies may be taken toward structural colors. Inspired by nature[1,2] pure dielectric structures based on photonic crystals in one or more dimensions have been demonstrated[3,4] and recently the use of ultrathin high-loss dielectrics on top of metal have led to bright colors.[5] The works on plasmonic colors have widely emphasized filters working in transmission[6−9] while only more recently plasmonic cavity resonances and LSPR concepts have been used for filters working in reflection.[10−15] The resonant behavior of the plasmonic systems often leads to large field enhancements that are advantageous in other applications such as surface-enhanced Raman spectroscopy.[16−20]

The structural color effects must possess at least three important properties to become relevant for use in consumer products. First, the color effect should be insensitive to varying viewing angles. Furthermore, it should be robust for everyday use. Finally, it should be up-scalable and economically affordable. We demonstrate a plasmonic metasurface that possesses all these qualities. Recently plasmonic resonators consisting of silver and gold have been used for color printing with resolution beyond the diffraction limit.[10,15] We use insight from hybridization theory[21] to build upon the work of Kumar[10] toward coloration of volume-produced plastic components, addressing the three criteria mentioned above: angle independence, wear resistance, and up-scalability.

Thin metal nanodisks can be tuned in size to modulate the optical response through the visible and near-infrared spectral range.[22] In our work, the colors are based on metal disks on top of dielectric pillars and hovering above a holey metal film, see Figure 1a−c. Rather than employing the common choice of silver or gold, we explore aluminum, which is a widely employed material in industrial processes while so far mainly being conceptually studied as a new plasmonic material.[23−27] Silver and gold are commonly preferred over aluminum for plasmonic applications due to lower ohmic losses. However, we find an advantage of the specific interband absorption properties of aluminum, which gives a pronounced difference in the dispersion of the surface plasmon polaritons (SPPs) supported by the metal−dielectric interfaces of the continuous (holey) film. As demonstrated later, the excitation of SPPs constitutes the main limitation on the angle independence of the observed color and here SPPs supported by aluminum have an advantage over SPPs on silver surfaces due to their k-space existence closer to the "light line" in the frequency range of the visible spectrum. In addition to this, gold has the disadvantage of having an interband transition threshold centered in the

Received: April 23, 2014
Revised: June 23, 2014

ACS Publications © XXXX American Chemical Society

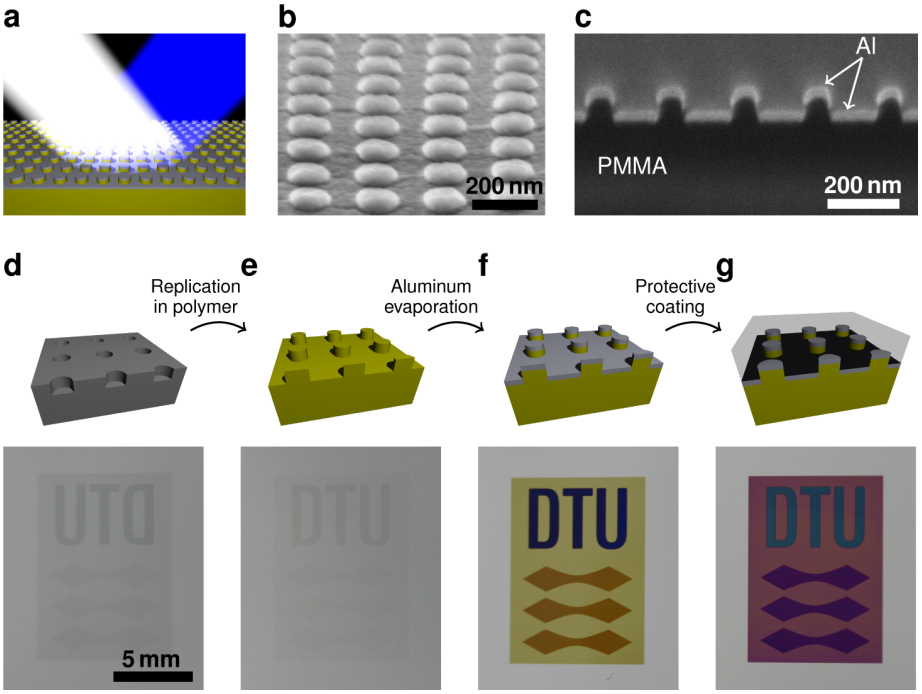

Figure 1. Basic concept of fabrication and working mechanism. (a) The reflected light is modified due to absorption resonances in the plasmonic nanostructure leading to colored reflections upon white-light illumination. The reflected color can be varied by tuning the surface geometry. (b) A SEM image of fabricated disks elevated above the holey plane seen from 15° above the horizon. (c) Cross-sectional SEM image obtained using focused ion-beam for sample preparation. (d) A master mold comprising nanohole arrays is used for the fabrication of polymer pillar arrays using hot embossing or injection molding. The photography shows a macroscopic sample with three different hole sizes leading to three different colors in the final sample. (e) A polymer pillar array replication of the master mold. (f) Aluminum is evaporated on top, creating the disk-hole structure thereby revealing colors due to the underlying polymer topography. (g) The structure is coated with a transparent material to protect from greasy contamination, fingerprints, and scratches. The resonance redshift introduced by the coating leads to clearly altered colors.

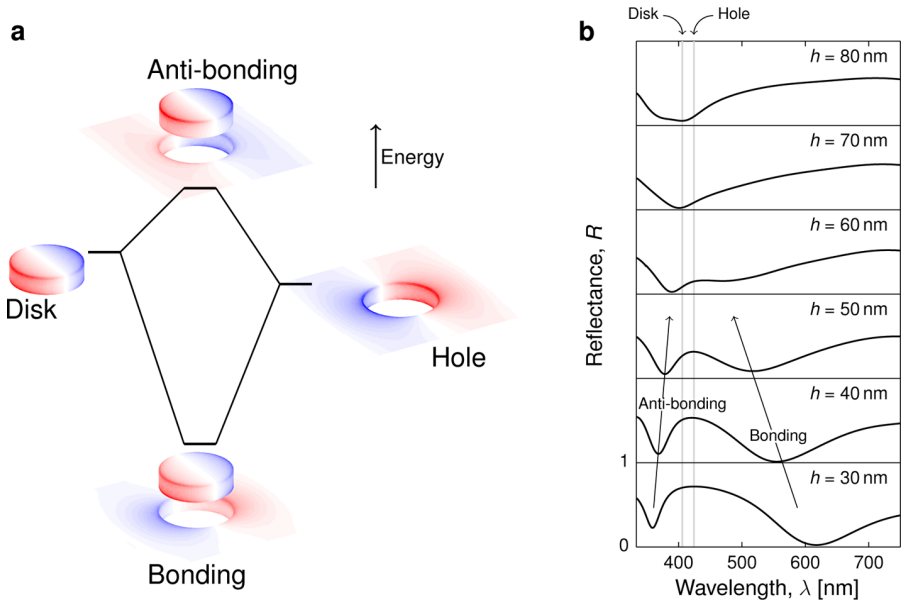

Figure 2. Plasmon hybridization due to disk-hole coupling. (a) Energy diagram illustrating the hybridization of the coupled plasmonic modes of the disks and holes of the structure into a low energy mode (bonding) and a high energy mode (antibonding). The simulated charge distributions of the pure disk and hole arrays show the dipolar nature of their resonances. For the full structure, the symmetric and antisymmetric coupling leads to an energy splitting. The shown structure is for D = 80 nm, Λ = 200 nm, h = 50 nm, and t = 20 nm embedded in material of refractive index of 1.5. It shows the symmetric and antisymmetric coupling between the disks and holes. (b) Reflectance spectra for same parameters as panel a but for varying pillar height, h. The two modes are seen as dips in the spectra. The coupling and thereby the energy splitting decreases with increasing pillar height leading to a shift of the resonances toward the natural resonances of the disk and hole arrays.

dx.doi.org/10.1021/nl5014986 | *Nano Lett.* XXXX, XXX, XXX−XXX

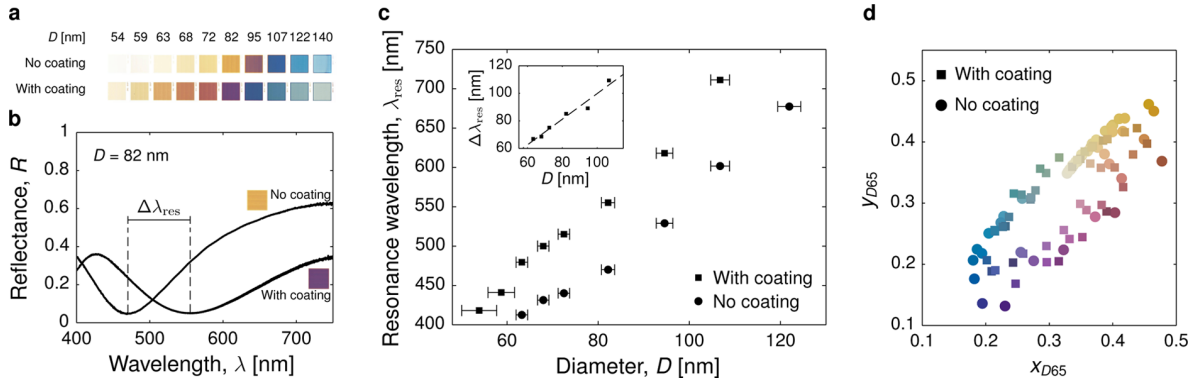

Figure 3. Diameter-dependent resonance and colors. (a) Images in bright-field microscopes of 0.8 × 0.8 mm^2 squares with period Λ = 200 nm and varying diameter. The coating-induced redshift is evident. (b) Reflectance spectra of structure with D = 82 ± 2 nm with and without coating indicating the change in resonance wavelength $\Delta\lambda_{res}$ due to the coating. (c) Resonance position as a function of disk diameter for Λ = 200 nm. The shift in resonance due to the coating is seen to be approximately linear with diameter. (d) CIE 1931 chromaticity coordinates of the fabricated samples for both the coated and the uncoated case (spectra in Supporting Information Figure S2). The color of each spot indicates the color of the corresponding sample.

visible spectrum whereas aluminum only facilitates interband transitions in a narrow wavelength range outside the visible spectrum.[28] For large-volume use of plasmonic metasurfaces in, for example, plastic consumables, the abundance and cost of aluminum makes it attractive. The integration in mass-fabrication systems is also eased significantly compared to, for example, silver where the need for an adhesion layer (such as titanium or chromium) and a capping layer (such as gold) to protect against sulphidation, complicates the metal deposition.

The fabrication scheme is presented in Figure 1d–g. A master mold is fabricated in silicon using electron-beam lithography (EBL) and dry etching. A fast single spot writing technique was employed,[29,30] which allows writing speeds higher than 1 cm^2/hour in the production of the silicon masters. This leads to a wider size distribution of the nanostructures than for conventional EBL resulting in inhomogeneous broadening of the resonances. This is however acceptable and compensated by the very large decrease in writing time. The finalized master consists of periodic hole arrays with period Λ, hole diameter D, and hole depth h. The master is a negative of the desired polymer surface, a periodic pillar array, which is fabricated in a hot embossing step. After replication, the desired pattern is practically invisible as the polymer–air index contrast is too low to significantly alter the surface reflectance of the nanostructured polymer surface. However, bright and angle-independent colors emerge when a thin aluminum film of thickness t is deposited on top of the textured polymer surface, see Figure 1f. The metal deposition must be directional in order to facilitate the creation of isolated metal disks. For situations with very large sample size and small evaporation source, this may lead to undesired side-wall deposition thereby defining the maximum sample size. When using roll-to-roll systems, this issue may be avoided due to the continuous deposition of metal.

Finally, a protective coating is deposited on top with a thickness significantly larger than the coherence length of broadband white light in order to avoid Fabry–Pérot interference affecting the color experience. The coating causes an increase in the effective refractive index surrounding the disk-hole nanostructure, which leads to a redshift of the resonances in the system and a corresponding color change as seen in the last step of Figure 1. The top coating is necessary to protect the structure from mechanical damage, fingerprints, greasy residue, and so forth. In this work, a UV-curable organic–inorganic hybrid material (Ormocomp, Micro resist technology GmbH) with good scratch resistance[31] has been used, but many different types of coatings are already used in large scale production to protect evaporated metal films of various kinds.

The colors of the structure are due to resonant absorption in the aluminum nanostructures. Both the disks and holes possess dipolar resonances on their own, which leads to increased absorption at specific wavelengths. When brought very close together the two modes hybridize into two new modes, a "bonding" mode that is characterized by a lower resonance frequency (longer wavelength) and an "antibonding" mode with higher resonance frequency.[21] Simulated surface charge distributions of the relevant modes are shown in Figure 2a for the specific structure of period Λ = 200 nm, diameter D = 80 nm, aluminum thickness t = 20 nm, and pillar height h = 50 nm. The low-energy mode is characterized by the charge oscillations in the disk and the hole being out-of-phase whereas for the high energy mode the charge oscillations are in phase. The effect on the reflectance spectrum is illustrated in Figure 2b where each of the two hybrid modes appear as significant dips in the reflectance spectra. It is seen how the energy splitting decreases, when the pillar height, h, increases thereby decreasing the coupling between the resonators. It is also seen that the strength of the "bonding" mode is highly dependent on low pillars (large coupling) and above h = 70 nm the hybridization is not seen in the reflectance spectra. For even higher pillars,[32] the behavior of the system moves toward a Fabry–Pérot-like regime where the disk array and the hole array each acts as separate mirrors with resonant reflection coefficients. It is found that when using aluminum as the plasmonic material a strong resonance of the hybrid "bonding" mode is key to the creation of tunable colors. This is seen from simulations (Supporting Information, Figure S1), which demonstrate how it is possible with strong coupling (low pillars) to obtain resonances across the entire visible spectrum by tuning the pillar diameter, while for vague coupling (high pillars) no such tuning is possible. Because we mainly utilize the "bonding" mode resonance we will in the following just denote the wavelength of this resonance λ_{res}.

dx.doi.org/10.1021/nl5014986 | Nano Lett. XXXX, XXX, XXX–XXX

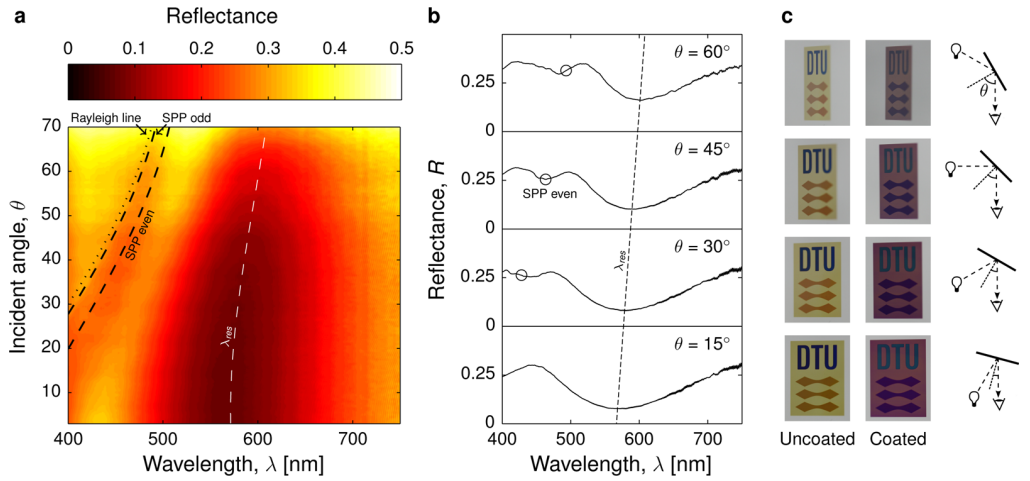

Figure 4. Angle dependence of reflected spectrum. (a) Measured angle-resolved spectra of coated sample with Λ = 200 nm and D = 86 ± 2 nm. The white dashed line indicates the reflectance minimum and the black dashed lines indicate the theoretical excitation of SPPs (odd and even modes) in a 20 nm Al film embedded in material of refractive index 1.5. The dotted line indicates the appearance of new diffraction orders (Rayleigh wavelength). The resonance is seen to shift very little even at very high angles. (b) Single spectra at four different angles of the same sample as in panel a. (c) Pictures of macroscopic patterns viewed at four different angles. The colors are seen to be almost identical even for very large angles. The gray background is the unstructured surface of the samples.

While securing the existence of the important hybrid "bonding" mode by fabricating very low pillars one must keep in mind that it is of great importance that the disks are separated from the lower lying film to avoid short circuiting of the capacitively coupled disk and hole planes. By preparing a cross section sample, using focused ion beam (FIB), we can confirm that in majority of cases the disk and the lower lying film are separated, see Figure 1c.

In the fabrication of the polymer pillars a certain rounding at the pillar end-face should be expected, compared to the perfect cylindrical shape used in simulations. The rounding is seen in Figure 1c. This effectively reduces the vertical gap between the disk and hole, which is why it is necessary to fabricate the pillars slightly higher than predicted by simulations for achieving comparable coupling. Fabricated pillars were h = 56 ± 4 nm high, measured by atomic force microscope, and the aluminum thickness was t = 20 nm, measured by quartz crystal microbalance during deposition.

The fixed pillar height and metal thickness leave the diameter and period as design parameters. In this work, diameters between 40−160 nm and periods ranging from 160 to 240 nm have been studied experimentally. Figure 3a shows color photos of Λ = 200 nm samples with and without the presence of a protective coating. Colors across the entire visible spectrum are produced at will by varying the disk diameter at fixed period. The measured reflectance spectra of disks with diameter 82 ± 2 nm are shown as example in Figure 3b. The coating induces a redshift $\Delta\lambda_{res}$ of the resonance due to increase in effective refractive index around the nanostructure. One should notice the high off-resonant reflectance in contrast to the low reflectance at resonance, which leads to very bright colors. For both the coated and uncoated case, the resonance position increases almost linearly with diameter. Specifically for the coated case, the resonance may be tuned on the wavelength interval 400−700 nm by tuning the diameter on the interval 50−110 nm. The coating-induced redshift is also found to increase linearly with diameter. Reflectance spectra for the other periods and diameters are provided in the Supporting Information (Figure S2). The effect of the period on the resonance position is less pronounced as it only influences the mutual coupling of neighboring resonators. The nearest-neighbor coupling does however influence how much a change in diameter alters the resonance position (the slope of Figure 3c). For a coated sample with Λ = 160 nm, a 1 nm increase in diameter leads to an approximate redshift of 7 nm whereas for Λ = 240 nm it only leads to an approximate redshift of 4 nm (see Supporting Information Figure S3). Although the period does not influence the resonance position significantly, it plays an important role in relation to the angular dependence.

The range of colors that may be produced using the proposed method is illustrated in Figure 3d where all experimentally measured spectra (see Supporting Information Figure S2) have been converted to CIE1931 chromaticity coordinates, thereby illustrating the color gamut of the method. It is noteworthy that there are points all around the achromatic point, illustrating the large degree of color tuning ability. There are however some colors that are difficult to produce when the effect is based on a spectral dip originating from resonant absorption. Very chromatic red and green are examples of such colors.

The angle independence of the reflective colors was investigated on larger samples (4 × 6 mm^2). The specular reflectance was measured with unpolarized light for incident angles at 3−70°, see Figure 4. Data are shown for a coated sample with Λ = 200 nm and D = 86 ± 2 nm. In the surface plot of Figure 4a, the broad dip in the reflectance is observed around a vacuum wavelength of 580 nm and is slightly red shifted by approximately 20 nm for increasing angle of incidence. This is the diameter-dependent plasmonic absorption resonance described previously. Individual reflectance spectra for four different angles are shown in Figure 4b, and the photographs in Figure 4c illustrate the angle independence of the color appearance. The changes of the CIE1931 chromaticity coordinates due to changing angles have been calculated based on the angle-resolved spectra and are presented in the Supporting Information (Figure S4). As seen in panels a and b, the strength of the resonance dip decreases with increasing angle of incidence. This is due to a decreasing component of

dx.doi.org/10.1021/nl5014986 | Nano Lett. XXXX, XXX, XXX−XXX

the electric field of the TM mode parallel to the dipole axis under consideration. A weak angle-dependent feature is observed at vacuum wavelength below 500 nm, which is caused by grating-assisted excitation of SPPs at the metal−dielectric interfaces. The dashed black lines indicate the calculated dispersion of the odd and even modes for a 20 nm aluminum film embedded in a material of refractive index 1.5. The Rayleigh line, where the first diffraction order appears, is plotted as a dotted line. Of the three anomalies, the even (high loss) SPP mode lies in the center of the angle-dependent dip, and in Figure 4b the circles indicate the position of this mode. It corresponds well with the dips in the measured reflectance spectra and the feature is attributed to this mode. The positions of the SPP anomalies depend on the grating-induced change in momentum parallel to the surface and are therefore highly dependent on the structure period. A longer grating period, Λ, will result in the anomalies appearing at lower angles, implying a higher degree of angle dependence, whereas a shorter period will lead to less impact on the spectra (see Figure S5 in Supporting Information). This implies a trade-off between obtaining low angular dependence and fabrication limitations due to dense structures with small grating period. Properties of the SPP modes have been investigated using near-field scanning optical microscopy (NSOM). The data are presented in the Supporting Information (Figure S6).

While the position of the Rayleigh line only depends on the grating period and the refractive index of the materials surrounding the metal, the dispersion relation for the SPPs also has a strong dependence on the dielectric constant of the metal. Hence, the position of the angle-dependent SPP modes (relative to the localized mode) makes the feasibility of angle-independent plasmonic structural colors strongly material dependent. As an example, we compare aluminum and silver in the Supporting Information (Figure S5). For aluminum, the SPP modes lie very close to the Rayleigh line and may therefore be moved out of the visible spectrum, even for high incident angles by using small periods. On the other hand, for silver films SPPs are excited at normal incidence, even for very short periods whereby the SPP modes spectrally intersect with the localized modes. This leads to phenomena such as avoided crossing between the two intersecting modes resulting in significant angle-dependent behavior of the color-producing mode. Because this is a property originating from the electronic structure of the chosen metal, this promotes aluminum over silver for use in this application.

Because of the subwavelength periodic nature of the structure, the color effect is only seen in the specular reflection. This limits the applicability under certain lighting conditions. For diffuse lighting conditions, an observer will experience uniform color, while illumination by very directional light sources will lead to a more varying color experience. To overcome this problem, one may introduce scattering in the protective film either by particles, surface roughness or by using semicrystalline (translucent) polymers as coating material. This will allow for diffuse reflectance from the surface similar to that of inks.

In conclusion, we demonstrate angle-insensitive scratch-resistant structural colors, where aluminum is used as a cheap and abundant plasmonic material. We utilize a hybrid disk-hole plasmonic mode, which provides angle-independent resonances tunable across the entire visible spectrum. Expensive nano-lithography should only be carried out once due to the subsequent replication-based fabrication and the structure geometry allows for a fast EBL technique to define macroscopic wafer-sized patterns. The functional structures are covered by a protective dielectric coating, causing a redshift of the plasmon resonance. The method holds potential for large scale implementation of structural colors in plastic products for daily use.

■ ASSOCIATED CONTENT

Supporting Information

Details about fabrication process, optical characterization, and simulations as well as supplementary figures (Figures S1−S6). This material is available free of charge via the Internet at http://pubs.acs.org.

■ AUTHOR INFORMATION

Corresponding Authors

*E-mail: (A.K.) anders.kristensen@nanotech.dtu.dk.
*E-mail: (N.A.M.) asger@mailaps.org.

Notes

The authors declare no competing financial interest.

■ ACKNOWLEDGMENTS

The authors thank Cameron Smith and Christoph Vannahme for advice on microscope measurements and Thomas Christensen for fruitful discussions on the data interpretation. The work was supported by the Danish National Advanced Technology Foundation (Contract No.: 007-2010-2) via the NanoPlast project and by the European Commission via the FP7MMP Integrated project PLAST4FUTURE (NMP2-SE-2012-314345). The work was also supported by the Danish Agency for Science, Technology and Innovation (International Network Programme, Israel-Danish international collaboration, Framework Grant 1370-00124A).

■ REFERENCES

(1) Vukusic, P.; Sambles, J. R. *Nature* **2003**, *424*, 852−855.
(2) Kinoshita, S.; Yoshioka, S.; Miyazaki, J. *Rep. Prog. Phys.* **2008**, *71*, 076401.
(3) Saito, A.; Miyamura, Y.; Nakajima, M.; Ishikawa, Y.; Sogo, K.; Kuwahara, Y.; Hirai, Y. *J. Vac. Sci. Technol. B* **2006**, *24*, 3248−3251.
(4) Chung, K.; Yu, S.; Heo, C.-J.; Shim, J. W.; Yang, S.-M.; Han, M. G.; Lee, H.-S.; Jin, Y.; Lee, S. Y.; Park, N.; Shin, J. H. *Adv. Mater.* **2012**, *24*, 2375−2379.
(5) Kats, M. A.; Blanchard, R.; Genevet, P.; Capasso, F. *Nat. Mater.* **2013**, *12*, 20−24.
(6) Ebbesen, T. W.; Lezec, H. J.; Ghaemi, H. F.; Thio, T.; Wolff, P. A. *Nature* **1998**, *391*, 667−669.
(7) Lee, H.-S.; Yoon, Y.-T.; shin Lee, S.; Kim, S.-H.; Lee, K.-D. *Opt. Express* **2007**, *15*, 15457−15463.
(8) Xu, T.; Wu, Y.-K.; Luo, X.; Guo, L. J. *Nat. Commun.* **2010**, *1*, 59.
(9) Inoue, D.; Miura, A.; Nomura, T.; Fujikawa, H.; Sato, K.; Ikeda, N.; Tsuya, D.; Sugimoto, Y.; Koide, Y. *Appl. Phys. Lett.* **2011**, *98*, 093113.
(10) Kumar, K.; Duan, H.; Hegde, R. S.; Koh, S. C. W.; Wei, J. N.; Yang, J. K. W. *Nat. Nanotechnol.* **2012**, *7*, 557−561.
(11) Lochbihler, H. *Opt. Lett.* **2013**, *38*, 1398−1400.
(12) Wu, Y.-K. R.; Hollowell, A. E.; Zhang, C.; Guo, L. J. *Sci. Rep.* **2013**, *3*, 1194.
(13) Si, G.; Zhao, Y.; Lv, J.; Lu, M.; Wang, F.; Liu, H.; Xiang, N.; Huang, T. J.; Danner, A. J.; Teng, J.; Liu, Y. J. *Nanoscale* **2013**, *5*, 6243−6248.
(14) Yan, M.; Dai, J.; Qiu, M. *J. Opt.* **2014**, *16*, 025002.
(15) Roberts, A. S.; Pors, A.; Albrektsen, O.; Bozhevolnyi, S. I. *Nano Lett.* **2014**, *14*, 783−787.

(16) Chu, Y.; Banaee, M. G.; Crozier, K. B. *ACS Nano* **2010**, *4*, 2804−2810.
(17) Caldwell, J. D.; Glembocki, O.; Bezares, F. J.; Bassim, N. D.; Rendell, R. W.; Feygelson, M.; Ukaegbu, M.; Kasica, R.; Shirey, L.; Hosten, C.; Al, C. E. T. *ACS Nano* **2011**, *5*, 4046−4055.
(18) Li, W.; Hu, J.; Chou, S. *Opt. Express* **2011**, *19*, 21098−21108.
(19) Li, W.; Ding, F.; Hu, J.; Chou, S. *Opt. Express* **2011**, *19*, 863−870.
(20) Cheng, C.-W.; Abbas, M. N.; Chiu, C.-W.; Lai, K.-T.; Shih, M.-H.; Chang, Y.-C. *Opt. Express* **2012**, *20*, 10376−10381.
(21) Prodan, E.; Radloff, C.; Halas, N.; Nordlander, P. *Science* **2003**, *302*, 419−422.
(22) Manjavacas, A.; García de Abajo, F. J. *Nat. Commun.* **2014**, *5*, 3548.
(23) Chen, Q.; Cumming, D. R. S. *Opt. Express* **2010**, *18*, 14056−14062.
(24) Langhammer, C.; Schwind, M.; Kasemo, B.; Zorić, I. *Nano Lett.* **2008**, *8*, 1461−1471.
(25) Chan, G. H.; Zhao, J.; Schatz, G. C.; Van Duyne, R. P. *J. Phys. Chem. C* **2008**, *112*, 13958−13963.
(26) Knight, M. W.; Liu, L.; Wang, Y.; Brown, L.; Mukherjee, S.; King, N. S.; Everitt, H. O.; Nordlander, P.; Halas, N. J. *Nano Lett.* **2012**, *12*, 6000−6004.
(27) Knight, M. W.; King, N. S.; Liu, L.; Everitt, H. O.; Nordlander, P.; Halas, N. J. *ACS Nano* **2014**, *8*, 834−840.
(28) Zorić, I.; Zäch, M.; Kasemo, B.; Langhammer, C. *ACS Nano* **2011**, *5*, 2535−2546.
(29) Gadegaard, N.; Thoms, S.; Macintyre, D. S.; Mcghee, K.; Gallagher, J.; Casey, B.; Wilkinson, C. D. W. *Microelectron. Eng.* **2003**, *68*, 162−168.
(30) Højlund-Nielsen, E.; Greibe, T.; Mortensen, N. A.; Kristensen, A. *Microelectron. Eng.* **2014**, *121*, 104−107.
(31) Sanchez, C.; Julin, B.; Belleville, P.; Popall, M. *J. Mater. Chem.* **2005**, *15*, 3559−3592.
(32) Lochbihler, H.; Ye, Y. *Opt. Lett.* **2013**, *38*, 1028−30.

A.5 Højlund-Nielsen et al. 2015

E. Højlund-Nielsen, X. Zhu, M.S. Carstensen, M.K. Sørensen, C. Vannahme, N.A. Mortensen, A. Kristensen (2015). "Polarization-dependent aluminum metasurface operating at 450 nm", *Optics Express*, 23(22), 28829. doi: 10.1364/OE.23.028829.

Polarization-dependent aluminum metasurface operating at 450 nm

Emil Højlund-Nielsen,[1] Xiaolong Zhu,[1] Marcus S. Carstensen,[1] Michael K. Sørensen,[1] Christoph Vannahme,[1] N. Asger Mortensen, and [2] Anders Kristensen[1,*]

[1]*Technical University of Denmark, DTU Nanotech, Ørsteds Plads, DK-2800 Kgs. Lyngby, Denmark*

[2]*Technical University of Denmark, DTU Fotonik, Ørsteds Plads, DK-2800 Kgs. Lyngby, Denmark*

anders.kristensen@nanotech.dtu.dk

Abstract: We report on a polarization-dependent plasmonic aluminum-based high-density metasurface operating at blue wavelengths. The fabricated sub-wavelength structures, tailored in size and geometry, possess strong, localized, plasmonic resonances able to control linear polarization. Best performance is achieved by rotating an elongated rectangular structure of length 180 nm and width 110 nm inside a square lattice of period 250 nm. In the case of 45 degrees rotation of the structure with respect to the lattice, the normal-incidence reflectance drops around the resonance wavelength of 457 nm from about 60 percent to below 2 percent.

© 2015 Optical Society of America

OCIS codes: (130.5440) Polarization-selective devices; (050.6624) Subwavelength structures; (220.0220) Optical design and fabrication; (240.6680) Surface plasmons.

References and links

1. X. M. Goh, Y. Zheng, S. J. Tan, L. Zhang, K. Kumar, C.-W. Qiu, and J. K. W. Yang, "Three-dimensional plasmonic stereoscopic prints in full colour," Nat. Commun. **5**, 5361 (2014).
2. E. Petryayeva and U. J. Krull, "Localized surface plasmon resonance: nanostructures, bioassays and biosensing - a review," Anal. Chim. Acta **706**, 8–24 (2011).
3. R. Gans, "Über die Form ultramikroskopischer Goldteilchen," Ann. Phys. **342**, 881–900 (1912).
4. G. Papavassiliou, "Optical properties of small inorganic and organic metal particles," Prog. Solid State Chem. **12**, 185–271 (1979).
5. S. Link and M. A. El-Sayed, "Shape and size dependence of radiative, non-radiative and photothermal properties of gold nanocrystals," Int. Rev. Phys. Chem. **19**, 409–453 (2000).
6. F.-J. Haug, T. Soderstrom, O. Cubero, V. Terrazzoni-Daudrix, and C. Ballif, "Plasmonic absorption in textured silver back reflectors of thin film solar cells," J. Appl. Phys. **104**, 064509 (2008).
7. F. Le, D. W. Brandl, Y. A. Urzhumov, H. Wang, J. Kundu, N. J. Halas, J. Aizpurua, and P. Nordlander, "Metallic nanoparticle arrays: a common substrate for both surface-enhanced Raman scattering and surface-enhanced infrared absorption," ACS Nano **2**, 707–718 (2008).
8. R. Adato, A. A. Yanik, J. J. Amsden, D. L. Kaplan, F. G. Omenetto, M. K. Hong, S. Erramilli, and H. Altug, "Ultra-sensitive vibrational spectroscopy of protein monolayers with plasmonic nanoantenna arrays," Proc. Natl. Acad. Sci. U. S. A. **106**, 19227–19232 (2009).
9. X. Zhu, S. Xiao, L. Shi, X. Liu, J. Zi, O. Hansen, and N. A. Mortensen, "A stretch-tunable plasmonic structure with a polarization-dependent response," Opt. Express **20**, 5237 (2012).
10. W. Chen, M. Tymchenko, P. Gopalan, X. Ye, Y. Wu, M. Zhang, C. B. Murray, A. Alu, and C. R. Kagan, "Large-area nanoimprinted colloidal Au nanocrystal-based nanoantennas for ultrathin polarizing plasmonic metasurfaces," Nano Lett. **15**, 5254–5260 (2015).
11. M. E. Stewart, C. R. Anderton, L. B. Thompson, J. Maria, S. K. Gray, J. A. Rogers, and R. G. Nuzzo, "Nanostructured plasmonic sensors," Chem. Rev. **108**, 494–521 (2008).

#249212 Received 15 Sep 2015; revised 15 Oct 2015; accepted 21 Oct 2015; published 27 Oct 2015
© 2015 OSA

12. H. Lu, X. Liu, D. Mao, and G. Wang, "Plasmonic nanosensor based on Fano resonance in waveguide-coupled resonators," Opt. Lett. **37**, 3780 (2012).
13. D. Gérard and S. K. Gray, "Aluminium plasmonics," J. Phys. D. Appl. Phys. **184001**, 184001 (2015).
14. A. L. Ramaswamy and P. Kaste, "A nanovision of the physiochemical phenomena occurring in nanoparticles of aluminum," J. Energ. Mater. **23**, 1–25 (2005).
15. L. Jeurgens, W. Sloof, F. Tichelaar, and E. Mittemeijer, "Thermodynamic stability of amorphous oxide films on metals: application to aluminum oxide films on aluminum substrates," Phys. Rev. B **62**, 4707–4719 (2000).
16. G. H. Chan, J. Zhao, G. C. Schatz, and R. P. Van Duyne, "Localized surface plasmon resonance spectroscopy of triangular aluminum nanoparticles," J. Phys. Chem. C **112**, 13958–13963 (2008).
17. P. West, S. Ishii, G. Naik, N. Emani, V. Shalaev, and A. Boltasseva, "Searching for better plasmonic materials," Laser Photonics Rev. **4**, 795–808 (2010).
18. J. Zhang, J.-Y. Ou, N. Papasimakis, Y. Chen, K. F. MacDonald, and N. I. Zheludev, "Continuous metal plasmonic frequency selective surfaces," Opt. Express **19**, 23279–23285 (2011).
19. C. Langhammer, M. Schwind, B. Kasemo, and I. Zorić, "Localized surface plasmon resonances in aluminum nanodisks," Nano Lett. **8**, 1461–1471 (2008).
20. M. W. Knight, N. S. King, L. Liu, H. O. Everitt, P. Nordlander, and N. J. Halas, "Aluminum for plasmonics," ACS Nano **8**, 834–840 (2014).
21. I. Zorić, M. Zäch, B. Kasemo, and C. Langhammer, "Gold, platinum, and aluminum nanodisk plasmons: material independence, subradiance, and damping mechanisms," ACS Nano **5**, 2535–2546 (2011).
22. S. J. Tan, L. Zhang, D. Zhu, X. M. Goh, Y. M. Wang, K. Kumar, C.-W. Qiu, and J. K. W. Yang, "Plasmonic color palettes for photorealistic printing with aluminum nanostructures," Nano Lett. **14**, 4023–4029 (2014).
23. H. Lochbihler, "Reflective colored image based on metal-dielectric-metal-coated gratings," Opt. Lett. **38**, 1398–1400 (2013).
24. J. Olson, A. Manjavacas, L. Liu, W.-S. Chang, B. Foerster, N. S. King, M. W. Knight, P. Nordlander, N. J. Halas, and S. Link, "Vivid, full-color aluminum plasmonic pixels," Proc. Natl. Acad. Sci. U.S.A. **111**, 14348–14353 (2014).
25. E. Prodan, C. Radloff, N. J. Halas, and P. Nordlander, "A hybridization model for the plasmon response of complex nanostructures," Science **302**, 419–422 (2003).
26. J. S. Clausen, E. Højlund-Nielsen, A. B. Christiansen, S. Yazdi, M. Grajower, H. Taha, U. Levy, A. Kristensen, and N. A. Mortensen, "Plasmonic metasurfaces for coloration of plastic consumer products," Nano Lett. **14**, 4499–4504 (2014).
27. C. Vannahme, M. Dufva, and A. Kristensen, "High frame rate multi-resonance imaging refractometry with distributed feedback dye laser sensor," Light Sci. Appl. **4**, e269 (2015).
28. P. G. Hermannsson, K. T. Sørensen, C. Vannahme, C. L. Smith, J. J. Klein, M.-M. Russew, G. Grützner, and A. Kristensen, "All-polymer photonic crystal slab sensor," Opt. Express **23**, 16529 (2015).
29. M. A. Green and M. J. Keevers, "Optical properties of intrinsic silicon at 300 K," Prog. Photovoltaics Res. Appl. **3**, 189–192 (1995).
30. E. Højlund-Nielsen, J. Weirich, J. Nørregaard, J. Garnaes, N. A. Mortensen, and A. Kristensen, "Angle-independent structural colors of silicon," J. Nanophotonics **8**, 083988 (2014).
31. S. Raza, S. I. Bozhevolnyi, M. Wubs, and N. A. Mortensen , "Nonlocal optical response in metallic nanostructures," J. Phys. Condens. Matter **27**, 183204 (2015).
32. E. Palik, *Handbook of Optical Constants of Solids* (Academic Press, 1986).

1. Introduction

The polarization of light is a fundamental attribute of electromagnetic waves, providing information about its spacial travel direction and clues to its past. Polarization properties have interesting applications within display technologies, high-density optical storage, anti-counterfeiting and bio-sensing [1, 2]. Here we present a polarization dependent plasmonic aluminum-based high-density metasurface operating at blue wavelengths. The sensory element performs in reflection mode and provides the possibility to detect polarization information by visual means.

The polarization dependent metasurface described here is based on sub-wavelength plasmonic rectangular structures. Similar freely suspended elongated ellipsoidal nanoparticles were first described as polarization dependent in 1912 by Gans [3], that predicted the splitting of surface plasmons into two distinct oscillation modes, namely the high-energy tranverse and the low-energy longitudinal oscillation of conduction band electrons [4, 5]. Unfortunately, freely suspended particles lack precise orientation control, which limits filter resolution.

In contrast, microfabricated plasmonic metasurfaces allow individual control of the shape,

#249212 Received 15 Sep 2015; revised 15 Oct 2015; accepted 21 Oct 2015; published 27 Oct 2015
© 2015 OSA

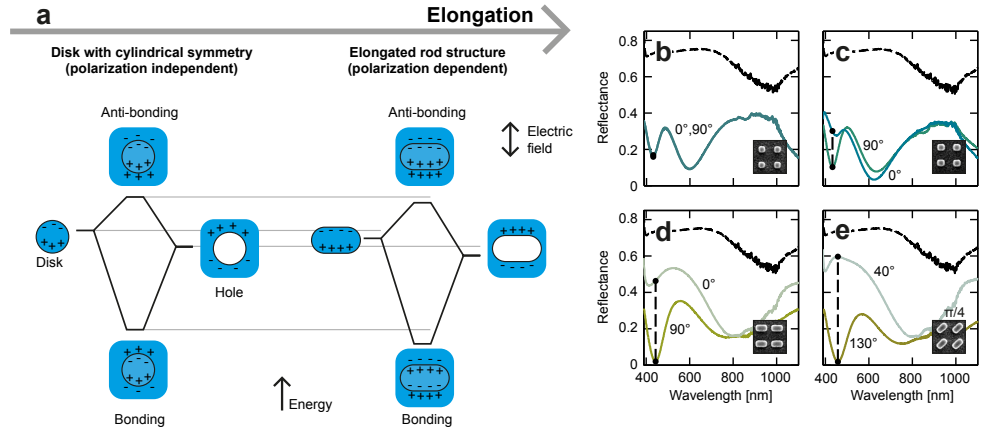

Fig. 1. Hybrid transverse mode concept by elongation of base plasmonic structure. a) Energy hybridization diagrams of circular and elongated structures at transverse polarization. b-e Representative reflectance spectra for different polarizations of various structures with CIE/sRGB calculated color coding. Top dashed lines show spectrum for non-structured surface.

position and orientation of the active entities. In particular, two-dimensional metasurfaces of well-controlled spatial arrangements have attracted considerable attention over the last two decades for their simple design and fabrication, and for their ability to enhance electromagnetic fields. Metasurfaces have been demonstrated to manipulate visible and infrared absorption [6–8] at high polarization conversion efficiencies for sensor applications [9–12].

Aluminum has attractive properties compared to typical plasmonic materials [13], such as silver and gold, due to its natural abundance, low cost, protective oxide layer for high durability [14–16] and plasmonic properties in the visible range [17–21]. Based on aluminum, reflective plasmonic colors utilizing the concept of localized surface plasmon resonances (LSPR) have been presented [22–24] and the hybridization between LSPR modes [25] has been used to design and fabricate polarization independent colors [26]. Polarization dependent aluminum metasurfaces have also been demonstrated for full-color stereoscopic printing by Goh *et al.* [1]. However the metasurface was based on electron beam lithography in HSQ directly on a silicon substrate, impeding fabrication scalability. Furthermore, the ellipse dimensions were varied from 100 nm to 190 nm within a lattice of period 400-500 nm, which indicates poor color contrast and angular dependence.

We present a similar ultra-thin high-density platform, however with a sub-wavelength period of 250 nm for better angular insensitivity and fabricated by a scalable nanoreplication process in hybrid polymer. Compared to Goh *et al.* [1], the presented platform is about four times smaller per unit-cell, mass-producible, and constitutes an important step towards application of polarization-dependent metasurfaces.

To enhance the performance of the metasurface, we rotate the structure with respect to the square lattice in order to elongate the plasmonic structure and increase the resonance strength. The concept of elongation and rotation of the base structure to utilize the hybrid transverse mode is illustrated in Fig. 1. In Fig. 1(a), energy hybridization diagrams for the transverse mode and the structure itself are sketched. In Figs. 1(b)-(e), typical reflectance spectra for different polarizations of various structures (insets) are plotted using CIE/sRGB calculated color coding (see Section 3 for experimental details). The resonance enhancement by rotation of the polarization-dependent resonance behavior around 450 nm is clearly seen.

#249212 Received 15 Sep 2015; revised 15 Oct 2015; accepted 21 Oct 2015; published 27 Oct 2015
© 2015 OSA

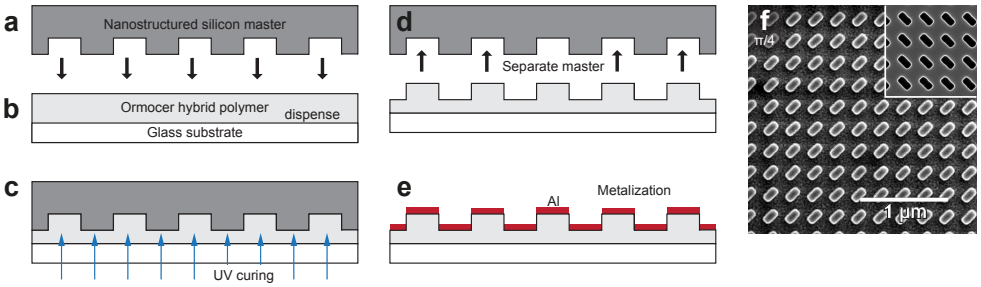

Fig. 2. Fabrication process for 250 nm periodic structures from pattern definition to metalized polymer replica. a-e) Sketch of fabrication process, see text. f) SEM image of metalized polymer replica for 45° rotation inside unit-cell. Corresponding SEM image of Si master can be seen as inset.

2. Fabrication

The plasmonic color filter was fabricated by UV nanoreplication, as sketched in Figs. 2(a)-(e). A silicon master containing areas with two-dimensional periodic structures was fabricated by electron beam lithography and dry etching, see Fig. 2(a). The master was anti-stiction coated with a few monolayers of perfluorodecyltrichlorosilane (FDTS) using molecular vapor deposition.

The sample replica was prepared by dispensing an UV curable hybrid polymer (OrmoComp, Micro Resist Technology GmbH, Germany) onto a borosilicate glass wafer acting as carrier substrate, see Fig. 2(b). The master was brought into contact with the soft hybrid polymer between the opaque silicon master and the transparent glass substrate. The polymer was cured by ultra-violet (UV) light through the glass substrate for 18 min, as shown in Fig. 2(c). After curing, the master and the hybrid polymer were manually separated, leaving the solidified hybrid material on the glass substrate with a nano-structured surface created as a negative of the master pattern, see Fig. 2(d). Finally, a 18 nm thin film of aluminum was deposited on top of the structure by electron beam evaporation in vacuum at a rate of about 1.0 nm/s. The vertical side walls and the height differences of about 50 nm of the polymer topography lead to the formation of isolated metal islands on top of the polymer pillars, as seen in Fig. 2(d).

Representative SEM images of patterns on the polymer replica and the corresponding master area can be seen in Fig. 2(f). The mirror symmetry between master and replica due to the replication process can be seen. The rectangular structures are rounded at the corners. In general, the fabrication process was optimized for a high yield and SEM inspections of the master and final samples did not reveal defects or pattern deviations.

3. Experiments

Figure 3 presents the experimental results. In Fig. 3(a), the polarization angle and the rotation angle of the structure are defined with respect to the basis lattice vector of the square lattice (x-axis). Normal incidence reflectance spectra were obtained for the metalized polymer samples using a modification of an experimental setup previously used for photonic crystal characterization [27, 28].

The setup is schematically illustrated in Fig. 3(b). Light from a broadband laser-driven light source (Energetiq EQ-99XFC) was fed to the setup via an optical fiber and collimated with a fiber collimator. A linear polarizer on a rotational stage was used to control the polarization of the light. The light was then focused with a lens and reflected into a 10x microscope objective by a beam splitter. The light then emerged collimated from the other side of the ob-

#249212 Received 15 Sep 2015; revised 15 Oct 2015; accepted 21 Oct 2015; published 27 Oct 2015
© 2015 OSA

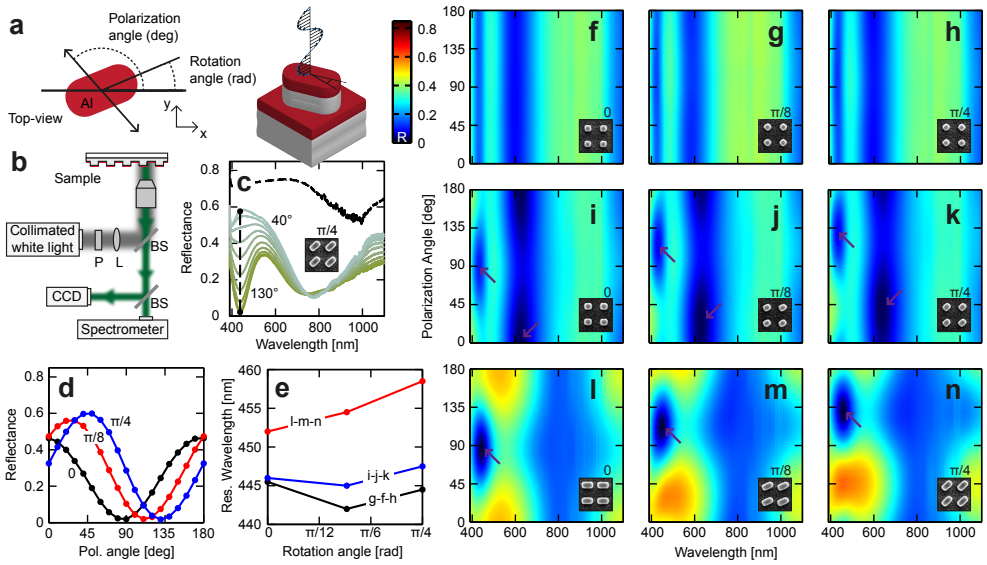

Fig. 3. Measured normal incidence reflectance spectra for metalized polymer samples. a) Definition of coordinate system and angles. b) Schematic illustration of optical setup. c) Reflectance as function of wavelength for different polarizations in the case of structure "n" with CIE/sRGB calculated color coding. Top dashed line shows spectrum for non-structured surface. d) Reflectance as function of polarization angle at resonance wavelength for elongated structures "l", "m", and "n". e) Resonance wavelengths as function of rotation angle. f-n) Reflectance as function of wavelength and polarization angle for all nine investigated topographies. Arrows indicate transverse (450 nm) and longitudinal (630 nm) resonances.

jective and illuminated the device at normal incidence. The reflected light traveled backwards through the objective and beam splitter and was then simultaneously focused by a microscope tube lens onto the slit of an imaging spectrometer (Acton SP-2756 Imaging Spectrograph with PIXIS100B Digital built-in camera and grating 150 g/mm) and a CCD camera via another beam splitter. Thus, positioning was controlled and recorded with the CCD camera while the reflected spectrum was analyzed with the spectrometer. Intensity counts were acquired from the spectrometer and signal counts were calculated by subtracting corresponding dark background spectra. In order to calculate the absolute reflectance, polished silicon was used as reference using well-established tabulated optical properties of silicon [29]. The reflectance was calculated as function of wavelength depending on polarization angle for a given sample area.

In Fig. 3(c), reflectance spectra for different polarization angles are shown for the structures seen in Fig. 2(f), respectively. The spectra are represented by calculated colors using a previously described methodology [30], where the reflectance is converted to a CIE XYZ color using a standard D65 light source and 2° CIE observer, and finally converted to sRGB color space for screen viewing. The resulting reflectance depends strongly on polarization. In Fig. 3(d), the reflectance is plotted as function of polarization angle at resonance wavelength for the series of elongated structures seen as insets in Figs. 3(l)-(n). In Fig. 3(e) the corresponding resonance wavelengths are plotted. Finally, in order to provide an overview, Figs. 3(f)-(n) visualize the reflectance spectra using contour-plots for different polarization angles for all nine investigated topographies with corresponding SEM images as insets.

#249212 Received 15 Sep 2015; revised 15 Oct 2015; accepted 21 Oct 2015; published 27 Oct 2015
© 2015 OSA

4. Numerical simulations

In order to support the experimental findings, simulations were conducted using a frequency-domain solver with periodic boundary conditions in the surface plane (CST Microwave Studio). Despite the nanometric dimensions, the smallest characteristic features are still sufficiently large to allow classical electrodynamics considerations [31]. Normal to the structures, the simulation domain was extending 300 nm away from the metal and at the boundaries Floquet ports were used. The frequency-dependent permittivity used for aluminum were from the handbook of Palik [32]. Substrate and coating were assumed to have a refractive index of 1.5.

Figure 4 presents the simulation results. In Fig. 4(a) the corresponding reflectance spectra of the structures in Fig. 2(n) at 40° and 130° polarization angle are seen, showing good agreement with the experimental results. In Fig. 4(b) the detailed 2D simulated reflectance spectra of the structures in Fig. 2(f) are seen, showing the resonance evolution with similar trends as seen in Fig. 3(n). In order to further illustrate this, an absolute field profile is presented in Fig. 4(c) based on the scaling seen in Fig. 4(d).

Based on the scaling seen in Fig. 4(e), the z-component of the electric field cross-section profiles in the center of the patches can be seen in Figs. 4(f)-4(n). The unit cell supports complex field distributions extending both into the metalair interface and the surroundings. This mode corresponds to a hybrid transverse mode resonating along the short axis of the plasmonic structure with a strong coupling at its resonant frequency. Eventually these plasmonic resonances presented here lead to the enhanced absorption and thereby reduced reflection. As a result, at the frequencies of these modes, the electric field concentrates at the sharp corners (as shown in the corresponding insets in Figs. 4(f)-4(n) and in Fig. 4(c)), which support a strong enhancement of the localized fields.

5. Discussion

From the experimental and numerical simulation results, a number of trends can be observed. First, two resonances can be observed for rounded-square structures, see Fig. 3(f). These resonances correspond to the well-known hybridization between LSPR modes [25] in aluminum nanodisks and nanoholes. The high energy resonance in the blue part of the spectra is seen to be more spectrally narrow than the low energy resonance in the red part of the visual spectrum. It is also clear that rotating the 100 nm rounded-square structure does not disturb the hybridization between the polarization-independent LSPR modes and hence no significant dependence of the reflectance on polarization angle can be observed, see Figs. 3(g)-3(h).

Secondly, elongating the base structures about 25 nm in one direction causes the reflectance to become somewhat polarization dependent, see Fig. 3(b). The high energy resonance is present when the polarized light is perpendicular to the base structure, e.g. at 90° for structure ”i”, see Fig. 3(i). The reflectance minimum follows accordingly for rotation of the rectangular structure with respect to the lattice, such that the minimum reflectance around a wavelength of 450 nm shifts to 135° for structure ”k” with rotation 45°, see. Fig. 3(k). This clearly indicates that the polarization dependence is connected to a transverse plasmonic mode of the metal disks.

Finally, elongating the length to about 190 nm (width ca. 110 nm) causes the reflectance at blue wavelengths to become strongly polarization dependent, see Fig. 3(l). It is also clear that the resonance strength is clearly enhanced, while the reflectance off-resonance is also higher. By elongating the plasmonic base structure, the hybridization modes become polarization dependent, such that the high energy mode has the character of a hybrid transverse mode. This is also seen in the simulations, see Fig 4(l). By rotation of the base structure, the resonance strength is further improved and the resonance wavelength increases slightly. In the case of 45° rotation angle for structure ”n”, the normal-incidence reflectance drops around the blue reso-

#249212 Received 15 Sep 2015; revised 15 Oct 2015; accepted 21 Oct 2015; published 27 Oct 2015
© 2015 OSA

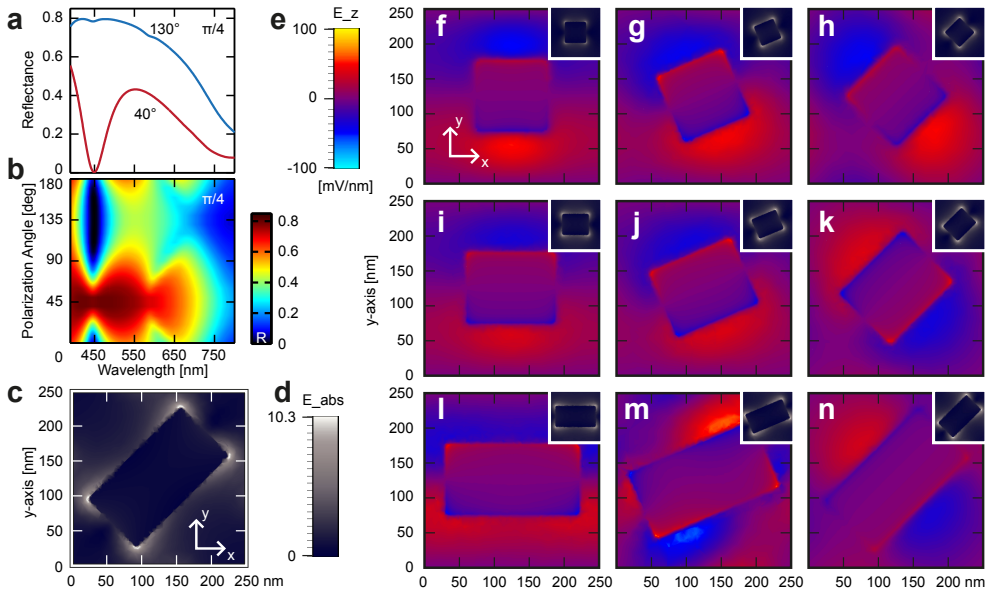

Fig. 4. Simulations. a) Reflectance spectra for structure ”n” at 40° and 130° polarization angle. b) Reflectance contour-plot for structure ”n”. c) Absolute electric field intensity for structure ”n”. d) Scale for absolute field intensity with maximum of 800 mV/nm. e) Scale for z-component of electric field for input field of 76.6 mV/nm. f-n) Plots of the electric field z-component inside the unit-cell, with inserts of the corresponding absolute field intensity for structures ”f”-”n” at the high-energy resonance for optimal polarization angle (90°, 113°, 135°) and phase. The hybrid transverse mode can be seen.

nance wavelength (457 nm) from about 60% to below 1.6%. This ”on/off” ratio of 33.4 creates a visible color discrepancy, see Fig 3(b). This agrees well with the simulations, see Fig 4(n).

6. Conclusion

In conclusion, we reported on a polarization dependent plasmonic aluminum-based metasurface operating at blue wavelengths. The fabricated subwavelength structures, displayed strong, localized, plasmonic resonances able to control linear polarization. Best performance was acheived by rotating an elongated rectangular structure of length 180 nm and width 110 nm inside a square lattice of period 250 nm. In the case of 45° rotation of the structure with respect to the lattice, the normal-incidence reflectance decreased around the resonance wavelength of 457 nm from about 60 percent to below 2 percent with a ratio of 33, thereby providing on/off controllability of reflectance for detection of polarized UV-visual light.

Acknowledgments

This work was supported by the European Commission via the FP7 MMP Integrated project Plast4Future (NMP2-SE-2012-314345).

#249212 Received 15 Sep 2015; revised 15 Oct 2015; accepted 21 Oct 2015; published 27 Oct 2015
© 2015 OSA

A.6 Højlund-Nielsen et al. 2015b

E. Højlund-Nielsen, J. Clausen, L.H. Thamdrup, M. Zalkovskij, T. Nielsen, T. Mäkelä, J. Ahopelto, N.A. Mortensen, A. Kristensen. “Plasmonic Structural Colors For Plastic Consumer Products” (“Roll-to-roll Imprinted Plasmonic Structural Colors”), *Advanced Manufacturing, Electronics and Microsystems TechConnect Briefs 2015*, Photonic Materials & Devices Chapter 5, Nano Science and Technology Institute, CRC Press Reference, ISBN 9781498747301, pp. 143 - 146.

Roll-to-roll Imprinted Plasmonic Structural Colors

E. Højlund-Nielsen*, T. Mäkelä**, J. Clausen***, L. Thamdrup****, M. Zalkovskij****, T. Nielsen****, J. Ahopelto**, N. A. Mortensen***, A. Kristensen*

* Technical University of Denmark, DTU Nanotech, Ørsteds Plads, DK-2800 Kgs. Lyngby, Denmark
** VTT Microsystems and Nanoelectronics, P.O. Box 1000, FI-02044 VTT, Finland
*** Technical University of Denmark, DTU Fotonik, Ørsteds Plads, DK-2800 Kgs. Lyngby, Denmark
**** NIL Technology ApS, Diplomvej 381, DK-2800 Kgs. Lyngby, Denmark

ABSTRACT

Plasmon color technology based on aluminum has recently been firmly established as a route towards structural coloring of polymeric materials. We report on the fabrication of colors by localized surface plasmon resonances (LSPR) using roll-to-roll printing and demonstrate a route for scalable production and commercial uptake of plasmonic colors.

Keywords: plasmonics, surface plasmons, color, nanolithography, roll-to-roll printing

1 INTRODUCTION

Today colorants, such as pigments or dyes, are used to color plastic-based consumer products, either as base for solid colored bulk polymer or in inks for surface decoration. After usage, the products must be mechanically sorted by color before recycling [1], limiting any large-scale efficient recycling effort. As an alternative to chemistry-based coloring, nano-scale structural coloring has been proposed [2] to reduce the number of materials needed and to increase pattern resolution. Here colors are created by structural based light-matter interactions in the surface. Thereby, the sorting by color can be avoided in the recycling state, as destruction of the nano-scale texture removes any color perception leaving a (semi)-transparent bulk polymer ready for reprocessing. Nano-scale structural coloring provides new perspectives for recycling and sustainability of plastic products.

Recently, plasmon color technology based on aluminum has been firmly established as a route towards structural coloring of polymeric materials [3, 4]. Aluminum has been shown to be superior to typical plasmonic materials, such as silver [5] and gold [6], due to its natural abundance, low cost, protective oxide layer for high durability [7, 8, 9] and attractive plasmonic properties in the visible range [10, 11, 12, 13, 14, 15, 16, 17]. Based on aluminum, reflective plasmonic colors utilizing the concept of localized surface plasmon resonances (LSPR) have been presented [3, 4, 18, 19]. Here, the hybridization between LSPR modes [20] in aluminum nanodisks and nanoholes has been used to design and fabricate bright angle-insensitive colors tunable across the visible spectrum. Finally, the structural color effects can be made robust for everyday use by applying a protective coating on top, which leads to a red-shift of the plasmonic resonances [3].

Due to these considerable advances, the research and development targets are now shifting from proof-of-concept based on LSPR modes in aluminum towards increasing the color gamut and introduce scalable fabrication methods, such as injection molding and roll-to-roll printing, for commercial viability compared to traditional pigment-based coloring.

Roll-to-roll printing is an emerging technology in the context of manufacturing micro- and nano-scale patterns and has been attracting interest because of its inherent advantages of low cost, high throughput and large area patterning [21, 22, 23, 24, 25, 26]. In recent years, a number of commercial applications have emerged, particularly optical displays, functional coatings and multifunctional films based on micron-sized structures [27]. Recently thermal roll-to-roll nanoimprint lithography with 100 nm one-dimensional grooves has been demonstrated [23], however general adaptation from the micro-scale to the nano-scale has proven difficult due to viscoelastic recovery in relatively fast printing processes. For these reasons thermal and pressure control of the imprint media are crucial. Based on previous work [28, 29] we now demonstrate two-dimensional 115 nm surface plasmon resonance structures with a high edge quality suitable for plasmonic color applications on a relatively large area.

Even though the printing speed used here is modest (0.3 m/min), the continuous roll process inherently makes it possible to process e.g. 500 m of film without stopping. By optimizing printing parameters, higher manufacturing speeds may be achieved if the pressure can be increased correspondingly. The web width (currently 60 mm) is completely scalable and thereby the system holds mass-volume capability.

Consequently, we report on plasmon structural colors produced by pattern transfer from a silicon master original, via a nickel shim, to a polymer surface using roll-to-roll techniques and subsequent metalization. Our study provides an engineering method to define a physical surface pattern that will yield a desired structural color, quantified by reflectance measurements. The use

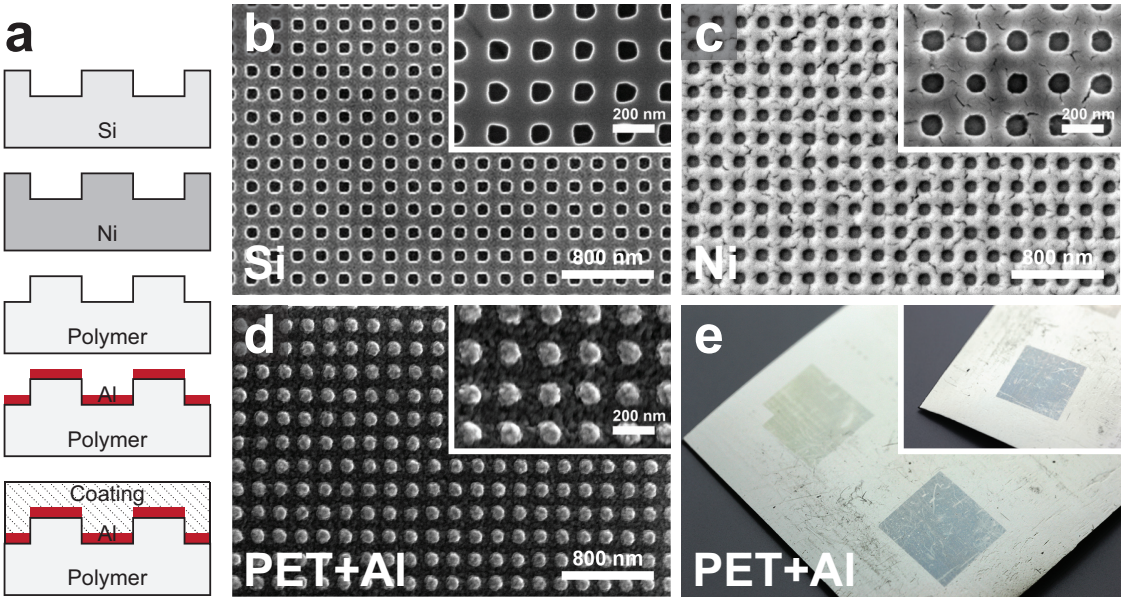

Figure 1: Fabrication process for 200 nm periodic structures from pattern definition to polymer metalized replica (blue area). a) Sketch. b) SEM images of Si master. c) SEM images of nickel master. d) SEM images of roll-to-roll polymer replication with aluminum on top. e) Photographs of the finished A-PET polymer surface without coating for 200 nm period (blue) and 300 nm period (green) areas of size 0.5 mm × 0.5 mm.

of roll-to-roll printing enables mass-volume production of plastic consumer surfaces with nano-scale based coloration for a wide range of applications.

2 FABRICATION

The fabrication process for making the plasmon colored samples is outlined in Fig. 1. First a silicon master was patterned by electron beam lithography and anisotropic dry etching. Subsequently, the silicon master was used in a double pattern inversion scheme to make a nickel shim with a thickness of 100 µm and a structure depth of 44 nm. The relatively thin nickel shim thickness was chosen due to the good bendabilty.

The replication process was carried out using a custom thermal roll-to-roll tool described in detail in Ref [21]. The nickel shim containing the structures for plasmonic colors was wrapped around a 66 mm diameter and 60 mm wide imprinting roll. Then a heated roll was pressed against a cold backing roll with a force of 600 N, resulting in a force between the rolls (NIP) of approximately 1000 N. The web materials tested included 100 um to 125 um thick polymethylmetcarylate (PMMA), polycarbonate (PC), amorphous polyethylene terephthalate (A-PET) and cellulose acetate (CA).

The temperature of the imprinting roll was adjusted to be above the film softening temperature, which is typically slightly below the glass transition temperature of the different materials. Roll-to-roll process printing temperatures are usually kept slightly below the film glass transition or the melting point temperature to avoid bending, wrinkling or other changes to the surface occurring at the glass transition temperature. Glass transition temperature for the used films, such as CA and PMMA, is 105 °C. For the A-Pet film, the glass transition temperature is 72 °C, but the melting temperature is 250 °C. A speed of 0.3 m/min was used, leading to an imprint time of roughly 0.3 s with a 3 mm contact length between the rolls. The contact length was varied by tuning the hardness of the backing roll. The best replication, with a disc diameter of 115 nm measured by SEM and a polymer structure depth of 40 nm measured by AFM, were obtained on A-PET at a printing temperature of 110 °C (± 2 °C).

After replication of the polymer samples, an aluminum metal layer was applied by electron beam evaporation in 2×10^{-6} mbar vacuum, see Fig. 1d. The deposition rate was 0.5 nm/s for a thickness of 16 nm measured by quartz crystal microbalance during deposition. Finally, samples were coated by approximately 50 µm of scratch-resistant commercial automotive lacquer. In terms of coating, the bulk part acts as a diffuser, mimicking the scattering properties of traditional paint, whereas the top surface of the coating creates a high-gloss visual appearance.

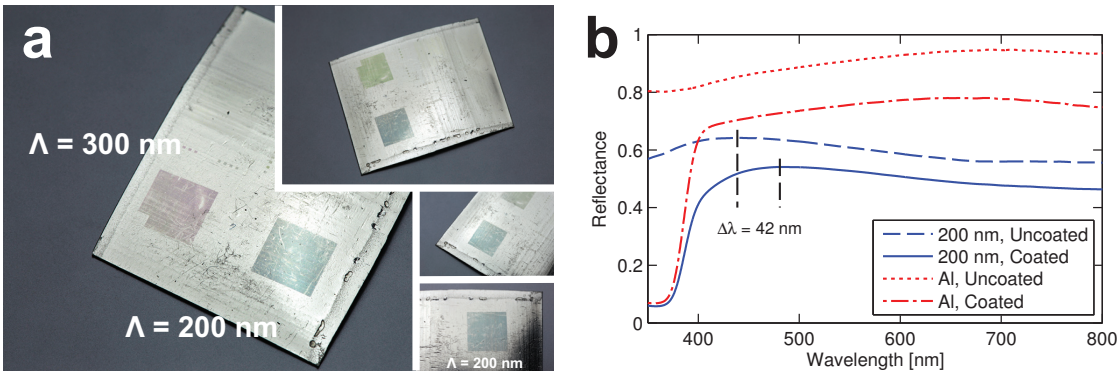

Figure 2: Sample after coating. a) Photographs with fixed light at different orientations. 200 nm period area has stable color response. b) Measured reflectance spectra by integrating sphere at 8 degrees incidence of 200 nm period area compared to non-structured aluminum surface. A red-shift is seen after coating.

3 RESULTS

Photographs taken under fixed light conditions of the sample after coating are shown in Fig. 2a. The sample scratches are due to the industrial grade film itself (CA from Clarifoil) and tear-and-wear mold degradation. The pattern with 200 nm period yields a distinct blue, angle-insensitive color-response, in agreement with simulation results (see supplemental material Figure S2 for Ref. [3]). Combined with the protective properties of the coating, our approach provides up-scalable production of durable structural colors.

In contrast to the blue 200 nm period pattern, the color-response of the 300 nm period pattern varies strongly with the orientation of the sample with respect to the light source and camera (see supplemental material). This dependence is well-described in literature [30, 3] and illustrates the requirement, due to the frequency-range of the human visible spectrum, for nano-scale patterns with periodicities in the order of 200 nm or smaller.

In Fig. 2b, measured reflection spectra by integrating sphere using a silicon specular reference can be seen for the 200 nm period pattern compared to the non-structured aluminum sample surface. A maximum in reflectance around a vacuum wavelength of 439 nm in the blue part of the spectrum is observed, as longer wavelengths are absorbed to a higher degree by the LSPR located in the red part of the spectrum. After coating, a red-shift of the maximum reflectance of approximately 42 nm can been be measured (the low ultra-violet reflectance is a property of the coating). This red-shift can also be directly observed by comparing photographs before and after coating (see Fig. 1e and 2a), where the blue color shifts to a blue-green color after coating. The red-shift of the maximum reflectance corresponds to a LSPR red-shift [3] and implies that the optical properties of the coating are important for the appearance.

4 CONCLUSION

In conclusion, we reported on the fabrication of plasmon color technology based on aluminum by LSPR using roll-to-roll printing on polymeric films. The use of the inherent mass-volume technique demonstrates a route for scalable production, which may lead to low-cost pattering and commercial uptake of plasmonic colors. Finally, nano-scale structural coloring provides new perspectives for recycling and sustainability of plastic products, as the colors are based on removable physical structures in the surface rather than traditional chemistry-based colorants.

ACKNOWLEDGMENTS

We acknowledge J. Scheel for photography. This work was supported by the European Commission via the FP7 MMP Integrated project Plast4Future (NMP2-SE-2012-314345).

REFERENCES

[1] Al-Salem, S. M., Lettieri, P., & Baeyens, J. (2009). Waste Management, 29(10), 2625-43. doi:10.1016/j.wasman.2009.06.004.

[2] Kumar, K., Duan, H., Hegde, R. S., Koh, S. C. W., Wei, J. N., & Yang, J. K. W. (2012). Nature Nanotechnology, 7(August), 557-561. doi:10.1038/nnano.2012.128.

[3] Clausen, J. S., Højlund-Nielsen, E., Christiansen, A. B., Yazdi, S., Grajower, M., Taha, H., & Mortensen, N. A. (2014). Nano Letters, 14(8), 4499-4504. doi:10.1021/nl5014986.

[4] Tan, S. J., Zhang, L., Zhu, D., Goh, X. M., Wang, Y. M., Kumar, K., ... Yang, J. K. W. (2014). Nano Letters, 14(7), 4023-4029. doi:10.1021/nl501460x.

[5] Si, G., Zhao, Y., Lv, J., Lu, M., Wang, F., Liu, H., ... Liu, Y. J. (2013). Nanoscale, 5(14), 6243-6248. doi:10.1039/c3nr01419c.

[6] Roberts, A. S., Pors, A., Albrektsen, O., & Bozhevolnyi, S. I. (2014). Nano Letters, 14(2), 783-787. doi:10.1021/nl404129n.

[7] Ramaswamy, A. L., & Kaste, P. (2005). Journal of Energetic Materials, 23(1), 1-25. doi:10.1080/07370650590920250.

[8] Jeurgens, L., Sloof, W., Tichelaar, F., & Mittemeijer, E. (2000). Physical Review B. doi:10.1103/PhysRevB.62.4707.

[9] Chan, G. H., Zhao, J., Schatz, G. C., & Duyne, R. P. Van. (2008). Journal of Physical Chemistry C, 112(36), 13958-13963. doi:10.1021/jp804088z.

[10] West, P. R., Ishii, S., Naik, G. V., Emani, N. K., Shalaev, V. M., & Boltasseva, a. (2010). Laser & Photonics Reviews, 4(6), 795-808. doi:10.1002/lpor.200900055.

[11] Knight, M. W., Liu, L., Wang, Y., Brown, L., Mukherjee, S., King, N. S., ... Halas, N. J. (2012). Nano Letters, 12(11), 6000-6004. doi:10.1021/nl303517v.

[12] Zhang, J., Ou, J.-Y., Papasimakis, N., Chen, Y., MacDonald, K. F., & Zheludev, N. I. (2011). Optics Express, 19(23), 23279-23285. doi:10.1364/OE.19.023279.

[13] Kulkarni, V., Prodan, E., & Nordlander, P. (2013). Nano Letters, 13(12), 5873-5879. doi:10.1021/nl402662e.

[14] Langhammer, C., Schwind, M., Kasemo, B., & Zoric, I. (2008). Localized surface plasmon resonances in aluminum nanodisks. Nano Letters, 8(5), 1461-1471. doi:10.1021/nl080453i.

[15] Chen, Q., & Cumming, D. R. S. (2010). Optics Express, 18(13), 14056-14062. doi:10.1364/OE.18.014056.

[16] Knight, M. W., King, N. S., Liu, L., Everitt, H. O., Nordlander, P., & Halas, N. J. (2014). ACS Nano, 8(1), 834-840. doi:10.1021/nn405495q.

[17] Zoric, I., Zch, M., Kasemo, B., & Langhammer, C. (2011). ACS Nano, 5(4), 2535-2546. doi:10.1021/nn102166t.

[18] Lochbihler, H. (2013). Optics Letters, 38(9), 1398-400. doi:10.1364/OL.38.001398.

[19] Olson, J., Manjavacas, A., Liu, L., Chang, W.-S., Foerster, B., King, N. S., ... Link, S. (2014). Proceedings of the National Academy of Sciences, 111(40), 14348-14353. doi:10.1073/pnas.1415970111.

[20] Prodan, E., Radloff, C., Halas, N. J., & Nordlander, P. (2003). Science, 302(5644), 419-422. doi:10.1126/science.1089171.

[21] Schleunitz, A., Spreu, C., Mäkelä, T., Haatainen, T., Klukowska, A., & Schift, H. (2011). Microelectronic Engineering, 88(8), 2113-2116. doi:10.1016/j.mee.2011.02.019.

[22] Mäkelä, T., Haatainen, T., & Ahopelto, J. (2011). Microelectronic Engineering, 88(8), 2045-2047. doi:10.1016/j.mee.2011.02.016.

[23] Kooy, N., Mohamed, K., Pin, L. T., & Guan, O. S. (2014). Nanoscale Research Letters, 9(1), 320. doi:10.1186/1556-276X-9-320.

[24] Peng, L., Deng, Y., Yi, P., & Lai, X. (2014). Journal of Micromechanics and Microengineering, 24(1), 013001. doi:10.1088/0960-1317/24/1/013001.

[25] Chang, C. Y., Yang, S. Y., & Sheh, J. L. (2006). Microsystem Technologies, 12(8), 754-759. doi:10.1007/s00542-006-0103-5.

[26] Yeo, L. P., Ng, S. H., Wang, Z., Wang, Z., & de Rooij, N. F. (2009). Microelectronic Engineering, 86(4-6), 933-936. doi:10.1016/j.mee.2008.12.021.

[27] Dumond, J. J., & Yee Low, H. (2012). Journal of Vacuum Science & Technology B: Microelectronics and Nanometer Structures. doi:10.1116/1.3661355.

[28] Mäkelä, T., Haatainen, T., & Ahopelto, J. (2011). Microelectronic Engineering 88, 2045-2047. doi:10.1016/j.mee.2011.02.016.

[29] Unno, N., Mkel, T., & Taniguchi, J. (2014). Journal of Vacuum Science & Technology B, Nanotechnology and Microelectronics, 32(6), 06FG03. doi:10.1116/1.4897132.

[30] Højlund-Nielsen, E., Weirich, J., Nørregaard, J., Garnaes, J., Asger Mortensen, N., & Kristensen, A. (2014). Journal of Nanophotonics, 8(1), 083988. doi:10.1117/1.JNP.8.083988.

A.7 Zhu et al. 2015

X. Zhu, C. Vannahme, E. Højlund-Nielsen, N.A. Mortensen, A. Kristensen, "Plasmonic color laser printing", *Nature Nanotechnology*, advance online publication, doi: 10.1038/nnano.2015.285.

nature nanotechnology

LETTERS

PUBLISHED ONLINE: 14 DECEMBER 2015 | DOI: 10.1038/NNANO.2015.285

Plasmonic colour laser printing

Xiaolong Zhu[1]*, Christoph Vannahme[1], Emil Højlund-Nielsen[1], N. Asger Mortensen[2]* and Anders Kristensen[1]*

Colour generation by plasmonic nanostructures[1,2] and metasurfaces[3,4] has several advantages over dye technology: reduced pixel area, sub-wavelength resolution and the production of bright and non-fading colours[5]. However, plasmonic colour patterns need to be pre-designed and printed either by e-beam lithography (EBL)[6–11] or focused ion beam (FIB)[12–14], both expensive and not scalable processes that are not suitable for post-processing customization. Here we show a method of colour printing on nanoimprinted plasmonic metasurfaces using laser post-writing. Laser pulses induce transient local heat generation that leads to melting and reshaping of the imprinted nanostructures[15]. Depending on the laser pulse energy density, different surface morphologies that support different plasmonic resonances leading to different colour appearances can be created. Using this technique we can print all primary colours with a speed of 1 ns per pixel, resolution up to 127,000 dots per inch (DPI) and power consumption down to 0.3 nJ per pixel.

The concept of our laser printing technique is illustrated in Fig. 1. The printable plasmonic metasurface is composed of metal disks on top of dielectric pillars, hovering above a perforated metal film, see Fig. 1a,b. This design with polymeric pillars can be implemented by nanoimprinting, roll-to-roll processing or injection-molding technologies based on a master template defined by EBL. We use abundant and recyclable aluminium as the plasmonic material, as it exhibits high plasma frequency and has recently been found to yield surface plasmon resonances (SPRs) from the visible to UV[16,17]. Abundant polymers and hybrid materials suitable for nanoimprinting can be used. For instance, PMMA (polymethylmethacrylate) or Ormocomp (Micro resist technology GmbH) are good candidates that can be imprinted in thermal-nanoimprint (PMMA) or UV-curing (Ormocomp) processes. Owing to the plasmon hybridization of the disk–hole system in the Al metasurface[18], reflected colours caused by resonant absorptions at specific wavelengths can be modified by changing the geometric parameters[6,19] (see Supplementary Fig. 1).

For a laser pulse of nanosecond duration, the instant energy is sufficiently high to heat the selected surface region above the melting temperature. The disks may thus transform their shapes into thicker disks or spheres in a crystallographic phase-transition process (Fig. 1c)[20,21], and finally they may be ablated away. By the excitation of SPR with electric field confinement, light energy is redistributed and concentrated in specific regions of the disk–hole unit cell, enabling a fine-tuning of the morphology by adjusting the input pulse energy density. In return, the change of morphology shifts the resonant frequency of the SPR, leading to a variation in reflected colours. This allows printing of colours on a specific plasmonic surface by controlling the laser parameters (such as power, spot size, frequency and so on) as well as the position of the laser spot (see Supplementary Movie I).

To realize a desired colour from laser irradiation, we modify the SPR through single-pulse laser exposure (1 ns, $\lambda = 532$ nm). As the input laser energy dosage is increased from 0–535 nJ in the focal plane of a 4× objective (spot size ~50 μm in diameter), the main SPR blueshifts from 600 to 500 nm and the printed colour varies from cyan to yellow (Fig. 2a). We further explore the continuous tuning of colours across the visible spectrum on metasurfaces with different parameters (Supplementary Figs 2 and 3). Remarkably, it is possible to obtain all of the CMY primaries (cyan, magenta and yellow) used in traditional colour printing. With sufficient laser intensity, the Al nanodisks can be annealed at their rims and evolved into spherical objects (Fig. 2b and Supplementary Fig. 4). Also, by increasing the laser intensity, the spheres are ablated from the polymer interface, owing to a rapid change in the centre of mass during the melting process that provides the particles with a repulsive momentum[22]. Furthermore, for a laser energy above 500 nJ, the holes in the continuous film on the substrate can even be enlarged in a controlled manner.

To describe the morphology transformation of the Al disks, we offer a simplified model of the complex thermodynamic phase transition. Neglecting gravity, we vary the thickness t of round-cornered disks (or the radius r of the sphere) while preserving the overall metal volume of the initial disks. Simulations with this model (Fig. 2c) predict the blueshift of SPRs and demonstrate a qualitative agreement with the corresponding measurements for different thermo-transition states. It should be noted that the measured spectra show a broadening of the resonances when compared with the simulated ones because of the defects in printing (Supplementary Fig. 5). From the simulated electric field enhancements for printed metasurfaces (Fig. 2d), we find that the local electric field decreases during the gradual transformation from disks to spheres. The field is strongly localized at the sharp corners of the unchanged disks (Fig. 2d (i)), dissipating in the intermediate shape (Fig. 2d (ii)) and finally dispersively covering the sphere (Fig. 2d (iii)). The absorbed heat power is directly related to the electric field distributed in the materials and can simply be expressed as

$$Q_{\mathrm{abs}}(\omega) = \frac{1}{2}\omega \int \varepsilon''(\omega)|\mathbf{E}(\omega)|^2 dV \qquad (1)$$

where ω is the angular frequency, $\varepsilon''(\omega)$ is the imaginary part of the dielectric function $\varepsilon = \varepsilon' + i\varepsilon''$, $\mathbf{E}$ is the electric field, and the integration is carried out over the volume of the unit cell. Thus, the heat absorption can obviously be improved by overlapping the lossy metal with a strong electric field. With the aid of the SPR, the electrical field is strongly localized and enhanced near the metal surface and exponentially decays into the surrounding medium, causing a strong heat power confined at the interface[23]. This process can be further understood by examining the simulated temperature evolutions during the initial nanoseconds for different structural morphologies (Fig. 2e) and the temperature distribution resulting from thermo–plasmonic heating (Fig. 2f), see also Supplementary Fig. 6.

[1]Department of Micro- and Nanotechnology, Technical University of Denmark, Kongens Lyngby DK-2800, Denmark. [2]Department of Photonics Engineering, Technical University of Denmark, Kongens Lyngby DK-2800, Denmark. *e-mail: xizhu@nanotech.dtu.dk; asger@mailaps.org; Anders.Kristensen@nanotech.dtu.dk

© 2015 Macmillan Publishers Limited. All rights reserved

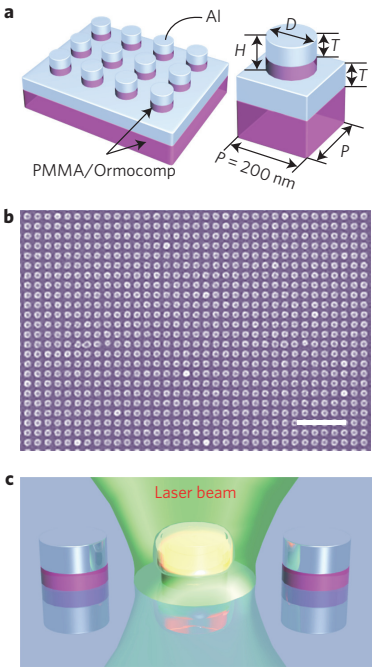

Figure 1 | Plasmonic structures for colour printing. a, Schematic illustrations of the plasmonic metasurface and a unit cell with parameter settings, where the periodicity, $P = 200$ nm, the thickness of Al is $T = 20$ nm, the height of the pillars is $H = 30$ nm and the diameter of the disks is D. **b**, A top-view SEM image of a plasmonic metasurface. Scale bar: 1 μm. **c**, A schematic illustration of laser printing. The printing is governed by photo-thermal reshaping of the metasurface.

Based on the trait of local plasmon heating, the plasmonic metasurfaces can be embedded in transparent polymers for laser printing (Fig. 3a)[24]. With the excitation of the SPR, the plasmon-enhanced photo-thermal melting ensures that the writing process only takes place at the plasmonic metasurface within the focal plane. As shown in Fig. 3a, the coating leads to a redshift of the resonances in the system and a corresponding colour change before and after laser printing because of the increased refractive index of the surroundings. A top coating offers the advantage of protecting the structure from mechanical damage, fingerprints, greasy residues, and so on, making the proposed 'plasmonic paper' more robust and fully flexible for colour printing in everyday applications (Fig. 3b). Impressively, by embedding 20 nm Al inside plastics, our printing method creates environmentally sound colouration solutions for consumer products (such as beverage bottles, toys and automotives), with only a ppm-level residue of Al for recycling.

For detailed expression of a colour image, it is necessary not only to produce single colour depth, but also colour mixing[9,25] or overlapping (Supplementary Fig. 7) to broaden the capability of our colour library. For a proof-of-concept demonstration, spatial colour mixing is carried out by coordinating the distribution of colour dots. By controlling the laser spot size and step dimension, we printed magenta colour dots onto the cyan background with different filling factors. The spot size is well below the resolution of the human eye so that the spatially distributed dots can be seen as a single mixed blue–violet colour (Fig. 3c,d). A simple averaging of two different colour spectra yields a similar result to the reflection spectrum of the mixed colour, proving the spatial mixing of distinct structural colours (Fig. 3e and Supplementary Fig. 8). Note that the spectrum of the mixed colour is slightly different from the theoretical prediction of a 50% mixture because of the fluctuation of the spot size. Despite the practical advantages of laser manipulation, colour generation by spatial mixing as a complementary strategy is ultimately necessary to accomplish full-colour printing[26]. In principle, a full colour library is possible by combining the already-rich colours (caused by laser reshaping directly) and the additional colour mixing options. Monochrome laser printing on the initially colourless plasmonic paper is also possible (Supplementary Fig. 9).

Plasmonic laser printing has a resolution that exceeds the diffraction limit. Conventional optics is restricted by the diffraction limit, meaning that a spatial resolution below a quarter of a micrometre seems entirely out of reach for visual applications. Interestingly, photon heating occurs only in the vicinity of the focal spot and the size of melted material can be reduced due to the Gaussian probability distribution of the photon fluence density. This property leads to a critical value of exposure energy where the melting reaction is initiated, which essentially defines a threshold that excludes the low-intensity wings from melting and thus reduces the size[27], as displayed in the upper panel in Fig. 4a. However, a small (for example 10%) fluctuation of the laser intensity would be detrimental for this mechanism. Surface plasmons possess two natural properties: subwavelength light confinement and intense field enhancement[28]. Applying a plasmonic super-lens, sub-diffraction-limited imaging with 60 nm half-pitch resolution has been implemented[29]. Here, we push the laser-induced colour printing to the sub-diffraction scale by exploiting plasmonic thermal reshaping. As indicated in the lower panel in Fig. 4a, the electric field is confined and enhanced at the plasmonic metasurface. The local field enhancement helps to localize the light intensity, thereby causing localized heating at the intended particle. This mechanism is the key to successfully realize: (1) a higher spatial resolution, as the melting at the unit cell can be well controlled within the disk; (2) a better stability, because only a laser fluctuation $\geq 100\%$ can heat and melt the nearest neighboring unit cell; and (3) a lower power, where 1% of the original laser power is feasible due to the 100-fold enhancement of the E-field intensity.

We are thus able to design laser-printed colour pixels of an arbitrary small size by choosing an appropriate but relatively low laser-pulse energy. To strengthen our conclusion, we applied a single nanosecond laser pulse focused through a 0.65 NA 40× objective (spot size ~4 μm) for printing. Considering a Gaussian distribution of the laser energy, only a small central region can reach and overcome the melting threshold, as manifested in the circles in Fig. 4b. We have achieved laser printing at the single-uni-cell level of the metasurface with a periodicity of 200 nm, which is smaller than the theoretical diffraction limit throughout the entire visible spectrum, as shown in the red circle in Fig. 4b. Furthermore, the actual melting part of a disk can be less than 50 nm when employing a single-pulse energy in a spot down to 0.3 nJ (the inset in Fig. 4b), resulting in the laser-induced manipulation of structures within the single unit cell. The reshaping part of the disk can even be smaller under a weaker intensity (see the results in Supplementary Fig. 10).

As the plasmonic heating flattens the sharp corners from the disk–hole system and eliminates the narrow nanogaps in between, the electromagnetic field enhancement is consequently weakened. The gradual change of geometry and the attenuation of intensity actually protect the printing area from reacting to multiple-pulse irradiation, as the first pulse degrades the geometry immediately, reducing the field intensities of subsequent pulses to below the threshold value. Moreover, the intensity gaps between these transition states of morphologies provide distinct power levels for reshaping, which delivers easier colour switching, mixing and overlapping, as shown in Fig. 4c.

To illustrate the capability of printing arbitrary images with colour and tonal control, we printed a selected image using a

© 2015 Macmillan Publishers Limited. All rights reserved

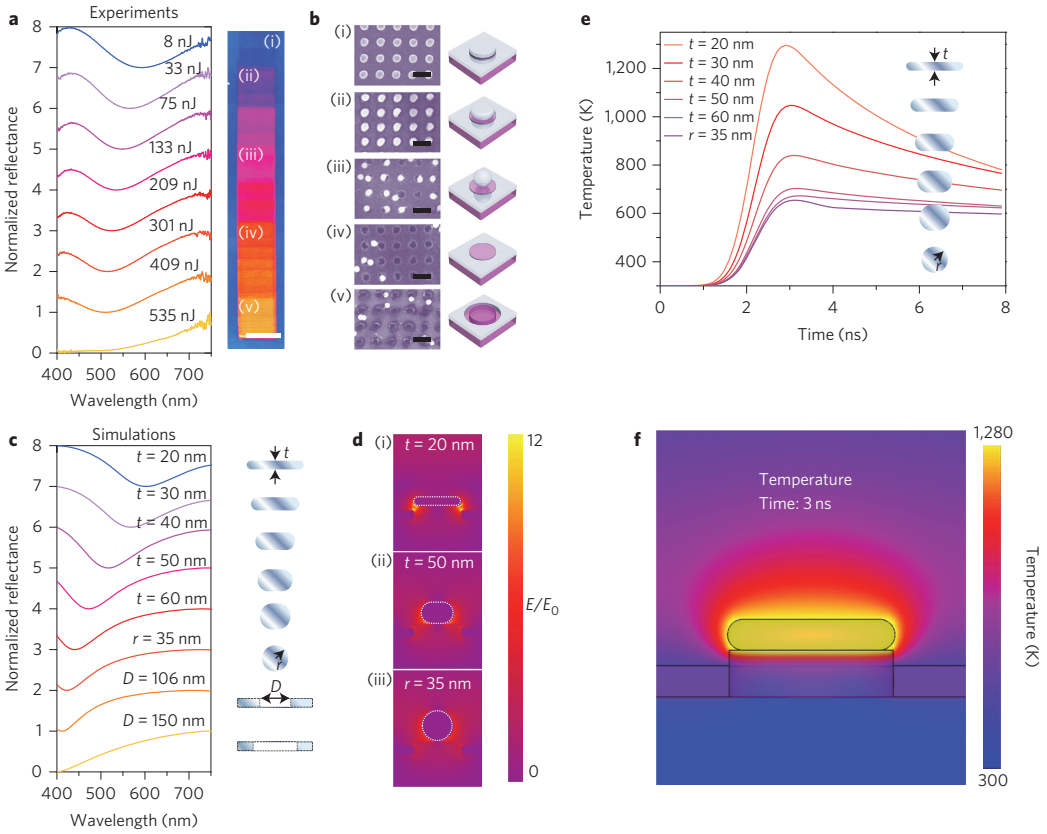

Figure 2 | Spectral and geometry analyses and numerical simulations. a, Left, measured spectra of the metasurface for $D = 106$ nm. The dips appear due to SPRs under increasing laser dosage from 0 to 535 nJ for single-pulse laser exposure (1 ns, $\lambda = 532$ nm, spot size: 50 μm). Right, corresponding 500 μm × 500 μm colour squares printed with a 10 μm step size. Scale bar: 500 μm. **b**, Left, SEM images of the colour areas in **a** (i)–(v). Scale bars: 200 nm. The related pulse energies are 0 (unexposed), 33, 133, 301 and 535 nJ. Right, 3D diagrams demonstrating the corresponding morphology evolutions. **c**, Simulated spectra of models by imitating the morphology transformation in measurements. The cross-sections in the right panel indicate the parameter settings. **d**, Simulated electric field enhancements (at $\lambda = 532$ nm) for selected morphologies of (i) $t = 20$ nm, (ii) $t = 50$ nm and (iii) $r = 35$ nm (sphere). **e**, Simulated temperature evolutions during the initial nanoseconds for different structural morphologies, which gradually change from a disk shape into a spherical particle. The cross-sectional views indicate the morphological change and highlight the various geometrical parameters. **f**, The corresponding temperature distribution in the initial structure after 3.0 ns when the initial thickness of the disk is $t = 20$ nm. The incident pulse power, absorbed energy and the heat power density distribution are shown in Supplementary Fig. 6. The 3D evolution of temperature over 8 ns is presented in Supplementary Movie 2.

single nanosecond laser pulse focused through a 0.8 NA 50× objective lens (spot size ~3 μm). To prove the ultimate capability, we actualized a colour design in a blue tone with a step size of 200 nm (see also Supplementary Fig. 10 and 11). The printed image was taken by an optical microscope with a 0.9 NA 100× objective lens. As the pixel is at the theoretical resolution limit of the optical microscope, printed pixels can only be distinguished in a blurred way (Fig. 4d). In Fig. 4e we exhibit laser prints of 9 images in different colours, which were taken by the same microscope with a 0.9 NA 100× objective lens. Although we have used a controlled laser power for patterning, the printing can also be performed with up to 5 colours, combining sub-diffraction-limit resolution and high sharpness (Fig. 4e). In particular, the images presented in Fig. 4d,e with about 125,000 pixels in total would fit into the cross-section of a human hair. Our plasmonic colour laser printer can perform printing technologies (for example, half-toning[26]) like any traditional printer, but at a super-high resolution (Fig. 4f). Moreover, it is worth noting that the image could also be laser-printed through a mask (Supplementary Fig. 12), a spatially modulated laser array or scanning mirrors, which would allow faster printing with a resolution approaching the single-unit-cell limit by building on the achievements in this work. With multicolour printing on plastic-based plasmonic metasurfaces, multinary code recording can be performed, paving the way for a low-cost recording apparatus (Supplementary Fig. 13). By incorporating the sub-wavelength recording and multinary plasmonic colour channels, a TB-level disk capacity for a DVD-sized disk with a single metasurface could potentially be realized.

In summary, we have demonstrated full-colour laser printing on plasmonic metasurfaces with sub-diffraction-limit resolution. The nanoimprinted metasurfaces are composed of a 20 nm Al film buried in a thin-film polymer that is flexible, economic and recyclable. Reconfigured by plasmon resonances, our laser printing process allows for recording speeds up to 1 Gbit s^{-1} with a spot energy down to 0.3 nJ. Colours are printed when only a single unit cell is modified by laser heating with individual pixels of 200 nm × 200 nm squares, thus enabling laser printing of colours at a resolution of ~127,000 DPI. This technology promises exciting avenues from large-scale colour printing and decoration to nanoscale colour patterning, encryption and data storage, where high information densities are pursued.

© 2015 Macmillan Publishers Limited. All rights reserved

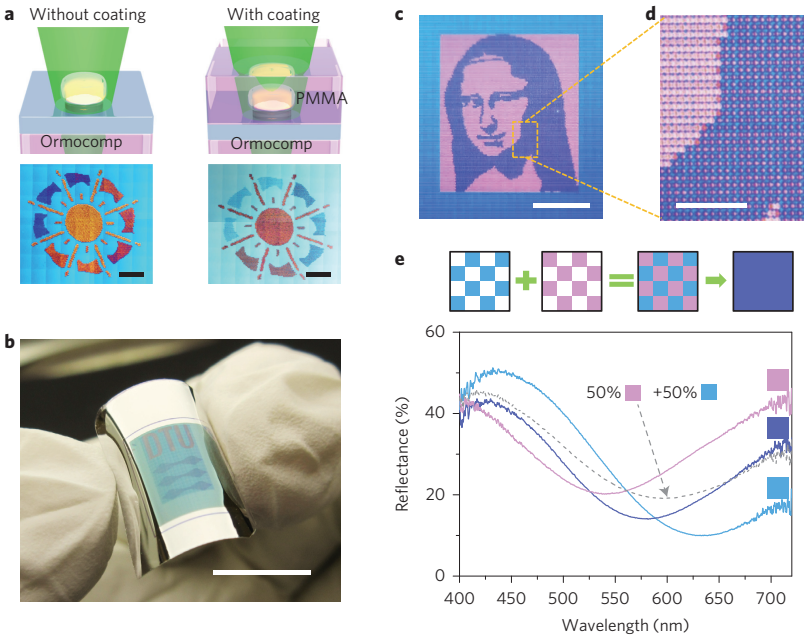

Figure 3 | Flexible and robust samples for colour printing and colour mixing. a, Illustrations and examples of laser printing on samples without (left) and with (right) polymer coating. Scale bars: 500 μm. **b**, A large-scale sample with plasmonic colours printed by a laser transmitted through the protecting polymer. Scale bar: 1 cm. **c**, A printed portrait of Mona Lisa photographed by a camera with a macro lens. Scale bar: 2 mm. **d**, A magnified image taken by a microscope exhibits colour dots with different dimensions. Scale bar: 500 μm. **e**, Corresponding reflection spectra of selected pixels with different colours: the background cyan colour, the printed magenta colour and the mixed blue-violet colour. Mixed colour dots make a new colour and a new spectrum.

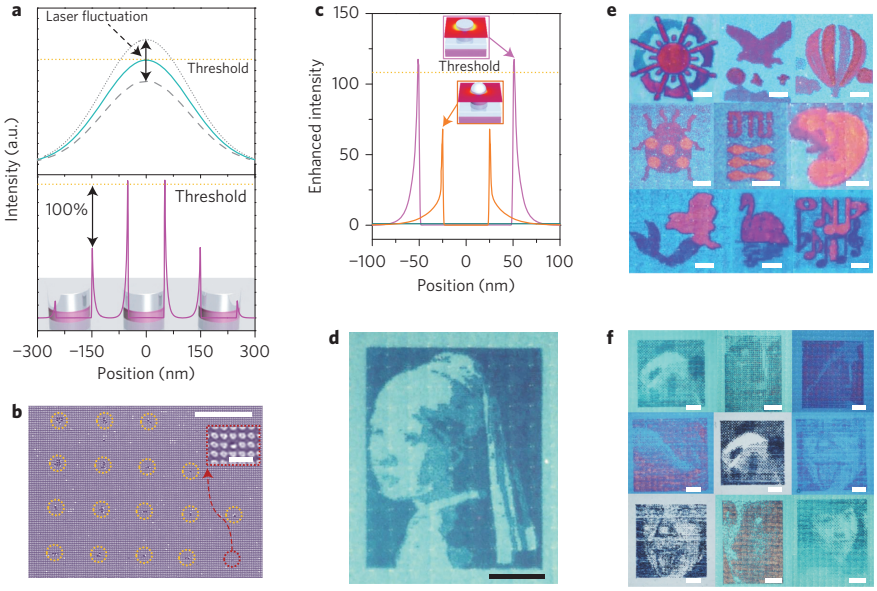

Figure 4 | Laser printing with sub-diffraction-limit resolution. a, Upper, sub-diffraction-limit laser printing without plasmonic reconfiguration, where dashed, solid and dotted lines respectively denote the laser-pulse energy below, at and above the melting threshold (the yellow dashed line). Bottom, advanced sub-diffraction-limit printing where photon energy is redistributed with optical field confinement and enhancement by the plasmonic metasurface. **b**, SEM image of voxels formed at exposure with different laser-pulse energies, decreases gradually from the upper left corner to the bottom right. Scale bar: 5 μm. The inset reveals an interesting area in the red dashed circle (scale bar: 500 nm). **c**, The field enhancements in the central section of the unit cells with a disk and a sphere, respectively. The insets show the corresponding 2D field distributions. **d**, A colour design in blue tone printed with single-unit-cell resolution (127,000 DPI). Scale bar: 10 μm. **e**, Printed images in different colour schemes with single-unit-cell resolution. The laser energy used for patterning was moderated to minimize the influence on different printing channels, whereas strong power will incite crosstalks of plasmonic energy distribution between the neighboring unit cells and degrade the resolution. Scale bars: 5 μm. **f**, A collection of images printed by gray-scale half-toning. The printing resolution is 63,500 DPI. Scale bars: 10 μm.

© 2015 Macmillan Publishers Limited. All rights reserved

Methods

Methods and any associated references are available in the online version of the paper.

Received 3 July 2015; accepted 4 November 2015;
published online 14 December 2015

References

1. Ebbesen, T. W., Lezec, H. J., Ghaemi, H. F., Thio, T. & Wolff, P. A. Extraordinary optical transmission through sub-wavelength hole arrays. *Nature* **391,** 667–669 (1998).
2. Maier, S. A. *Plasmonics: Fundamentals and Applications* (Springer, 2007).
3. Pendry, J. B., Schurig, D. & Smith, D. R. Controlling electromagnetic fields. *Science* **312,** 1780–1782 (2006).
4. Leonhardt, U. Optical conformal mapping. *Science* **312,** 1777–1780 (2006).
5. Dean, N. Colouring at the nanoscale. *Nature Nanotechnol.* **10,** 15–16 (2015).
6. Kumar, K. *et al.* Printing colour at the optical diffraction limit. *Nature Nanotechnol.* **7,** 557–561 (2012).
7. Wu, Y.-K., Hollowell, A. E., Zhang, C. & Guo, L. J. Angle-insensitive structural colours based on metallic nanocavities and coloured pixels beyond the diffraction limit. *Sci. Rep.* **3,** 1194 (2013).
8. Roberts, A. S., Pors, A., Albrektsen, O. & Bozhevolnyi, S. I. Subwavelength plasmonic color printing protected for ambient use. *Nano Lett.* **14,** 783–787 (2014).
9. Tan, S. J. *et al.* Plasmonic color palettes for photorealistic printing with aluminum nanostructures. *Nano Lett.* **14,** 4023–4029 (2014).
10. Goh, X. M. *et al.* Three-dimensional plasmonic stereoscopic prints in full colour. *Nature Commun.* **5,** 5361 (2014).
11. Ellenbogen, T., Seo, K. & Crozier, K. B. Chromatic plasmonic polarizers for active visible color filtering and polarimetry. *Nano Lett.* **12,** 1026–1031 (2012).
12. Zeng, B., Gao, Y. & Bartoli, F. J. Ultrathin nanostructured metals for highly transmissive plasmonic subtractive color filters. *Sci. Rep.* **3,** 2840 (2013).
13. Cheng, F., Gao, J., Luk, T. S. & Yang, X. Structural color printing based on plasmonic metasurfaces of perfect light absorption. *Sci. Rep.* **5,** 11045 (2015).
14. Yokogawa, S., Burgos, S. P. & Atwater, H. A. Plasmonic color filters for cmos image sensor applications. *Nano Lett.* **12,** 4349–4354 (2012).
15. Chichkov, B. N., Momma, C., Nolte, S., von Alvensleben, F. & Tünnermann, A. Femtosecond, picosecond and nanosecond laser ablation of solids. *Appl. Phys. A* **63,** 109–115 (1996).
16. Knight, M. W. *et al.* Aluminum plasmonic nanoantennas. *Nano Lett.* **12,** 6000–6004 (2012).
17. Olson, J. *et al.* Vivid, full-color aluminum plasmonic pixels. *Proc. Natl Acad. Sci. USA* **111,** 14348–14353 (2014).
18. Prodan, E., Radloff, C., Halas, N. & Nordlander, P. A hybridization model for the plasmon response of complex nanostructures. *Science* **302,** 419–422 (2003).
19. Clausen, J. S. *et al.* Plasmonic metasurfaces for coloration of plastic consumer products. *Nano Lett.* **14,** 4499–4504 (2014).
20. Wang, Y. M. *et al.* High aspect ratio 10-nm-scale nanoaperture arrays with template-guided metal dewetting. *Sci. Rep.* **5,** 9654 (2015).
21. Chen, X., Chen, Y., Yan, M. & Qiu, M. Nanosecond photothermal effects in plasmonic nanostructures. *ACS Nano* **6,** 2550–2557 (2012).
22. Zywietz, U., Evlyukhin, A. B., Reinhardt, C. & Chichkov, B. N. Laser printing of silicon nanoparticles with resonant optical electric and magnetic responses. *Nature Commun.* **5,** 3402 (2014).
23. Baffou, G., Quidant, R. & Garca de Abajo, F. J. Nanoscale control of optical heating in complex plasmonic systems. *ACS Nano* **4,** 709–716 (2010).
24. Zijlstra, P., Chon, J. W. M. & Gu, M. Five-dimensional optical recording mediated by surface plasmons in gold nanorods. *Nature* **459,** 410–413 (2009).
25. Kim, H. *et al.* Structural colour printing using a magnetically tunable and lithographically fixable photonic crystal. *Nature Photon.* **3,** 534–540 (2009).
26. Ulichney, R. *Digital Halftoning* (MIT Press, 1987).
27. Kawata, S., Sun, H., Tanaka, T. & Takada, K. Finer features for functional microdevices. *Nature* **412,** 697–698 (2001).
28. Barnes, W. L., Dereux, A. & Ebbesen, T. W. Surface plasmon subwavelength optics. *Nature* **424,** 824–830 (2003).
29. Fang, N., Lee, H., Sun, C. & Zhang, X. Sub-diffraction-limited optical imaging with a silver superlens. *Science* **308,** 534–537 (2005).

Acknowledgements

This work was supported by the European Commission through the FP7MMP Integrated project PLAST4FUTURE (NMP2-SE-2012-314345). The authors thank C. Smith and K. T. Sørensen for technical support and W. Yan, J. Clausen and S. Xiao for fruitful discussions.

Author contributions

X.Z., N.A.M. and A.K. conceived the ideas. X.Z. and E.H.-N. fabricated the nanoimprinted samples. X.Z. performed the simulations. C.V. suggested and built the optical setup for laser printing. X.Z. and C.V. developed the codes. X.Z. implemented the laser printing and prepared the figures. A.K. and N.A.M. provided feedback on the experiments. All authors contributed to the writing of the manuscript.

Additional information

Supplementary information is available in the online version of the paper. Reprints and permissions information is available online at www.nature.com/reprints. Correspondence and requests for materials should be addressed to X.Z., N.A.M. and A.K.

Competing financial interests

The authors declare no competing financial interests.

© 2015 Macmillan Publishers Limited. All rights reserved

Methods

Sample preparation. Firstly, a silicon master mold was fabricated by applying electron-beam lithography (EBL, JEOL JBX-9500FS 100 keV prototype) and dry etching. We used a fast single-spot writing technique, where EBL with a focused Gaussian beam was used to define shapes directly. The single-spot exposure strategy uses the EBL system as a raster scan tool to write a large area, when the beam step size is larger than the spot size[30]. The sample was fabricated on a 0.5 mm thick, 4 inch Borofloat glass wafer, upon which a thin film of Ormocomp mixed with ma-T 1,050 thinner (25% w/w, both microresist technology) was deposited. A silicon stamp with an anti-stiction coating was employed for replicating the pillar structure through room temperature nanoimprinting into the Ormocomp layer. The Ormocomp film was cured by exposure to UV light and separated from the silicon master, and subsequently peeled from the Borofloat glass substrate. Then, a 20 nm Al film was deposited by an electron beam evaporator (Alcatel SCM 600) at 5 Å s^{-1} after imprinting under a process pressure of 10^{-6} –10^{-5} mbar. For polymer-coated samples, a sufficiently thick layer of PMMA (10% 950PMMA in Anisole, MicroChem Corp) was spin-coated (500 rpm, ~10 μm) on top to avoid Fabry–Pérot interference.

Optical setups. The optical setup for laser colour printing is schematically illustrated in Supplementary Fig. 14a. It comprises a Nikon Ti-U inverted microscope where a laser (CryLaS FDSS532-150) emitting 1 ns pulses at 532 nm is used for printing. The laser pulse energy is controlled with a half-wave plate on a computer-controlled rotation stage combined with a polarizing beam splitter. The laser beam is focused onto the input port of a module of the microscope, which accepts fiber-coupled laser input sources for diffraction-limited focusing onto the sample. A white light source can also be coupled in for illumination, not shown in the figure. In this work, the sample was mounted on a computer-controlled piezo nanopositioning stage (Mad City Labs Nano H50 series piezoelectric stage, 0.1 nm resolution, 50 μm travel, XY axes), which was placed on a computer-controlled motor stage. The optical setup for spectroscopic imaging is illustrated in Supplementary Fig. 14b. A high-intensity white light source (Energetiq EQ-99XFC fiber coupled laser driven light source) is used for illumination. An image of the surface is projected onto the control CCD array, CCD1. A duplicated image of the device surface is projected onto the entrance slit of an imaging spectrometer with a 150 g mm^{-1} grating (Acton SP-2756 imaging spectrograph with PIXIS100B digital CCD camera, 100 × 1, 340 pixels, CCD2) by a beam splitter. Optical micrographs were acquired using a Nikon Eclipse L200 microscope with a Nikon digital camera (DS-Fi1). Photographs were taken by a Canon IXUS camera.

Laser printing. For spot-by-spot printing, a function generator was used to select single 1 ns pulses from the pulse train of the laser with the power tuned accordingly for each spot. Motor/piezo stages, rotators and laser controllers were connected to a computer via I/O equipment. A Matlab code was used to switch the laser on and off and select the repetition rate via the function generator, control the laser energy via the half-wave plate and the polarizing beam splitter, and move the piezo/motor stages for laser printing of images in a raster scan.

Numerical simulation. The plasmonic metasurface was simulated by CST (www.CST.com) microwave studio software. Reflection spectra and field distributions of structures under different conditions (thermal reshaping, oxide coating and so on) were simulated by the finite element method. An EM–thermal co-simulation approach was applied to solve the coupled electromagnetic and heat transfer problem. The results are presented and further discussed in the Supplementary Information.

References

30. Højlund-Nielsen, E., Greibe, T., Mortensen, N. A. & Kristensen, A. Single-spot e-beam lithography for defining large arrays of nano-holes. *Microelectron. Eng.* **121,** 104–107 (2014).

© 2015 Macmillan Publishers Limited. All rights reserved

A.8 Højlund-Nielsen et al. 2016 (submitted)

Plasmonic colors: Toward mass-production of metasurfaces

Emil Højlund-Nielsen[*], Jeppe Clausen[†], Tapio Mäkela[‡], Lasse Højlund Thamdrup[§], Maksim Zalkovskij[§], Theodor Nielsen[§], Nello Le Pira[¶], Jouni Ahopelto[‡], N. Asger Mortensen[†], Anders Kristensen[*]

January 7, 2016

Plasmonic metasurface coloration has attracted considerable attention in recent years due to its industrial potential. So far, demonstrations have been limited to small patterned areas fabricated using expensive techniques with limited scalability. Here we levitate the technology beyond the common size and volume-limitations of nanofabrication and demonstrate aluminum-coated polymer-based colored metasurfaces of square-centimeter size by embossing, injection molding, roll-to-roll printing, and film insert molding. We compare the different techniques and discuss the requirements and bottlenecks in terms of master fabrication, replication, metallization, and protection coating for large scale production of sub-wavelength metasurfaces. Most notably, we demonstrate that plasmonic metasurface colors are compatible with film insert molding. The results indicate a promising future for plasmonic colors as a viable alternative for decorating mass-produced polymer parts.

Today, colorants, such as pigments or dyes, are used to color plastic consumer products, either as base for bulk-colored products or in inks for surface decoration. Given the high societal attention to environment and recycling of waste materials, used plastic products must be mechanically sorted by color before recycling [1]. This poses limitations on the efficiency of large scale recycling efforts. As an alternative to chemistry-based coloring, nano-scale structural coloring has been proposed [2] to minimize usage of additives and post-production steps and to increase pattern resolution. Here, colors are achieved by means of resonant light-matter interactions on a nano-patterned surface. Specifically, we propose a inter-compatible polymer-metal-coating system, as seen in Figure 1. Thereby, the sorting by color can arguably be avoided in the recycling stage, see Figure 1a, as destruction of the nano-scale surface topology removes the color properties thus leaving the bulk polymer ready for re-processing, with only a ppm-level residue of aluminum for recycling. As such, nano-scale metasurface coloring provides new perspectives for the sustainability of plastic products.

Recently, aluminum-coated plasmonic structures have been firmly established as a route towards creating colorful polymeric materials [3, 4]. Aluminum has been argued to be superior to typical plasmonic materials, such as silver [5] and gold [6], due to its natural abundance, low cost, protective oxide layer for high durability [7, 8, 9] and attractive plasmonic properties in the visible range [10, 11, 12, 13, 14, 15, 16, 17]. Based on aluminum, reflective plasmonic colors utilizing the concept of localized surface plasmon resonances (LSPR) have been presented [3, 4, 18, 19], see Figure 1b. Here, the hybridization between LSPR modes [20] in aluminum nano-disks and nano-holes has been used to design and fabricate bright colors that are tunable in the visible spectrum. Finally, the structural color effects can be made robust for everyday use by applying a protective coating on top, which leads to a red-shift of the plasmonic resonances [3]. Simulated reflectance spectra are provided in Figure 1c. Previously reported demonstrations have been limited to patterned areas only visible under an optical microscope and to expensive techniques of limited scalability.

Here, we consider polymer replication techniques that are suited for mass-production. Polymers have been known for a long time as a replication material with nanometer resolution [21], although the underlying solidification mechanisms are still being debated [22]. Today, commercial injection molding is routinely used to replicate dense features down to 150 nm in the case of Blu-Ray discs and 5 nm lateral replication resolution has been achieved [23, 24, 25, 26]. This suggests, that the lower limit of replication is primarily determined by the topology of the master and independent of polymer-chain dimensions. Here, we combine polymer replication with plasmonic metasurfaces based on LSPR modes to produce color metasurfaces with in-

[*]Technical University of Denmark, DTU Nanotech, Ørsteds Plads, Building 345E, DK-2800 Kgs. Lyngby, Denmark. Corresponding author: anders.kristensen@nanotech.dtu.dk.

[†]Technical University of Denmark, DTU Fotonik, Ørsteds Plads, Building 343, DK-2800 Kgs. Lyngby, Denmark.

[‡]VTT Microsystems and Nanoelectronics, P.O. Box 1000, FI-02044 VTT, Finland.

[§]NIL Technology ApS, Diplomvej 381, DK-2800 Kgs. Lyngby, Denmark.

[¶]C.R.F. S.C.p.A, Strada Torino 50, 10043 Orbassano, TO, Italy.

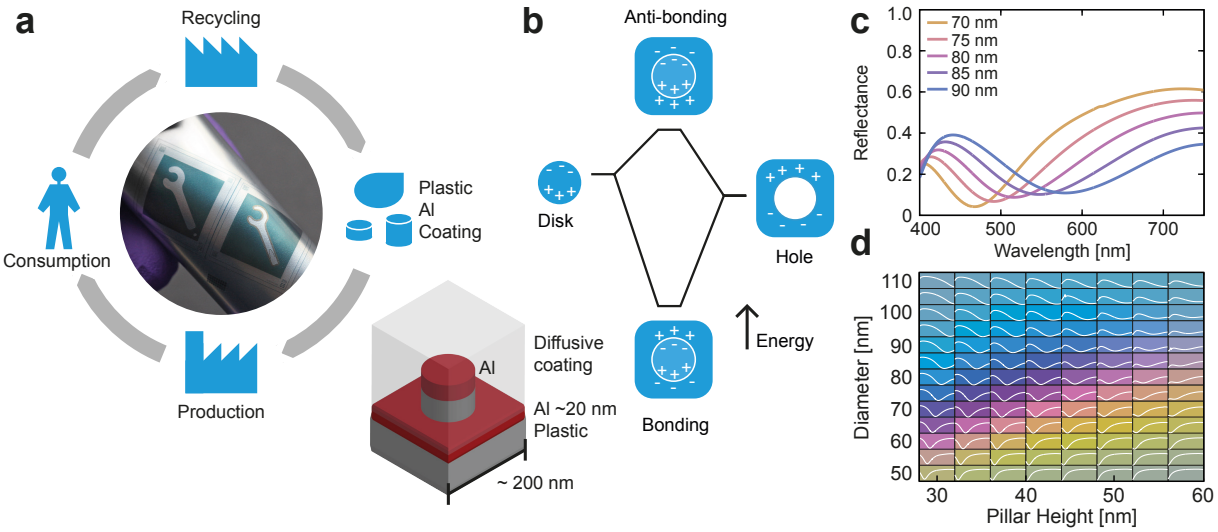

Figure 1: Metasurface color concept based on localized surface plasmon resonances. a) Recycle-based component life cycle and photograph of a rolled-up embossed 50 µm thick polymer with 20 nm aluminum and a protective diffusive top coating system. Macroscopic bending does not affect the color properties. b) Energy hybridization band diagram and sketch of typical geometries. c) Simulated normal-incidence reflectance spectra based on a refractive index of 1.5 for both plastic and clear coating. d) Similar simulated reflectance spectra for typical dimensions converted into colors.

dustrial applicability.

1 Roll-to-roll Printing

Roll-to-roll printing is an emerging technology in the field of manufacturing micro- and nano-scale patterns and it has been attracting interest because of its inherent advantages of low cost, high throughput and large area patterning [27, 28, 29, 30, 31, 32]. In recent years, a number of commercial applications have emerged, particularly optical displays, functional coatings and multifunctional films based on micron-sized structures [33]. Roll-to-roll thermal nanoimprint lithography with 100 nm linear grooves has been demonstrated [29], however general adaptation from the micro-scale to the nano-scale has proven difficult due to viscoelastic recovery experienced in the relatively fast printing process. Therefore, strict control of the temperature and utilized pressure on the imprinted foil is crucial. Roll-to-roll extrusion coating has also been demonstrated [34]. Based on previous work [35, 28], we demonstrate two-dimensional 115 nm surface plasmon resonance structures with a high edge quality suitable for plasmonic coloring on a relatively large area, see Figure 2.

1.1 Roll-to-roll Fabrication

The fabrication process for making the colored samples is outlined in Figure 2b. First a silicon master was patterned by electron beam lithography and anisotropic dry etching. Subsequently, the silicon master was used in a double pattern inversion scheme to make a nickel shim with a thickness of 100 µm and a structure depth of 44 nm. The nickel shim thickness was tuned to allow for a high degree of bendability.

The polymer replication process was carried out using a custom thermal roll-to-roll tool described in detail in Ref [27]. The flexible pre-patterned nickel shim was wrapped around a roll with a diameter of 66 mm. Then a heated roll was pressed against a cold backing roll with a force of 600 N, resulting in a force between the rolls (NIP) of approximately 1000 N. The utilized web materials included 100 µm to 125 µm thick polymethylmetcarylate (PMMA), polycarbonate (PC), amorphous polyethylene terephthalate (A-PET) and cellulose acetate (CA).

The temperature of the imprinting roll was adjusted to be above the film softening temperature, which is typically slightly below the glass transition temperature T_g of the different materials. Roll-to-roll process printing temperatures are usually kept slightly below the glass transition or the melting temperature to avoid bending, wrinkling or other changes to the surface oc-

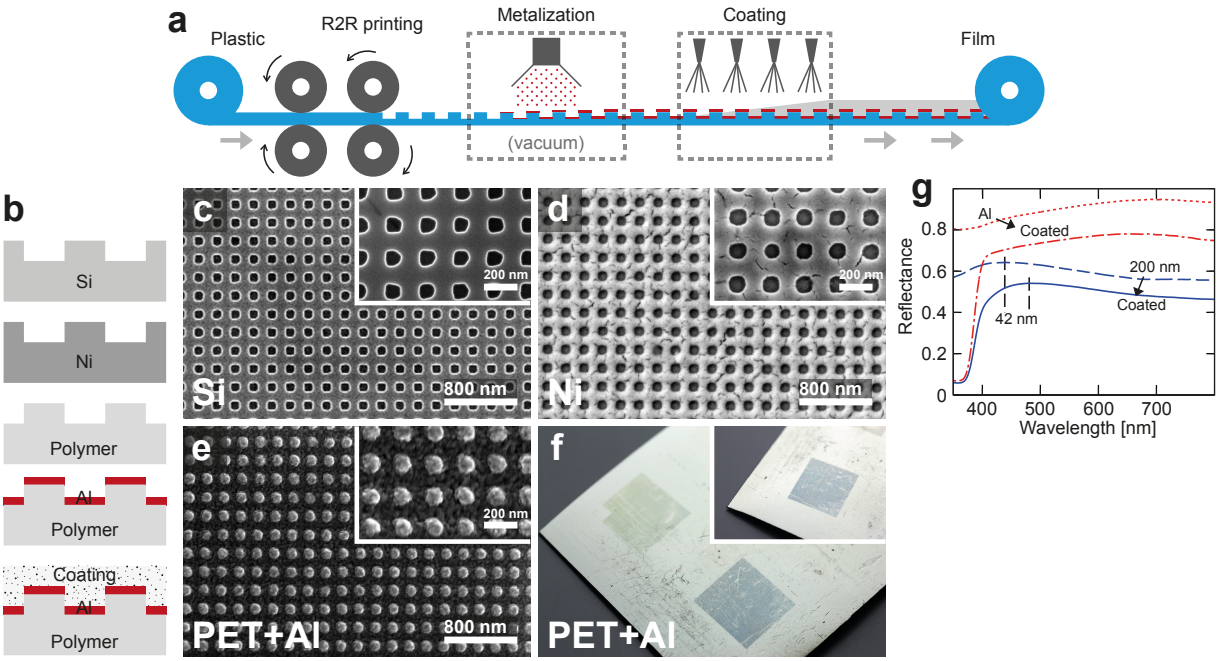

Figure 2: Roll-to-roll nano-printing. a) Schematic of roll-to-roll process. b) Sketch of fabrication process from pattern definition to metalized polymer replica. c) SEM images of Si master. d) SEM images of nickel master. e) SEM images of roll-to-roll polymer replication with aluminum on top. f) Photographs of the finished A-PET polymer surface without coating for 200 nm period (blue) and 300 nm period (green) areas of size 0.5 mm x 0.5 mm. (g) Measured reflectance spectra by integrating sphere at 8 degrees incidence of 200 nm period area (blue curves) compared to non-structured aluminum surface (red curves) with (solid lines) and without coating (dashed lines). A red-shift is seen after coating.

curring at the glass transition temperature. The glass transition temperature for CA and PMMA films is 105 °C. For the A-Pet film, the glass transition temperature is 72 °C and the melting temperature is 250 °C. A speed of 0.3 m/min was used, leading to an imprint time of roughly 0.3 s with a 3 mm contact length between the rolls. The contact length was varied by tuning the hardness of the backing roll. The best replication was obtained when considering pillars with a diameter of 115 nm (SEM) and a height of 40 nm (AFM) on A-PET at a printing temperature of 110 °C (± 2 °C).

After production of the polymer samples, an aluminum layer was deposited by electron beam evaporation in 2×10^{-9} bar vacuum, see Figure 2e. The deposition rate was 0.5 nm/s for a thickness of 16 nm measured by quartz crystal microbalance during deposition. Finally, samples were coated by approximately 50 µm of scratch-resistant commercial automotive lacquer in a two step process, where the first layer of acrylic copolymer (AU175 Flattening Binder, Axalta Coating Systems) acts as a diffuser, mimicking the scattering properties of traditional paint, and the top layer (3760S Ultra Productive VOC Hi-Temp Clear, DuPont) creates a high-gloss visual appearance.

1.2 Roll-to-roll Results

Photographs, taken under fixed light conditions, of the sample after coating are shown in Figure 2f. The sample scratches are due to the industrial grade film itself and wear-and-tear mold degradation. The pattern with 200 nm period yields a distinct blue color-response, in agreement with the simulation results shown in Figure 1d. Combined with the protective properties of the coating, our approach provides scalable mass production of durable structural colors. In contrast to the blue 200 nm period pattern, the color-response of the 300 nm period pattern varies strongly with the orientation of the sample with respect to the light source and camera. This dependence is well-described in literature [36, 3] and illustrates the requirement, due to the frequency-range of the human visible spectrum, for nano-scale patterns with periodicities on the order of 200 nm or smaller.

In Figure 2g, measured reflection spectra by integrating sphere using a silicon specular reference can be seen for the 200 nm period pattern compared to the non-structured aluminum sample surface. A maximum in reflectance around a vacuum wavelength of 439 nm in the blue part of the spectrum is observed, as longer wavelengths are absorbed to a higher degree by the LSPR located in the red part of the spectrum. After coating, a red-shift of the maximum reflectance of approximately 42 nm can been be measured (the low ultra-violet reflectance is a property of the coating). The red-shift of the maximum reflectance corresponds to a LSPR red-shift [3] and implies that the optical properties of the coating must be included in any design considerations.

Even though the printing speed used here is modest (0.3 m/min), the nature of the continuous roll process inherently makes it possible to process e.g. 500 m of film without stopping. By optimizing printing parameters, higher manufacturing speeds may be achieved if the pressure can be increased correspondingly. The web width (currently 60 mm) is completely scalable and thereby the system offers mass-production capabilities. The use of roll-to-roll printing enables large volume fabrication of consumer products with nano-scale polymer surface coloration for a wide range of applications.

2 Film Insert Molding

Film Insert Molding (also known as in-mold decorating/labeling, IMD/IML) is a well-known industrial technique [37, 38] used to apply surface coatings or decorations onto components to enhance durability and aesthetic value [39]. The one-step decoration technique is often favored due to its simplicity over multi step processes, such as silk-screen printing and painting [40]. Figure 3 summarizes the results. The main advantage of the technique, in terms of nanoreplication, is the use of conventional equipment and processes without modifications.

Figure 3a outlines an industrial implementation scheme for achieving metasurfares. In the configuration used here, the outer surface is nano-patterned which calls for a protective coating to be implemented. The manufactured metasurface is produced by embossing in this work, however other techniques such as roll-to-roll printing or injection molding can be used to increase flexibility and speed.

2.1 Film Insert Molding Fabrication

The fabrication process for making the plasmon colored samples is outlined in Figure 3b. First, the metasurface insert was prepared. The pattern was defined by electron beam lithography and anisotropic dry etching in silicon and subsequently transferred by embossing (CNI tool, NIL Technology) PC and PMMA foils using a pressure of 6.5 bar at a temperature of 150 °C for 8 min. Then Al was deposited using the same process as for the roll-to-roll printed samples.

The film insert molding tests were performed on a Sandretto 65 tons tool using 400 bars of injection pressure and a 180 °C temperature threshold. The machine back-injected PMMA (PLEXIGLAS® 8N, Evonik) exhibiting good flow, high mechanical strength, surface hardness and abrasion resistance. Both PC and PMMA embossed film inserts were used.

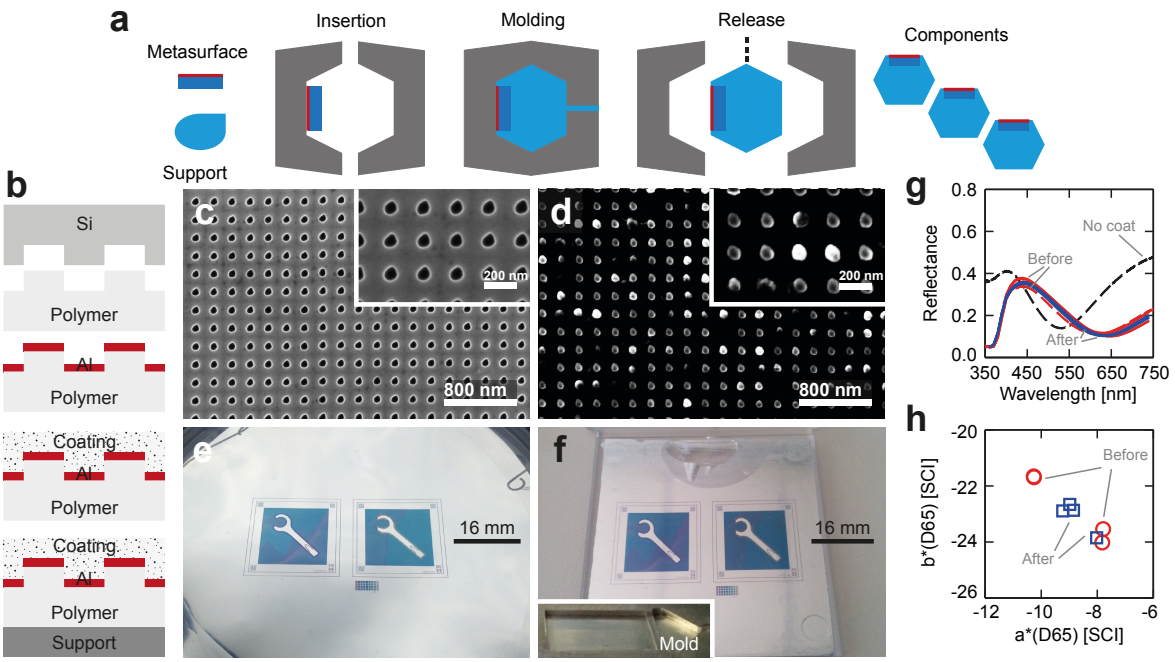

Figure 3: Film Insert Molding. a) Schematic of general film insert process. b) Sketch of fabrication process for 200 nm periodic structures from pattern definition to metalized polymer component. c) SEM images of Si master. d) SEM images of polymer metasurface by embossing with 20 nm aluminum on top. e) Photograph of aluminum coated PMMA foil based on 200 nm periodic pattern. f) Photograph of film insert molding component after 400 bars of injection pressure and 180 °C threshold for back-injecting PMMA material. g) Reflectance spectra of sample before and after film insert molding. h) Plots of the shift in colormetric values.

2.2 Film Insert Molding Results

The results can be seen in Figure 3e-h. The foil shown in Figure 3e comprises a thin film of aluminum embedded between a patterned PMMA carrier foil and a protective surface coating. A 200 nm periodic 2D array of nanoscale cylinders was replicated on the surface of the PMMA foil to obtain the blue plasmonic metasurface. Variations in the pillar replication fidelity introduce purple shades to the otherwise blue pattern. In Figure 3d, the same sample foil forms the surface of a molded component by back-injection. The artifacts on the top of the component are due to the double sided tape on an otherwise flat mold surface holding the metasurface in place before molding. This indicates that the thickness of the metasurface film should be increased for more demanding mold geometries in order to withstand shear forces during molding.

In terms of color, no changes can be seen by the eye when comparing Figure 3e and Figure 3f. To quantify this, Figure 3g plots the reflectance spectra of two samples before and after the film insert molding and Figure 3h plots the corresponding colormetric values with a non-observable CIELAB 1976 color difference metric of $\Delta E^* \cong 1.30$. Intuitively, the durable top coating system prevents the nano-pillars from collapsing. Instead the pressure is distributed throughout the macroscale component thereby eliminating shear forces at the aluminum interface. Thereby, we demonstrate that implementing plasmonic colors by film insert molding on large freeform plastic components is possible without degradation of the color properties as a result of the high process pressure.

3 Injection Molding

Injection molding is the preferred industrial process for polymer replication due to low cycle times and the multitude of technologies established for full process automation [41, 42]. The results of the injection molding trials are provided in Figure 4.

In conventional injection molding, the polymer solidification is coupled to the cavity filling process [43]. As the molten polymer is injected into the cold mold cavity, it starts to cool and solidify from the mold surface where the melt comes in contact. Consequently, the polymer molecules near the surface are elongated due to shear flow and elongation flow and freeze when they come in contact with the cold mold surface, creating a frozen-in molecular orientation in the "skin layer" [44]. To avoid this, the bulk mold temperature or at least the contact surface often needs to be above the glass-transition temperature of the polymer. Therefore, the most important factor for achieving good replication of micro and nano-structures is generally agreed to be a strict control of the mold temperature [25, 45].

Commonly, a variotherm process is utilized during injection molding. Here, active heating and cooling of the mold is employed during each cycle. Whereas conventional injection molding uses cycle times from 1–30 s, variotherm processes may require 100–300 s for each replication when accurate thermal control is required [46]. To avoid variotherm processes, other solutions based on insulation layers have been proposed [43, 47, 48]. Advanced mold designs and manipulators have been developed to reduce the cycle time below 30 s at the price of more complex and expensive mold fabrication schemes and less thermal control of the mold surface. These involve heating of the mold material itself by Joule [49, 50, 51] or induction heating [52, 53]. Other methods employ external heating of the mold surface, such as infrared heating [54] or steam heating [55]. Laser-heating of the mold has also been used to achieve extremely rapid mold heating on the order of 300 °C per second [56], although with a spatially inhomogeneous temperature profile over a small area. Several of these methods have demonstrated cycle times comparable to conventional injection molding. However, with considerable added hardware complexity.

In the context of nanoreplication, a schematic for large scale implementation can be seen in Figure 4a. First, the mold or an insert is prepared with the inverse nano-structured topology. Then the plastic is injected and the component is released. Finally the necessary post-processing in the form of metallization and coating completes the production cycle. The direct injection molding requires nano-structures embedded in the mold surface, which was solved in this work by utilizing a nickel shim insert fabricated by electroplating from a silicon master.

3.1 Injection Molding Fabrication

In Figure 4b, the fabrication process is outlined. The nickel-shim for injection molding was made in the same manner as the roll-to-roll nickel shim.

The injection molding was carried out in an Arburg 270S machine using a commercial grade of the terpolymer acrylonitrile butadiene styrene (ABS). The polymer melt was injected at 230 °C with an injection pressure of 679 bar. After injection, a holding pressure of 800 bar for 1.5 s and then 450 bar for 2.0 s was applied. A manual variotherm process was used were the mold temperature was cooled from 131 °C to 80 °C. After demolding, the samples were metallized by electron beam deposition and coated using the same procedure as used for all other samples.

3.2 Injection Molding Results

The results can be seen in Figure 4c-h for 200 nm periodic structures from pattern definition to metalized polymer component. In Figure 4c, SEM images of the nickel shim can be seen, while

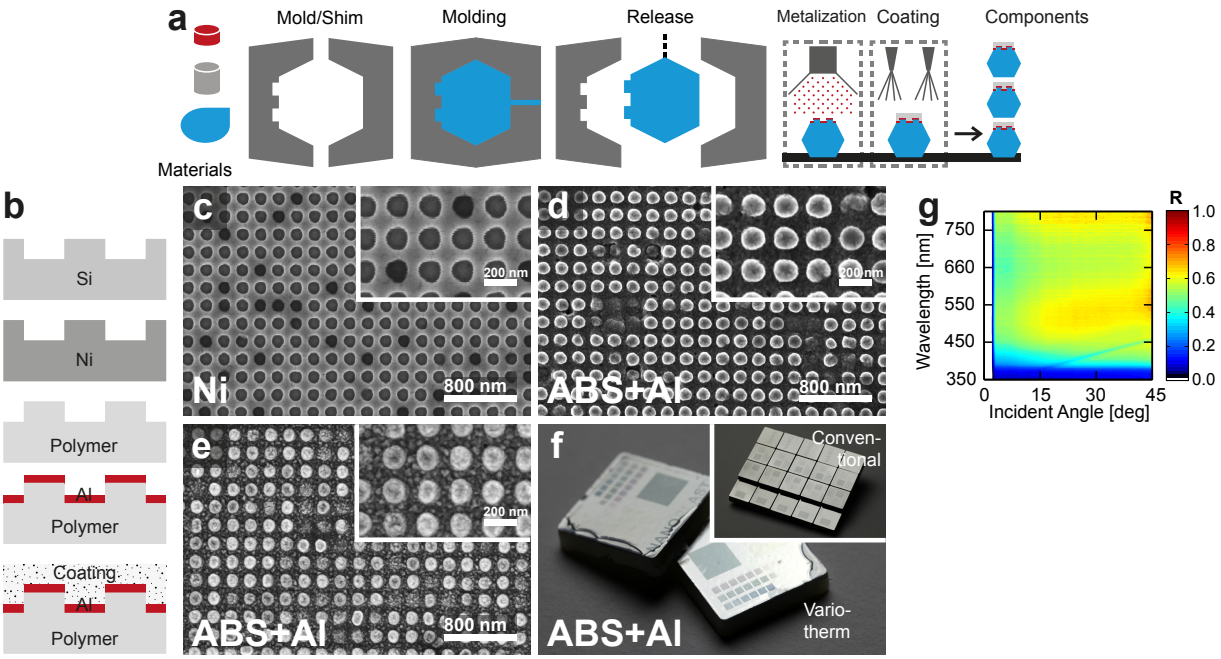

Figure 4: Injection molding. a) Schematic of process. b) Sketch of fabrication process for 200 nm periodic structures from pattern definition to metalized polymer component. c) SEM images of master. d) SEM images of variotherm metalized replica. e) SEM images of metalized conventional replica. e) Photographs of samples produced using a variotherm process and a conventional monotherm process (inset). g) Specular reflectance angular-resolved spectra.

Figure 4d shows the replicated structures based on a variotherm process. The pattern defect is found to be related to degradation of the polymer material as a result of long cycle times, as it does not appear during conventional molding as seen in Figure 4e. In Figure 4f, photographs of the final samples after metallization can be seen.

4 Discussion

The replication of micro and nano-structures is governed by the rheological properties of the polymer (e.g. non-newtonian fluid-dynamics) and thermodynamics at the interface between polymer and the surface of the replicating tool. The initial contact temperature at the interface between two semi-infinite solid bodies with different initial temperatures T_1 and T_2 is determined by [47]:

$$\frac{T_1 - T_0}{T_0 - T_2} = \left(\frac{(\kappa \rho c_p)_2}{(\kappa \rho c_p)_1} \right)^{\frac{1}{2}}, \qquad (1)$$

where κ is the thermal conductivity, ρ is the density, c_p is the specific heat capacity, and subscripts 1 and 2 refer to the polymer and tool respectively. Equation (1) is strictly speaking only valid for semi-infinite bodies, however, in many cases, it provides reasonable quantitative estimates. For conventional molding with a nickel master, the impact surface temperature of the polymer melt is below the glass transition temperature for a broad range of parameters and materials, which explains the low quality of the roll-to-roll and injection molding trials. Chrome-based coatings or hydrogen silsesquioxane can be used to increase the impact surface temperature at isothermal mold conditions [57, 58].

5 Conclusion

In conclusion, we reported on different techniques for mass-producing plasmonic colors based on aluminum thin film coating by LSPR using roll-to-roll printing, film insert molding and direct injection molding of polymeric materials. The use of mass-production techniques demonstrates a route for scalable production, which may lead to low-cost pattering and commer-

cial uptake of plasmonic colors. Most notably, we demonstrated that plasmonic metasurface colors by film insert molding is possible without degradation of the color under high pressure. Nano-scale structural coloring provides new perspectives for recycling and sustainability of plastic products, as the colors are based on removable physical structures in the surface rather than traditional chemistry-based that in some cases are distributed throughout the bulk volume of polymer parts.

Finally, we note that the present approach to plasmonic metasurface fabrication may be combined with the recent demonstration of a sub-sequent laser-post-processing for high-resolution printing of vivid colors [59].

Acknowledgement

We acknowledge Kristoffer Mathisen, Lea Berthou, Darmin Catak for experimental help and Jesper Scheel for photography. This work was supported by the European Commission via the FP7 MMP Integrated project Plast4Future (NMP2-SE-2012-314345).

References

[1] S M Al-Salem, P Lettieri, and J Baeyens. Recycling and recovery routes of plastic solid waste (PSW): a review. *Waste Manag.*, 29(10):2625–43, oct 2009.

[2] Karthik Kumar, Huigao Duan, Ravi S Hegde, Samuel C W Koh, Jennifer N Wei, and Joel K W Yang. Printing colour at the optical diffraction limit. *Nat. Nanotechnol.*, 7(August):557–561, sep 2012.

[3] Jeppe S Clausen, Emil Højlund-Nielsen, Alexander B Christiansen, Sadegh Yazdi, Meir Grajower, Hesham Taha, Uriel Levy, Anders Kristensen, and N Asger Mortensen. Plasmonic Metasurfaces for Coloration of Plastic Consumer Products. *Nano Lett.*, 14(8):4499–4504, aug 2014.

[4] Shawn J Tan, Lei Zhang, Di Zhu, Xiao Ming Goh, Ying Min Wang, Karthik Kumar, Cheng-Wei Qiu, and Joel K W Yang. Plasmonic Color Palettes for Photorealistic Printing with Aluminum Nanostructures. *Nano Lett.*, 14(7):4023–4029, jul 2014.

[5] Guangyuan Si, Yanhui Zhao, Jiangtao Lv, Mengqian Lu, Fengwen Wang, Hailong Liu, Ning Xiang, Tony Jun Huang, Aaron J Danner, Jinghua Teng, and Yan Jun Liu. Reflective plasmonic color filters based on lithographically patterned silver nanorod arrays. *Nanoscale*, 5(14):6243–6248, jul 2013.

[6] Alexander S Roberts, Anders Pors, Ole Albrektsen, and Sergey I Bozhevolnyi. Subwavelength Plasmonic Color Printing Protected for Ambient Use. *Nano Lett.*, 14(2):783–787, feb 2014.

[7] Alba L. Ramaswamy and Pamela Kaste. A Nanovision of the Physiochemical Phenomena Occurring in Nanoparticles of Aluminum. *J. Energ. Mater.*, 23(1):1–25, mar 2005.

[8] L. Jeurgens, W. Sloof, F. Tichelaar, and E. Mittemeijer. Thermodynamic stability of amorphous oxide films on metals: Application to aluminum oxide films on aluminum substrates. *Phys. Rev. B*, 62(7):4707–4719, aug 2000.

[9] George H. Chan, Jing Zhao, George C. Schatz, and Richard P. Van Duyne. Localized Surface Plasmon Resonance Spectroscopy of Triangular Aluminum Nanoparticles. *J. Phys. Chem. C*, 112(36):13958–13963, sep 2008.

[10] P.R. West, S. Ishii, G.V. Naik, N.K. Emani, V.M. Shalaev, and A. Boltasseva. Searching for better plasmonic materials. *Laser Photon. Rev.*, 4(6):795–808, nov 2010.

[11] Mark W Knight, Lifei Liu, Yumin Wang, Lisa Brown, Shaunak Mukherjee, Nicholas S King, Henry O Everitt, Peter Nordlander, and Naomi J Halas. Aluminum plasmonic nanoantennas. *Nano Lett.*, 12(11):6000–6004, nov 2012.

[12] Jianfa Zhang, Jun-Yu Ou, Nikitas Papasimakis, Yifang Chen, Kevin F. MacDonald, and Nikolay I Zheludev. Continuous metal plasmonic frequency selective surfaces. *Opt. Express*, 19(23):23279–23285, nov 2011.

[13] Vikram Kulkarni, Emil Prodan, and Peter Nordlander. Quantum Plasmonics: Optical Properties of a Nanomatryushka. *Nano Lett.*, 13(12):5873–5879, dec 2013.

[14] Christoph Langhammer, Markus Schwind, Bengt Kasemo, and Igor Zorić. Localized surface plasmon resonances in aluminum nanodisks. *Nano Lett.*, 8(5):1461–1471, 2008.

[15] Qin Chen and David R S Cumming. High transmission and low color cross-talk plasmonic color filters using triangular-lattice hole arrays in aluminum films. *Opt. Express*, 18(13):14056–14062, jun 2010.

[16] Mark W Knight, Nicholas S King, Lifei Liu, Henry O Everitt, Peter Nordlander, and Naomi J Halas. Aluminum for Plasmonics. *ACS Nano*, 8(1):834–840, jan 2014.

[17] Igor Zorić, Michael Zäch, Bengt Kasemo, and Christoph Langhammer. Gold, platinum, and aluminum nanodisk plasmons: Material independence, subradiance, and damping mechanisms. *ACS Nano*, 5(4):2535–2546, 2011.

[18] Hans Lochbihler. Reflective colored image based on metal-dielectric-metal-coated gratings. *Opt. Lett.*, 38(9):1398, may 2013.

[19] Jana Olson, Alejandro Manjavacas, Lifei Liu, Wei-Shun Chang, Benjamin Foerster, Nicholas S King, Mark W Knight, Peter Nordlander, Naomi J Halas, and Stephan Link. Vivid, full-color aluminum plasmonic pixels. *Proc. Natl. Acad. Sci.*, 111(40):14348–14353, sep 2014.

[20] E Prodan, C Radloff, N J Halas, and P Nordlander. A hybridization model for the plasmon response of complex nanostructures. *Science*, 302(5644):419–422, oct 2003.

[21] L Reimer and C Schulte. Elektronenmikroskopische Oberflächenabdriicke und ihr Auflösungsvermögen. *Naturwissenschaften*, 9(19):489–97, 1966.

[22] H. Schift, C. David, M. Gabriel, J. Gobrecht, L.J. Heyderman, W. Kaiser, S. Köppel, and L. Scandella. Nanoreplication in polymers using hot embossing and injection molding. *Microelectron. Eng.*, 53(1-4):171–174, jun 2000.

[23] D Macintyre and S. Thoms. The fabrication of high resolution features by mould injection. *Microelectron. Eng.*, 41-42:211–214, mar 1998.

[24] Nikolaj Gadegaard, Stephan Mosler, and Niels B. Larsen. Biomimetic Polymer Nanostructures by Injection Molding. *Macromol. Mater. Eng.*, 288(1):76–83, jan 2003.

[25] Maria Matschuk and Niels B Larsen. Injection molding of high aspect ratio sub-100 nm nanostructures. *J. Micromechanics Microengineering*, 23(2):025003, feb 2013.

[26] Maria Matschuk, Henrik Bruus, and Niels B. Larsen. Nanostructures for all-polymer microfluidic systems. *Microelectron. Eng.*, 87(5-8):1379–1382, may 2010.

[27] Arne Schleunitz, Christian Spreu, Tapio Mäkelä, Tomi Haatainen, Anna Klukowska, and Helmut Schift. Hybrid working stamps for high speed roll-to-roll nanoreplication with molded sol-gel relief on a metal backbone. *Microelectron. Eng.*, 88(8):2113–2116, aug 2011.

[28] Tapio Mäkelä, Tomi Haatainen, and Jouni Ahopelto. Roll-to-roll printed gratings in cellulose acetate web using novel nanoimprinting device. *Microelectron. Eng.*, 88(8):2045–2047, aug 2011.

[29] Nazrin Kooy, Khairudin Mohamed, Lee Pin, and Ooi Guan. A review of roll-to-roll nanoimprint lithography. *Nanoscale Res. Lett.*, 9(1):320, jan 2014.

[30] Linfa Peng, Yujun Deng, Peiyun Yi, and Xinmin Lai. Micro hot embossing of thermoplastic polymers: a review. *J. Micromechanics Microengineering*, 24(1):013001, jan 2014.

[31] C. Y. Chang, S. Y. Yang, and J. L. Sheh. A roller embossing process for rapid fabrication of microlens arrays on glass substrates. *Microsyst. Technol.*, 12(8):754–759, feb 2006.

[32] Lip Pin Yeo, Sum Huan Ng, Zhenfeng Wang, Zhiping Wang, and Nicolaas Frans de Rooij. Micro-fabrication of polymeric devices using hot roller embossing. *Microelectron. Eng.*, 86(4-6):933–936, apr 2009.

[33] Jarrett J. Dumond and Hong Yee Low. Recent developments and design challenges in continuous roller micro- and nanoimprinting. *J. Vac. Sci. Technol. B Microelectron. Nanom. Struct.*, 30(1):010801, 2012.

[34] Swathi Murthy, Maria Matschuk, Qian Huang, Nikolaj K. Mandsberg, Nikolaj A. Feidenhans'l, Peter Johansen, Lars Christensen, Henrik Pranov, Guggi Kofod, Henrik C. Pedersen, Ole Hassager, and Rafael Taboryski. Fabrication of Nanostructures by Roll-to-Roll Extrusion Coating. *Adv. Eng. Mater.*, pages n/a–n/a, sep 2015.

[35] Noriyuki Unno, Tapio Mäkelä, and Jun Taniguchi. Thermal roll-to-roll imprinted nanogratings on plastic film. *J. Vac. Sci. Technol. B, Nanotechnol. Microelectron. Mater. Process. Meas. Phenom.*, 32(6):06FG03, nov 2014.

[36] Emil Højlund-Nielsen, Johannes Weirich, Jesper Nørregaard, Joergen Garnaes, N. Asger Mortensen, and Anders Kristensen. Angle-independent structural colors of silicon. *J. Nanophotonics*, 8(1):083988, may 2014.

[37] Seong Yun Kim, Seung Hwan Lee, Soo Jin Baek, and Jae Ryoun Youn. Thermoviscoelastic Behavior of Film-Insert-Molded Parts Prepared under Various Processing Conditions. *Macromol. Mater. Eng.*, 293(12):969–978, dec 2008.

[38] D Lee, W.-A. Chen, T.-W. Huang, and S.-J. Liu. Factors Influencing the Warpage in In-Mold Decoration Injection Molded Composites. *Int. Polym. Process.*, 28(2):221–227, may 2013.

[39] Y. W. Leong, S. Yamaguchi, M. Mizoguchi, H. Hamada, U. S. Ishiaku, and T. Tsujii. The effect of molding conditions on mechanical and morphological properties at the interface of film insert injection molded polypropylene-film/polypropylene matrix. *Polym. Eng. Sci.*, 44(12):2327–2334, dec 2004.

[40] Y. W. Leong, M. Kotaki, and H. Hamada. Effects of the molecular orientation and crystallization on film-substrate interfacial adhesion in poly(ethylene terephthalate) film-insert moldings. *J. Appl. Polym. Sci.*, 104(4):2100–2107, may 2007.

[41] Julien Giboz, Thierry Copponnex, and Patrice Mélé. Microinjection molding of thermoplastic polymers: a review. *J. Micromechanics Microengineering*, 17(6):R96–R109, jun 2007.

[42] Can Yang, Xiao-Hong Yin, and Guang-Ming Cheng. Microinjection molding of microsystem components: new aspects in improving performance. *J. Micromechanics Microengineering*, 23(9):093001, sep 2013.

[43] Bwng H. Kim and Nam P. Suh. Low Thermal Inertia Molding (LTIM). *Polym. Plast. Technol. Eng.*, 25(1):73–93, mar 1986.

[44] J.C. Viana. Development of the skin layer in injection moulding: phenomenological model. *Polymer (Guildf).*, 45(3):993–1005, feb 2004.

[45] A.-C. Liou and R.-H. Chen. Injection molding of polymer micro- and sub-micron structures with high-aspect ratios. *Int. J. Adv. Manuf. Technol.*, 28(11-12):1097–1103, may 2006.

[46] Christian Gornik. Injection Moulding of Parts with Microstructured Surfaces for Medical Applications. *Macromol. Symp.*, 217(1):365–374, oct 2004.

[47] Ming J Liou and Nam P Suh. Reducing residual stresses in molded parts. *Polym. Eng. Sci.*, 29(7):441–447, apr 1989.

[48] Donggang Yao and Byung Kim. Development of rapid heating and cooling systems for injection molding applications. *Polym. Eng. Sci.*, 42(12):2471–2481, dec 2002.

[49] Youngmin Kim, Yong Choi, and Shinill Kang. Replication of high density optical disc using injection mold with MEMS heater. *Microsyst. Technol.*, 11(7):464–469, jul 2005.

[50] Cheng-Long Xiao and Han-Xiong Huang. Multiobjective optimization design of heating system in electric heating rapid thermal cycling mold for yielding high gloss parts. *J. Appl. Polym. Sci.*, 131(6):n/a–n/a, mar 2014.

[51] Guilong Wang, Guoqun Zhao, and Yanjin Guan. Thermal response of an electric heating rapid heat cycle molding mold and its effect on surface appearance and tensile strength of the molded part. *J. Appl. Polym. Sci.*, 128:n/a–n/a, 2012.

[52] Keun Park and Sang-Ik Lee. Localized mold heating with the aid of selective induction for injection molding of high aspect ratio micro-features. *J. Micromechanics Microengineering*, 20(3):035002, mar 2010.

[53] J Bekesi, J J J Kaakkunen, W Michaeli, F Klaiber, M Schoengart, J Ihlemann, and P Simon. Fast fabrication of super-hydrophobic surfaces on polypropylene by replication of short-pulse laser structured molds. *Appl. Phys. A*, 99(4):691–695, jun 2010.

[54] Pei-Chi Chang and Sheng-Jye Hwang. Experimental investigation of infrared rapid surface heating for injection molding. *J. Appl. Polym. Sci.*, 102(4):3704–3713, nov 2006.

[55] Jitao Liu, Guoqun Zhao, Guilong Wang, and Yanjin Guan. Fully Coupled Transient Heat Transfer and Melt Filling Simulations in Rapid Heat Cycle Molding with Steam Heating. *Polym. Plast. Technol. Eng.*, 50(4):423–437, feb 2011.

[56] Walter Michaeli and Fritz Klaiber. Development of a system for laser-assisted molding of micro- and nanostructures. *J. Vac. Sci. Technol. B Microelectron. Nanom. Struct.*, 27(3):1323, 2009.

[57] Thor Christian Hobæk, Maria Matschuk, Jan Kafka, Henrik J Pranov, and Niels B Larsen. Hydrogen silsesquioxane mold coatings for improved replication of nanopatterns by injection molding. *J. Micromechanics Microengineering*, 25(3):035018, mar 2015.

[58] John M. Stormonth-Darling and Nikolaj Gadegaard. Injection Moulding Difficult Nanopatterns with Hybrid Polymer Inlays. *Macromol. Mater. Eng.*, 297(11):1075–1080, nov 2012.

[59] Xiaolong Zhu, Christoph Vannahme, Emil Højlund-Nielsen, N. Asger Mortensen, and Anders Kristensen. Plasmonic colour laser printing. *Nat. Nanotechnol.*, (December):1–6, dec 2015.

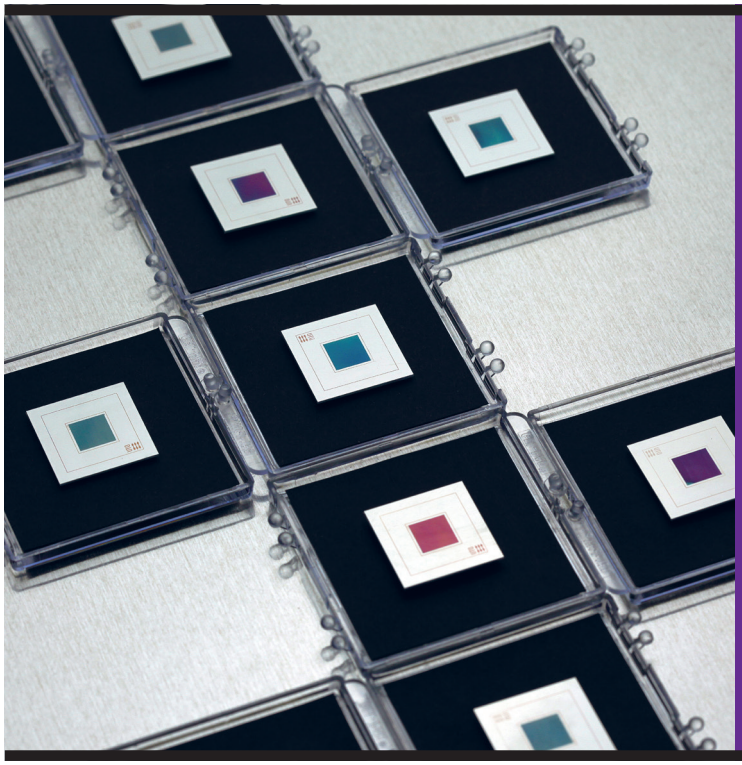

Copyright: Emil Højlund-Nielsen
All rights reserved

Published by:
DTU Nanotech
Department of Micro- and Nanotechnology
Technical University of Denmark
Ørsteds Plads, building 345B
DK-2800 Kgs. Lyngby